RELEASE OF FISSION XENON FROM HIGH SURFACE AREA URANIUM TARGETS

A THESIS

Presented to

The Faculty of the Division of Graduate

Studies and Research

By

Milton Eccles McLain, Jr.

In Partial Fulfillment

of the Requirements for the Degree

Doctor of Philosophy

in the School of Nuclear Engineering

Georgia Institute of Technology

September, 1972

In presenting the dissertation as a partial fulfillment of the requirements for an advanced degree from the Georgia Institute of Technology, I agree that the Library of the Institute shall make it available for inspection and circulation in accordance with its regulations governing materials of this type. I agree that permission to copy from, or to publish from, this dissertation may be granted by the professor under whose direction it was written, or, in his absence, by the Dean of the Graduate Division when such copying or publication is solely for scholarly purposes and does not involve potential financial gain. It is understood that any copying from, or publication of, this dissertation which involves potential financial gain will not be allowed without written permission.

Milton E. McLain, Jr.

7/25/68

RELEASE OF FISSION XENON FROM HIGH SURFACE AREA URANIUM TARGETS

Approved:

J. A. Knight, Jr., Chairman

H. M. Neumann

W. W. Graham, III

D. S. Harmer

Date approved by Chairman: Sept. 14, 19

ACKNOWLEDGMENTS

The research effort described in this thesis is the end result of a lengthy investigation in which the support, both physical and moral, of many persons was essential for success.

My thesis advisor, Dr. J. A. Knight, Jr., devoted many hours from his crowded research schedule to discuss the work and comment on the thesis as it was developed. Other members of the reading committee brought to the task an unusual variety of technical competence which has substantially contributed to the completion of this work.

The research discussion with Dr. D. M. Walker and Mr. R. C. McFarland, and the essential electronic assistance of Mr. R. E. Meek are most sincerely appreciated. The aid of Mr. R. A. Hearn in the preparation of radioisotope standards is gratefully acknowledged. The diligent work of Mr. H. T. Johnson in constructing the special shield plug for the reactor made the loop experiment possible.

Without the patient assistance and cooperation of the Georgia Tech Research Reactor Operations Group not a single uranium-235 nucleus could have been fissioned. Furthermore, their assistance was readily given even with the odd work hours imposed by a part-time graduate student's research.

The efforts of Dr. S. Spooner in obtaining the neutron diffraction patterns were vital to this work, as were the scanning electron microscopy by Mr. J. L. Hubbard and the electron microprobe measurements by Mr. J. W. Johnson.

All of the obvious problems in such a complex research effort which have been alluded to in the preceding acknowledgments are insignificant in comparison to the sacrifices brought to the altar of academic achievement by my wife, Lila, and daughters Loren, Kathryn, and Deborah. This unfortunate group has suffered through seven years of periodic neglect. Their unfailing support and continued affection has not gone without notice and deep appreciation. Without such devotion and sacrifice from my family, this document would not have been completed.

TABLE OF CONTENTS

TABLE OF CONTENTS (Concluded)

LIST OF TABLES

LIST OF TABLES (Concluded)

LIST OF ILLUSTRATIONS

LIST OF ILLUSTRATIONS (Continued)

LIST OF ILLUSTRATIONS (Continued)

LIST OF ILLUSTRATIONS (Continued)

LIST OF ILLUSTRATIONS (Concluded)

SUMMARY

Fission-produced xenon-135 is potentially the preferred isotope for medical applications in the diagnosis of lung and circulatory disorders. This radionuclide has a more favorable gamma-ray energy and higher gamma-ray abundance than xenon-133 which is presently in use.

The concept of the application of high surface area uranium targets for the simultaneous production and separation of the gaseous fission products was proven practical. This method does not require hot cell facilities for processing irradiated uranium targets, nor does it incur the liability of volumes of high-level liquid radioactive wastes as a consequence of chemical processing of irradiated targets.

The ability of the synthetic zeolites (molecular sieves) to absorb uranyl ions was studied and proven suitable for the preparation of high surface-area uranium-235 reactor targets. Such targets may contain up to 10 percent uranium by weight. Measured effective diffusion coefficients and activation energy for the ion exchange process from methanol solvent were consistent with data previously reported for similar ion exchange processes. The rate controlling step in the ion exchange of uranyl ion from methanol solutions of uranyl nitrate hexahydrate onto molecular sieve beads was shown to be uranyl ion diffusion through the inter-crystallite space of the beads. The beads are formed of approximately two micron diameter crystallites cemented together with clay binder.

The microporous structure of the Type 13X molecular sieves was shown experimentally to release up to 46 percent of the xenon-135 fission product from irradiated uranium-loaded material. The rate of release is rapid, but apparently limited by a trapping mechanism. The trapping sites are probably the small sodalite cage units of the molecular sieve crystal structure.

The laboratory data on the release of xenon fission product gases from uranium-loaded synthetic zeolites were applied to the design of a prototype reactor loop apparatus for the continuous production of xenon-135. This prototype was constructed, installed, and operated in the Georgia Tech Research Reactor. The loop target consisted of 1.35 grams of 93 percent enriched uranium-235 on Type 13X molecular sieve beads. Operated at a thermal neutron flux of 5.45×10^{11} nv the loop produced 150 millicuries of xenon-135 per 14 hours of reactor operation.

Temperatures in excess of 500°C were experienced by the target during operation of the loop. Self-heating was the limiting factor in xenon-135 production in the prototype apparatus. Application of the techniques of neutron diffraction, scanning electron microscopy, and electron microprobe X-ray analysis was able to relate degradation of the target efficiency to thermal damage of the uranium-loaded region of the molecular sieve target beads.

CHAPTER I

INTRODUCTION

Radioactive xenon-133 is routinely used by the medical profession in the diagnosis of respiratory disease, quantitative measurement of lung function, and in dynamic, in vivo studies of regional blood circulation. Some use of xenon-133 in industrial tracer applications has also been made (1).

The gaseous radioactive isotopes of xenon are produced in high yield during thermal neutron induced fission of uranium-235. The first production for distribution of the radioisotope xenon-133 began in September 1962 from the Oak Ridge National Laboratory. In the year 1971, almost 1800 curies of xenon-133 were shipped from that U. S. Atomic Energy Commission facility.

The principal deficiency of xenon-133 (5.3 day half-life) in its application as a radioactive tracer is the rather low energy of its gamma-ray (81 keV) which is emitted in only 35 percent of xenon-133 decays. Characteristics of chemical inertness and short biological half-life (15 minutes) combine to minimize patient radiation dose. These advantageous properties are, of course, common to all xenon radioisotopes.

Eleven radioactive xenon nuclides are known to be produced in the fission process. These nuclides and their basic properties are summarized in Table 1. The only xenon isotope having a reasonable half-life for application to practical problems other than xenon-133 is 9.2 hour xenon-135.

Table 1. Xenon Radionuclides Produced in ^{235}U Fission (2)

Atomic Mass	Half-life	Principal Gamma-ray (keV)
133	5.27 days	81
135	9.16 hours	249.6
135m	15.7 minutes	526.8
137	8.82 minutes	455.6
138	14.2 minutes	258.2
139	39.7 seconds	219
140	14.3 seconds	805.5
141	1.72 seconds	Several of unknown intensities
142	1.24 seconds	571.7
143	0.96 second	Unknown
144	8.8 seconds	Unknown

As shown in Table 1, xenon-135 emits a 249.6 keV gamma-ray following 97.1 percent of its disintegrations. This is an ideal energy for medical diagnostic gamma-ray scanning. Xenon-135 would, therefore, be superior to the presently used xenon-133 for medical applications and could be successfully applied as a gaseous radioactive tracer to other practical problems in industry, if readily available. Figure 1 gives the decay schemes for xenon-133 and -135 (3).

Irradiation of natural xenon for purposes of production of useful quantities of xenon-135 via the $^{134}Xe(n,\gamma)^{135}Xe$ reaction is impractical due to the effective activation cross section of only 20 millibarns (4,5). The low density of the gas also contributes to the unsuitability of production by neutron irradiation of xenon gas targets. This leaves uranium-235 fission as the only practical method of production.

The 9.16 hour half-life of xenon-135 has precluded its routine production by the Oak Ridge National Laboratory isotope production facilities. Likewise, two commercial radioisotope manufacturers who began production of xenon-133 in 1971 do not perform their fission product separations within sufficient time after irradiation of the uranium-235 target to recover the xenon-135.

A few investigators interested in decay scheme studies or exploratory work with applications of xenon-135 have prepared this isotope by chemical dissolution of irradiated uranium oxide or uranium metal targets, which releases the gaseous fission product nuclides (6-9). This approach does not lend itself to production of xenon-135 at regular rates of hundreds of millicuries to curies per day. The target materials are expensive

XENON-133 DECAY SCHEME SHOWN
PRODUCES GAMMA-RAYS OF THE
FOLLOWING ENERGIES (MeV):

0.356, 0.276, 0.054, 0.382
0.302, 0.220, 0.161, 0.0796, 0.081

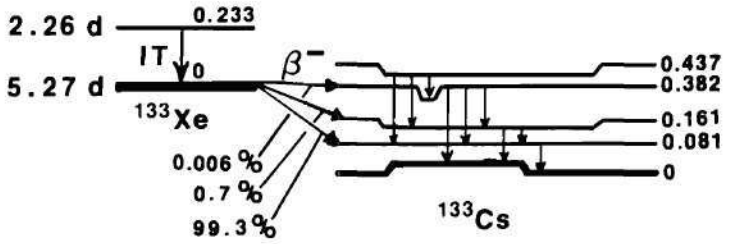

XENON-135 DECAY SCHEME SHOWN
PRODUCES GAMMA-RAYS OF THE
FOLLOWING ENERGIES (MeV):

0.840, 0.781, 0.61, 0.36, 0.250

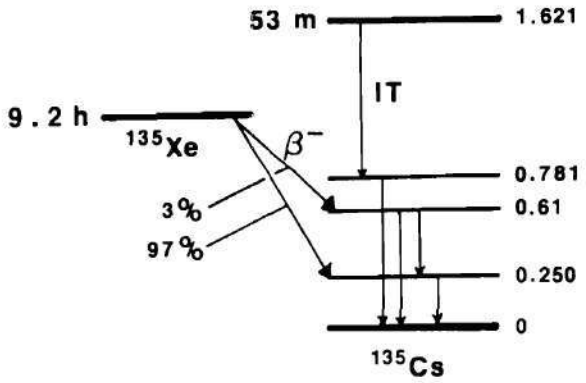

Figure 1. ^{133}Xe and ^{135}Xe Decay Schemes
(from reference 3)

and large volumes of high level radioactive liquid wastes are generated which require disposal.

High surface area uranium-235 targets, when irradiated, should release substantial fractions of the gaseous fission products. This is analogous to the classical "emanation" phenomenon observed in the release of radon gas from compounds of radium (10). This method has been applied to production of small quantities of the short-lived fission product gases for purposes of decay scheme and half-life measurements (11,12).

In related work, Chleck (13) has described the use of "kryptonates" formed by the infusion of krypton-85 under the influence of high temperature and pressure into a variety of materials. These "kryptonates" will release the radioactive gas upon heating or chemical attack of the material.

A real advance in the production of the gaseous fission product radionuclides would be realized by the development of a uranium target capable of semi-permanent installation in a reactor from which the fission product gases could be separated by flow of a carrier gas through the target. The radioactive gases would then be separated from the carrier gas by facilities external to the reactor. This concept would avoid the problems of a one-time target expense, disposal of large quantities of radioactive wastes, and the necessity for extensive hot cell facilities for remote processing of the extremely radioactive irradiated targets. Such a system would permit the production of these radionuclides at nuclear reactors with limited auxiliary facilities.

Thin layers of uranium oxide (U_3O_8) have been studied as sources of radioactive fission products. Such deposits can be formed by thermal degradation of uranyl nitrate coatings or by electrolytic deposition onto

metal foils. They possess adequate thermal and radiation stability. The technology for their preparation is well-developed and they are worthy of examination.

Hydrous silicon dioxide (silica gel) is an amorphous form of silica which is known to have a very high surface area and to be porous to diffusion of gases. Some work has been done on the ability of silica gel to adsorb metal cations by ion exchange (14) and this appears feasible for uranium. Silica gel is stable at high temperatures and is moderately resistant to radiation damage. The potential use of silica gel as the supporting material for the uranium was considered reasonable.

Synthetic crystalline aluminosilicates ("molecular sieves") have the necessary high surface area to enhance the release of the fission product gases. They also exhibit ion exchange absorption of metal cations. These molecular sieves have the required temperature and radiation resistance necessary to withstand the reactor environment of gamma and neutron radiation. This combination of properties on the part of the synthetic aluminosilicates made them the material of choice in this investigation.

The study of suitable high surface area support materials for uranium and the development of a practical method for production of xenon-135 was undertaken in three rather distinct, but interrelated parts. Chapter II is concerned with the consideration of the three possible target materials; i.e., thin uranium oxide coatings on metal surface, uranium-loaded silica gel, and uranium-loaded molecular sieves. Chapter III examines the release of gaseous fission products (specifically xenon-133 and xenon-135) on a laboratory scale from test support materials.

Chapter IV applies the information learned in Chapters II and III to the design, construction, operation, and evaluation of a xenon-135 production prototype reactor loop in the Georgia Tech Research Reactor.

CHAPTER II

HIGH SURFACE AREA URANIUM TARGET DEVELOPMENT

1.0 Technical Background

1.1 General

The initiation of this study was prompted by work in radiation chemistry of fission fragments at Georgia Institute of Technology in 1965 (15). In this work a thin layer of uranium-235 oxide (U_3O_8) was prepared by coating aluminum foil with a solution of uranyl nitrate (93 percent enriched in the mass-235 isotope) in collodion and then igniting the coated foil in air at 500°C. In this earlier study the radiation effects of the energetic fission fragments on liquid hydrocarbons were examined. The experimental procedure was to subject the uranium-coated aluminum foil to reactor thermal neutron irradiation while the foil was submerged in the hydrocarbon liquid contained in a sealed quartz vial. Data on the identity and quantity of the various products of the fission fragment radiation damage to the hydrocarbon were obtained by gas-liquid chromatographic separations of the liquid and gaseous phases from the irradiated vial. Although the carbon and hydrogen from the liquid under study did not produce radioactive products as a result of the neutron irradiation, there was concern as to the fate of the radioactive fission products captured by the hydrocarbon during the irradiation of the sample. Gamma-ray spectra of the hydrocarbon liquid and of samples of the gas space above the liquid revealed that the principal radioactive nuclide present was

xenon-133. The predominance of this nuclide is explained by its occurrence near the heavy fragment maximum in the fission yield curve (16) as shown in Figure 2, and the properties of the inert gases. Several days had elapsed between removal from the reactor and examination of the liquid and gaseous phases by gamma-ray spectrometry. This explains the absence of shorter-lived xenon-135 and krypton fission product nuclides, all of which have half-lives shorter than 10 hours with the exception of krypton-85 (10.76 years). Krypton-85 emits a gamma-ray with only 0.41 percent of its disintegrations and this factor coupled with its slow decay rate made detection unlikely.

This work pointed to the possible use of high surface area uranium targets for simultaneous production and separation of gaseous fission product radionuclides.

In-pile release experiments at Harwell, England (17) have also demonstrated the quantitative aspects of recoiling fission fragment implantation in source backing and container walls. In addition, the data from these experiments with thin U_3O_8 deposits suggest that, with the proper target (high surface area:mass ratio), the gaseous fission product release fraction may be sufficiently large for the design of a practical process for the production of these useful radionuclides.

It is of interest at this point to examine the relationship of surface area to volume as a function of particle radius. The surface area (A) of a particle of radius r is:

$$A = 4\pi r^2$$

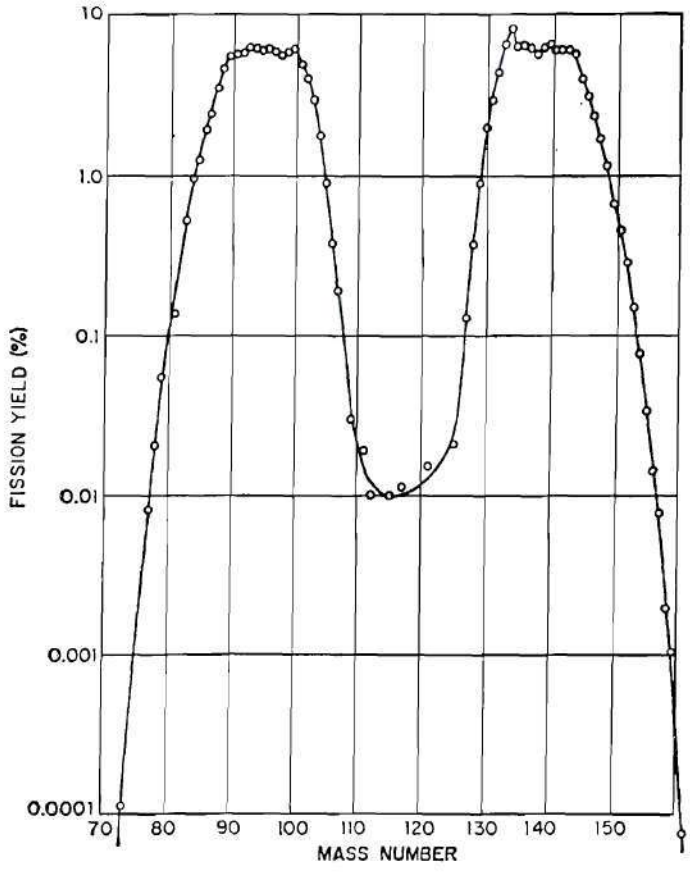

Figure 2. Mass Yield Curve for Thermal Neutron Fission of ^{235}U (from reference 16)

The volume (V) of this same particle is:

$$V = \frac{4}{3} \pi r^3$$

The ratio of surface area to volume for this particle is, therefore:

$$\frac{A}{V} = \frac{3}{r}$$

The results of a set of calculations of this ratio as a function of particle diameter are shown in Figure 3. The choice of a target material containing uranium in a very finely-divided form can (as shown in Figure 3) gain considerable advantage from the increased "specific surface."

The literature of nuclear technology abounds with references pertaining to the release of fission product xenon from uranium and uranium compounds. However, almost without exception, until now the interest has been directly associated with the design and performance of reactor fuel materials where the prime objective was maximizing retention of the radioactive fission product gases. The exception to this is the extensive research and development associated with the homogeneous reactor concept. An integral part of that reactor design is the continuous processing of the fuel solution for removal of the high cross section fission products; e.g., xenon-135 with a thermal neutron cross section of 2.7×10^6 barns. For purposes of developing a procedure for production of xenon fission product isotopes, it is not considered practical to irradiate uranium solutions due to the difficulty of reliable target containment and related safety implications.

A phenomenon similar in principle to the release of fission product

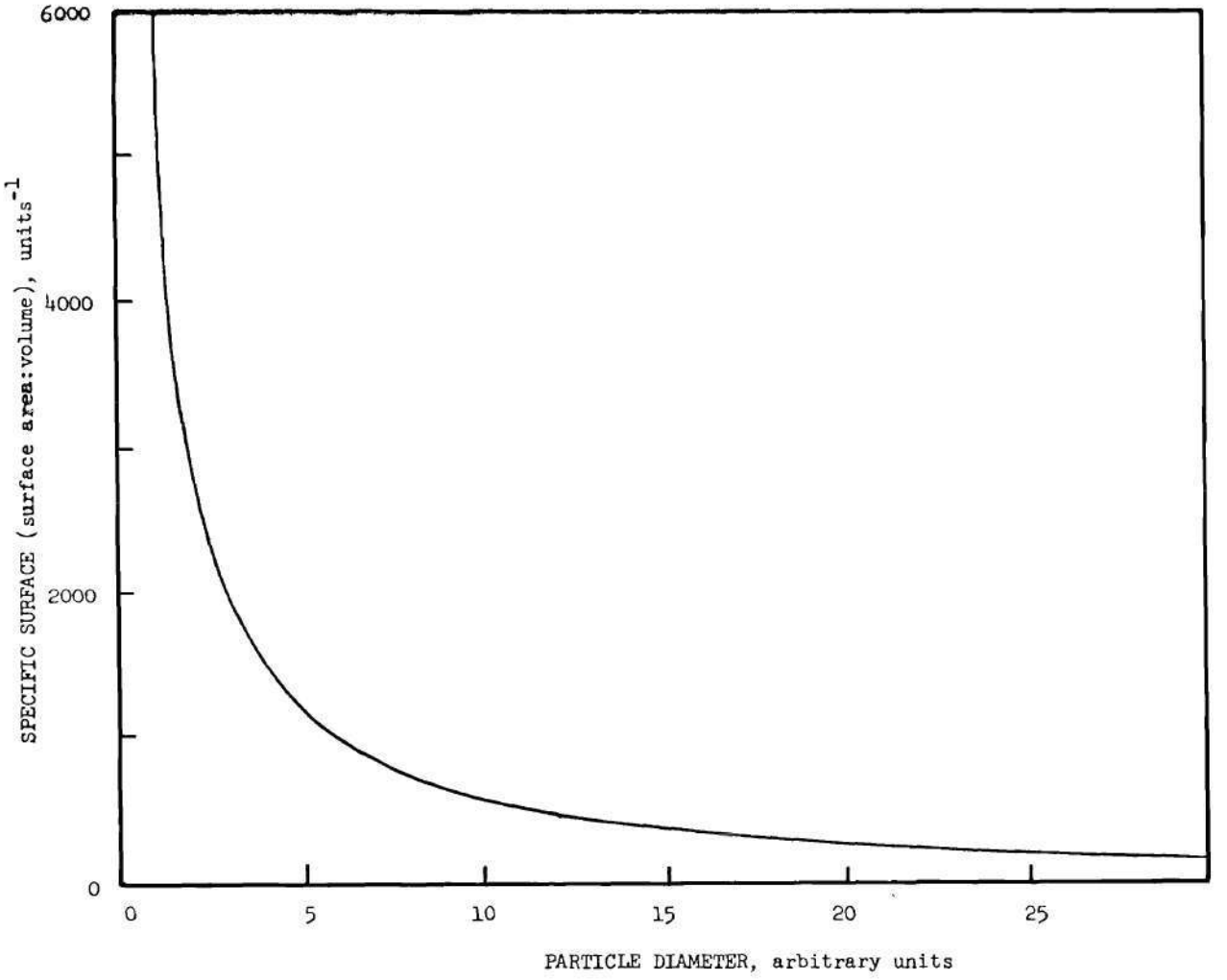

Figure 3. Specific Surface as a Function of Particle Diameter

xenon under study here is emanation (10). This term refers to the escape of radioactive inert gas daughters from substances containing their parent nuclides. The total "emanating power" or fractional emission is due to the sum of the inert gas daughter escaping through the recoil process at the time of parent alpha decay and the subsequent release by diffusion through the sample matrix before the individual gas atom decays.

Recent work at McMaster University in Canada (11,12) utilized the "emanating power" of such materials as uranyl stearate, hydrous zirconium oxide, and others in the preparation of xenon-138 and other very short-lived fission product nuclides for purposes of gamma-ray spectrometric decay scheme studies. This work, as well as other attempts using zirconium phosphate, suffered because of acute radiation damage to the high surface area material upon which the uranium was deposited. This resulted in serious reduction in the fraction of fission product gases released. No mechanism for the target deterioration was proposed by the investigators.

The basic requirements for an acceptable supporting material for the uranium-235 target are: 1) high specific surface area (large surface area per gram); 2) toleration of relatively high temperatures to withstand fission self-heating as a necessary consequence of the fission process; 3) low susceptibility to radiation damage; and 4) a capacity for incorporation of reasonable quantities of uranium into or onto the supporting medium.

Three classes of materials were considered to be reasonable choices to meet the requirements just outlined: 1) uranium oxide electrodeposited on metal surfaces; 2) uranyl ions ion exchanged onto silica gel; and 3)

synthetic aluminosilicates (molecular sieves) as the ion exchange material for uranyl ions.

1.2 Electrodeposited Uranium Oxide Films

The U_3O_8 films were selected for consideration because of their relative ease of preparation and the background of information available for fission gas release from similar materials. The Harwell work gives encouragement that thin U_3O_8 films may make suitable targets for efficient release of fission product gases (Table 2). Of interest are the improved capture efficiencies for the recoiling fission fragments when nitrogen carrier gas is used in comparison to helium. The greater density of nitrogen reduces the fission fragment range and, thereby, increases the fraction of fragments captured in the gas space around the target. In this work at Harwell, the uranium films were prepared by the evaporation of a solution of uranyl nitrate in collodion and subsequent ignition to U_3O_8. More precision and uniformity in film thickness can be attained when the film is deposited electrolytically. The electrolysis of aqueous solutions of uranyl nitrate has long been used as a technique for the preparation of thin uranium deposits on metal disks for the purpose of assay by alpha particle counting (18-23). The chemical activity of uranium metal precludes the electrodeposition of uranium metal from aqueous electrolyte solutions. Electrodeposition of uranium metal has been achieved from non-aqueous solvents and from molten salt electrolytes. This was the method by which the first pure uranium metal was prepared by the Manhattan Project during World War II (24).

Table 2. In-Pile Emission of Radioactive Rare Gases from U_3O_8 on Platinum (17)

DIDO REACTOR EXPERIMENTS

neutron flux 2.7×10^{13} neutrons/cm^2/sec — temperature 375°C

vessel dimensions 4.7 cm diameter, 6.7 cm long — U_3O_8 thickness 0.6 μ

Results obtained using Nitrogen as carrier gas

	^{135}Xe	^{85m}Kr	^{133}Xe
calculated rate of emission by recoil (N_c) atoms/sec	243×10^6	59×10^6	255×10^6
measured rate of emission (N_o) atoms/sec	27.0×10^6	7.7×10^6	90.0×10^6
measured percentage capture efficiency (100 N_o/N_c)	11.1	13.1	35
theoretical percentage capture efficiency (100 F_t)	12.5	7.3	12.5
ratio of measured to theoretical percentage capture efficiencies	0.9	1.8	2.7

Results obtained using Helium as carrier gas

	^{135}Xe	^{85m}Kr	^{133}Xe
calculated rate of emission by recoil (N_c) atoms/sec	243×10^6	59×10^6	255×10^6
measured rate of emission (N_o) atoms/sec	3.8×10^6	2.3×10^6	13.4×10^6
measured percentage capture efficiency (100 N_o/N_c)	1.6	3.8	5.3
theoretical percentage capture efficiency (100 F_t)	< 2	< 2	< 2

Table 2. (Concluded)

BEPO REACTOR EXPERIMENTS

neutron flux 1.0×10^{12} neutrons/cm^2/sec

temperature 375°C

vessel dimensions 4.4 cm diameter, 7.2 cm long

U_3O_8 thickness 3.0 μ

	Carrier gas	^{135}Xe	^{85m}Kr	^{133}Xe
measured percentage capture efficiency	NITROGEN	27.5	24.0	53.0
theoretical percentage capture efficiency	NITROGEN	11.0	6.5	11.0
measured percentage capture efficiency	HELIUM	4.1	3.8	8.7
theoretical percentage capture efficiency	HELIUM	< 2	< 2	< 2

$$\text{Measured percentage capture efficiency} = \frac{\text{measured rate of emission}}{\text{calculated rate of emission}} \times 100$$

Electrodeposition of uranium as hydrous oxide on platinum, copper, and stainless steel can be achieved from a variety of electrolyte solutions. Oxalate, acetate, fluoride, nitrate, and carbonate electrolytes have all been successfully used in the electrodeposition of uranium from aqueous solutions, but the oxalate is superior in that it produces deposits exhibiting better adherence to the metal cathode surface. This permits the successful preparation of deposits up to one mg cm^{-2} without flaking of the deposited oxide.

The chemical identity of the hydrous uranium oxide deposited on the cathode when the uranyl nitrate solution is electrolyzed has not been definitely established. Choppin (25) refers to it as $U(OH)_4$, which is equivalent to $UO_2 \cdot 2H_2O$. However, heating in air at 700 °C results in a conversion of the hydrous oxide to U_3O_8:

$$3UO_2 \cdot xH_2O + O_2 \longrightarrow U_3O_8 + xH_2O$$

Since U_3O_8 is stable in air and at elevated temperatures, the deposited hydrous uranium oxide will be converted to U_3O_8 for the experiments in this investigation.

1.3 Uranium Ion Exchanged Onto Silica Gel

Silica gel (hydrous silicon dioxide) is a commonly used desiccant. It is normally used in a granular form and is an amorphous, chemically inert, extremely porous form of silicon dioxide. Silica gel has a typical pore diameter of 10 Å (26) and a specific surface area of 600-800 $m^2 g^{-1}$ (27). These parameters vary with the conditions of synthesis of the particular silica gel. Synthesis of silica gel is relatively simple. A

typical procedure (28) is to mix two solutions--one solution of sodium silicate and one of dilute hydrochloric acid. A gel quickly forms which, when washed, then dried at 150°C and calcined at 550°C, is the familiar silica gel frequently used as a desiccant in the laboratory and for industrial applications.

Silica gel exhibits cation exchange properties. The tetravalent silicon atom is highly electronegative causing the Si-O-H grouping to be weakly acidic. When the proton dissociates, cations can be bound at this site when silica gel is contacted with solutions of these cations. Figure 4 shows the dependence of the distribution coefficient for the ion exchange of uranyl ions (UO_2^{+2}) on silica gel as a function of solution pH (14). The distribution coefficient is defined as the milliequivalents of an ion adsorbed per gram of exchanger divided by the milliequivalents per milliliter of that ion remaining in solution. It is, therefore, a measure of the efficiency or completeness of the exchange reaction between the exchanger and a particular dissolved ion. Calculating from the data in Figure 4 at pH 3 for uranyl ion, the distribution coefficient for silica gel is found to be 0.0126. This is a very low value when compared, for example, with the distribution coefficient of Ba^{+2} ions on Dowex-50x8 (a sulfonated polystyrene-divinylbenzene copolymer resin exchanger) in 1 M hydrochloric acid which has a value of 127 (29). The ability of silica gel to ion exchange uranyl ions has been noted by others (30). The saturated capacity is given as 1.2 - 1.4 milliequivalents per gram, whereas typical exchange capacities for the conventional sulfonated organic copolymer resins are in the range of 3-6 milliequivalents per gram.

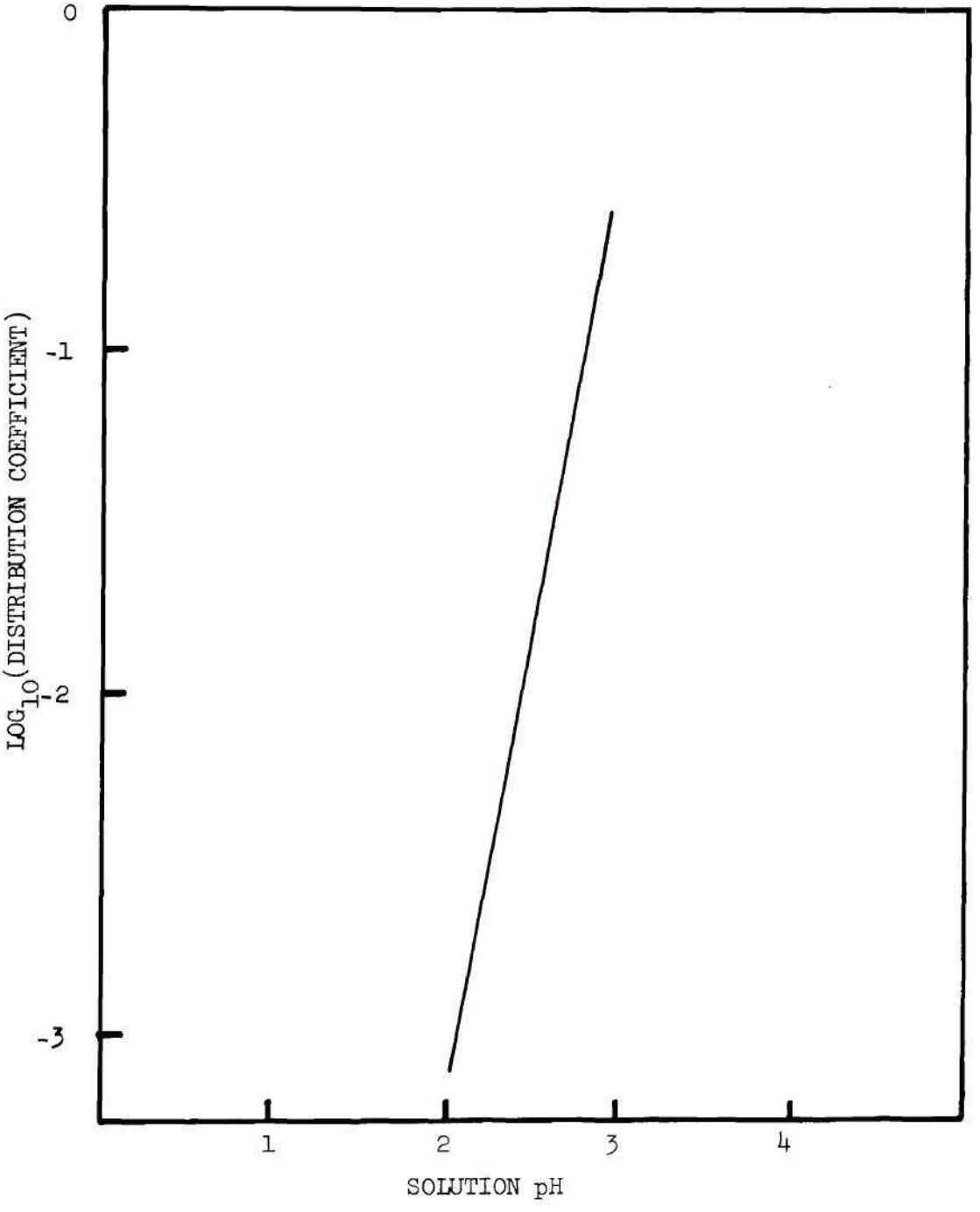

Figure 4. Absorption of Uranyl Ions on Silica Gel (from reference 14)

Silica gel is, therefore, a rather ineffective ion exchange material when compared with conventional ion exchangers.

As noted in the brief description of a synthesis method for silica gel, in which the product was calcined at 550°C, the high temperature tolerance of this material appears to be adequate. It is common for reactor experiments to be limited to an upper temperature of about 500°C since contact with aluminum structural metal (melting point: 659.7°C) is often unavoidable.

Abundant information on the effects of radiation energy deposition in silica gel is available as a result of extensive work on radiation chemical processing and silica gel catalyst activation by gamma-radiation energy transfer. Synergistic interactions of radiation and the high surface area of silica gel were thoroughly investigated (31). These studies involved gamma radiation effects almost exclusively. Gamma radiation at the two megarad level was reported to increase the absorption rate and capacity of silica gel for hydrogen, oxygen, and nitrogen absorption. Exposure to the intense neutron and gamma radiation of a nuclear reactor was shown (32) to cause a reduction in surface area which was more pronounced in high surface area silica gel (800 $m^2 g^{-1}$) than with lower surface area material (200 $m^2\ g^{-1}$).

Another investigation in France (33) demonstrated a strong sintering effect when silica gel was irradiated with neutrons to a dose of 10^{19} neutrons cm^{-3}. The specific surface area and total pore volume were reduced. Electron microscopy demonstrated the presence of distinct centers of crystallization in the irradiated material which was initially completely

amorphous. This may be the result of localized melting and recrystallization (thermal spikes).

Combined thermal neutron and gamma radiation was found to decrease the capacity of silica gel for Ca^{+2} ion adsorption (34).

Thermal neutron irradiation of silica gel to a dose of 3×10^{19} neutrons cm^{-2} accompanied by 8×10^{18} neutrons cm^{-2} in the 0.4 - 1 MeV energy range, 6.8×10^{16} neutrons cm^{-2} at energies greater than 1 MeV, and 1.2×10^{13} roentgens gamma radiation resulted in a 20 percent reduction in surface area and pore volume (35).

In summary, silica gel does have the basic properties needed, but suffers from a rather low ion exchange capacity and experiences degradation in porosity as a result of radiation damage. Further consideration of the use of silica gel as the support material for uranium in this work was not warranted.

1.4 Uranium Ion Exchanged Onto Molecular Sieves

In the 18th century the Swedish mineralogist, Baron Cronstedt, observed that certain crystalline aluminosilicate minerals appeared to melt and boil simultaneously upon heating (36). From the two Greek words "zeo," to boil, and "lithos," stone, he formed the name "zeolite" for these minerals.

The zeolites fall into one of the six mineralogical classes of silicate minerals, the tectosilicates. The principal feature which distinguishes the tectosilicates is a three-dimensional framework of SiO_4 tetrahedra. The sharing of the oxygen atoms by neighboring silicon atoms forms a three-dimensional atomic arrangement, resulting in a very stable structure. This tectosilicate class is further subdivided into five

subgroups:

(1) SiO_2 group
(2) Feldspar group
(3) Scapolite group
(4) Feldspathoid group
(5) Zeolite group

The natural zeolite minerals are a family of hydrated silicates similar in composition and structure. Table 3 lists the natural zeolites and their basic properties and chemical compositions (37).

One distinguishing feature of the zeolite structure is that it includes AlO_4 tetrahedra alternating with the basic SiO_4 tetrahedra. Cations such as sodium and calcium are attached to the structure to compensate for the net negative charge left as a result of the trivalent aluminum atoms. These ions can be replaced by other cations and are the means by which the zeolites exhibit cation exchange properties. Figure 5 shows the basic atomic arrangement in two dimensions.

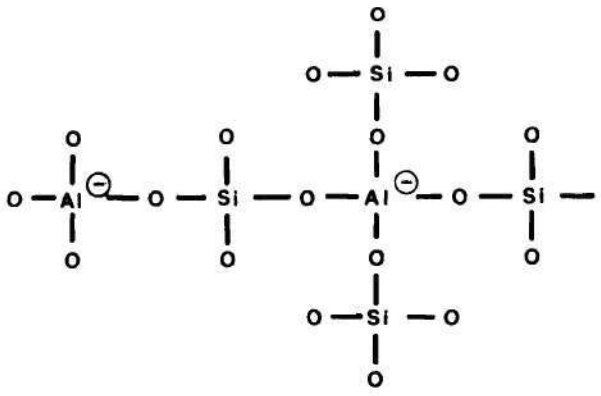

Figure 5. Two-Dimensional Representation of an Aluminosilicate Framework

Table 3. The Natural Zeolites. Chemical and Physical Properties (37)

Mineral	Composition	Cryst.	Hardness	Sp.Gr.*	Refract. Index	Color**
Analcite	$Na_2Al_2Si_4O_{12}\cdot 2H_2O$	C	5-5.5	2.2-2.3	1.4874	-,W
Brewsterite	$BaSrAl_2Si_6O_{16}\cdot 5H_2O$	M	5	2.1-2.5	1.512	W,Y,Gr
Cancrinite	$Na_8CaAl_8Si_9O_{35}\cdot 3H_2O\cdot 2CO_2$	H	5-6	2.4-2.5	1.524	W,Y,Gr
Chabazite	$CaNa_2Al_2Si_4O_{12}\cdot 6H_2O$	H	4-5	2.1-2.2	1.480 1.485	W,R,Flesh
Edingtonite	$Ba_4Al_2Si_3O_{10}\cdot 4H_2O$	R	4-4.5	2.7-2.8	1.549	W,grnW,Pk
Epistilibite	$CaAl_2Si_6O_{16}\cdot 5H_2O$	M	3.5-4	2.25	1.510	W
Erionite	$CaMgNa_2K_2Al_2Si_6O_{16}\cdot 6H_2O$	H				
Faujasite	$CaNa_2Al_2Si_4O_{20}\cdot 8H_2O$	C				
Gismondite	$CaK_2Al_2Si_2O_8\cdot 4H_2O$	M	4.5	2.265	1.539	-,W,r,gr
Gmelinite	$CaNa_2Al_2Si_4O_{12}\cdot 6H_2O$	H	4.5	2-2.1	1.465 1.485	yW,grnW,rW,R
Harmotome	$BaK_2Al_2Si_5O_{14}\cdot 5H_2O$	M	4.5	2.4-2.5	1.505	W,Gr,Y,R,Br
Heulandite	$CaNa_2Al_2Si_6O_{16}\cdot 5H_2O$	M	3.5-4	2.1-2.2	1.499	W,R,Gr,Br,-

Table 3. (Concluded)

Mineral	Composition	Cryst.	Hardness	Sp.Gr.*	Refract. Index	Color**
Laumonite	$CaNa_2Al_2Si_4O_{12}\cdot 4H_2O$	M	3-4	2.2-2.4	1.524	W,y,GrR
Levynite	$CaAl_2Si_3O_{10}\cdot 5H_2O$	H	4-4.5	2.1-2.2	1.496	W,gr,p,y
Methascolecite						
Metathomsonite						
Mesolite of Natrolite and Scolecite	$Na_2Al_2Si_3O_{10}\cdot 2H_2O$	M	5	2.29	1.505	W,-
Mordenite	$CaNa_2Al_2Si_4O_{12}\cdot 6H_2O$	H				
Natrolite	$Na_2Al_2Si_3O_{10}\cdot 2H_2O$	M	5-5.5	2.2-2.35	1.482	-,W,gr,yr,R
Phillipsite	$K_2CaAl_2Si_4O_{12}\cdot 4.5H_2O$	M	4-4.5	2.2-2.4	1.500	W,r
Scolecite	$CaAl_2Si_3O_{10}\cdot 3H_2O$	M	5-5.5	2.16-2.4	1.519	-.W,Y
Staurolite	$Fe_2Al_{10}Si_4O_{25}\cdot H_2O$	R	7-7.5	3.65-3.77	1.741	dBr,br,Blk,y,yBr
Stilbite	$Na_2CaAl_2Si_6O_{16}\cdot 6H_2O$	M	3.5-4	2.0-2.2	1.498	W,Y,Br,R
Thomsonite	$Ca_2Na_4Al_4Si_4O_{16}\cdot 5H_2O$	M	5-5.5	2.3-2.4	1.503	W,rGrn
Zoisite	$Ca_4Al_6Si_6O_{25}\cdot H_2O$	R	6-6.5	3.2-3.4	1.703	grW,Gr,yBr,grn

*C-Cubic, H-hexagonal, M-monoclinic, R-rhombic.

**W-white, Y-yellow, Gr-gray, Grn-green, Bl-blue, Pk-pink, R-red, Brn-brown, Blk-black, - -colorless.

The earliest work on the study of the ion exchange process was done with natural clays and zeolites (38). Applications to chemical separations in analysis (39), as well as industrial usages were made of the cation exchange abilities of natural zeolites. Synthetic zeolites, first prepared in 1905, were used for softening of mineralized water (40), but these early synthetic zeolites were amorphous materials lacking the regular crystalline structure of the natural zeolites.

Natural zeolites (crystalline aluminosilicates) can be divided into three groups: fibrous zeolites, e.g. natrolite; plate or lamellar zeolites, e.g. heulandite; and cubic or rhombohedral zeolites, e.g. analcite and chabazite. The last group is constructed of open, three-dimensional frameworks of SiO_4 and AlO_4 tetrahedra and is representative of the type which has proven more useful in practical modern industrial applications.

The regular, crystalline structure of the cubic group of natural zeolites is such that an open cage structure with interconnecting channels is created. The empty channels within this cubic structure are normally occupied by adsorbed water molecules. This water is not, however, like chemically bound water of hydration, i.e. essential to the structural integrity of the crystal. Heating of the hydrated form of the zeolites drives off the water with no damage to the structure. This open and stable structure is responsible for the most widely applied property of the zeolites, that of vapor adsorption. The open structure causes the zeolites to have a "microporosity" on a molecular scale which results in a typical specific surface area of 700 $m^2\ g^{-1}$. As a consequence, van der Waals forces between vapor molecules and the zeolite internal surface area cause strong adsorption of gases into the three-dimensional cubic zeolites.

Figure 6 is representative of data for heat of adsorption of gases on natural, cubic structured zeolites. This adsorption behavior is very similar to the curves representing the van der Waals adsorption of gases on glass, charcoal, and graphite (41). It has been shown that the adsorption of gases on zeolites obeys the Langmuir absorption principle which is based on considerations of the kinetics of gas adsorption (42,43).

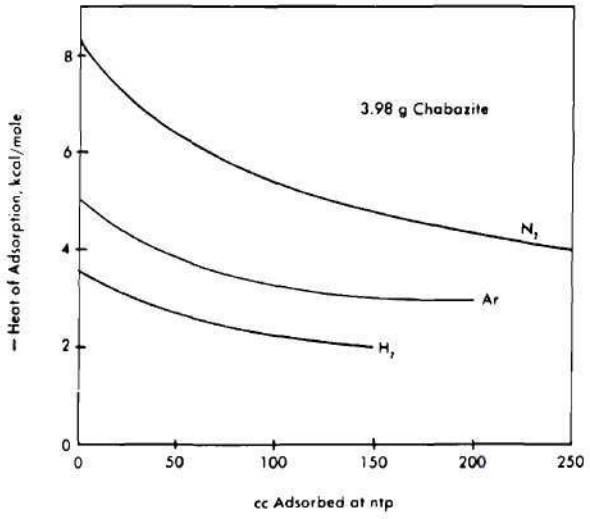

Figure 6. Typical Heat of Absorption Data for Gases on Chabazite (from reference 41)

McBain (44) studied the selective adsorption of water and alcohol vapors by the natural cubic structure zeolite, chabazite. He was the first to note the effect of the very regular pore size (a result of the three-dimensional, cage-like structure) on the behavior of chabazite as an adsorbent. Smaller molecules, e.g. water and low molecular weight aliphatic alcohols are readily adsorbed by chabazite while larger molecules are not adsorbed at all. McBain gave the name "molecular sieves" to these materials as a reference to their ability to discriminate between

gases based on the adsorbed molecule dimensions.

In the period immediately following World War II industrial interest increased rapidly in the use of adsorption for the separation of atmospheric gases, drying of organic gases and fluids, and other industrial applications. Of the many types of adsorbents studied, the natural zeolites were superior for many applications. Unfortunately, they are not very abundant in nature. This lack of a large natural supply coupled with a rather large chemical and physical variability in the natural minerals made their large scale commercial use impractical. About 1950 the Linde Division of Union Carbide Corporation began research aimed at the synthesis of pure, man-made zeolites. By 1953, over thirty zeolite species had been prepared in the laboratory as a result of this research. These included crystal structures identical to natural zeolites as well as novel structures not found in nature (45).

The most useful of the synthetic zeolites are referred to as Type A and Type X. These are similar in structure to the cubic natural zeolites. Type X has the basic structure of the natural zeolite faujasite. Figure 7 shows the spacial arrangement of the basic tetrahedral "building block" of the zeolites with a central Si or Al atom and its four chemically bound oxygen atoms. These tetrahedra can be arranged in rings and prisms as shown in Figure 7. Al or Si atoms are located at the apices and connecting oxygen atoms are midway between apices connected by a line. The oxygen atoms not directly connected with the "unit cell" shown in Figure 7 are not depicted.

The basic rings and prisms of silicon and aluminum tetrahedra can

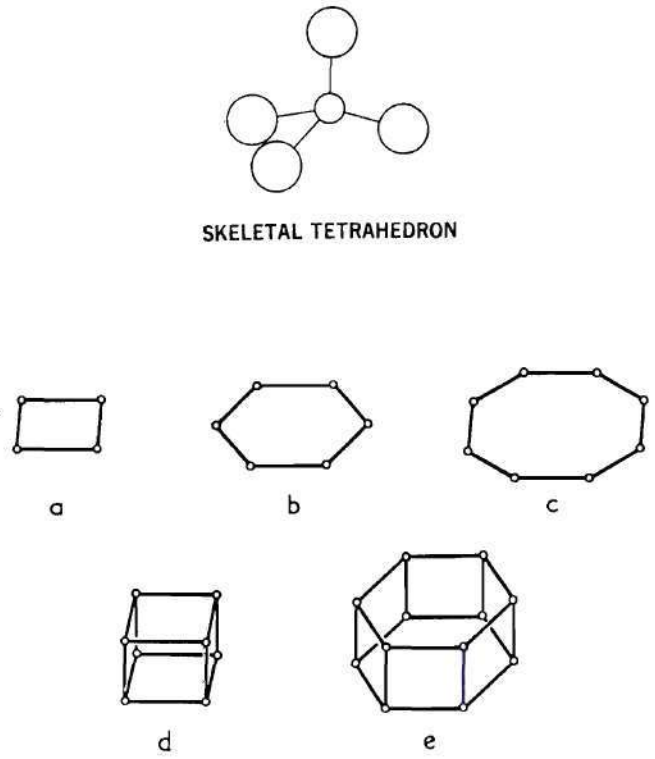

Figure 7. Some of the Rings and Prisms Encountered in Zeolite Structures (from reference 46)
Al or Si atoms are located at the apices and O atoms are located midway between apices connected by a line.
(a)Ring of four tetrahedra, (b)ring of six tetrahedra, (c)ring of eight tetrahedra, (d)double ring of four (cube), (e)double ring of six (hexagonal prism)

build the many three-dimensional "unit cells" shown in Figure 8. The sodalite truncated or cubic octahedron structure (Figure 8b) can be stacked to form the basic structure of the Type A or Type X zeolites. The sodalite cage itself encloses a cavity 6.6 Å in internal diameter with connecting openings 2.2 Å in diameter.

If the sodalite octahedra are stacked in a cubic array (Figure 9a) by linking a ring of four tetrahedra of one cage (or cell) to a ring of four tetrahedra of a second cage through four shared oxygen atoms, the Type A lattice is formed. Type A contains the largest diameter eight-membered ring of tetrahedra since it is planar, whereas other rings of eight tetrahedra deviate from planarity (Figure 8). The internal cavity of this Type A structure (Figure 8f) has a diameter of 11Å. The openings into this cage are partially blocked by the cations present in the structure to offset the negative charge excess in the aluminum tetrahedra. If these cations are sodium, the effective diameter of these openings is 4.2 Å. If larger potassium ions are exchanged for the sodium ions, the effective diameter is decreased to about 3 Å. Substitution of divalent calcium ions causes an increase in the diameter of this access to the cage to 5 Å. Even though the calcium ion is larger than the sodium, one divalent calcium ion replaces two monovalent sodium ions in the structure and the net result is a more open cage.

If the sodalite cages are stacked in a tetrahedral array by connecting adjacent rings of six tetrahedra with six shared oxygen atoms, the Type X or faujasite lattice is produced (Figure 9b). This structure is the face-centered cubic or diamond lattice. This arrangement (Figure 8g)

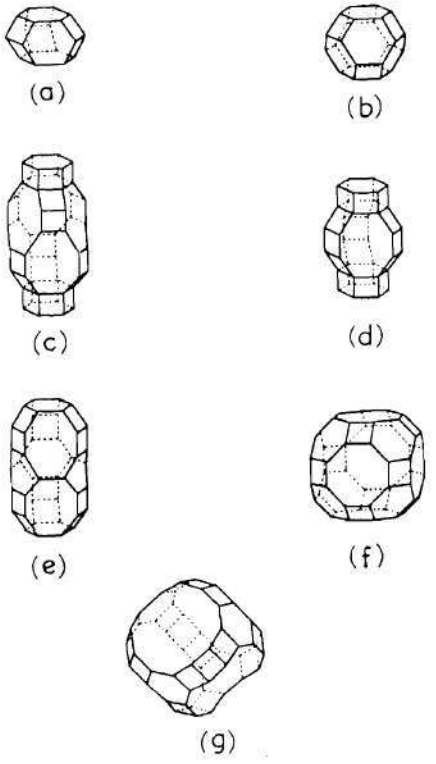

Figure 8. Skeletal Diagrams of the Largest Cavities in Zeolites (from reference 46)
(a)cancrinite, (b)sodalite, (c)chabazite, (d)gmelinite, (e)erionite, (f)Linde Type A, (g)faujasite, Linde Type X

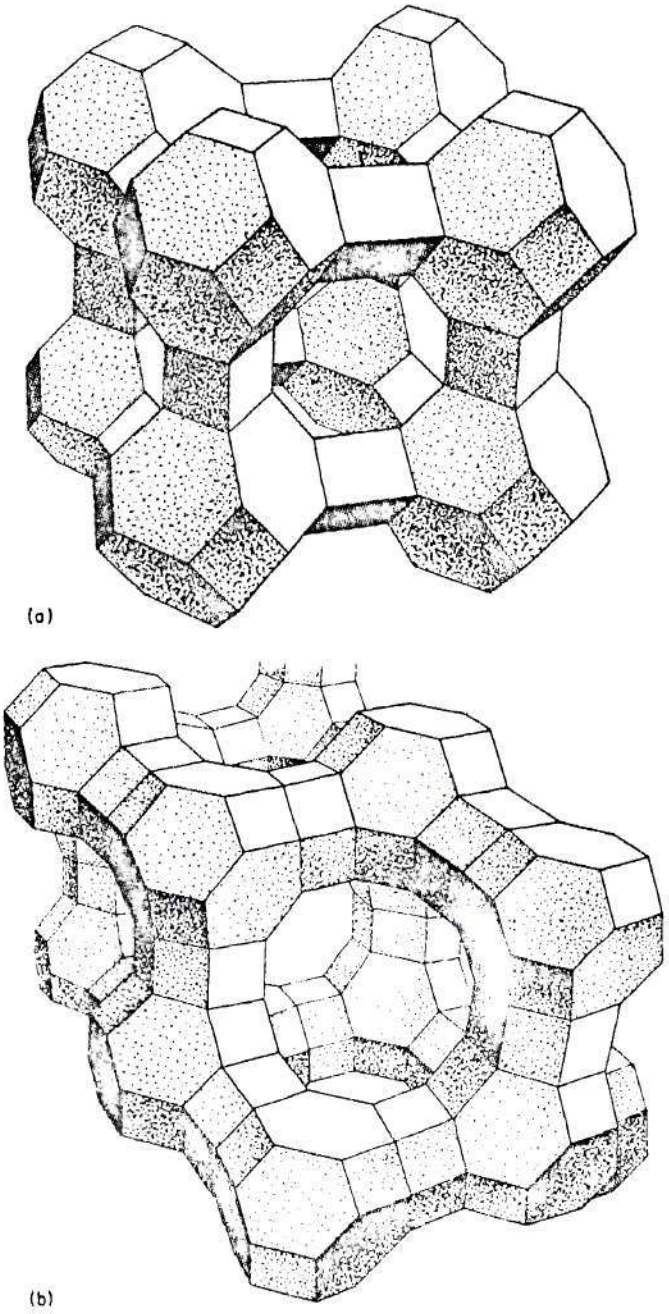

Figure 9. Arrangements of Sodalite Cages or Cubo-octahedra in Zeolite Structures (from reference 46)
(a)Linde Type A, (b)faujasite, Linde Type X

leaves the largest openings (12-membered rings) and the largest cage structure of the zeolite family. The openings into the cage in the Type X, faujasite-structured zeolite have a diameter of 10 Å with an effective opening of 7.5 Å in the sodium form.

Manufacture of the synthetic zeolites is described pictorially in the process flow diagram shown in Figure 10 (47).

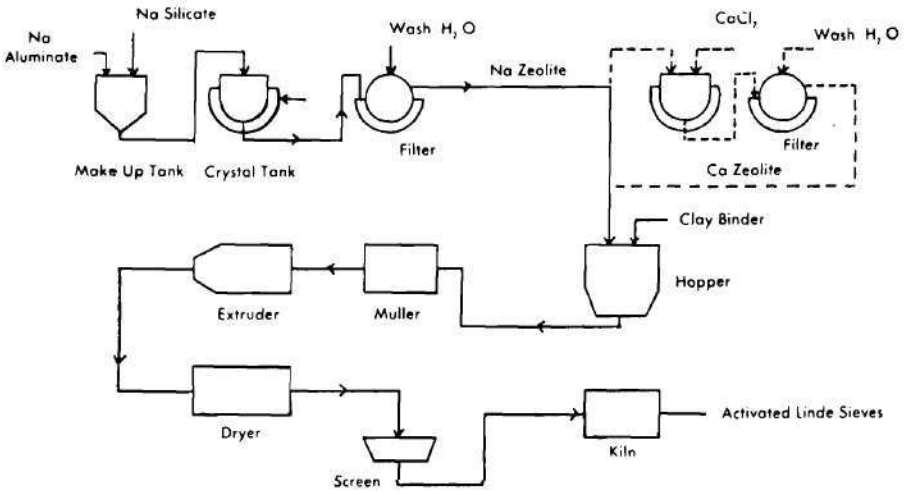

Figure 10. Flow Diagram for Production of Molecular Sieves (from reference 47)

Sodium silicate and sodium aluminate solutions are metered into the makeup tank. The proportion of silicon to aluminum, the solution pH, and the temperature used during the process determine the crystal structure of the product zeolite. When mixed, these solutions form a gel which is heated in the crystallization tank to about 100 °C. Crystallization time varies with the type zeolite being formed and the temperature of the process, but ranges from 45 minutes for Type A to 6 hours for Type X at 100 °C.

The sodium form zeolite crystals leaving the crystallization step are filtered and washed. The crystal sizes vary from 0.1 to 10 μ in diameter. For industrial applications such a finely divided powder is impractical, so clay binder is normally added (approximately 20 percent by weight), blended with the aluminosilicate crystals, and the mixture extruded into pellets or formed into spherical particles. After drying and screening, the zeolite product is fired in a kiln at 650°C. This step dehydrates or activates the zeolite and cements the micron-sized zeolite crystals together with clay binder into the pellet or sphere shapes.

Both Type A and Type X zeolites are structured in three-dimensions, resulting in a three-dimensional channel structure. There are many zeolites, however, that do not have this three-dimensional channel system. In these zeolites, large channels parallel to one axis are often interconnected by smaller diameter channels. The natural zeolite, mordenite, is an example of this type of crystal structure. Non-planar rings of 12 tetrahedra in mordenite cause a reduction in effective ring diameter to 6.8 Å compared to 7.5 Å in faujasite. Furthermore, these channels are not interconnected. Table 4 summarizes the structural and chemical data for several natural and synthetic zeolites. Note the reduced ion exchange capacity for mordenite which is partially a result of this restricted access to the exchangeable sodium ions due to the lack of interconnecting, three-dimensional structure (46).

The ion exchange capacities given in the last column of Table 4 represent the total exchange capacity of the zeolite and are found to correspond to the actual exchange capacity only in the case of exchange

Table 4. Zeolite Structure and Ion Exchange Data (46)

Species	Idealized unit cell contents	Cavities (number of tetrahedra in unit) and free diameter, Å	Free diameter of channel and number of tetrahedra per ring (in parentheses)	Ion-exchange capacity, meq/g (anhydrous)
Analcite	$Na_{16}[(AlO_2)_{16}(SiO_2)_{32}]\cdot 16H_2O$			4.95
Gmelinite	$Na_8[(AlO_2)_8(SiO_2)_{16}]\cdot 24H_2O$	Hexagonal prisms(12)	6.9 (12)	4.95
Chabazite	$Ca_2[AlO_2)_4(SiO_2)_8]\cdot 13H_2O$	Hexagonal prisms(12)	3.7-4.2(8)	4.95
Erionite	$(Ca,etc.)_{45}[(AlO_2)_9(SiO_2)_{27}]\cdot 27H_2O$	Hexagonal prisms(12)	3.6-4.8(8)	3.86(Ca)
Cancrinite hydrate	$Na_6[(AlO_2)_6(SiO_2)_6]\cdot 5H_2O$		6.2 (12)	7.04
Sodalite hydrate	$Na_6[(AlO_2)_6(SiO_2)_6]\cdot 4H_2O$	Cubooctahedra(24)6.6	2.6 (6)	7.04
Phillipsite	$(K,Na)_{10}[(AlO_2)_{10}(SiO_2)_{22}]\cdot 20H_2O$		4.2-4.4(8)	4.67(Na)
Heulandite	$Ca_4[(AlO_2)_8(SiO_2)_{28}]\cdot 24H_2O$		2.4-6.1(8)	
			3.8-4.5(8)	3.45
			4.1-6.2(10)	
Stilbite	$Na_2Ca_4[(AlO_2)_{10}(SiO_2)_{26}]\cdot 28H_2O$		4.1-6.2(10)	
			2.7-5.7(8)	4.24
Clinoptilolite	$(Ca,Na_2,K_2)_3[(AlO_2)_6(SiO_2)_{30}]\cdot 24H_2O$		2.4-6.1(8)	
			3.8-4.5(8)	2.64(Ca)
			4.1-6.2(10)	

Table 4. (Concluded)

Species	Idealized unit cell contents	Cavities (number of tetrahedra in unit) and free diameter, Å	Free diameter of channel and number of tetrahedra per ring (in parentheses)	Ion-exchange capacity, meq/g (anhydrous)
Mordenite	$Na_8[(AlO_2)_8(SiO_2)_{40}]\cdot 24H_2O$		6.7-7.0(12)	
			2.9-5.7(8)	2.62
Faujasite	$(Na_2,Ca)_{32}[(AlO_2)_{64}(SiO_2)_{128}]\cdot 256H_2O$	Hexagonal prisms(12)	7.4 (12)	5.02(Ca)
		Cubooctahedra(24)6.6	2.5 (6)	
		26-Hedron(48)11.8		
Linde A	$Na_{96}[(AlO_2)_{96}(SiO_2)_{96}]\cdot 216H_2O$	Cubes(8)		
		Cubooctahedra(24)6.6	4.1 (8)	4.95
		Truncated cubooctahedra(48)11.4	2.5 (6)	
Linde X	$Na_{85}[(AlO_2)_{85}(SiO_2)_{107}]\cdot 256H_2O$	Hexagonal prisms(12)	7.4 (12)	
		Cubooctahedra(24)6.6	2.5 (6)	6.34
		26-Hedron(48)11.8		
Linde Y	$Na_{52}[(AlO_2)_{52}(SiO_2)_{140}]\cdot 256H_2O$	Hexagonal prisms(12)	7.4 (12)	
		Cubooctahedra(24)6.6	2.5 (6)	4.10
		26-Hedron(48)11.8		

of small ions where ion sieving by the cage openings does not affect the process. Sherry (48) found in exchanging Ba^{+2} ions onto Type X synthetic zeolite, that 16 of the 85 Na^{+} ions in a unit cell (formula: $Na_{85}(Al_2)_{85}(SiO_2)_{107} \cdot 256\ H_2O$) could not be replaced with the Ba^{+2} ions. In order to reach those 16 Na^{+} ions that were not exchanged, the Ba^{+2} ions must diffuse through 6-membered rings of tetrahedra forming the sodalite cages and the hexagonal prisms connecting the sodalite cages. This result is consistent with the crystal radius for Ba^{+2} of 1.35 Å (49) which prohibits its passage through the smaller openings of the zeolite crystal structure. Because of this ion sieving action, the actual measured ion exchange capacity of a zeolite may vary for different cations.

Based on published ionic crystal radii for U^{+6} and O^{-2} of 0.80 and 1.32 Å, respectively (50), the maximum ionic dimension of the unsolvated uranyl ion is estimated to be approximately 6.8 Å. Type X zeolite (maximum effective opening diameter of 7.5 Å in the sodium form) should be capable of exchange with the uranyl ion, but Type A (3-5 Å windows) should not. Water of hydration bound to the uranyl ions will have to be stripped if the ionic diameter is to permit entry into the cage of even the Type X zeolite. This may be expected to affect the ion exchange kinetics for uranyl ions. It has been shown that hydration of the La^{+3} ions retards the exchange rate for Type X zeolite (51).

Diffusion of fission product xenon from Type X molecular sieves should be relatively unhindered. The atomic diameter of xenon is 4.4 Å (52). If the fission fragment comes to rest in the large cage (12-membered tetrahedra ring), it will readily diffuse from the crystal. On the other hand, if it stops within a sodalite octahedron, it may be trapped

and unable to diffuse through the 2.2 Å windows.

Reports of radiation damage studies of molecular sieves are rare. One Russian study (53) indicated that 3×10^6 roentgens of gamma radiation produced increased adsorption capacity for air at lower temperatures, but little change at 350-400°C. The adsorbed gases were held more tightly to the zeolites and heating was necessary for release. No investigations of reactor irradiation or fission fragment effects have been found.

In summary, molecular sieves appear to be particularly promising materials for use as the base for the high surface area uranium target. Uranyl ion exchange appears feasible, xenon release by diffusion should be efficient, and radiation stability is anticipated to be adequate.

2.0 Experimental

2.1 Electrodeposition of Uranium Oxide

As discussed in Section 1.1, the electrodeposition of uranium from aqueous solution as the hydrous uranium oxide has been used for a long time as a method for preparation of very thin, uniform uranium sources on metal disks for purposes of quantitative alpha particle counting. Of the many electrolytes used, the oxalate solution is reported to give the most even distribution of the uranium oxide films which are of greater thickness due to superior adherence of the deposit to the metal cathode surface.

Optimum conditions selected for the electrolysis are (25):

> A volume of 0.4 M ammonium oxalate electrolyte sufficient to provide 1.5 ml cm^{-2} of cathode surface area (diluted to necessary volume to fill electrolysis cell).

Current density of 0.15 ampere cm^{-2} of cathode surface area.
Temperature of 80 °C or greater.

Nickel was used as the cathode material. This metal functions well as the cathode in the electrodeposition process, can readily withstand high temperatures in post-irradiation heating experiments, and does not acquire significant long-lived radioactivity as a result of reactor neutron irradiation.

Initial electrolytic deposition experiments were done using rectangular nickel metal coupons cut from nickel sheet. The dimensions were 1 cm x 3 cm x 0.13 cm thick. The electrolysis cell consisted of two parallel plates of nuclear grade graphite (1/4 inch thick) with 1/4 inch thick polymethylmethacrylate plastic strips connecting the two graphite anodes. The nickel cathode was suspended in the electrolyte in the space between the graphite anodes.

This nickel coupon was electrolyzed in the ammonium oxalate solution described earlier and containing 600 mg of uranyl nitrate (depleted in uranium-235). Examination by alpha particle counting of the black coating on the nickel surface following the electrolysis confirmed the presence of uranium. However, autoradiographs of the plated coupon surfaces revealed an uneven uranium deposit with greater density near the edges due to higher current density at the edges of the metal cathode.

This initial result pointed out the unsatisfactory nature of the planar nickel cathode under the conditions used. It was surmised that this failure to attain a uniform deposit thickness could be avoided if cylindrical cathodes were used and these cathodes were rotated about their

axes during the electrolysis. Nickel tubing of 3/8 inch outside diameter with 0.035 inch wall thickness was used to fabricate the cylindrical cathodes which were 5.1 cm in length. The outer surface of these nickel tubes was polished with successively finer grades of carborundum, finishing with 4/0 grade emery polishing paper and white rouge on a cloth. After polishing, the tubes were washed with detergent and finally with carbon tetrachloride in an ultrasonic cleaner bath.

The initial anode material, graphite, was found to be unsatisfactory at higher current densities due to degradation and release of finely divided graphite particles into the electrolyte. The presence of this suspended graphite lowered the cell resistance until the reduction of the uranyl ions at the cathode was halted.

With this information, the final design of the electrolysis cell was made. Figure 11 is a representation of the final cell design. It used four 1/4 inch outside diameter platinum-10 percent rhodium tubes as anodes arranged symmetrically in the beaker and press-fitted into a brass mounting ring. It was necessary to protect the solution-side of the brass mounting ring with a plastic disk sealed with RTV silicone rubber to prevent corrosion of the brass by the ammonium oxalate electrolyte. Copper contamination in the electrolyte was deposited onto the cathode along with the uranium oxide.

The cathode holder was constructed of Type 347 stainless steel. This facilitated cleaning of the deposited uranium oxide from the holder between runs by dissolution of the uranium oxide with nitric acid. The cathode holder has end sections of the same diameter as the cathode tube.

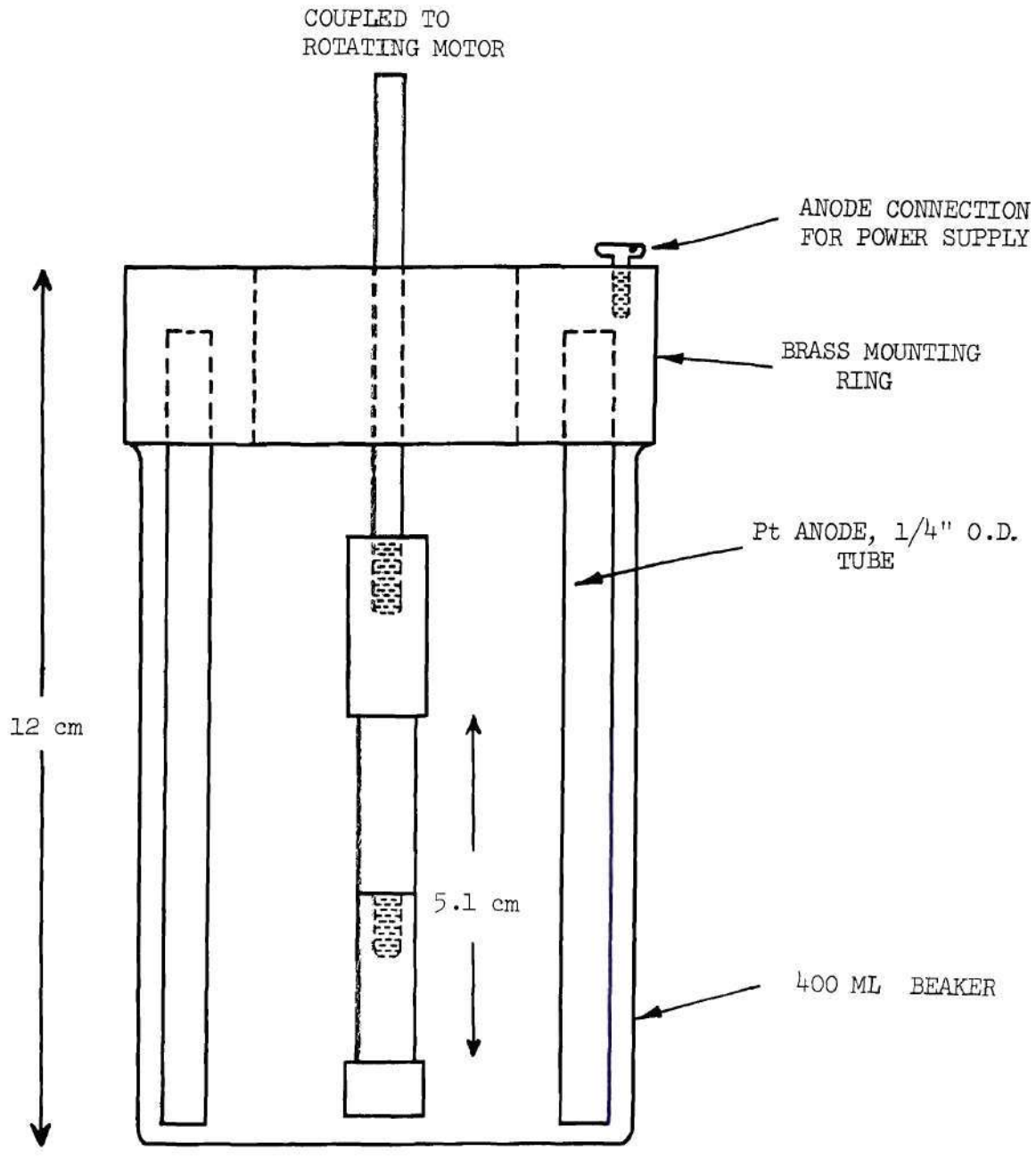

Figure 11. Platinum Anode Cell

This prevents current density gradients near the ends of the nickel tubes which were noted earlier to cause non-uniform uranium oxide deposition. The cathode and holder were rotated during electrolysis at 20 rpm by an electric motor.

The rate of uranium oxide deposition was determined using the final cell design. The electrolyte consisted of 50 ml 0.4 M ammonium oxalate solution diluted to 400 ml with distilled water; 4.72 milligrams uranyl nitrate hexahydrate (UNH) was added as a 5 ml volume of aqueous solution. Initial voltage was 24 volts and the current was 5 amperes. Using different nickel tubes, electrolysis runs were made for varying times and the deposit weight determined after rinsing the cathode in distilled water and methyl alcohol. Figure 12 is a graph of the electrolysis times versus deposited hydrous uranium oxide under these conditions. Cell power dissipation was 120 watts at the beginning of the electrolysis and the current density was 0.3 ampere cm^{-2}. This was sufficient to cause the electrolyte to reach the boiling temperature in about 30 minutes of operation. Application of the method of least squares gives a rate of deposition of the hydrous uranium oxide of 0.20 milligram per minute. The "goodness of fit" parameter or regression coefficient for this set of data was 0.99.

If visual observations of the nickel cathode surface are made during the early portions of the electrodeposition, an interference layer effect can be seen as the color of the deposit on the cathode surface changes from deep blue, to gold, to black as the deposit thickness increases.

The results of these experiments with electrodeposition of hydrous uranium oxide onto nickel metal surfaces indicate that a satisfactory coating can be achieved with a deposit thickness of about one milligram

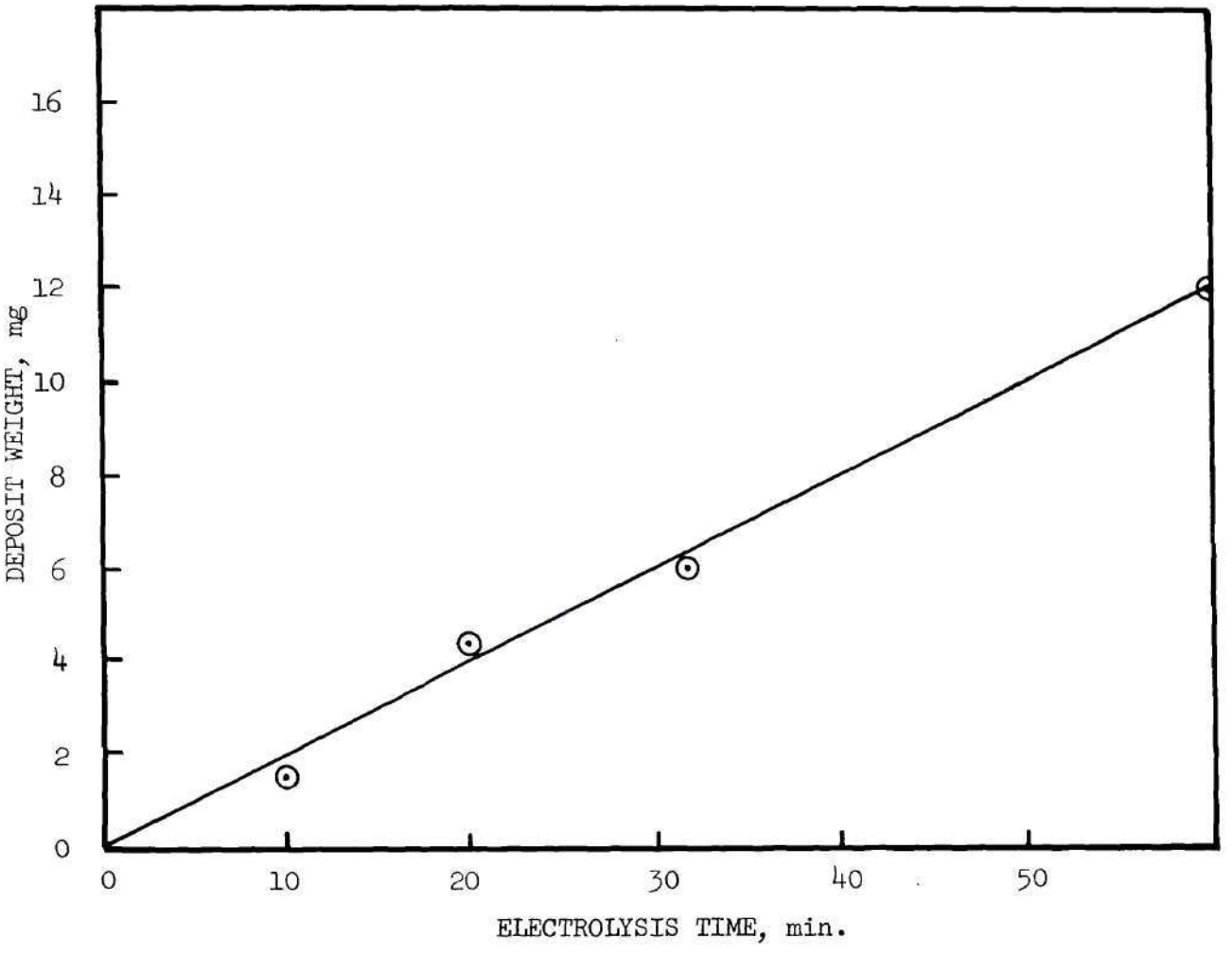

Figure 12. Rate of Electrodeposition of Uranium Oxide

per square cm. The deposited oxide is reasonably sturdy. It can be partially wiped from the nickel surface with tissue, but demonstrated no tendency to flake off without friction against another object. The deposit has very good uniformity over the entire cathode surface.

2.2 Ion Exchange of Uranyl Ion by Molecular Sieves; Aqueous Systems

Although the ion exchange of uranyl ions by synthetic zeolites had not been reported previously, the estimated dimensions of this ion indicate that partial exchange for the sodium ions in large pore diameter locations in molecular sieves should be possible.

If any of the synthetic zeolites would exhibit a capacity for uranyl ion exchange, it will be the Type X with the 12-membered faujasite ring structure.

A 2 cm diameter ion exchange column was prepared with 12.75 grams of 80-100 mesh, ground and sieved Linde 13X molecular sieves (prepared from Linde 13X pellets by Guild Corporation for gas chromatograph column packing and labeled "Hycar 80/100 mesh"). The molecular sieve bed depth was 6.5 cm. The column was backwashed with deionized water to insure physical homogeneity. A glass wool plug was placed on top of the bed of molecular sieves. The bed was then washed with 200 ml of deionized water. A solution of uranyl nitrate hexahydrate (UNH) containing 28.5 mg uranium per ml was prepared by dissolving 30.081 grams UNH (Fisher Scientific Company, Certified ACS Grade, depleted in uranium-235) in 500 ml deionized water. This solution was passed through the molecular sieve bed in the column at a rate of 4 ml per minute. Ten ml fractions of the effluent were

collected. This flow was continued until the yellow color of the UNH appeared in the column effluent. This occurred when about 90 ml of solution had passed through the column. A deionized water wash of the molecular sieves was begun after 150 ml of the UNH solution had passed through the column. Effluent pH was measured with a Beckman Zeromatic pH meter using a Fisher Scientific Microprobe Combination Electrode. Each fraction of the effluent was analyzed for sodium and uranium by neutron activation analysis. One ml aliquots of each fraction were pipetted into 1.5 ml polyethylene vials for neutron activation analysis.*

Table 5 gives the results from this column ion exchange experiment. Figure 13 is a graphical presentation of the data given in Table 5. Fractions 10 through 16 developed yellow precipitates of sodium diuranate ($Na_2U_2O_7$) upon standing overnight. Addition of 5 drops of concentrated nitric acid redissolved the precipitate. It was observed that the yellow coloration due to the uranium deposited on the column was concentrated in the lower third of the column and did not migrate during the water wash.

A core sample of the molecular sieve bed was taken by pressing a 9.5 mm outside diameter thin-wall glass tube through the bed along its axis. The core was sectioned into 0.5 cm segments, dried, and these segments analyzed for uranium content by neutron activation analysis as described earlier. The results are given in Table 6.

Several conclusions were drawn from these results:

(a) The uranyl ion was exchanged for sodium ion by the molecular sieves, but this was not the sole mechanism operating in the column whereby

*See Appendix A for details on analytical procedures.

Table 5. Dynamic Column Study of UO_2^{+2} Exchange on Type 13X Molecular Sieves

Fraction No.	pH	Na (mg/ml)	U (mg/ml)	Remarks
1	9.5	0.035	N.D.*	
2	9.2	0.22	N.D.	
3	9.0	1.44	N.D.	
4	8.2	2.44	N.D.	
5	7.7	2.63	N.D.	
6	7.7	2.70	N.D.	
7	7.6	2.58	N.D.	
8	7.4	2.66	N.D.	
9	5.9	2.56	0.20	
10	4.8	2.50	6.85	UO_2^{+2} color in eluent
11	4.5	1.91	18.4	
12	4.4	1.60	28.2	
13	4.2	1.21	31.4	
14	4.0	1.01	35.1	
15	4.1	0.87	35.2	
16	4.0	0.81	35.1	Water wash begun
17	4.0	0.73	36.5	
18	3.9	0.53	28.6	
19	4.5	0.17	2.4	
20	5.0	0.08	0.61	
21	5.3	0.05	0.28	
22	5.3	0.04	0.20	
23	5.5	0.03	0.14	
24	5.8	0.03	0.11	
25	6.0	0.02	0.06	
26	6.6	0.01	0.08	

*N.D. = not detected

Note: UNH feed solution pH = 2.6; deionized water wash effluent pH = 11.5.

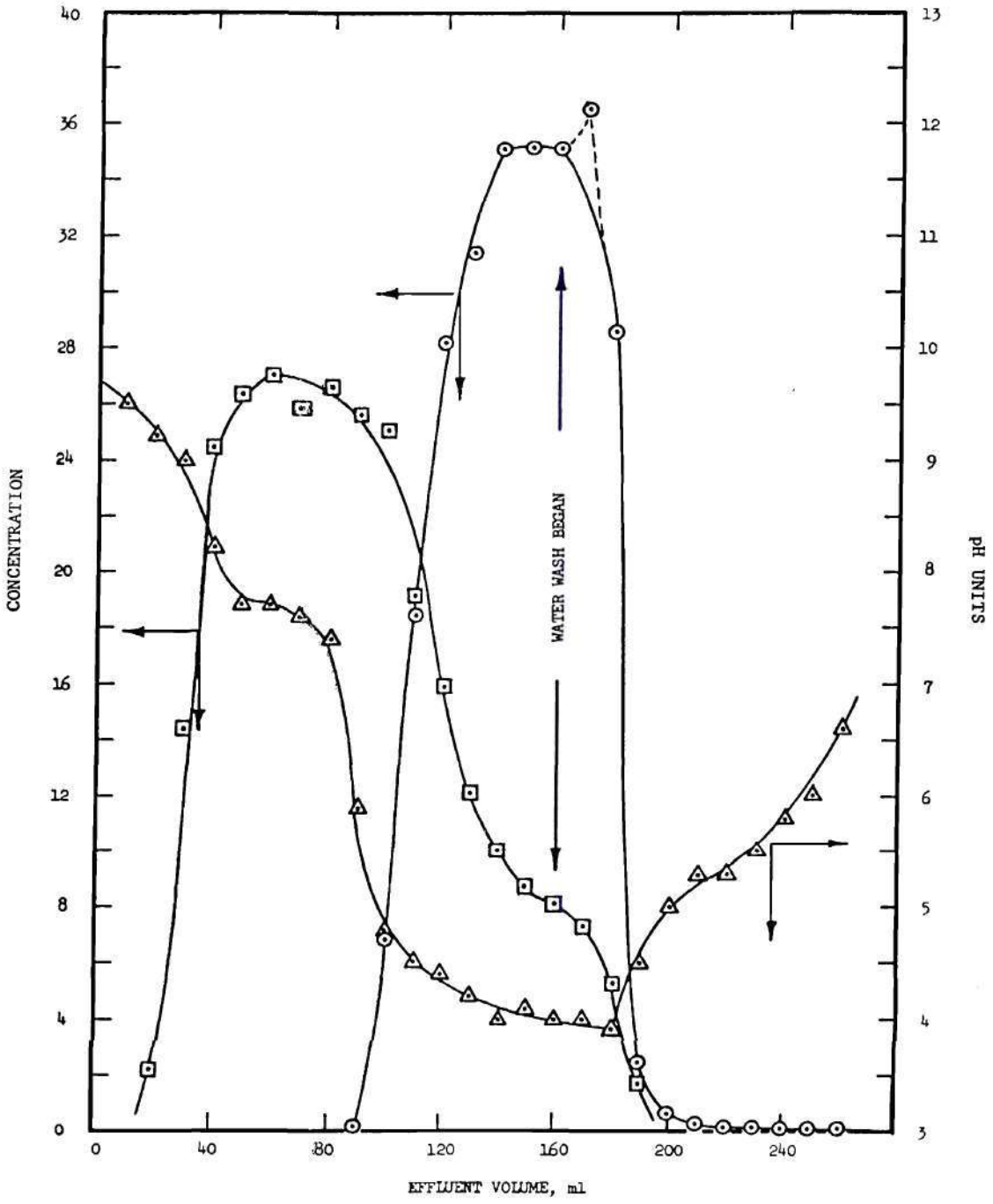

Figure 13. Dynamic Column Study of UO_2^{+2} Exchange on Type 13X Molecular Sieves
⊙ U concentration, mg ml^{-1}
⊡ Na concentration, mg ml^{-1} x 10
△ effluent pH

Table 6. Distribution of Uranium Along Axis of Molecular Sieve Column

Segment No.	U(mg/g)
1 (top)	57
2	55
3	59
4	60
5	68
6	87
7	130
8	170
9	180
10	180
11	180
12	170
13 (bottom)	240 (very deep yellow)

uranium was removed from the solution. The uranyl ion concentration entering the column was 0.24 milliequivalents per ml. The maximum sodium ion concentration in the effluent was only 0.12 milliequivalents per ml.

(b) The competing mechanism was precipitation of UO_2^{+2} within the column bed as sodium diuranate due to the high equilibrium pH of the molecular sieves in contact with water. Addition of 1 N NaOH solution to 10 ml of the UNH solution with pH monitoring revealed that a deep yellow precipitate of the sodium diuranate formed at pH greater than 4.4. This confirms data by Britton (54) on the basicity of metal cations which indicated a precipitation pH of 4-5 for UO_2^{+2}. The pH-dependent formation of diuranate from uranyl ions is expressed by the equilibrium:

$$2Na^+ + 3\ H_2O + 2UO_2^{+2} \rightleftharpoons Na_2U_2O_7 + 6H^+$$

The low pH of the UNH feed solution redissolved the diuranate precipitated on the upper sections of the molecular sieve bed and this was responsible for the peak concentration of about 35 mg uranium per ml in the effluent which was greater than the feed solution concentration of 28.5 mg uranium per ml. This is consistent with the peaking of the uranium concentration at 170 ml effluent volume and the maximum uranium content in the lowest bed core segment. The uranyl nitrate solution flow was terminated just before its acidity could remove all the precipitated diuranate from the bed.

(c) The elevated pH of solutions in contact with molecular sieves is due to the basic nature of oxygen sites in the molecular sieve. Washing of a column containing 26.8 grams of the Type 13X molecular sieves

with 1000 ml of deionized water gave an effluent with a pH of 9.7. This pH represents the effect of the hydrogen ion exchange equilibrium between the zeolite and water. Hydrogen ion is high on the ion exchange order of preference by the synthetic zeolites as shown in Table 7 (55).

(d) The Type 13X molecular sieves demonstrate an ion exchange capacity under these experimental conditions of approximately 58 mg uranium (0.5 milliequivalents of UO_2^{+2}) per gram even at the low pH required to maintain the uranyl ion in solution. The distribution coefficient measured for the exchange of the uranyl ion onto the Type 13X molecular sieves at pH $\cong$ 3 is 2.04. Unfortunately, the zeolite structure is unstable (56) at such low pH due to loss of aluminum from the structure.

To confirm the conclusions drawn from the column experiment with aqueous uranyl nitrate solution just described, a batch equilibration experiment using 1.37 grams of 45/60 mesh Type 13X molecular sieves and 50 ml of an aqueous solution containing 2.36 mg UNH per ml was conducted. The mixture was stirred at room temperature (25°C) and samples withdrawn periodically. The samples were centrifuged in polypropylene tubes to separate the molecular sieve fines from the solution and avoid loss of uranium from solution by adsorption on glass tube walls. The supernate was analyzed for uranyl ion concentration by colorimetric determination in sodium carbonate-peroxide solution (see Appendix A).

Measurements of pH during this equilibration were made to attempt to correlate the pH change with the column study results. Initial pH was 3.7, but increased to 4.4 in the first three minutes of stirring. After five minutes the pH was 5.1 and a definite change in color to a deeper

Table 7. Cations Exchanged on Synthetic Zeolites (Molecular Sieves) (55)

Type 4A		Type 13X	
Order of Preference	Ion	Order of Preference	Ion
1	Ag^{+}	1	Ag^{+}
2	Cu^{++}	2	Cu^{++}
3	Th^{++++}	3	H^{+}
4	Al^{+++}	4	Ba^{++}
5	H^{+}	5	Al^{+++}
6	Zn^{++}	6	Th^{++++}
7	Sr^{++}	7	Sr^{++}
8	Ba^{++}	8	Hg^{++}
9	Ca^{++}	9	Cd^{++}
10	Co^{++}	10	Zn^{++}
11	Au^{+++}	11	Ni^{++}
12	K^{+}	12	Ca^{++}
13	Na^{+}	13	Co^{++}
14	Ni^{++}	14	NH_4^{+}
15	NH_4^{+}	15	K^{+}
16	Cd^{++}	16	Au^{+++}
17	Hg^{++}	17	Na^{+}
18	Li^{+}	18	Mg^{++}
19	Mg^{++}	19	Li^{+}

yellow had occurred. This corresponds to formation of the diuranate compounds at this less acidic pH. At this time the pH was reduced to 2.6 by addition of two drops of concentrated nitric acid. This dispelled the deep yellow color. Three minutes later the pH had again risen to 4.1. By dropwise addition of nitric acid the pH was maintained in the range 2.9 to 5.0 for the duration of the experiment. Figure 14 is a graph of the percent UO_2^{+2} remaining in solution versus contacting time and seems to be asymptotic to a value of about 30 percent remaining in solution at infinite time. It was calculated that about 1.02 milliequivalents of UO_2^{+2} were exchanged onto the molecular sieves and would represent a loading equal to 0.74 milliequivalent of UO_2^{+2} per gram of molecular sieves. This is in reasonable agreement with the 0.5 milliequivalent per gram value found in the column experiment if the drastic differences in the manner of conducting the two experiments are considered.

Review of the problems associated with the uranyl ion exchange from aqueous solutions onto molecular sieves due to incompatible ambient pH of the molecular sieves led to consideration of non-aqueous solvents. The very small dissociation constants for non-polar organic solvents would not promote hydrogen exchange as is the case with water.

Therefore, the use of non-aqueous solvents for the exchange process would be appropriate to avoid the pH problem just described. This would present a solubility problem for most salts which are not reasonably soluble in non-polar solvents, but uranyl nitrate is very soluble in many organic liquids (57).

The selection of a suitable non-aqueous solvent for a study of the

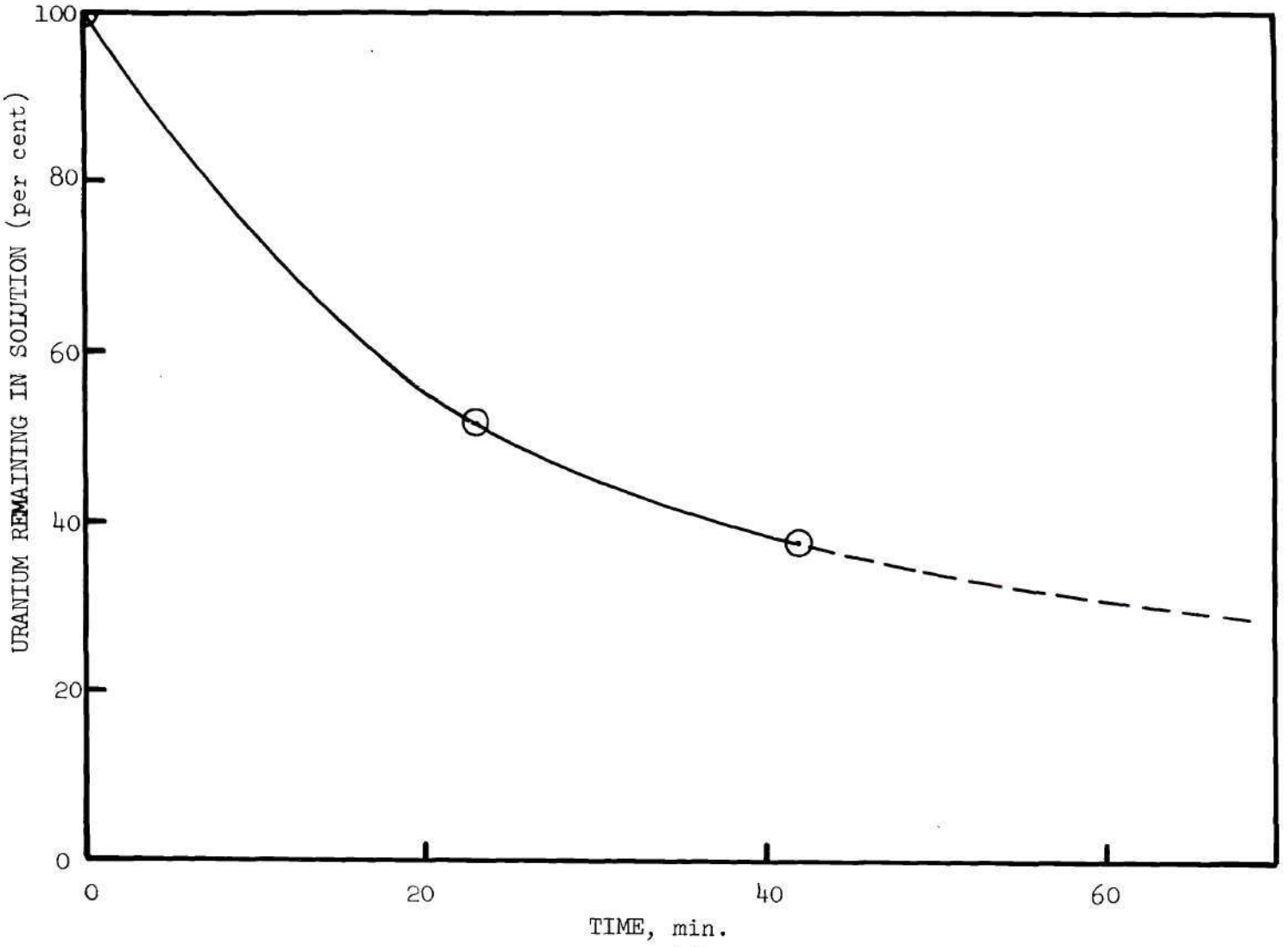

Figure 14. Exchange Rate of UO_2^{+2} on Type 13X Molecular Sieves (Aqueous System)

ion exchange of uranyl ions by molecular sieves is guided by the need for a reasonable solubility for UNH, small molecular dimensions to permit perfusion through the zeolite structure, and preference for a volatile solvent which can be easily evolved by heating the molecular sieves after the exchange. Table 8 gives values for the solubilities of UNH in a number of organic liquids (58).

Methanol is well suited for this application. It has the highest solubility for uranyl nitrate of all the solvents listed in Table 8. It demonstrates an effective molecular diameter of 3-4 Å in adsorption studies on molecular sieves. The boiling point of methanol is 65°C. The use of methanol as a solvent for the ion exchange of alkali metal and alkali earth cations onto Type 13X molecular sieves was reported by Huang, et al. (59) and Radak (60). This work demonstrated that the exchange rate and distribution coefficient decreased with decreasing dielectric constant of the solvent when water and the aliphatic alcohols were studied. The dielectric constant of methanol is 31.66, compared to 78.7 for water and 23.56 for ethanol.

Based on the physical properties and solvent behavior demonstrated in ion exchange processes, methanol was selected as the solvent in examining the ion exchange of uranyl ion onto molecular sieves in this investigation.

2.3 Ion Exchange of Uranyl Ion by Molecular Sieves; Non-aqueous Systems

The initial data on uranyl ion exchange by synthetic zeolites from methanol solution were obtained by stirring 1.92 grams of dry Linde Type

Table 8. Solubility of Uranyl Nitrate Hexahydrate (UNH) in Organic Solvents at 20°C (58)

Solvent	$gUO_2(NO_3)_2/g$ Solvent[a]
Methanol	0·675[b]
Ethanol	0·615[b]
Propanol	0·529[b]
Isopropanol	0·549[b]
Butanol	0·462[b]
n-Pentanol	0·387[c]
n-Hexanol	0·341[c]
n-Heptanol	0·310[c]
n-Octanol	0·280[c]
2-Octanol (capryl alcohol)	0·271[c]
2-Ethyl-1-hexanol	0·235[c]
Cyclohexanol	0·403[c]
Acetone	0·617[b]
Methyl ethyl ketone	0·547[b]
Methyl propyl ketone	0·484[c]
Methyl n-butyl ketone	0·425[c]
Methyl isobutyl ketone	0·428[c]
Methyl t-butyl ketone	0·415[c]
Methyl amyl ketone	0·382[c]
Acetophenone	0·312[c]
Nitromethane	0·140[b]
Nitroethane	0·051[b]
1-Nitropropane	0·011[b]
Diethyl ether	0·491[c]
Furan	0·003[b]
Tetrahydrofuran	0·464[c]
Dioxane	0·291[b]
Dibenzyl ether	0·017[b]
Water	0·540[b]

[a]Uranyl nitrate hexahydrate is the starting material. The solubility is expressed in terms of grams $UO_2(NO_3)_2$/gram solvent-rich phase.

[b]Single liquid phase in equilibrium with solid.

[c]Two liquid phases in equilibrium with solid, solubilities being given for the solvent-rich (upper) phase.

13X molecular sieve powder (no clay binder) in 100 ml methanol containing 141 mg uranium as uranyl nitrate hexahydrate (UNH). After 45 minutes of stirring, a sample of the methanol was taken. Centrifugation was used to avoid contamination of the solvent fraction with fines from the molecular sieve powder. The methanol was colorimetrically analyzed for uranium content. Only 22 mg of the initial 141 mg of uranium remained in the solution. Analysis of another sample taken after 13 hours of stirring revealed less than 5 mg uranium remaining in solution (limit of analytical sensitivity). The removal of about 136 mg of uranium from solution by the molecular sieves represents the exchange of 1.14 milliequivalents of UO_2^{+2} for sodium present in the molecular sieve structure. To verify the sodium exchange, the methanol aliquot was analyzed for sodium by neutron activation analysis; 1.20 milliequivalents of sodium were present in the methanol solvent. A methanol blank was prepared by contacting fresh methanol with a similar quantity of Linde Type 13X powder with no UNH added to the methanol; 0.13 milliequivalent of sodium was removed from the molecular sieves. Re-equilibration of the same molecular sieve powder sample with a fresh batch of methanol again removed 0.13 milliequivalent of sodium ion. Therefore, the total milliequivalents of sodium ion in solution due to uranyl ion replacement is 1.20 less 0.13, or 1.07 milliequivalents. This is in excellent agreement with the 1.14 milliequivalents of uranyl ion removed from the solution. It, furthermore, demonstrates that the exchange process is occurring with the UO_2^{+2} ion, otherwise this agreement in the exchanging cation equivalents would not be found experimentally.

The constant fractional removal of sodium by pure methanol is either the result of hydrogen ion exchange from the methanol, an expression of the limit of solubility of sodium nitrate in methanol, or the effect of small quantities of water still held on the molecular sieve powder or as impurity in the methanol.

Since the dissociation constant for the equilibrium:

$$CH_3OH \underset{}{\overset{K_d}{\rightleftharpoons}} CH_3O^- + H^+$$

is very small (~ 10^{-16}) and the solubility of sodium nitrate in methanol is reported to be 320 mg per 100 ml (61), the last explanation is the most plausible. Subsequent experimental data showed the exchanged sodium concentration in the methanol to be independent of the methanol:molecular sieve ratio. This observation is consistent with either the water-contaminated methanol (typically specified as 0.05 percent by the manufacturer) or the methanol dissociation hypothesis.

This experiment demonstrated conclusively that uranyl ions undergo true ion exchange with Type 13X molecular sieves and that the methanol is a satisfactory solvent in which to conduct the exchange reaction.

Two additional sets of data describing the ion exchange of uranyl ion in methanol solution onto molecular sieves were needed: (1) rate of exchange, and (2) experimental equilibrium data for the exchange which will define the exchange capacity.

It had been assumed that the larger pore diameter of the Type 13X molecular sieves would permit more ready access of the uranyl ions to exchangeable cations located within the three-dimensional structure than

with the smaller-pore Type A molecular sieves. This difference should be evident in a study of the rate and degree of exchange by these two types of synthetic zeolites.

An experimental measurement of the effect of the pore diameter difference between Type 13X and Type 5A was made by contacting 3.99 grams Type 13X pellets (Davison Chemical; 8-12 mesh) with 210 ml methanol containing 1.17 milliequivalents of UNH and 3.57 grams Type 5A (Davison Chemical; 8-12 mesh) with the same volume and UNH concentration. The UNH solutions were stirred by a magnetic stirring bar and the molecular sieve pellets were suspended in the solution contained in a cellulose tissue bag to prevent attrition by the grinding action of the rotating stirring bar. The containers were stoppered to prevent loss of methanol by evaporation. The temperature of the systems reached equilibrium at 33°C due to heat from the stirring motor. Samples of the UNH solution (0.05 - 0.10 ml) were taken periodically for uranyl ion analysis by spectrophotometry. Sensitivity and precision of this analysis was improved over the peroxide method described earlier by using the colorimetric reagent 1,3-diphenyl-1,3-propanedione (DPPD) which chelates the uranyl ion forming a complex which absorbs strongly at 400 millimicrons (see Appendix A).

The data from this experiment to measure the rate of exchange onto Type 13X and Type 5A synthetic zeolites are listed in Table 9 and plotted as a graph in Figure 15. Time required to reach equilibrium for the two zeolites is similar, but the distribution coefficient demonstrated by the Type 13X is calculated to be 175 at the last data point, whereas it is only 14 for the Type 5A at that time. Subsequent additions of UNH to increase the methanol concentration resulted in increases in the uranium

Table 9. Rate of UO_2^{+2} Exchange on Type 13X and Type 5A Molecular Sieve Beads

Conditions: 3.99 g Type 13X; 3.57 g Type 5A
Solution volume = 210 ml
1.17 milliequivalents UO_2^{+2}
Temperature = 33°C
Size range: 8-12 mesh

Contact time (hours)	UO_2^{+2} Exchanged (meq/g molecular sieve)	
	13X	5A
1.85		0.019
2.00	0.058	
4.08		0.029
4.22	0.093	
19.42		0.059
19.53	0.21	
23.12		0.064
23.25	0.22	

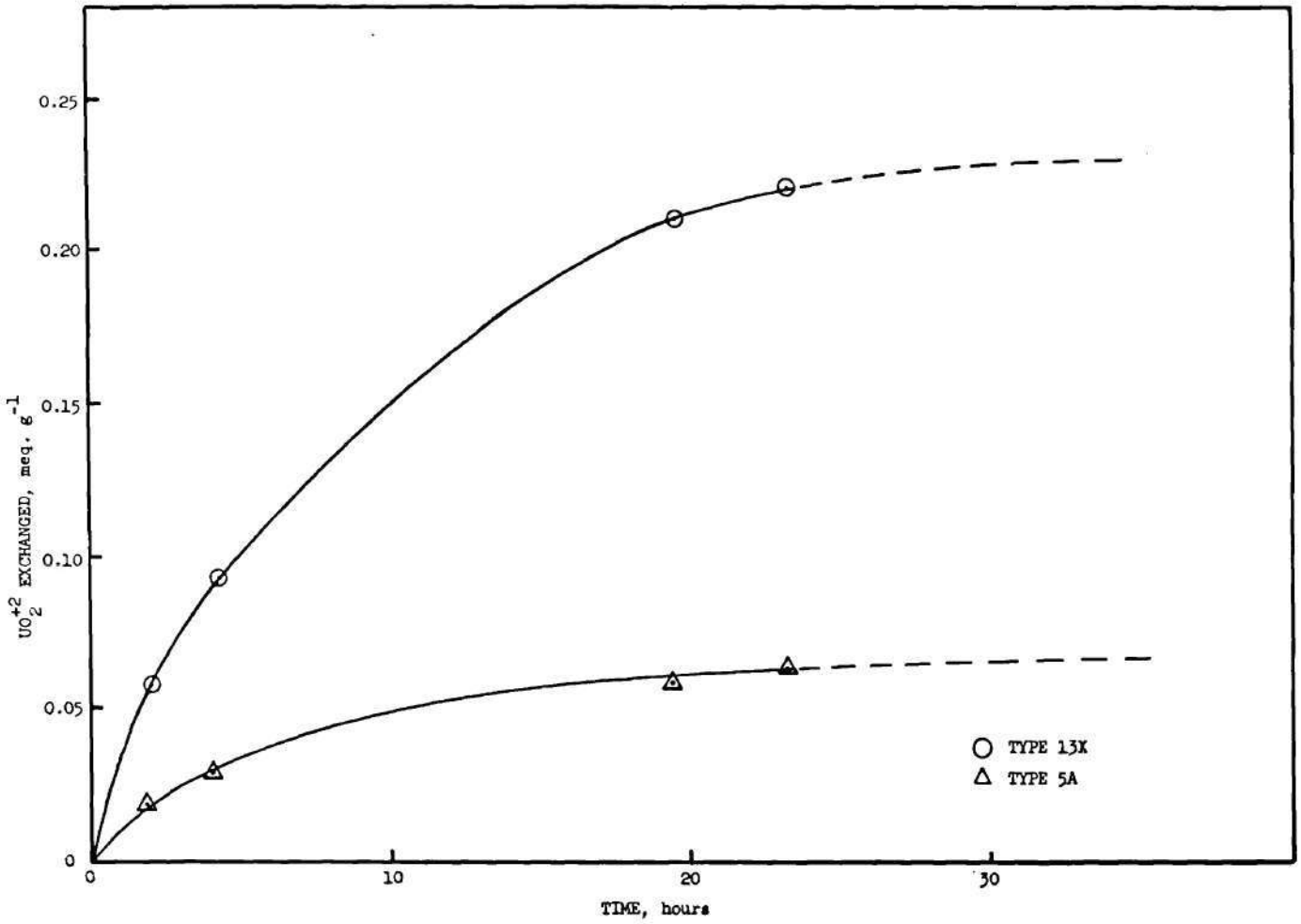

Figure 15. UO_2^{+2} Exchange Rates on Pelletized Molecular Sieves (Non-Aqueous System, Methanol)

exchanged onto both types of molecular sieves to values of 0.60 and 0.30 milliequivalent per gram for the Type 13X and Type 5A, respectively.

Since xenon release by diffusion from the molecular sieve pores will also be enhanced by the larger pore diameter, all further work was done using Type 13X molecular sieves.

2.4 Kinetics and Capacity for Uranyl Ion Exchange

An experiment was conducted to determine the influence of temperature on the rate and capacity of Type 13X exchange of uranyl ions from methanol solution. Type 13X (Davison Chemical; 8-12 mesh) pellets (2.43 grams) were weighed out and placed into a 400 ml round-bottom flask fitted with a water-cooled reflux condenser. Two hundred and twenty-five ml of methanol containing 353 mg uranium as UNH (3 milliequivalents of UO_2^{+2}) were added and the flask heated with an electric mantle so that the methanol refluxed at a slow rate. Samples of the methanol were removed periodically by insertion of a pipette through the reflux condenser. These methanol samples were analyzed for uranium by the DPPD spectrophotometric procedure (see Appendix A). Assuming the loss of uranium from solution to be due to exchange by the molecular sieves (this was demonstrated earlier), the concentration of uranium on the molecular sieves was calculated.

This boiling methanol (65°C) experiment was conducted in parallel with an experiment at room temperature (25°C) using 2.90 grams Type 13X molecular sieves contacted with an identical volume of methanol solution on UNH of the same concentration. This methanol solution was stirred continuously by a magnetic stirrer. Samples removed at various times were also analyzed for uranium spectrophotometrically. Figure 16 shows the results of these two experiments at different temperatures. A definite

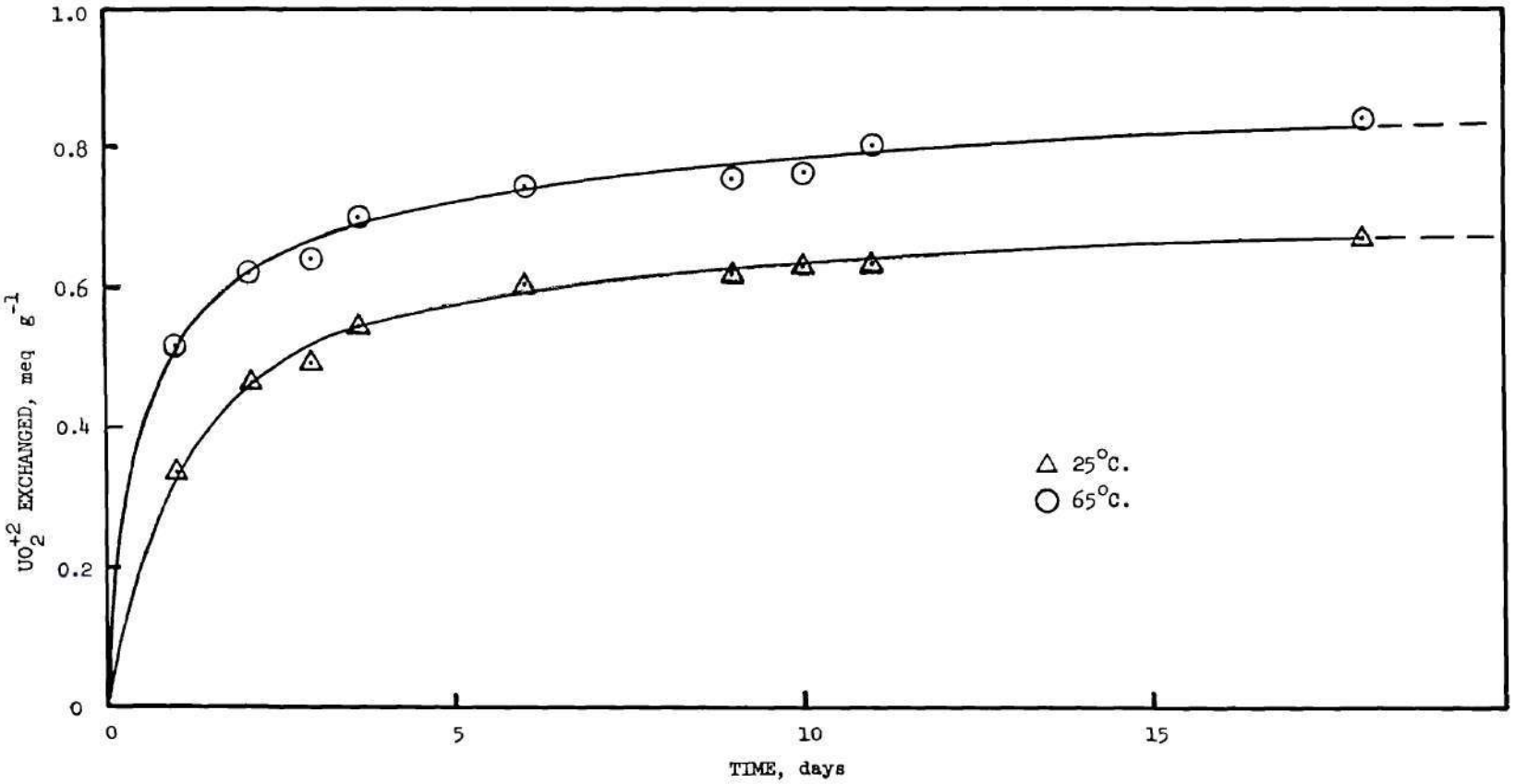

Figure 16. Exchange of UO_2^{+2} from Methanol Solution by Type 13X Molecular Sieves, 8-12 Mesh Pellets. Influence of Temperature on Exchange Reaction

increase in the equilibrium distribution coefficient is noted at 65°C. The distribution coefficient calculated from the experimental data obtained at 25°C was 149, while this coefficient at 65°C was 211.

Exchange rates in zeolites have been shown (62,63) to be controlled by ion diffusion within the solid zeolite structure. For spherical particles this diffusion-controlled rate of exchange is expressed by the following equation in the initial phase of the experiment where the change in dissolved, exchangeable cation concentration is small and the concentration of exchanged cation in solution is low (see Appendix C):

$$\frac{Q_t}{Q_\infty} = \frac{6}{r}\sqrt{\frac{Dt}{\pi}}$$

where

Q_t = the amount of exchange at time t

Q_∞ = the amount of exchange at infinite time (equilibrium)

r = radius of the exchanger particle

D = apparent or effective diffusion coefficient

t = contacting time

As will be shown in Section 2.5, the rate-controlling step in the exchange of uranyl ions onto the molecular sieve pellets is not the ion exchange rate of the individual octahedral crystallites, but the diffusion rate of the uranyl ions into the pellet matrix composed of the aluminosilicate crystallites bound together with a fibrous clay. The spheres of clay-bound molecular sieves used in these measurements were 8-12 mesh which is equivalent to a diameter range of 1.41 to 2.38 mm, or an average radius of 0.095 cm.

Note that the term Q_t/Q_∞ represents the fraction of the equilibrium exchange attained. If this term is plotted versus the square root of the contacting time, a straight line with slope equal to $6/r\sqrt{\frac{D}{\pi}}$ will result for the initial portion of the curve. Determination of this slope will permit calculation of the effective diffusion coefficient, D.

The experimental data represented in Figure 16 were recalculated to give the fraction of equilibrium attained. For this purpose, equilibrium exchange concentrations of uranium in the Type 13X molecular sieves were taken as 0.68 and 0.83 milliequivalent per gram at 25°C and 65°C, respectively. Figure 17 is the result of this data treatment. If the initial portions of these curves are assumed to be straight lines, they have slopes (as calculated by least square fitting) of 0.468 and 0.620 $day^{-1/2}$ for the 25°C and 65°C curves, respectively. For these slope determinations the initial five points from the 25°C curve and the first three points from the 65°C curve were used. Using the average radius of 0.095 cm for the 8-12 mesh molecular sieve spheres used, the effective diffusion coefficient at 25°C was calculated to be 2.0×10^{-9} $cm^2 sec^{-1}$; and at 65°C, 3.5×10^{-9} $cm^2 sec^{-1}$.

The statement was made earlier that the rates of exchange of uranyl ions by Type 13X and by Type 5A (see Table 9 and Figure 15) were similar. Figure 18 is a plot of the data from Table 9 after calculating the fraction of equilibrium attained versus the square root of the contacting time. Most notable is the fact that the two sets of data for the different types of molecular sieves fall onto the same line within experimental error. This may be interpreted to mean that the diffusion coefficient or the

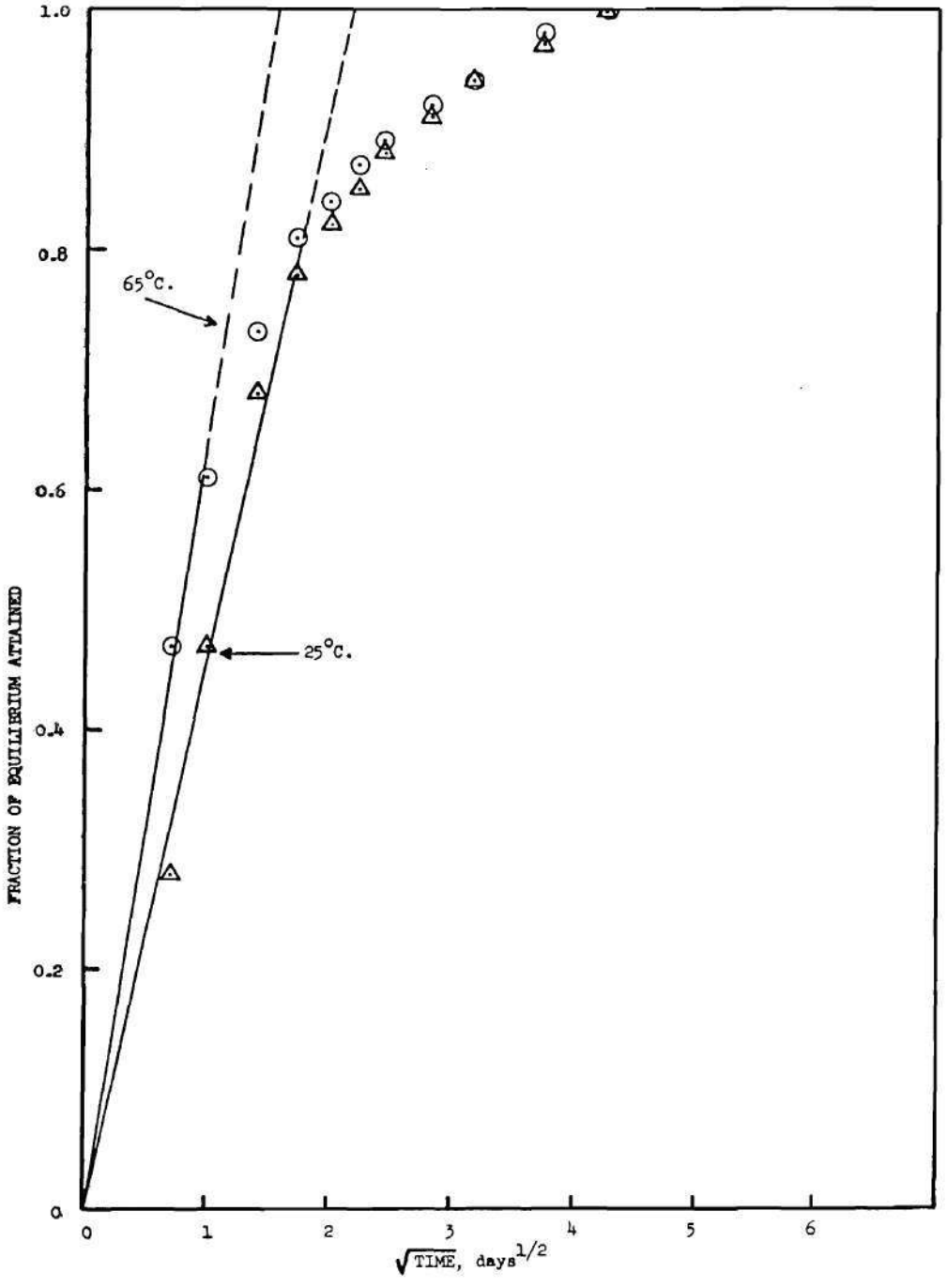

Figure 17. Fraction of UO_2^{+2} Exchange Equilibrium Attained vs Square Root of Contacting Time for Type 13X Molecular Sieves

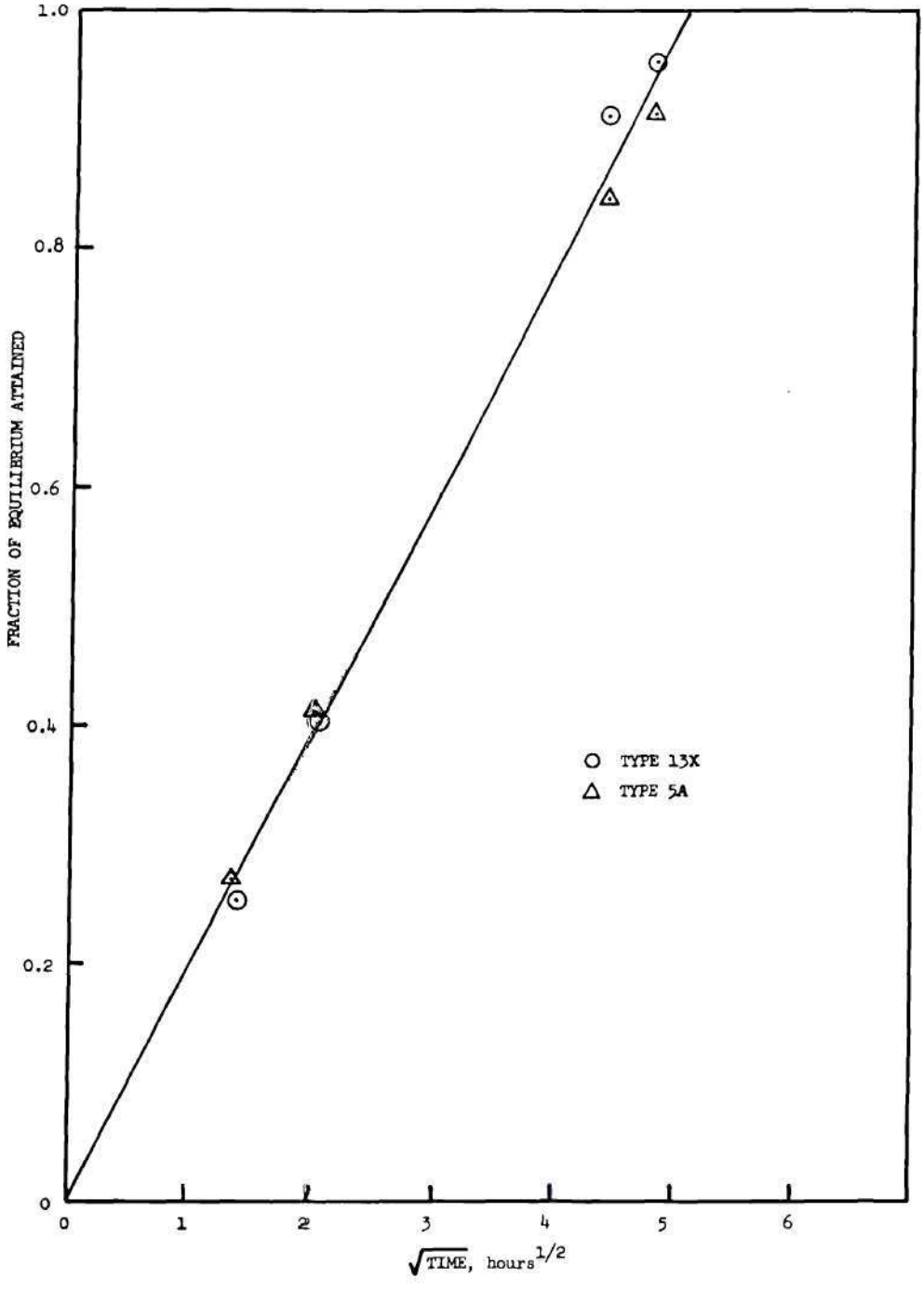

Figure 18. Fraction of UO_2^{+2} Exchange Equilibrium Attained vs Square Root of Contacting Time for Type 13X and Type 5A, 8-12 Mesh Molecular Sieve Pellets

rate constant for the rate-determining step in the exchange reaction in the molecular sieve spheres is independent of the pore-size distribution in the molecular sieves. The calculated diffusion coefficient is now 8.5×10^{-9} $cm^2 sec^{-1}$. This is definitely higher than the values of the diffusion coefficient measured for Type 13X as described above. The discrepancy is attributed in part to an invalid value for the average molecular sieve pellet radius. The experiment using Type 5A pellets was the first to use molecular sieve pellets from a new bottle. Subsequent examination revealed that a segregation of smaller diameter spheres occurs with those near the top having a smaller average diameter.

Knowing the effective diffusion coefficients at two temperatures, the activation energy of the exchange reaction can be estimated by the use of the Arrhenius expression:

$$D = D_o \, e^{-E/RT}$$

where

D = effective diffusion coefficient

D_o = constant

E = activation energy for exchange

T = exchange reaction temperature, degrees Kelvin

R = gas constant = 1.98718 calories per gram ion

If this equation is rearranged to:

$$\ell nD = - \frac{E}{RT} + \ell nD_o$$

we can graphically or algebraically determine the slope, -E/R, when ℓnD is plotted versus the reciprocal absolute temperature, 1/T. For the

Type 13X molecular sieve ion exchange of uranyl ions from methanol solution, the slope is calculated to be -1399 which gives a value of 2.78 kilocalories per gram ion as the activation energy for this diffusion controlled exchange reaction. The value for the constant D_o is equal to 2.2×10^{-7} $cm^2 sec^{-1}$.

The exchange equilibrium of 0.83 milliequivalents of uranyl ions per gram of Type 13X molecular sieve pellets at 65°C is equivalent to the exchange replacement of fourteen sodium counterions per unit cell, $Na_{85}(AlO_2)_{85}(SiO_2)_{107}$, by seven UO_2^{+2} ions. This agrees well with experimental data of Hoinkis and Levi (64) and Barrer and Falconer (63), who demonstrated the very rapid exchange of barium cations for sixteen sodium counterions located in the large cavities of Type 13X aluminosilicates. The reported value of the apparent diffusion coefficient for this rapid exchange is 1.2×10^{-11} cm^2 sec^{-1}, and the activation energy for barium exchange was 9.7 kilocalories per gram ion.

Ames (65) measured the apparent diffusion coefficients and activation energies for the exchange of Na^+, Cs^+, Sr^{+2}, and Ce^{+3} cations with Type 13X molecular sieve spheres with clay binder. The measured apparent diffusion coefficients and activation energies are given in Table 10. The agreement with the data from this work is excellent. Solvated uranyl ion with its low charge density and being easily polarized would be expected to exhibit a lower activation energy than reported for those cations in Table 10.

Table 10. Self Diffusion Coefficients and Activation Energies in Type 13X Molecular Sieve Pellets (65)

Cation System	Apparent Diffusion Coefficient ($cm^2 sec^{-1}$)	Activation Energy [kcal $(g\ ion)^{-1}$]
Na^+	1.56×10^{-7}	10.7
Cs^+	1.15×10^{-7}	12.9
Sr^{+2}	5.37×10^{-8}	8.1
Ce^{+3}	2.46×10^{-9}	5.1

Ames assumed the rate determining step to be the intracrystallite diffusion which the data gathered in the present study disproves. Although the diffusion coefficient for the crystallite is estimated to be on the order of 10^{-11} $cm^2 sec^{-1}$, which is 100 times smaller than that measured for the molecular sieve pellets, it must be remembered that the actual diffusion rate is inversely dependent on the square of the particle radius. This factor is calculated to be approximately 10^6 in the case under investigation, i.e. 0.095 cm sphere radius compared to 10^{-4} cm for the individual crystallites. This more than compensates for the difference in the diffusion coefficients and makes the diffusion inside the sphere of cemented crystallites (but outside the crystallites) the rate-determining factor for these materials.

Since these exchange measurements on the Type 13X molecular sieves were done on spherical pellets containing the aluminosilicates cemented together with attapulgite clay, it was of concern to determine the possibl interference due to ion exchange of uranyl ions by the clay binder. The

ion exchange capacity of attapulgite for cation absorption is given as 0.18 - 0.22 milliequivalent per gram (66) which is approximately five times smaller than that measured for the molecular sieves for uranyl ions. Furthermore, this quoted capacity for the clay is for smaller cations and the actual capacity for the larger uranyl cations would be smaller yet. The conclusion is that the influence of the clay binder (15-20 percent by weight) in the molecular sieve spheres on the exchange of uranyl ions would be negligible.

One complication which was noted during the conduct of the experiments involving UNH solutions in methanol was a change in solution color accompanied by precipitation. At higher UNH concentrations (greater than approximately 5 mg per ml) in methanol, the uranium(VI) valence state seems capable, in the presence of the molecular sieves, of oxidation of the methanol. The result is reduction of uranium(VI) to uranium(IV) as indicated by a change in solution color from the uranium(VI) yellow to the green color characteristic of uranium(IV). Furthermore, the uranium-(IV) is insoluble in methanol and precipitates as a green sludge. Addition of three drops of 30 percent hydrogen peroxide solution to the 200 ml of solution caused a return to the normal uranium(VI) yellow color and redissolved the uranium(IV) precipitate. This oxidation-reduction reaction has not been observed in methanol solutions of UNH at much greater concentrations and may, therefore, be due to some catalytic effect of the molecular sieves.

2.5 Physical Examination and Properties of Uranium-Loaded Molecular Sieves

The most apparent change in the molecular sieves noted after loading

with appreciable quantities of uranyl ions is the yellow, or buff color imparted by the uranium content. The intensity of the color is proportional to the degree of uranyl ion exchange. The color is stable at high temperatures. Heating at 500°C does not affect this color; however, a change to tan was noted at approximately 650°C.

It is essential for the proper function of the synthetic zeolite as a porous uranium target base that the microporous structure remain intact after uranyl ion exchange. Historically, X-ray diffraction techniques have been used to examine the crystal structure of these zeolite compounds. Attempts during this investigation to examine the structure of uranyl-loaded zeolite by X-ray diffraction were unsuccessful due to the absorption of the X-ray beam by the dense uranium.

Thermal neutron diffraction offered the advantage of absence of strong absorption of the incident radiation, particularly if uranium depleted in high cross section, fissionable uranium-235 were used to prepare the loaded zeolite.

Using a neutron diffraction apparatus attached to the Georgia Tech Research Reactor, neutron diffraction patterns were successfully taken for Type 13X powder, Type 13X pellets, and Type 13X pellets saturated with depleted uranium. Figure 19 shows the consistency of the neutron diffraction patterns obtained, indicating no gross structural modification due to the uranyl ion insertion into the zeolite. The diffraction pattern for the uranium-loaded molecular sieve pellets was not influenced by the clay binder since differences in patterns for the 13X powder and pellets (both without uranium) were undetectable. These patterns were made using a neutron wavelength of 3 Å.

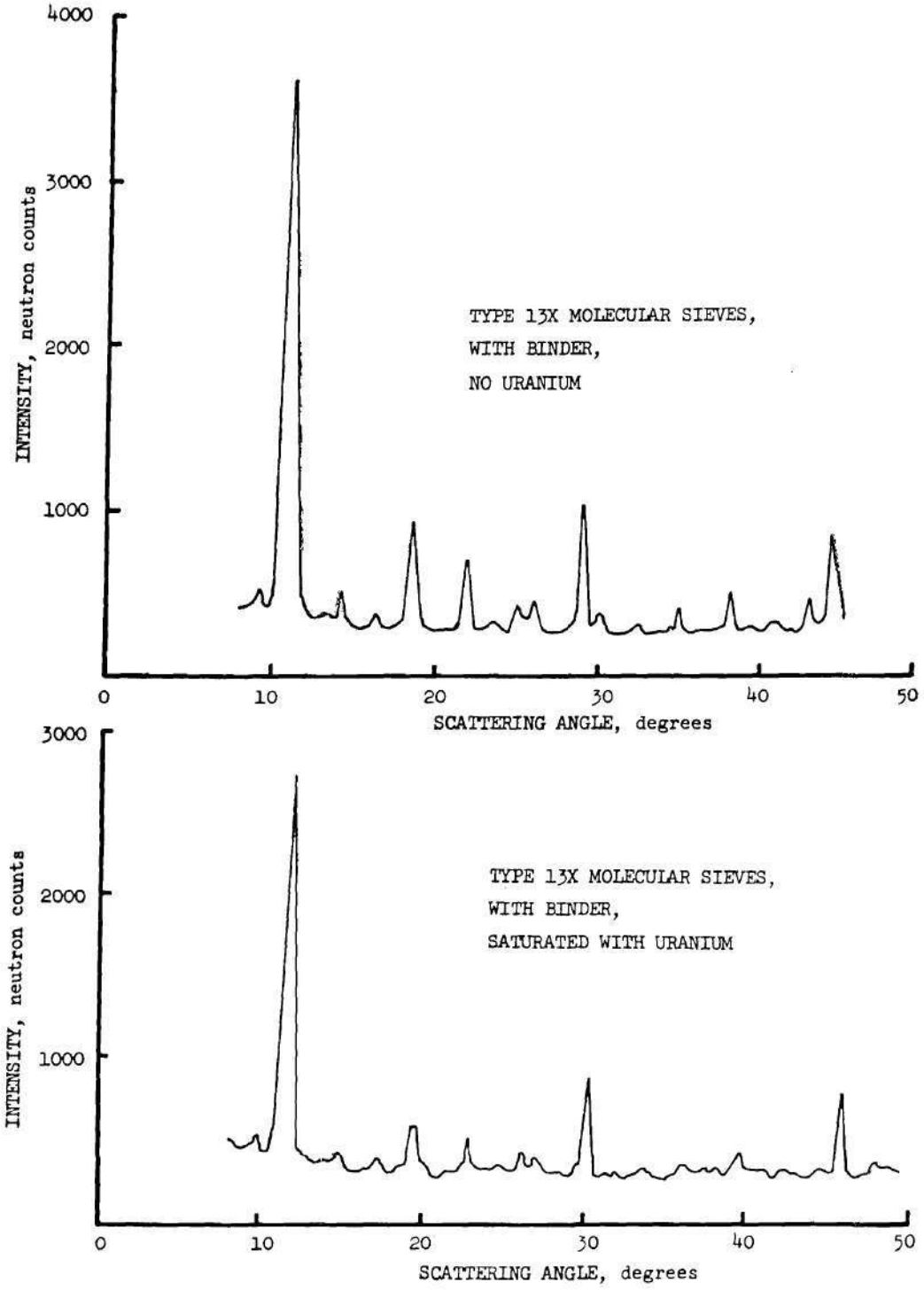

Figure 19. Neutron Diffraction Patterns of Normal and Uranium-Loaded Molecular Sieves

The scanning electron microscope (SEM) was used to examine the relationship of the clay binder to the aluminosilicate crystallites and to ascertain the dimensions of the crystallites. The procedure was first to coat the surface of the specimen to be examined with a film of gold-palladium alloy by vacuum evaporation. This produces a surface replica possessing high reflectivity for the electron beam. Using a Cambridge Mark IIa Stereoscan SEM, the pictures shown in Figures 20, 21, and 22 were made. In these photographs the clay binder is seen as a fibrous web adhering to the surfaces of the aluminosilicate octahedra. The clay had the fibrous appearance of attapulgite. Information was later obtained from the manufacturer (67) confirming the clay as attapulgite and giving the specifications for clay content as ranging from 15 to 20 percent by weight. Note the SEM photographs of the surface indicating a general coating of the surface by the clay binder.

Examination of both uranium-loaded and plain molecular sieves on the SEM revealed no visible change in internal or surface structure which might be related to the incorporation of the uranium.

Measurements taken from the SEM photographs indicate the average diameter of the crystallites to be 2.5×10^{-4} cm with a range of 1.5×10^{-4} cm to 3.0×10^{-4} cm.

When cleaving the molecular sieve spheres in order to examine the interior with the SEM, it was noted that the yellow color attributed to uranyl ion exchanged by the crystalline did not fully penetrate the sphere. This coloration extended from the outer surface into the bead for a distance equal to about one third of the bead diameter in the lot of uranium-loaded molecular sieve beads examined. To confirm the yellow coloration

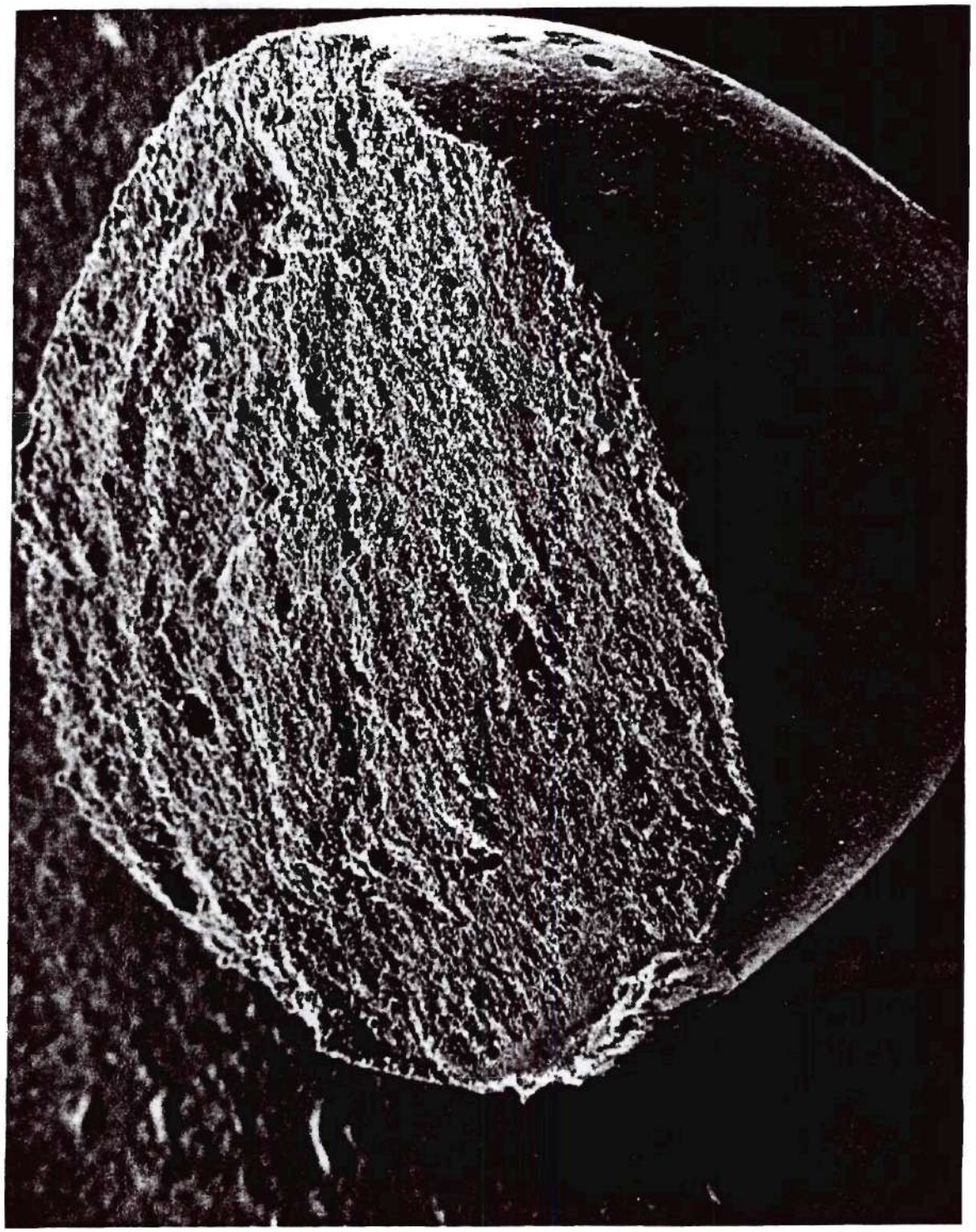

Figure 20. Fractured Type 13X Molecular Sieve Bead
Magnification: X 75

Figure 21. Type 13X Molecular Sieve Bead Inner Structure Showing Zeolite Crystallites and Clay Binder
Magnification: X 6000
The clay is the fibrous material between the crystallites

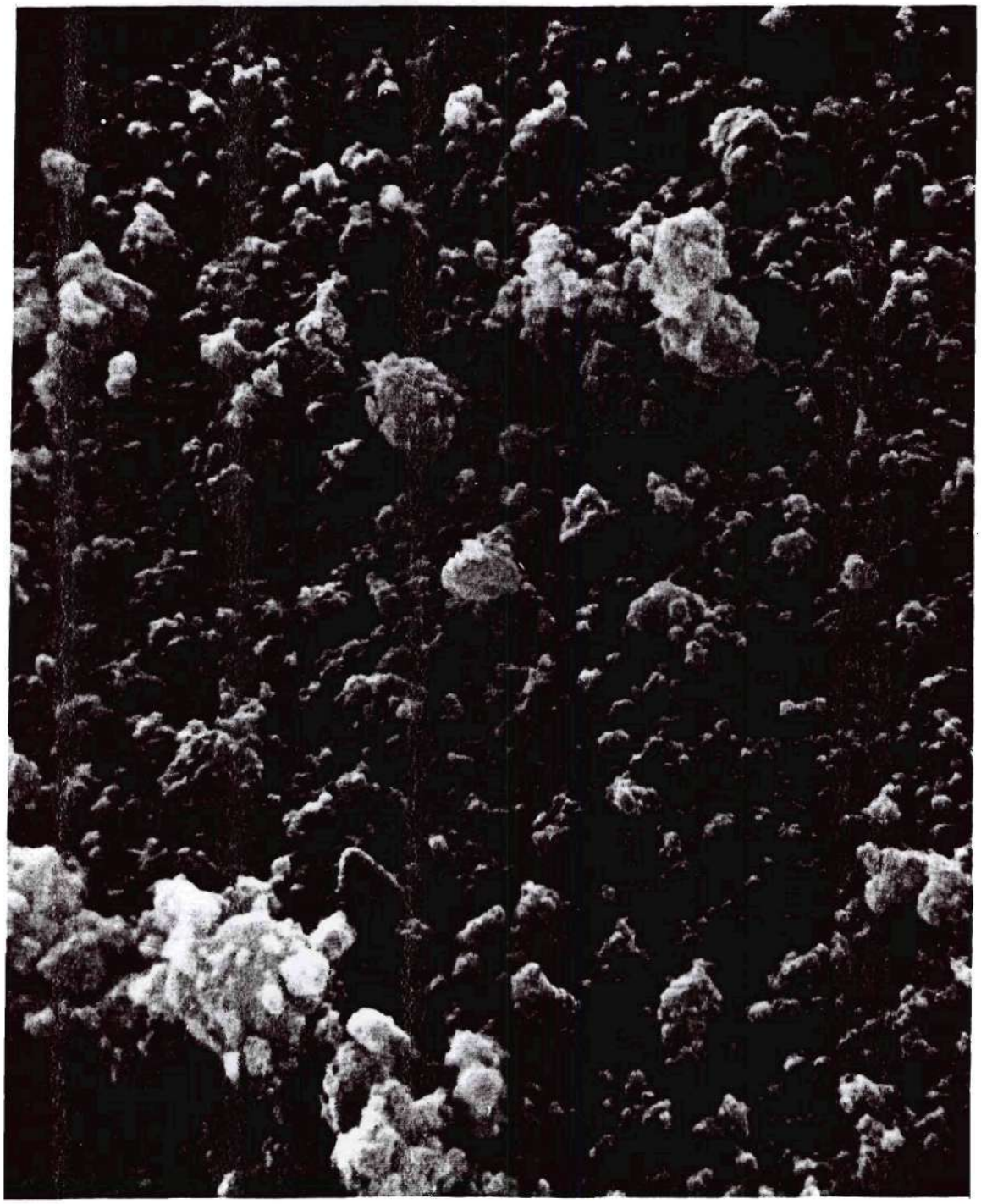

Figure 22. Type 13X Molecular Sieve Bead Outer Surface
Magnification: X 9000

as an indication of the extent of uranyl ion exchange within the bead, an electron microprobe scan was made across the diameter of a cleaved, uranium-loaded bead using an Acton Laboratories Model MS 64 electron microprobe unit. This apparatus scans an electron beam one micron in diameter across the specimen and detects the X-rays emitted from the specimen as a result of excitation by the electron beam. The lithium-drifted silicon X-ray detector is coupled to a pulse-height analyzer so that X-ray energies from specific elements may be counted. With the pulse-height analyzer set for counting the uranium X-rays, the microprobe provides a plot of relative uranium concentration versus distance as it scans the specimen.

The initial microprobe scan of the bead in which the color segregation was visually noted revealed that the uranium penetration into the bead surface corresponded to the observed depth of the yellow region of the sphere.

This was an indication that the ion exchange process proceeded from the outer bead surface towards the center in a manner analogous to the downward vertical progression of a saturated region in an ion exchange column operation. This is due to the high rate of exchange of the uranyl ions by the aluminosilicate crystallites compared to the rate of diffusion of the uranyl ions into the clay-bound crystallite spheres. This was discussed in Section 2.4.

If this is the explanation for this exchange behavior, the accumulation of uranium by exchange onto the crystallites will be limited to the outer region of the molecular sieve sphere until saturation of this

portion is achieved and will then proceed towards the center of the sphere--resulting in a band of constant, saturated uranium concentration.

A set of Type 13X (Davison Chemical; 8-12 mesh) molecular sieve pellets was prepared containing from 2.5 to 25 milligrams of uranium per gram of molecular sieves. These were made by adding appropriate quantities of UNH to methanol and contacting this solution with the molecular sieves until exchange equilibrium was reached. Samples of uranium-loaded spheres from each concentration (including a uranium-saturated bead) were examined after cleaving into halves by the electron microprobe. Figure 23 shows typical uranium distributions in these molecular sieve beads. Some lack of homogeneity was evident, but in general the uranium concentration near the surface increases with increasing uranium loading until the 25 milligrams per gram level was reached. At this point some increase in the width of the exchanged region begins to appear and in the uranium-saturated specimen a relatively constant uranium content is found to the center of the bead. The main cause of the irregularity in the uranium distribution is attributed to microscopic non-uniformity in the packing of the crystallites in the bead which results in channeling of the diffusion of uranyl ions during the exchange process.

3.0 Summary and Conclusions

Experimentation with electrodeposition of hydrous uranium oxide from dilute ammonium oxalate solutions of UNH proved capable of producing deposits up to one milligram per square centimeter in thickness. When ignited in air at temperatures in excess of 500°C the deposited hydrous uranium oxide is converted into U_3O_8. The electrodeposited uranium when

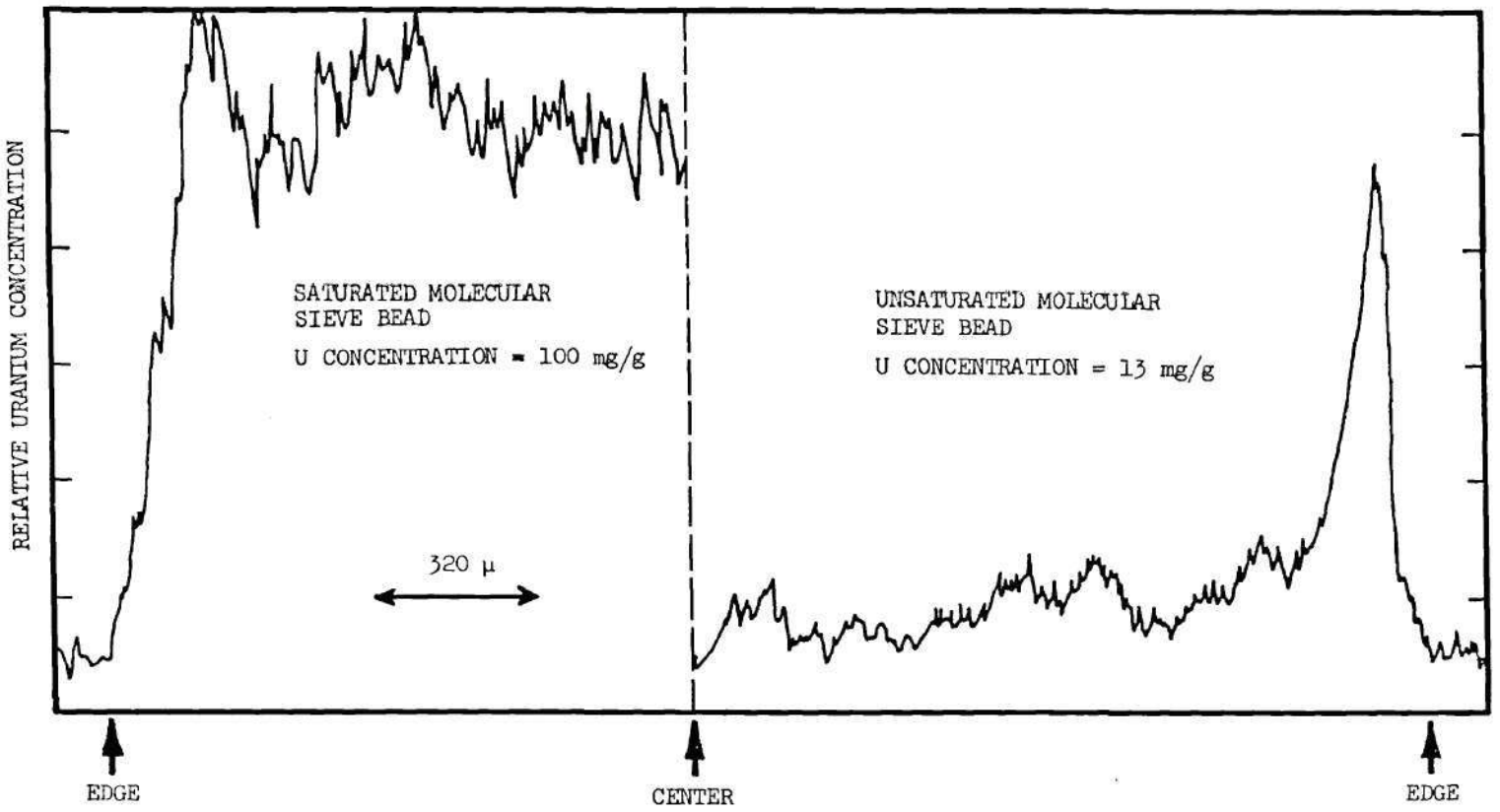

Figure 23. Uranium Distributions in Molecular Sieve Beads. Electron Microprobe Scans across Fractured Surfaces of Uranium-Loaded Beads

prepared as described in Section 2.1 is evenly deposited and reasonably resistant to removal by wiping from the nickel metal cathode surface.

The ion exchange loading of uranyl ions onto molecular sieves has been demonstrated. It is necessary to use non-aqueous solutions of uranyl nitrate in order to avoid precipitation of the uranium as a diuranate due to inherent high pH of aqueous solution in equilibrium with the synthetic aluminosilicates. Methanol was selected as a suitable solvent based on considerations of its solvent properties for UNH and its small molecular dimensions, permitting free access to the microporous structure of the synthetic zeolites.

The measured distribution coefficient for uranyl ion exchange onto 4 grams of Type 13X molecular sieves was 175 when contacted with a methanol solution of UNH containing 9.7 milliequivalents of UO_2^{+2} per liter. The same measurement using Type 5A molecular sieves resulted in a measured distribution coefficient of only 14. This demonstrated the effect of the smaller pore diameter in the Type A synthetic zeolites which screen out the large UO_2^{+2} ions from portions of the three-dimensional zeolite structure.

The maximum exchange capacity of the Type 13X molecular sieves for uranyl ion exchange was measured to be 0.83 milliequivalents of UO_2^{+2} per gram at 25°C while Type 5A would exchange only 0.3 milliequivalent per gram.

Apparent or effective diffusion coefficients for the Type 13X molecular sieve pellets were measured to be 2.0×10^{-9} $cm^2 sec^{-1}$ at 25°C and 3.5×10^{-9} $cm^2 sec^{-1}$ at 65°C. This agrees well with data for other ion diffusion rates measured in these materials by other investigators.

The rate determining step in the ion exchange of uranyl ion from methanol solution onto Type 13X molecular sieve pellets (with clay binder) was determined to be the intracrystallite diffusion through the bead rather than the diffusion into the individual crystallites at which point the ion exchange reaction occurs.

This mechanism was suggested by the observation of the distribution of uranium in partially exchanged molecular sieve beads in which the uranium was found only in the outer shell of the sphere. This is consistent with the values for the measured apparent diffusion coefficient for the aggregated crystallite spheres and reported apparent diffusion coefficients for the pure aluminosilicate crystallites for ion exchange with similar large cations. The very small dimensions of the crystallites (1-2 μ) more than compensate for the smaller value for the diffusion coefficients in this phase of the bead. This results in the rate of exchange in the bead being limited by the rate at which uranyl ions can diffuse into the interstitial spaces between the crystallites. The energy or enthalpy of activation was measured to be 2.8 kcal per gram ion. This low value is consistent with the relative ease of diffusion of the uranyl ions into the zeolite crystallite aggregate.

The saturated Type 13X molecular sieves were shown to have exchanged 16 percent of the sodium cations for uranyl ions. This is in good agreement with the reported 18 percent of the sodium cations which are available for Ba^{+2} exchange due to their location in the large diameter of the faujasite structure.

High concentrations of UNH in methanol (> 5 mg per ml) were found

to cause oxidation of the methanol resulting in reduction of the U(VI) to U(IV) and precipitation of the U(IV) salt due to insolubility in methanol. This reaction was not observed in pure UNH-methanol solutions and is, therefore, attributed to a catalytic effect of the molecular sieve high surface area.

Using the preparative methods described, thin U_3O_8 targets deposited on nickel metal and uranium-loaded molecular sieves have been studied for emission of fission-produced xenon isotopes as described in Chapter III.

CHAPTER III

RELEASE OF FISSION PRODUCT XENON FROM HIGH SURFACE AREA TARGETS

1.0 Technical Background

1.1 The Fission Process

As depicted in Figure 2, the thermal neutron induced fission of a uranium-235 nucleus results in the formation of two fission fragments of unequal mass. The most probable masses are known to be approximately 95 and 135. The resulting primary fission products have high neutron-to-proton ratios when compared to the value of the ratio for the "line of stability" on the chart of the nuclides. Successive decay down the isobaric chains by repeated beta particle emission (an average of three per chain) stabilizes the fission product nuclei by reducing the neutron-to-proton ratio until it falls on the stability line. Through this process the approximately 80 different primary fission products produce over 200 different radioactive species during the post-fission decay.

Radioactive xenon nuclides appear in the decay chains for mass numbers 131, 133, and 137 through 144. Table 11 is a compilation of the decay modes and half-lives of the participating nuclides in these decay series (2).

Quantitative aspects of such complex decay chain transitions which involve multiple radioactive species were first expressed mathematically by Bateman (68). Appropriate versions of the Bateman equations were developed describing the fission product decay chains and are given in

Table 11. Decay of Fission Product Chains which Involve Radioactive Xenon Nuclides

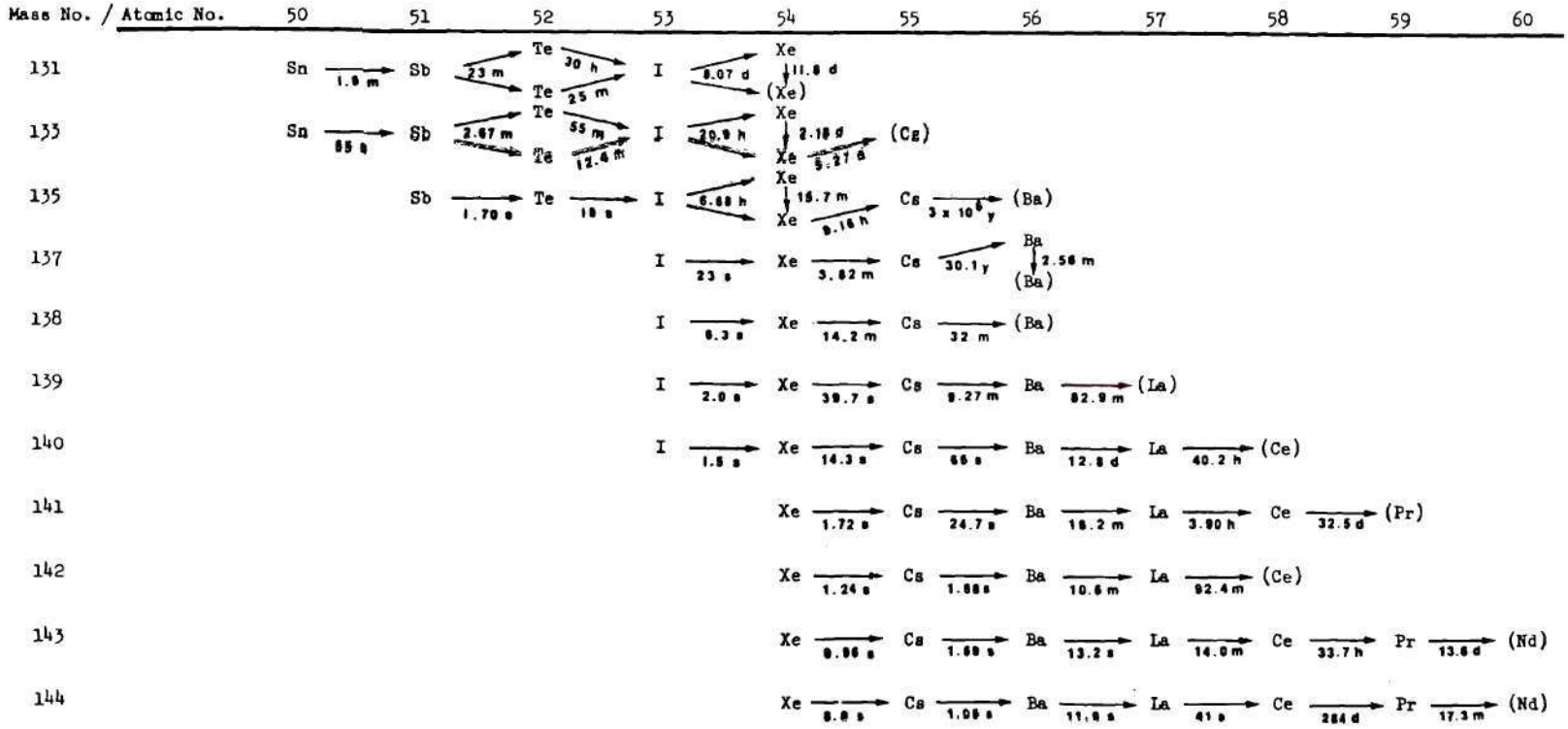

Half-life notations: s = seconds
m = minutes
h = hours
d = days
y = years
( ) = stable end of chain

Appendix B.

Since in the decay of chains producing both xenon-133 and xenon-135, the immediate precursor, iodine, is produced by the decay of a relatively short-lived tellurium nuclide, it is valid to consider the xenon as the second member of the chain provided that the decay time since removal from the reactor is long in comparison to the tellurium precursor half-life. This was the case in all of the experimental work performed in this investigation.

As given in Appendix B, the expression for the number of atoms of the second member of a decay chain is:

$$N_2 = \lambda_1 P \left[\frac{(1 - e^{-\lambda_1 T}) e^{-\lambda_1 t}}{\lambda_1 (\lambda_2 - \lambda_1)} + \frac{(1 - e^{-\lambda_2 T}) e^{-\lambda_2 t}}{\lambda_2 (\lambda_1 - \lambda_2)} \right]$$

where

N_2 = number of atoms of the daughter nuclide

P = rate of production of precursor atoms

λ_1 = decay constant for precursor nuclide

λ_2 = decay constant for daughter nuclide

T = irradiation time

t = decay time

Since the activity in disintegrations per unit time for the daughter nuclide is given by:

$$A_2 = \lambda_2 N_2$$

the term N_2 may be replaced by A_2/λ_2 and the equation reduces to:

$$A_2 = P\left[\frac{\lambda_1(1 - e^{-\lambda_2 T})e^{-\lambda_2 t} - \lambda_2(1 - e^{-\lambda_1 T})e^{-\lambda_1 t}}{\lambda_1 - \lambda_2}\right]$$

If the production rate, P, is redefined as:

$$P = \sigma \emptyset N Y$$

where

σ = fission reaction cross section, cm^2

$\emptyset$ = thermal neutron flux, n cm^{-2} sec^{-1}

N = number of uranium-235 atoms

Y = fission yield (fraction of fissions resulting in formation of precursor atoms)

then:

$$A_2 = \sigma \emptyset \frac{W}{235} N_A Y\left[\frac{\lambda_1(1 - e^{-\lambda_2 T})e^{-\lambda_2 t} - \lambda_2(1 - e^{-\lambda_1 T})e^{-\lambda_1 t}}{\lambda_1 - \lambda_2}\right]$$

where

W = weight of uranium-235, grams

N_A = Avogadro's number, 6.023×10^{23} atoms per gram atomic weight

In the case of xenon-135, for example, a small fraction of the uranium-235 fissions produce xenon-135 directly, rather than through the decay chain route. As shown in Appendix B, the first member of the chain (which would represent xenon-135 produced directly by fission) is given by:

$$N_1 = \frac{P}{\lambda_1}(1 - e^{-\lambda_1 T})\, e^{-\lambda_1 t}$$

or by

$$A_1 = P(1 - e^{-\lambda_1 T})e^{-\lambda_1 t}$$

Incorporation of this direct yield source of fission product into the expressions for the second member of the decay chain from above gives:

$$A_2 = P_i \left[\frac{\lambda_1(1 - e^{-\lambda_2 T})e^{-\lambda_2 t} - \lambda_2(1 - e^{-\lambda_1 T})e^{-\lambda_1 t}}{\lambda_1 - \lambda_2}\right]$$

$$+ P_d \left[(1 - e^{-\lambda_2 T})e^{-\lambda_2 t}\right]$$

where

P_i = production rate indirectly through the iodine precursor

P_d = production rate directly by direct yield in the fission process

and

$$A_2 = \sigma\phi \frac{W}{235} N_A \left\{Y_i \left[\frac{\lambda_1(1 - e^{-\lambda_2 T})e^{-\lambda_2 t} - \lambda_2(1 - e^{-\lambda_1 T})e^{-\lambda_1 t}}{\lambda_1 - \lambda_2}\right]\right.$$

$$\left. + Y_d \left[(1 - e^{-\lambda_2 T})e^{-\lambda_2 t}\right]\right\}$$

where

Y_i = precursor fission yield

Y_d = direct fission yield

Use of the appropriate version of these equations permits the calculation of the quantity of xenon-133 or xenon-135 present in an irradiated uranium target if either of the following sets of information is known:

a) thermal neutron flux
   mass of uranium-235 in target
   absolute fission yields of the pertinent nuclides
   irradiation time
   decay time

b) fission rate during irradiation
   irradiation time
   decay time

Figures 24 and 25 represent the ingrowth and decay of xenon-133 and xenon-135, respectively, as calculated with the equations given here.

The literature abounds with fission product yield data. Due to innate difficulties in defining and measuring neutron flux, the experimental determination of absolute fission yields for specific nuclides is difficult. Much more reliable is the relative yield of the various fission products when determined from a single irradiated specimen of uranium-235. Such relative values do not suffer from the usual uncertainties of neutron flux. If another fission product is determined quantitatively and the fission rate calculated using rearranged versions of the equations describing the fission chain decay just given, this value for the fission rate may be used to calculate the xenon fission production without requiring knowledge of either the neutron flux or the uranium content of the target.

Farrar and Tomlinson (69) have reported their carefully measured fission yields as well as a summary of the results of other investigators. Their measurements were made using a mass spectrometer and agreed well with other reported data. From their data, values of 6.63 percent for the mass-133 chain and 6.45 percent for the mass-135 chain total absolute fission yields were used in this study. Examination of the variations in

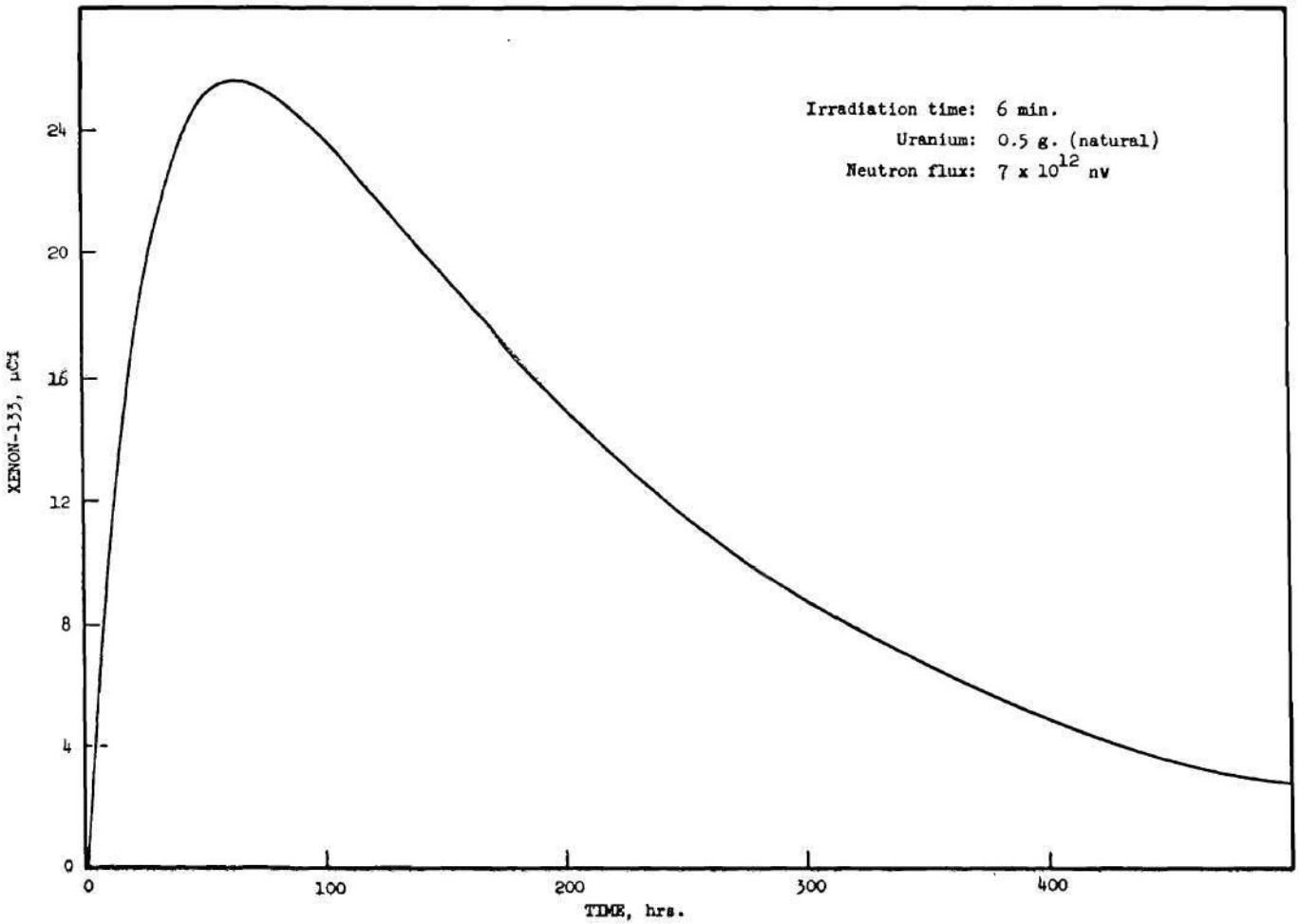

Figure 24. Ingrowth and Decay of ^{133}Xe After Removal from Reactor

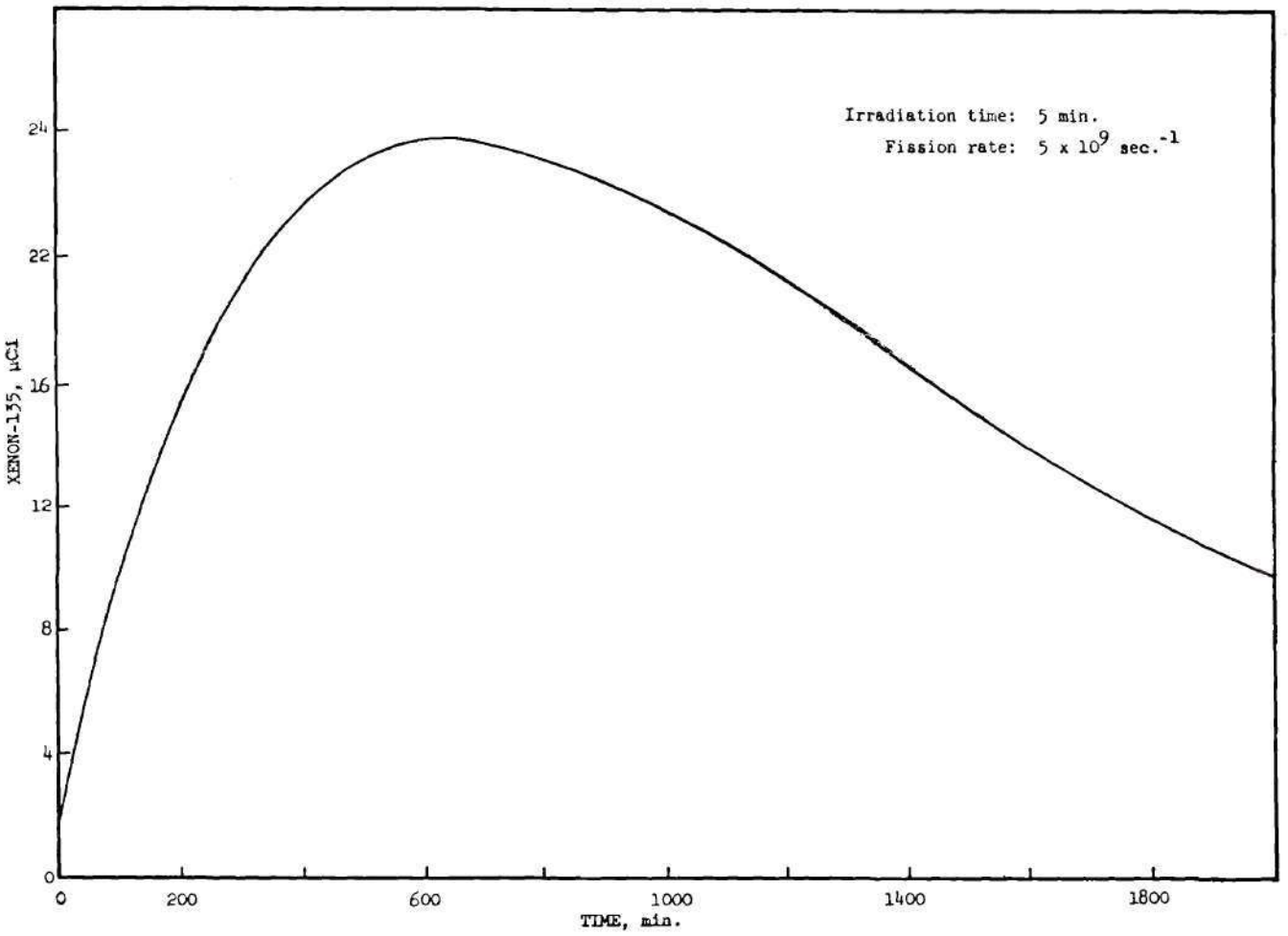

Figure 25. Ingrowth and Decay of ^{135}Xe After Removal from Reactor

reported absolute fission yields for these mass chains indicated a precision of ± 5 percent of the values reported. Relative fission yields, however, are expected to be in better agreement. Calculations from the summary of data by Farrar and Tomlinson give a value of two percent for the average standard deviation of the relative yield data for the two mass chains of interest in this study.

According to Grant, et al. (2), the fractional direct fission yields for the two mass numbers are as shown in Table 12. These values were used in the calculations of this investigation.

Table 12. Fractional Direct Fission Yields for Masses 133 and 135

Element	Mass 133	Mass 135
Sn	0.0117	0.0975
Sb	0.4706	0.0975
Te	0.5030	0.5001
I	0.0147	0.3658
Xe	0.0	0.0363

1.2 Fission Fragment Energetics

At the conclusion of the fission event the two fission fragments possess the major portion of the 200 MeV energy released by the mass loss during fission. Table 13 outlines the distribution of the available fission energy (70).

The energetic fission fragments may escape from the surface layers of the uranium target when the fission event occurs at a point in the target within a distance from the surface less than the fission fragment range in the target material.

Table 13. Approximate Distribution of Fission Energy

	MeV
Kinetic energy of fission fragments	165
Instantaneous gamma-ray energy	7
Kinetic energy of fission neutrons	5
Beta particles from fission products	7
Gamma-rays from fission products	6
Neutrinos	10
TOTAL FISSION ENERGY	200

Since momentum is conserved in the separation of the fission fragments after the fission process, the kinetic energies of the two particles are not equal:

$$m_\ell v_\ell = m_h v_h \quad \text{(conservation of momentum)}$$

$$\tfrac{1}{2} m_\ell v_\ell^2 (m_\ell) = \tfrac{1}{2} m_h v_h^2 (m_h)$$

Then:

$$E_\ell = \frac{m_h}{m_\ell} E_h$$

where

m_ℓ and m_h are the masses of the light and heavy fission fragments, respectively;

v_ℓ and v_h are the velocities of the light and heavy fission fragments, respectively; and

E_ℓ and E_h are the kinetic energies of the light and heavy fission fragments, respectively.

This demonstrates that the kinetic energy is distributed in an inverse proportion to the mass ratio of the two fragments. In the case of

xenon-133 and its typical complementary fission product of mass 101, the ratio of kinetic energies would be 1.32. Table 14 gives some data for a sample fission event (71).

Table 14. Approximate Physical Properties of the Most Probable Products of the Fission of ^{235}U by Thermal Neutrons

	Light Fragment	Heavy Fragment
Mass number	97	138
Nuclear charge	38 (Sr)	54 (Xe)
Kinetic energy	95 MeV	67 MeV
Initial velocity	1.4×10^9 cm/sec	0.93×10^9 cm/sec
Initial ionic charge	20e	22e
Mean range in air	2.5 cm	1.9 cm

During the fission process and concurrent acceleration of the fragments, many orbital electrons are stripped from the fragments, leaving them with a large net positive charge (see Table 14). As the fragment moves through the target material it interacts by exchange of electrons with target atoms as well as by elastic nuclear collisions. Figure 26 represents the slowing-down process as it occurs in a gas absorber for the light and heavy fragments (72). The intense ionization, elastic nuclear collision processes and resulting radiation damage which constitute the fission fragment stopping mechanism are of importance as factors affecting fission gas release by "diffusion" processes as will be discussed later.

Due to the high charge and large mass of the fission fragments, their range is rather small when compared to alpha and beta particles.

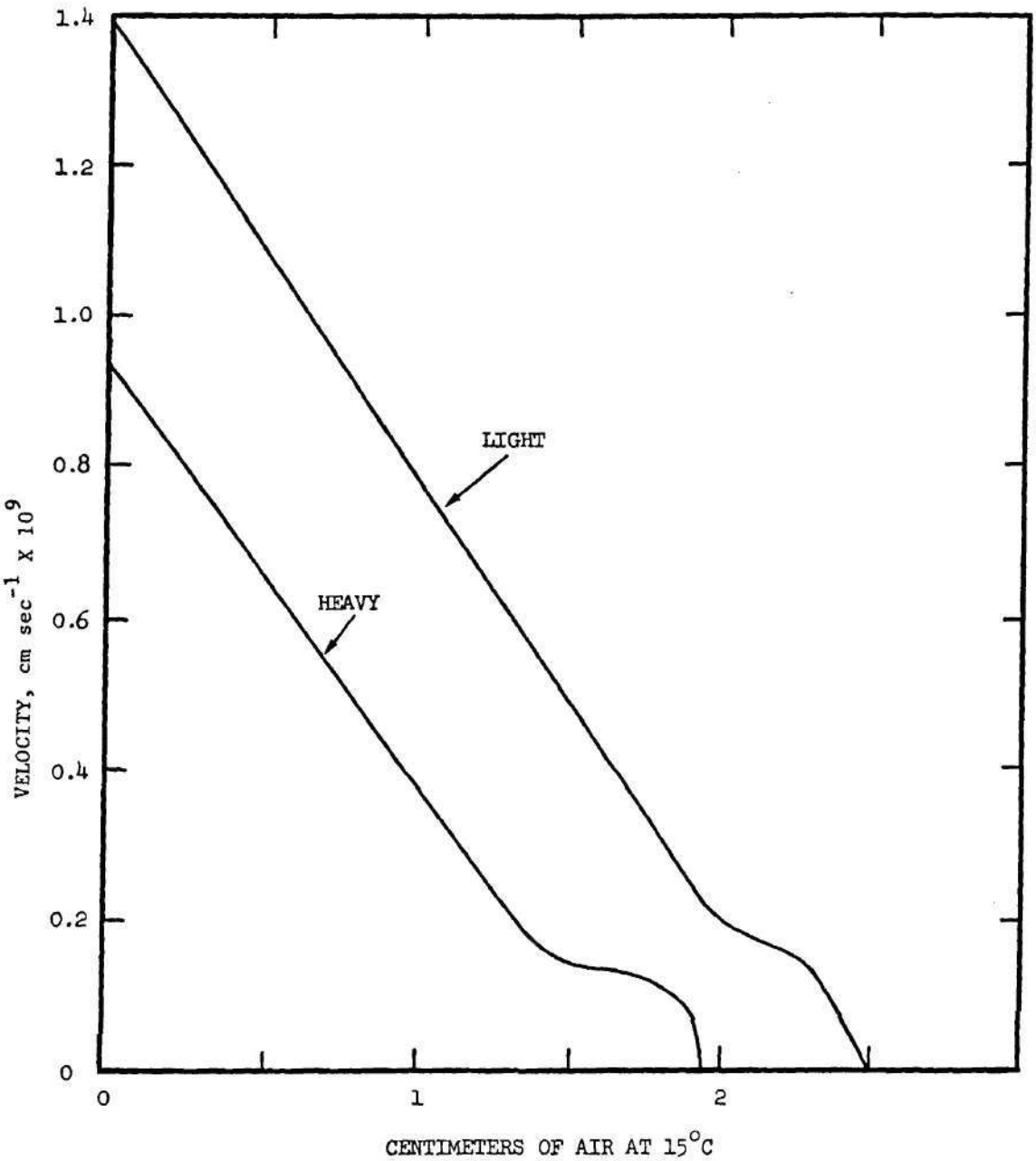

Figure 26. Velocity-Distance Relationships for Fission Fragments in Air (from reference 72)

Katcoff et al.(73) measured the effect of fission fragment mass on range in air. Figure 27 shows the results of their measurements. Note the apparent reduction in fission fragment kinetic energy for symmetric fission (near mass number 120).

The approximate range of an average mass fission fragment in various materials is given in Table 15 (74).

Table 15. Approximate Range of Fission Fragments *from Thermal Neutron Fission of* ^{235}U

Material	Range	
	(μ)	(mg/cm^2)
Aluminum	14	3.7
Copper	5.9	5.2
Silver	5.3	6.1
Gold	5.9	11.1
Uranium	6.6	12.6
Uranium oxide (U_3O_8)	14	10.0

The direct recoil release of fission product gases from a thin film of uranium oxide was investigated by a group at Harwell (17). This study was made "in-pile," the release being measured during irradiation by sweeping the fission product gases from the uranium oxide target with nitrogen or helium gases. The target used had a thickness of 0.6 micron and a density of 0.17 milligram per cm^2. Some interesting results were obtained even though the counting equipment was somewhat crude by today's standards (a single-channel pulse height analyzer with NaI(Tl) crystal detector). Table 2 (Chapter II) presents the results obtained in this Harwell study measuring the direct recoil releases of xenon-135, krypton-85m, and xenon-133 from thin uranium oxide targets.

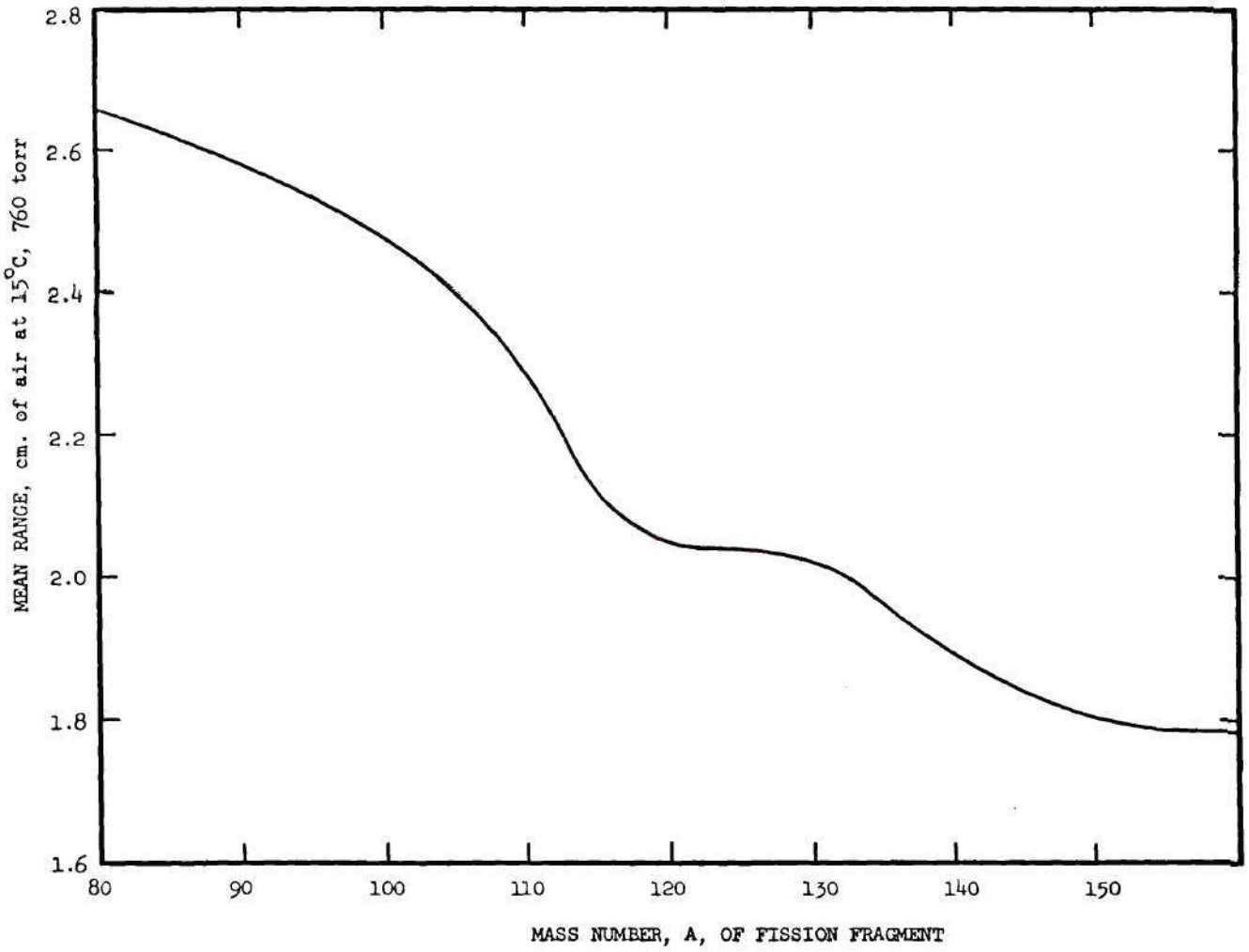

Figure 27. Mean Range of Fission Fragments in Air as Function of Mass Number (from reference 73)

The calculated rates of emission given in Table 2 are based on 50 percent of the fission rate production for xenon-133. Fifty percent loss was assumed due to recoil into the film backing material. The theoretical capture efficiency in the carrier gas is based on a value of 4.7 cm for the range of the xenon-133 fragment in nitrogen and 24 cm in helium at the 375°C operating temperature. The Harwell group suggests the explanation for a capture efficiency higher than expected for xenon-133 in the sweep gas is that the 5.27 day half-life of this nuclide allows it to diffuse from the silica apparatus walls where the portion not caught in the sweep gas was deposited due to recoil. This premise explains the observed experimental data. An appreciable fraction of the recoiling atoms would be captured within one micron of the surface of the silica and the diffusion length for xenon in silica at this temperature is on the order of one micron. Undoubtedly, some release from the metal backing material and accelerated release due to high surface area augmentation by "knock-out" of groups or clusters of molecules by the high energy primary fission fragments contributed to the measured xenon-133 "capture efficiency."

These in-pile release experiments at Harwell have demonstrated the effects of recoiling fission fragment implantation in fission source backings and container walls. In addition, the data from these experiments with uranium oxide suggest that, in the proper target (high surface area/mass ratio), the xenon fission gases release fractions may be sufficiently large for the design of a practical process for the production of these radionuclides.

Calculational estimation of the recoil range of the heavy fission

fragment in the molecular sieve matrix can be made using the following empirical expression (75):

$$\overline{R} = 0.56\ A^{\frac{1}{3}}\overline{R}_a$$

where

$\overline{R}$ = average range in molecular sieve, mg cm^{-2}

A = effective atomic weight

$\overline{R}_a$ = average range in air, cm

The effective atomic weight of the molecular sieves may be calculated by:

$$A_e = \overline{A}_{Al,Si}\ \frac{\rho_{ms}}{\overline{\rho}_{Al,Si}}$$

where

A_e = effective atomic weight

$\overline{A}_{Al,Si}$ = average atomic weight of Al and Si (27.5)

ρ_{ms} = density of molecular sieves (2.0 g cm^{-3})

$\overline{\rho}_{Al,Si}$ = density of Al and Si (average) (2.5 g cm^{-3})

Inserting these values into the equation gives the effective atomic weight of 22 for the molecular sieves. Calculation of the range using this effective atomic weight gives the result of 3.0 mg cm^{-2} for the range of the heavy fission fragment in molecular sieves. This is equivalent to a thickness of 15 μ.

If the dimensions of the uranium-containing aluminosilicate crystallites are considered (average diameter of two microns), it is realized that the recoiling fission fragments are most likely to escape the crystallite in which the fission occurred and come to rest at a location in

another particle. The electron microprobe examinations of the uranium-loaded molecular sieve beads (described in Chapter II) revealed that the uranium was concentrated in the outer shell of the bead when less than a saturated condition existed. Furthermore, the electron microprobe measurements indicated that the uranium-containing shell was about 400-500 microns in thickness. From this information it can be calculated that only four percent of the uranium is within 15 microns of the bead surface and capable of direct escape from the bead by recoil. The isotropic nature of the fission process will reduce the expected recoil losses to less than two percent.

1.3 Mechanisms for Post-Irradiation Fission Gas Release

Temperature dependent post-irradiation release of fission gases from irradiated targets has been consistently described in the literature as "diffusion" release. The reason for this explanation has been that an Arrhenius plot (logarithm of the release rate versus reciprocal temperature) gave a straight line over portions of the release curves. It has been proposed by Hurst (76) and Carroll and Sisman (77) that the temperature dependence of the release phenomenon is not primarily diffusion in the classical sense, but instead is controlled by the probability of the fission gas atoms being trapped and released from traps within the target crystalline structure. This is known as the "defect-trap" model and grew from the observations of decreased release rates at higher fission densities. If diffusion were occurring along vacancies in the crystal lattice created by radiation damage from fission fragments, the release rate would be expected to increase with increasing fission rate or fission

density. Figure 28 shows how the apparent diffusion coefficient, contrary to the foregoing statement, is drastically decreased by increasing fission density (78).

Traps in uranium dioxide target material have been classified into three groups: (1) intrinsic traps, e.g., voids, grain boundaries, and other inherent flaws in the material; (2) point defects produced as a result of fission fragment radiation damage; and (3) clusters of point defects, also a result of radiation damage.

The "defect-trap" theory proposes that a diffusing fission product atom is trapped by one of the above listed traps, but that it then has a probability of escape which is temperature dependent. The point defects, which are radiation-induced, have a temperature-dependent lifetime and if they do not trap a fission product atom or combine to form a cluster, they will eventually anneal and vanish. Thus, the point defect concentration during a lengthy irradiation may reach an equilibrium determined by the radiation damage rate (neutron flux) and temperature (annealing rate). The increase of trap concentration with neutron flux (flux determines fission rate) explains the decrease in fission gas release rate under high fission rate conditions.

The "defect-trap" model also predicts grain boundaries to act as trapping sites. Figure 29 presents the results obtained by Carroll and Sisman (77) when release rates of krypton-88 were measured from single *crystal uranium dioxide (no grain boundaries) and fine grain uranium di*-oxide (grain size of 3 μ, many grain boundaries).

MacEwan and Morel (78) have critically examined the post-irradiation release of xenon fission gas from uranium dioxide. For small fractional

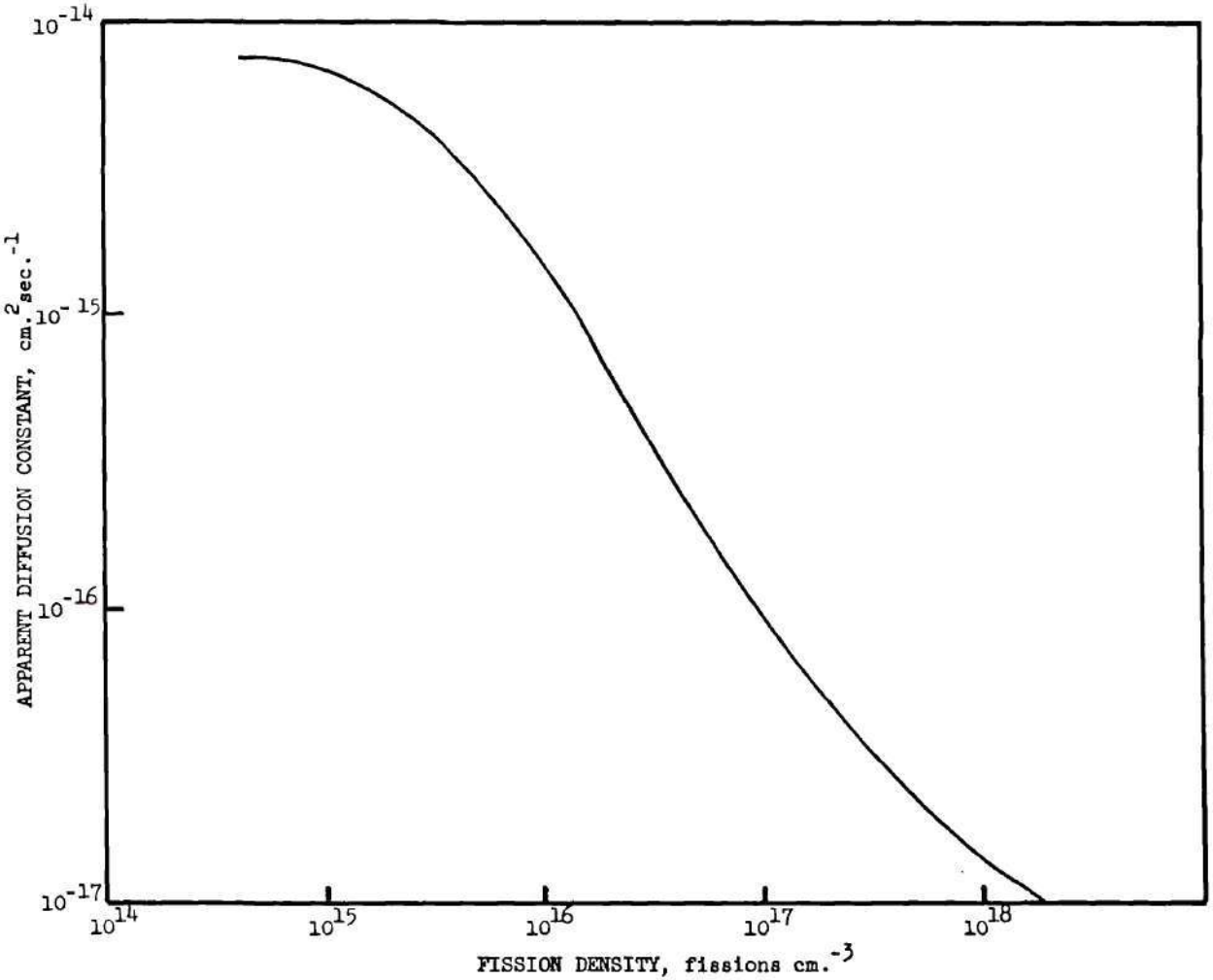

Figure 28. Effect of Fission Density on Apparent Diffusion Coefficient for Fission Product Xenon in UO_2 (from reference 78)

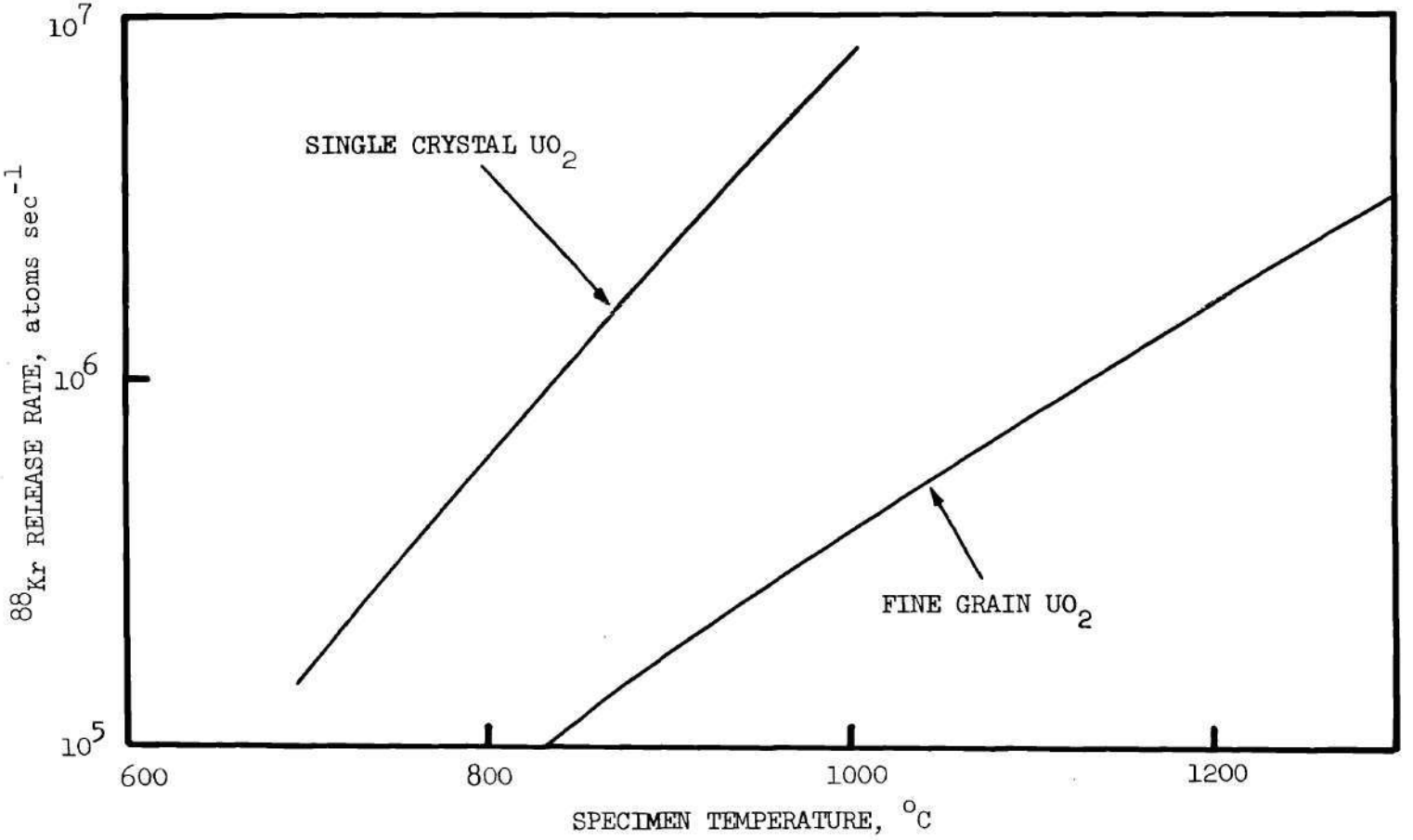

Figure 29. Temperature-Dependent ^{88}Kr Release Rate Normalized to Single Crystal Surface Area (from reference 77)

release (less than 0.5) the diffusion of xenon from uranium dioxide target particles is described by:

$$f = \sqrt{4Dt/\pi}\ \frac{S}{V}$$

where

f = the fractional release of gas

t = the annealing time

D = the apparent diffusion constant

S/V = the surface area/volume ratio (specific surface area)

This equation may be modified to (see Appendix C):

$$f = \frac{6}{r}\sqrt{\frac{Dt}{\pi}}$$

where

r = radius of the particle

As was shown in Chapter II, where this expression was applied to the measurement of diffusion coefficients for solvated uranyl ions into molecular sieve beads, a plot of the fraction of the total xenon released versus $(\text{time})^{\frac{1}{2}}$ should give a straight line for a purely diffusion-controlled release mechanism.

Typical values for the apparent diffusion coefficient for xenon in uranium dioxide as reported by MacEwan and Morel average 8.2×10^{-15} $cm^2 sec^{-1}$ for samples subjected to low fission density (10^{14} fissions cm^{-3}) at a temperature of 1400°C. The magnitude of this diffusion coefficient is indicative of the extremely slow rate of diffusion of xenon in uranium dioxide.

MacEwan and Morel were the first to view the migration of xenon

in uranium dioxide from a quantitative standpoint based on the diffusion model established by Hurst. This model treats the escape of a sparingly soluble gas from a sphere in which it is initially homogeneously distributed and which contains a stable array of trapping sites. "Stable" means a constant cross sectional area for the total trap content in the specimen. The mean distance that a xenon atom can diffuse before encountering a trap is expressed by:

$$L^2 = d/(3 \sum_i \pi n_i r_i^2)$$

where

L = the mean diffusion distance before being trapped

d = unit movement distance

n_i = the number of traps per cm^3 of radius r_i

Hurst applied this mean diffusion distance in the diffusion equation as a dimensionless trapping parameter:

$$\beta = r/(\pi L)$$

where

r = the radius of sphere from which the gas is diffusing.

A separate trapping parameter, β, would be applied for each type of trapping site and the overall trapping parameter would be:

$$\beta = (\beta_1^2 + \beta_2^2)^{\frac{1}{2}}$$

Another dimensionless parameter, γ, describes the possibility of a xenon atom returning to the lattice from a trapped position:

$$\gamma = (r^2 b)/(\pi^2 D)$$

where

b = the probability of an atom escaping from a trap in a unit time

D = the diffusion constant

In practice, the intermediate case exhibits a fractional release, f, where a fraction, Y, of the gas is initially trapped:

$$f = [(1-Y)F] + YG$$

MacEwan and Morel utilized this approach in their study of xenon-133 release from uranium dioxide. The increase in the trapping parameter was correlated with greater radiation damage induced trap density at high integrated neutron exposures. Due to the slowness of the xenon release process, the percent xenon-133 released was less than one percent in two days of heating at 1400°C from uranium dioxide single-crystal particles of 30.8 microns radius.

In summary, from the studies of Carroll and Sisman, and of MacEwan and Morel, a logical picture of the fission gas release process consistent with experimental behavior for uranium dioxide was evolved:

1) The release rates are consistent with those calculated from Hurst's solution to the diffusion equation.

2) Pre-existing microporosity in the uranium dioxide target material accounts for trapping of the fission gas in specimens exposed to low fission density.

3) Xenon trapping (as exemplified by retention) increased with fission density due to radiation damage-induced trap production, and was a linear function of fission density.

4) The average time for a xenon atom to remain in a pre-existing trap site was 13 days at 1400°C, while the average trap residence time for xenon in the smaller radiation-induced traps was about five days.

More recently, Ong and Elleman (80) developed analytical solutions for the diffusion-trapping models proposed by Hurst, MacEwan, and Morel. In considering the release of fission recoil injected rare gas atoms in the presence of homogeneously distributed traps in a solid matrix, Ong and Elleman defined a rate constant for trapping, k_1, and a rate constant for release of gas atoms from traps, k_2. They pointed out how, for various assumed values of diffusion coefficients, trap concentrations, and trap retention times the resulting fractional release versus $(\text{time})^{\frac{1}{2}}$ curves demonstrated varying deviations from classical diffusion behavior. Figure 30 illustrates that even for small fractional xenon releases the influence of trapping may be sufficient to modify the linear relationship of the fraction released with $(\text{time})^{\frac{1}{2}}$ characteristic of classical diffusion.

Many earlier investigators had assumed the slow release following a rapid initial release (or "burst release") represented a classical diffusion controlled release mechanism. The analysis by Ong and Elleman demonstrated that the "burst" could be explained by this competition between diffusion and trapping and that the slow release was determined by the rate of release from traps.

In the case of no trapping in the matrix ($k_1=0$), the diffusion is classical in nature and the plot representing fraction released versus $(\text{time})^{\frac{1}{2}}$ is a straight line. For large values of k_1 (rapid trapping) and

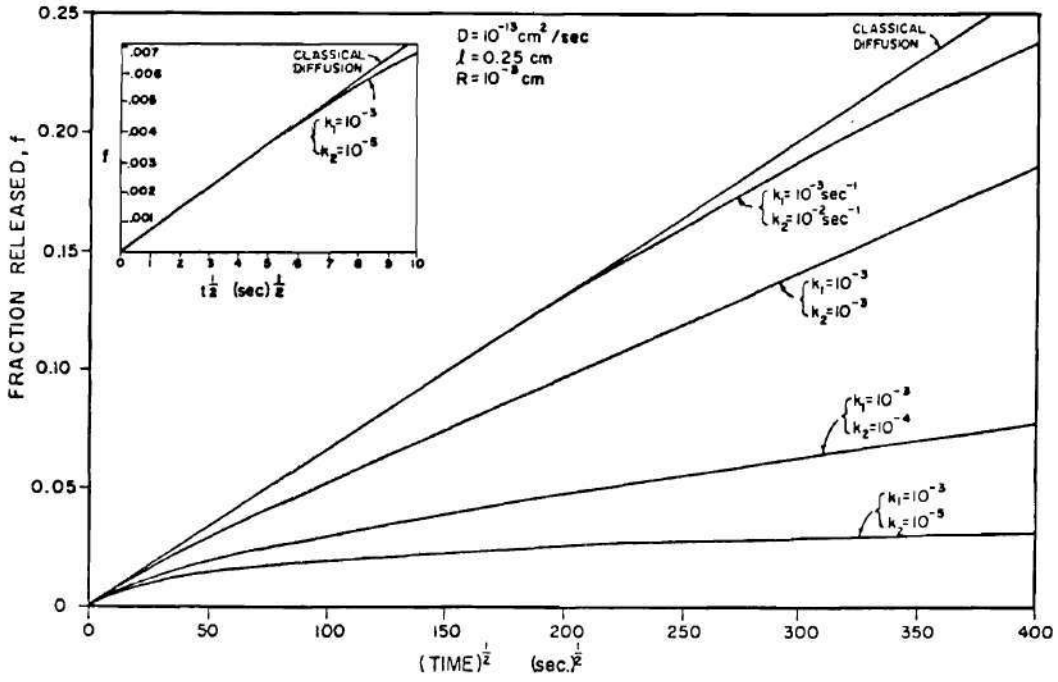

Figure 30. Predicted Gas Release from Irradiated Uranium (from reference 79)

small values of k_2 (slow rate of release from traps, "deep traps"), a large portion of the total released xenon escapes early, as shown in Figure 30.

When the structures of the synthetic zeolitic aluminosilicates are considered in light of this diffusion-trapping theory, it is seen that the three-dimensional, interconnected octahedral framework offers abundant natural trapping sites for fission produced xenon atoms in the form of molecular-size voids. At the low fission densities used in the experimental investigations (10^{14} fissions per gram), the radiation damage-induced defect trapping sites will be insignificant in comparison to the pre-existing natural structural traps of the zeolite crystalline framework. Also, since the aluminosilicate crystallites are individual single crystals, the grain-boundary effects referenced for polycrystalline uranium dioxide are absent.

As will be shown in the description of experimental work in this chapter, sorption of xenon at cryogenic temperatures by Type 13X molecular sieves is readily and completely reversible. Complete desorption of xenon is rapidly achieved at 25°C. Breck (80) has shown that the capacity for xenon absorption on Type X zeolite is 60 percent that of argon and krypton when compared by atom concentration per unit cell of the zeolite. Table 16 gives the data on gas adsorption by Type X zeolite according to Breck. Also given in this compilation is the minimum kinetic diameter of the gas molecules and the equivalent liquid volume of the adsorbed gases. Notable is the rather constant volume adsorbed with the exception of water which is probably capable of limited access to the smaller sodalite

Table 16. Adsorption of Gases and Vapors by Type X Zeolite (80)

Molecule	σ (Å)[a]	Temperature (°C)	Pressure (mm Hg)	Amount adsorbed (ml/g)[b]	No. of adsorbed molecules per unit cell
Ar	3.40	-183	760	0.304	141
Kr	3.60	-183	17	0.268	116
Xe	3.96	- 78	700	0.253	74
O_2	2.46	-183	760	0.312	149
N_2	3.64	-196	760	0.347	133
n-pentane	4.3	25	205	0.296	34
Neopentane	6.2	25	700	0.264	29
Benzene	---	25	76	0.298	45
Cyclohexane	---	25	45	0.253	31
H_2O	2.65	25	25	0.360	264
$(C_4H_9)_3N$	8.1	25	1	0.292	16.4

[a] σ, minimum kinetic diameter of molecule in Å.

[b] Calculated on the assumption that the density of the adsorbed phase is that of the liquid under the same conditions.

Table 17. Encapsulation of Gases in Type A Zeolite (81)

Gas	σ (Å)	Encapsulation		Amount Encapsulated	
		Temperature (°C)	Pressure (Atm)	cm^3 STP/g	After t Days at 25°C
CH_4	3.8	350	2650	105 , t = 4	98 , t = 37
C_2H_4	3.9	250	830	81 , t = 2	76 , t = 35
Ar	3.4	350	2650	109 , t = 3	77 , t = 79
Kr	3.6	350	4300	90.5, t = 1	90.5, t = 30

octahedra through the 2.2 Å ring openings. Breck also gives data on the differential adsorption of oxygen and nitrogen by Type A zeolites which indicate that a variation of 0.3 Å in the cage aperture diameter would have occurred over the temperature interval 80-300°K. This is reasonable due to variation in molecular vibrational amplitudes. This means that the aperture into the zeolite cage structure is effectively larger at higher temperatures. This effect in combination with the increase of the gas molecule kinetic energy with temperature may be expected to influence the release of xenon from the irradiated molecular sieves.

"Zeolite encapsulates" were reported by Breck (81). These were prepared by heating Type A zeolites with gases having minimum kinetic diameters normally too large to permit adsorption by passage through the 4.2 Å openings into the cage structure of this zeolite. Combination of high temperature and high pressure resulted in entrance of these larger molecules into the zeolite cages. Quenching, while maintaining the pressure, produced the "zeolite encapsulates" which are similar to the clathrate type "compounds" of inert gases and multiple-ring, cyclic organic structures. Table 17 gives data on the preparation and stability of such "zeolite encapsulates."

An examination of the kinetic energy of the gas molecules which enabled them to distort sufficiently to enter the cage structure is of interest. According to the Maxwell-Boltzmann distribution law, the most probable velocity, v, of gas molecules of mass, M, at absolute temperature, T, is given by (82):

$$v = \sqrt{\frac{2\ RT}{M}}$$

where

R = gas constant, 8.3314×10^{7} ergs $deg^{-1} mole^{-1}$

At 350°C (623°K) the value of the most probable velocity is 2.77×10^{4} cm sec^{-1}, which for xenon-135 is equivalent to 1.24 kcal $mole^{-1}$. This is the energy of those xenon-135 molecules (atoms) having the most probable velocity at 350°C.

As has been pointed out earlier in this section, the primary fission fragments share the approximate 165 MeV of kinetic energy from the fission process. The heavy fragment may typically have an energy of about 70 MeV, which is equal to more than 10^{9} kcal $mole^{-1}$.

Furthermore, successive beta particle emissions as the primary fission fragments proceed to decay down the chains cause the fission product atoms to experience energetic recoil. Evans (83) gives an expression for the maximum recoil energy, E_m, of the daughter atom following beta particle emission:

$$E_m = E_\beta \left[\frac{E_\beta}{2Mc^2} + \frac{m_o}{M} \right]$$

where

E_m = recoil energy, ergs

E_β = maximum beta particle energy, ergs

M = mass of daughter nucleus, grams

c = velocity of light, 3×10^{10} cm sec^{-1}

m_o = electron rest mass

In the case of xenon-135, the iodine-135 precursor decays by emission of a beta particle with a maximum energy of 1.4 MeV or 2.24×10^{-6} erg. The nuclear mass of 135 atomic mass units is equal to 2.26×10^{-22} gram.

Applying these values and the other constants to calculate the maximum recoil energy of the xenon-135 nucleus gives 2.14×10^{-4} erg, or 13.3 MeV, or 308 kcal $mole^{-1}$. This is a very high energy in comparison to the most probable energy of 1.24 kcal $mole^{-1}$ which enabled the oversized gas atoms to enter the Type A zeolite cages, forming the "zeolite encapsulates."

A search for bond energy data pertinent to the zeolite structure uncovered a value of 192 kcal $mole^{-1}$ for the diatomic Si-O bond and 120 kcal $mole^{-1}$ for Al-O (84). The average value of 156 kcal $mole^{-1}$ is a conservative approximation of the bond energies in the Al-O-Si-O structure of the zeolites. The significance of this estimated bond energy is that, even if the overwhelming kinetic energy of the primary fission fragments were not available, the recoil from the several successive beta particle emissions would be sufficient to disrupt the virgin zeolite structure.

2.0 Experimental Design and Equipment

2.1 Plan for Investigation

Initially the two forms of high-surface area uranium targets described in Chapter II, i.e., electrodeposited uranium oxide and uranium-loaded molecular sieves, were evaluated on the basis of relative efficiency in release of the fission-produced xenon radionuclides. Based on this information gathered in the evaluation, a choice was made as to which of these two types of targets is superior.

The problem of calculation of the quantity of xenon fission product produced was examined. It is not feasible to measure the total xenon fission product present in an irradiated uranium target directly by gamma-ray spectrometry due to the large quantities of other radioactive nuclides

also produced by irradiation of the target material. The use of activation foil measurements of thermal neutron flux and calculation of xenon fission product production from values for absolute fission yields was evaluated in comparison to the measurement of fission rate in the specific uranium target by quantification of another fission product and utilization of relative fission yields for this fission product and for the xenon nuclide. The latter method also avoids the need to determine the quantity of uranium present in the irradiated target.

Next, a detailed study of the performance of the selected target was made. This included measurements of the influence of temperature on the maximum xenon released and the effects of uranium concentration on xenon release behavior.

The data on the rates of xenon fission gas release from the irradiated target material were used to calculate the diffusion coefficient for xenon in the molecular sieve matrix. The fraction of the fission-produced xenon released was compared with the probabilities for deposition of the fission fragments in the cage structure of the molecular sieve crystalline framework.

The information gathered in the experimental work described in this part was then applied to the design and operation of a prototype xenon fission gas production loop apparatus installed in the GTRR as described in Chapter IV.

2.2 Apparatus and Facilities

Georgia Tech Research Reactor. The source of neutrons for irradiation of the uranium targets was the one megawatt, heavy-water cooled and

moderated Georgia Tech Research Reactor (GTRR). This is an operating facility of the Engineering Experiment Station at the Georgia Institute of Technology. The GTRR provides a maximum thermal neutron flux of 1.5 $\times 10^{13}$ neutrons per square centimeter per second (nv) at the one megawatt (thermal) power level. Available neutron flux ranges from this maximum down to 10^{10} nv. Both the vertical irradiation facilities in the graphite reflector region (typical thermal neutron flux: 5×10^{11} nv) and the pneumatic transfer systems (typical thermal neutron flux: 8×10^{12} nv) were used in this investigation for irradiation of uranium targets. Figure 31 is a plan view of the GTRR showing fuel element and irradiation positions.

Counting Equipment. Identification and quantitative measurement of fission products induced by the irradiation of uranium targets in the GTRR thermal neutron flux were accomplished by gamma-ray spectrometry. Spectrometers with either a thallium-activated sodium iodide [NaI(Tl)] scintillation detector or the high-resolution lithium-drifted germanium [Ge(Li)] semiconductor detector were used.

The gamma-ray spectrometer system using the scintillation detector utilized a three inch diameter by three inch long solid NaI(Tl) crystal coupled to a three inch photomultiplier tube (Harshaw Chemical Company, Model 12S12 Integral Line Assembly). The output from this detector was fed to a 400-channel pulse height analyzer (Technical Measurements Corporation, Model 404C). High voltage for detector operation, as well as digital data readout, was provided by a combination high voltage supply and parallel printer (Technical Measurements Corporation, Model 500P). Integration of gamma-ray spectrum peaks was facilitated by the incorporation of an integrator-resolver unit (Technical Measurements Corporation,

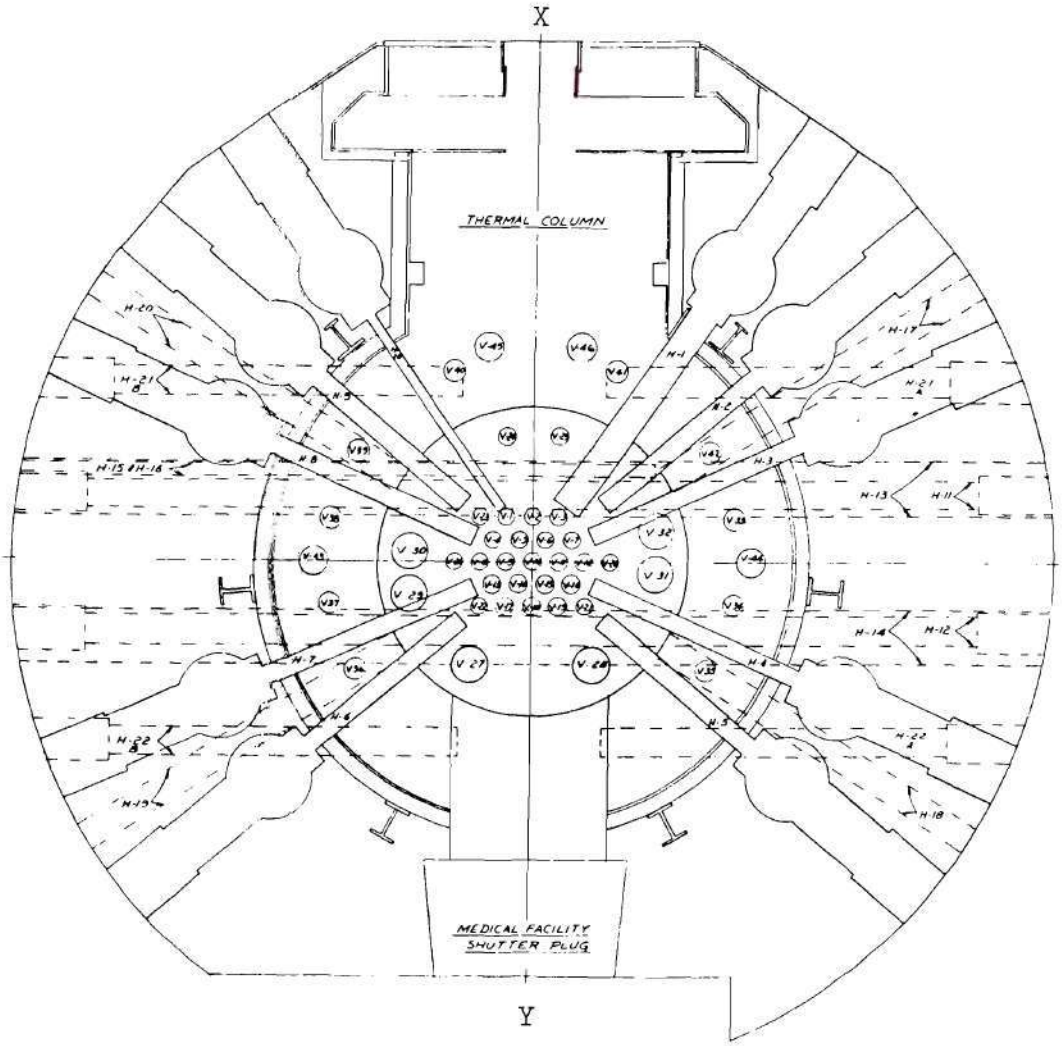

Figure 31. GTRR Irradiation Facilities

Model 522). Figure 32 (System A) is a block diagram of this multi-channel gamma-ray spectrometer system.

An alternate arrangement (Figure 32, System B) using the same NaI(Tl) scintillation detector was used in studies of xenon release over extended time periods. The principal difference was that an automatic timer was designed and constructed to control the pulse height analyzer and data readout. Furthermore, the data readout was accomplished through the option of either an IBM computer typewriter or a punched paper tape output (Tally Register Corporation, Model 420) by a type-punch-read control unit (Technical Measurements Corporation, Model 520) interfaced to the pulse height analyzer. A punched paper tape reader (Tally Register Corporation, Model 424) was used to read the punched tape data through the pulse height analyzer to the typewriter data output after the completion of an experimental run.

A high-resolution gamma-ray spectrometry system was also used in this study for the counting of irradiated pure uranium targets for xenon yield measurements and the determination of fission rate by fission product quantification (see Section 2.2). The heart of the high-resolution system was a 54 cc Ge(Li) detector which was rated at 10 percent efficiency compared to a three inch by three inch NaI(Tl) scintillation detector at 1.33 MeV gamma-ray energy. The energy resolution of this Ge(Li) detector was 2.15 keV full width at one-half maximum at 1.33 MeV. Other specifications and characteristics of this Ge(Li) detector are:

Manufacturer:	ORTEC, Inc.
Model No.:	8001-0923
Serial No.:	GS-330
Dimensions:	43.3 mm diameter; 40.6 mm long

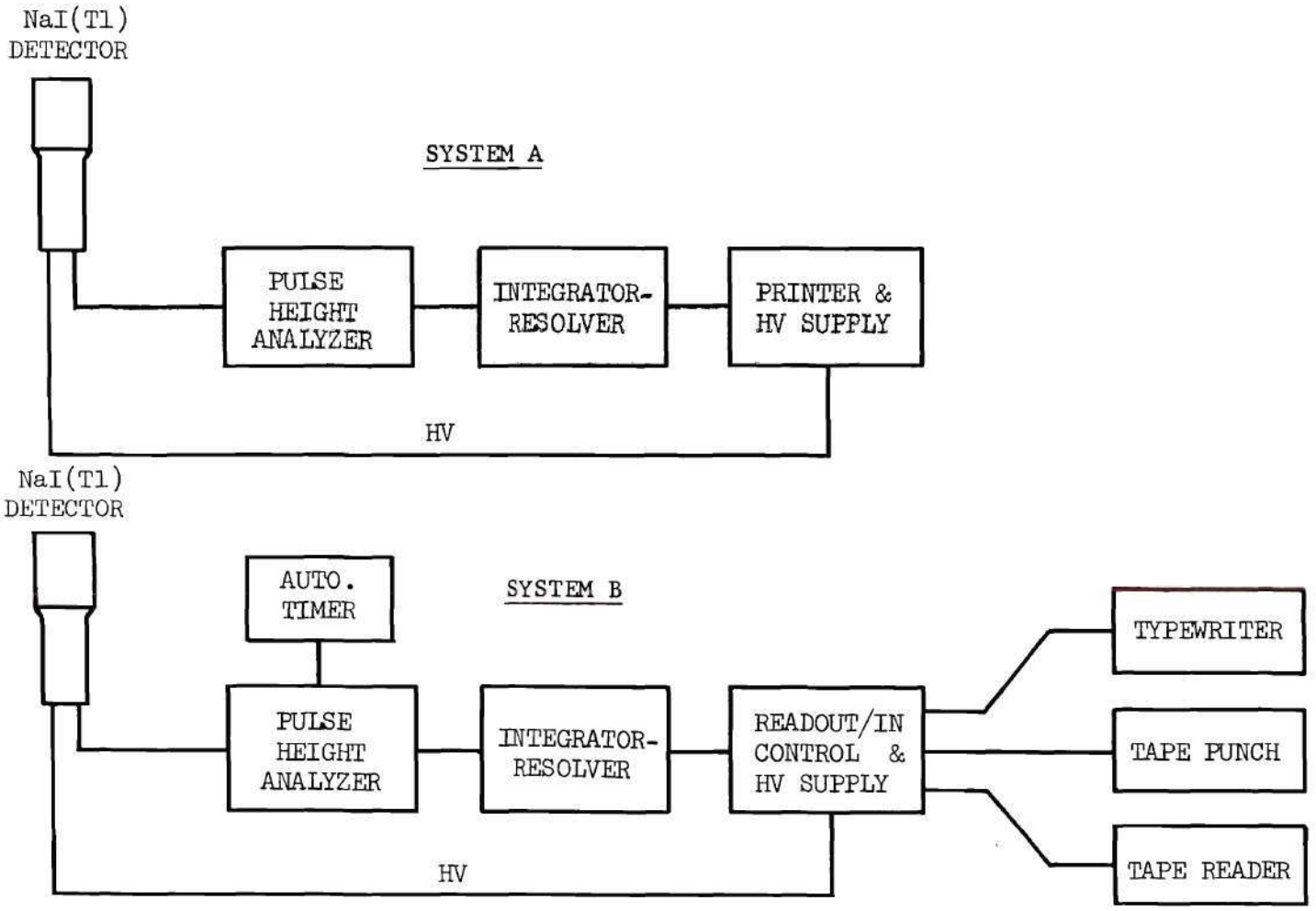

Figure 32. NaI(Tl) Scintillation Detector Gamma-Ray Spectrometer

Drift depth:	17.5 mm
Diffusion depth:	0.8 mm
Total active volume:	53.9 cc
Absorbing layers:	0.5 mm Al; 1.0 mm Teflon; 0.0 mm Ge dead layer
Operating bias voltage:	+3000 volts
Peak-to-Compton ratio for 1.33 MeV:	31:1

In order to maintain the low temperature necessary to operate and maintain the Ge(Li) detector, it was mounted in a vacuum cryostat and cooled by a supply of liquid nitrogen (LN_2) contained in a 31 liter dewar beneath the detector and cryostat.

The pulses from the Ge(Li) detector interaction with gamma-rays were passed through a preamplifier (ORTEC, Model 120-2F), mounted on the cryostat, to an amplifier (Tennelec, Model TC 200) as shown in Figure 33. The amplified and shaped pulses were then sent to a 1024-channel pulse height analyzer (Nuclear Data, Model 2200) where they were stored in a channel proportional to their pulse height. The resulting gamma-ray spectrum could be read out in digital form either through a solenoid operated IBM Selectric typewriter or a high speed paper tape punch (Teletype Corporation, Model BRPE-11). An X-Y coordinate plotter (Hewlett-Packard, Model 7590C) was connected to the pulse height analyzer and made spectrum plots available. Re-examination of spectra stored on punched paper tape was made possible by a punched paper tape reader (Teletype Corporation, Model CXB2).

Quantitative data reduction from the gamma-ray spectra from the Ge(Li) detector system was facilitated by interfacing a small programmable computer (Hewlett-Packard, Model 9100B) to the pulse height analyzer through a data transfer unit (Applied Physical Technology, Model 2291).

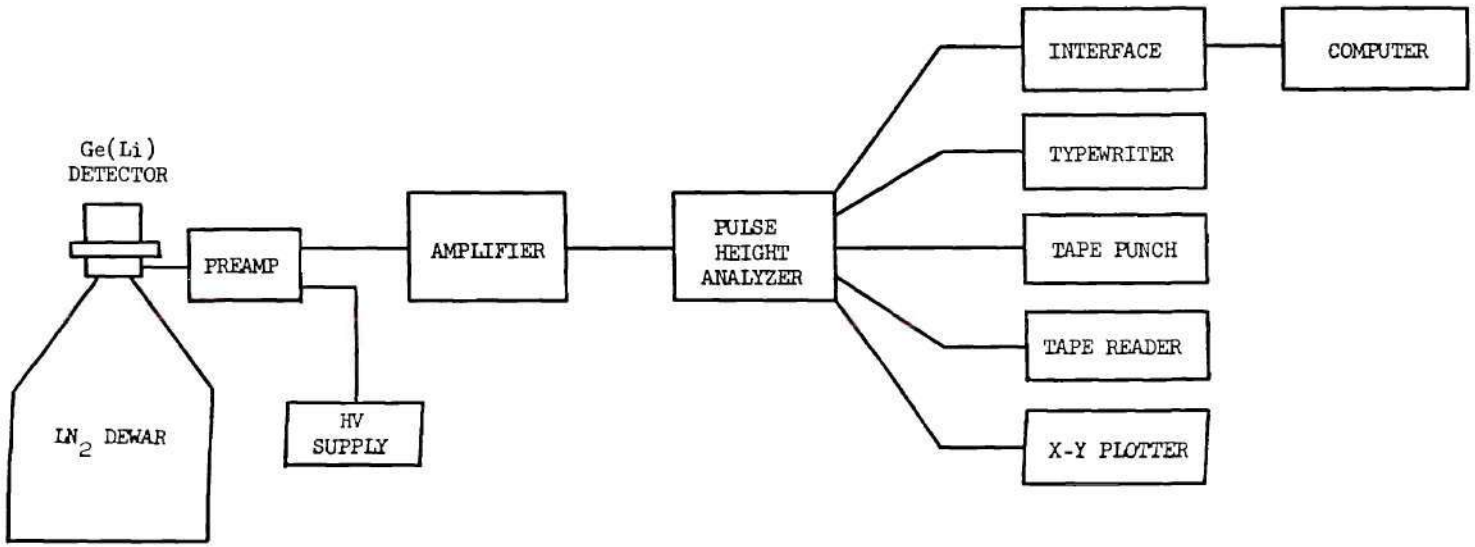

Figure 33. Ge(Li) Gamma-Ray Spectrometer

This arrangement permitted the use of the computer to perform peak area integrations and peak energy determinations directly from the pulse height analyzer memory without first recovering the actual digital data.

Apparatus for Xenon Collection and Measurement. Xenon release measurements at room temperature were made in the early part of this investigation by irradiation of the uranium loaded molecular sieves or uranium oxide coated nickel tube sealed in an aluminum irradiation can. After irradiation, the xenon content of the air space in the can above the uranium-containing materials was determined by puncture of the can with the apparatus shown in Figure 34. This device permitted flushing of the gas space in the irradiation can with helium carrier gas to remove released fission product gases into the trapping system for quantitative measurement. The irradiation cans were constructed of Type 1100 aluminum (commercial grade pure aluminum) and were relatively soft, permitting easy puncture by the helium inlet and outlet needles.

For studies at elevated temperatures the irradiated targets were heated in a special chamber shown in Figure 35. This chamber was placed in a one inch diameter quartz tube inserted through a tube furnace (Lindberg Hevi Duty, Type 54241A). This furnace was connected to a temperature controller unit (Lindberg Hevi Duty, Type 59344) and had a maximum operating temperature of 1200°C with a control precision of ± 5°C. Helium carrier gas passing through the heated chamber flushed released fission product gases from the target into the trapping system. Target temperature was measured by an iron-constantan thermocouple attached to the outer surface of the special chamber. The output from the thermocouple was converted to a temperature indication by a thermocouple reader (Thermo

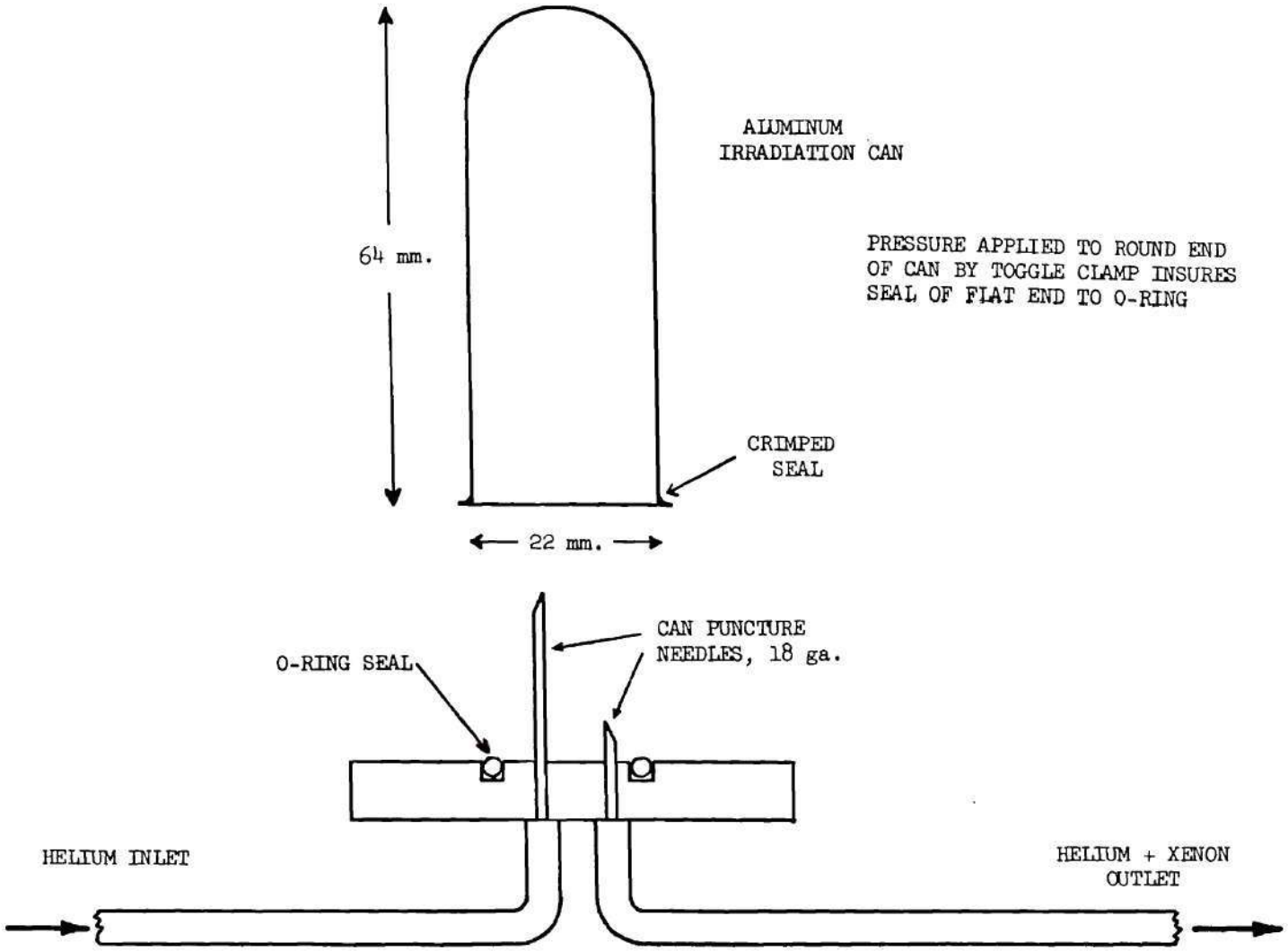

Figure 34. Irradiation Can Puncture Apparatus

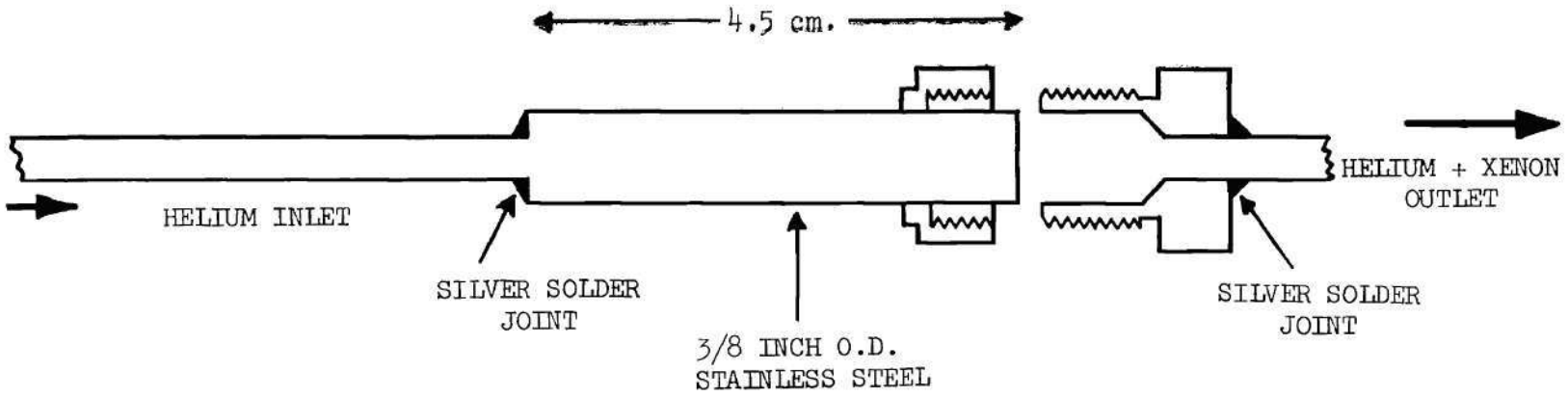

Figure 35. Chamber for Heating Irradiated Uranium-Loaded Molecular Sieves

Electric Company, Mini Mite Pyrometer Indicator).

The fission gas trapping system is shown diagrammatically in Figure 36 in relationship to the two target flushing systems just described. The xenon fission product gases are trapped on the bed of liquid nitrogen cooled 45-60 mesh Type 5A molecular sieves (Hycar M45/60, No. 022-045-5A, Guild Corporation). This cold trap is positioned near a three inch by three inch NaI(Tl) scintillation detector. Details A and B of Figure 36 give the trap dimensions and the trap-detector geometry. A second cold trap was initially included and connected in series with the cold trap just described, but the early experiments demonstrated that a single trap was adequate to quantitatively remove and retain the xenon fission gases. The second trap was not used thereafter.

A trap for removal of fission product iodine was designed into the trapping system ahead of the xenon cold trap. It was anticipated that, of all the other fission produced radionuclides, iodine would be the most likely to be released and contaminate the xenon cold trap. It has been shown (85) that molecular sieves, Type 13X, loaded with silver by ion exchange with silver nitrate solution, are efficient absorbers of iodine vapor. Silver-loaded molecular sieves were prepared and loaded into a cylindrical trap, one inch in diameter by four inches long. Cooling of the silver-loaded molecular sieves for trapping iodine is not required and no absorption of xenon occurs on this material at room temperature.

It was demonstrated experimentally (see Section 2.3, this chapter) that the xenon was removed from the helium carrier gas flow by the upper portion of the molecular sieve trap packing which made the source-detector

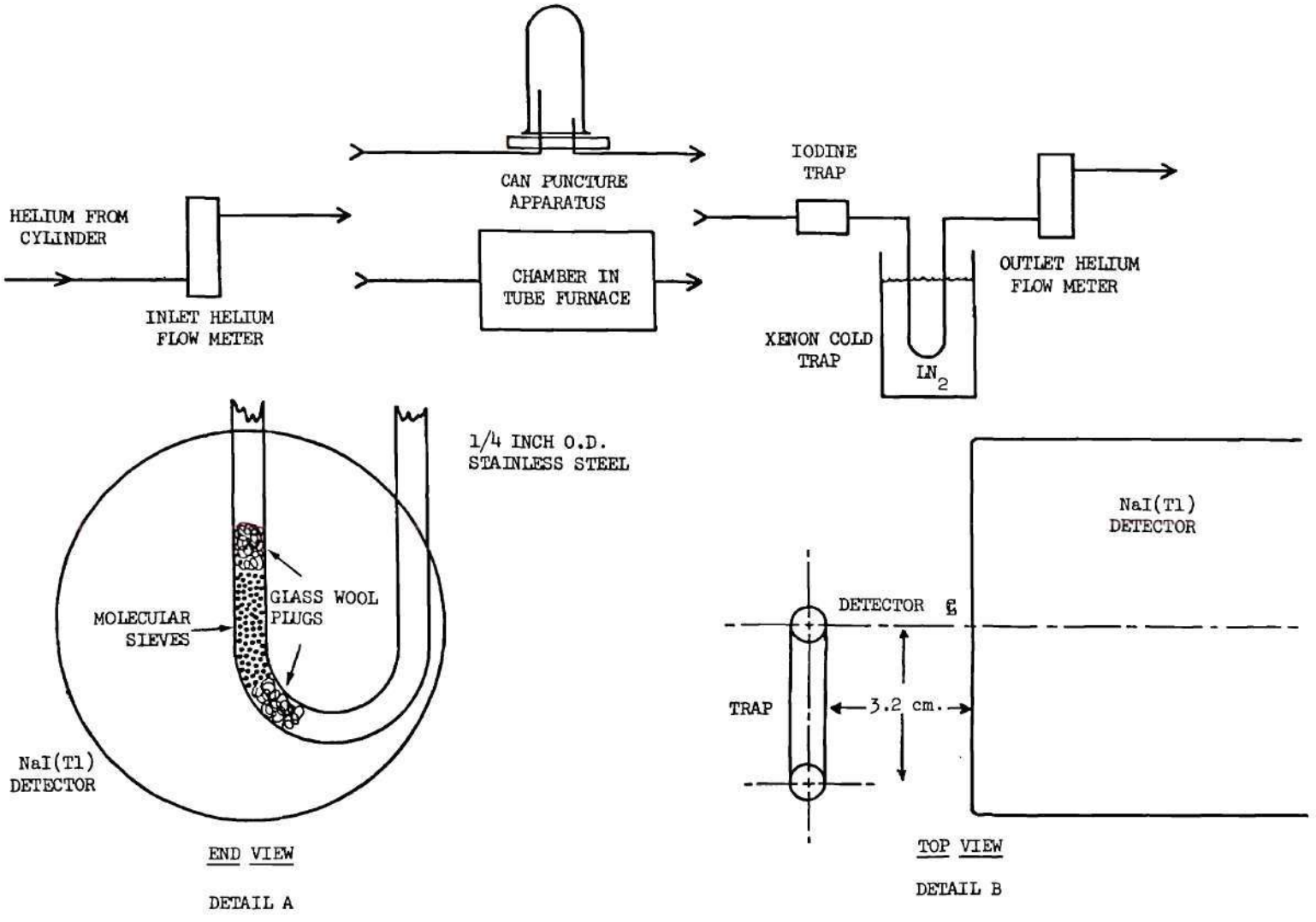

Figure 36. Xenon Trapping System

counting geometry constant as well as relatively uncomplicated.

The helium supply cylinder was fitted with a two-stage regulator, a flow meter with needle valve for regulation, and a bellows-sealed, toggle operated shut-off valve. The flow meter was not calibrated for helium flow measurements, but was calibrated by measuring the time required to fill an inverted, water-filled 50 ml gas buret at various flow meter scale readings. Another flow meter was placed on the helium outlet line from the trapping system to insure detection of system helium leaks or other abnormal flow conditions.

Extended runs requiring overnight or longer operation of the trapping system were troubled by the inability of the liquid nitrogen dewar around the xenon cold trap to remain full over this period of time. To circumvent this difficulty a liquid nitrogen level controller was designed and constructed which maintained the coolant level to within ± 1 cm of the selected level. The sensor used in this controller was an inexpensive silicon diode which exhibits a drastic change in resistance when immersed in the liquid nitrogen (colder) as compared with the resistance when in the gas space (warmer) immediately above the liquid surface. Figure 37 is a schematic diagram of the circuit of this controller.

2.3 Experimental Procedures

Calibration of Counting Equipment. In order to obtain quantitative measurements of fission produced xenon radionuclides and neutron-activated flux monitor wires, it was essential that the counting efficiencies of both the NaI(Tl) scintillation detector and the 54 cc Ge(Li) semiconductor detector be accurately determined for the gamma-ray energies and counting

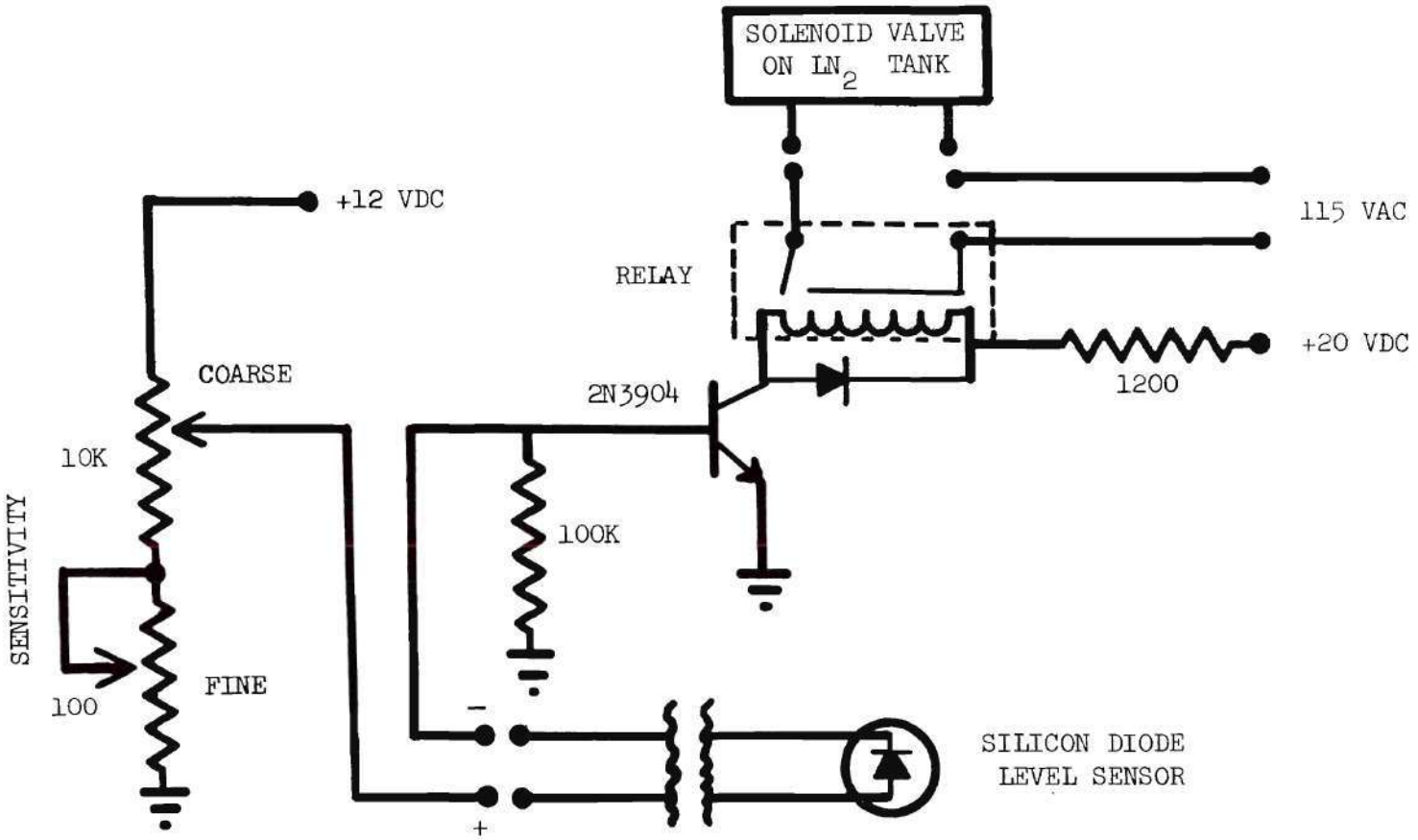

Figure 37. Liquid Nitrogen Level Controller

geometries encountered in the experimental measurements.

NaI(Tl) Detector Calibration. Measurements of released xenon nuclides from irradiated targets were made with the NaI(Tl) scintillation detector positioned adjacent to the xenon cold trap as previously shown in Figure 36. Table 18 gives the details of the gamma-ray emissions from the two xenon nuclides of interest in this study, xenon-133 and xenon-135 (86).

Table 18. Gamma-Ray Emissions from Fission Product Xenon

	Energy (keV)	Absolute Intensity*
Xenon-133:	79.6	0.67
	81.0	41.6
	160.7	0.07
	384.1	0.02
Xenon-135:	158.2	0.19
	249.6	97.1
	358.5	0.15
	373.1	0.01
	407.5	0.38
	607.9	2.63
	654.6	0.03
	731.9	0.05
	812.6	0.06

*Number of gamma-rays per 100 disintegrations.

It is apparent from examination of this table of gamma-ray energies and intensities that the gamma-rays of choice for optimum sensitivity in the measurement of xenon-133 and xenon-135 are the 81.0 keV and the 249.6 keV emissions, respectively.

Counter efficiency determinations for the 81.0 keV xenon-133 gamma-ray were simplified by the availability of a standardized solution of

cadmium-109 which emits its principal gamma-ray with an energy of 88 keV. Wolicki, et al. (87) published calculated efficiencies for a NaI(Tl) detector of these dimensions which indicate that an error of less than one percent would be incurred by using the 88 keV gamma-ray from the cadmium-109 without correction to calculate the detector for counting the 81 keV xenon-133 gamma-ray.

The cadmium-109 standard solution was supplied by the Amersham/Searle Corporation and had the following specifications:

Code No.:	CUZ 54
Ampoule No.:	S9/28/12
Activity:	10.86 μCi ^{109}Cd at 1200 GMT April 24, 1969
Half-life:	453 days
Total mass of solution:	5.123 grams
Concentration:	2.119 μCi per gram of solution
Accuracy:	± 2% (one sigma)
Carrier content:	100 μg cadmium as $CdCl_2$ in 0.1 N HCl

A portion of this standard solution of cadmium-109 was used to measure the counting efficiency of the NaI(Tl) detector for xenon-133 on the cold trap molecular sieve bed. The standard solution was contained in a flame-sealed glass ampoule when received from the supplier. After breaking the neck from one ampoule, a 0.5 ml aliquot was pipetted from the standard solution onto the molecular sieve bed of a trap made identically to the xenon cold trap as previously shown in Figure 36. Weighing of the standard trap before and after addition of the standard solution of cadmium-109 indicated the quantity of standard solution which had been placed in the trap tube on the molecular sieve bed. The trap was then dried at 90°C for 14 hours to remove excess water. The ends of the trap tube were sealed with silicone rubber to prevent ingress of water vapor

from the atmosphere which could possibly increase the losses of the 88 keV gamma-rays from the cadmium-109 standard on the molecular sieve bed of the trap.

Spectra were taken of the cadmium-109 standard with a NaI(Tl) detector both in the stainless steel tube trap and deposited on plastic film (no absorber between source and detector). Cadmium-109 decays by electron capture to 40 second half-life silver-109m. The decay results in emissions of characteristic silver X-rays of three keV and 22 keV. Furthermore, the 88 keV gamma-ray has a high probability for internal conversion by interaction with atomic electrons. The data sheet accompanying the standard solution gave a value of 29.4 for the total internal conversion coefficient, α, where:

$$\alpha = \frac{N_e}{N_\gamma}$$

where

N_e = number of conversion electrons emitted per unit time

N_γ = number of gamma-rays emitted per unit time

If we define the total disintegration rate as N_T, then

$$N_\gamma = \frac{N_e}{\alpha}$$

$$N_e = N_T - N_\gamma$$

therefore,

$$N_\gamma = \frac{N_T - N_\gamma}{\alpha}$$

and

$$N_\gamma = \frac{N_T}{\alpha + 1}$$

Substituting the given value of 29.4 for α gives:

$$N_\gamma = (3.29 \times 10^{-2})\ N_T$$

Figure 38 is a reproduction of the two gamma-ray spectra obtained by counting the cadmium-109 with and without the stainless steel tube wall absorber. Most notable is the complete absorption of the 22 keV silver X-ray by the tube wall.

With the trap tube containing the known quantity of cadmium-109 in the same position by the NaI(Tl) detector as occupied by the xenon cold trap (see Figure 36) and submerged in a liquid nitrogen-filled dewar, the net counting rate of the 88 keV gamma-ray peak was determined. After correcting the given standard value for decay and internal conversion, a counting efficiency of 11.4 percent was calculated for the trapped xenon-133 81 keV gamma-ray. The position of the liquid nitrogen filled dewar which determined the pathlength of liquid nitrogen through which the gamma-rays must travel to reach the detector was found to influence the count rate by less than one percent.

By counting another aliquot of the cadmium-109 standard deposited on a planchet (no absorber between source and detector) and placed in the same position as the trap, it was determined that 33 percent of the 88 keV cadmium-109 gamma-rays were lost by absorption in the wall of the stainless steel tube from which the trap was constructed.

The only available reference standard which was useful for determination of the counting efficiency for the 249.6 keV xenon-135 gamma-ray was selenium-75. Unfortunately, although it was used in the calibration

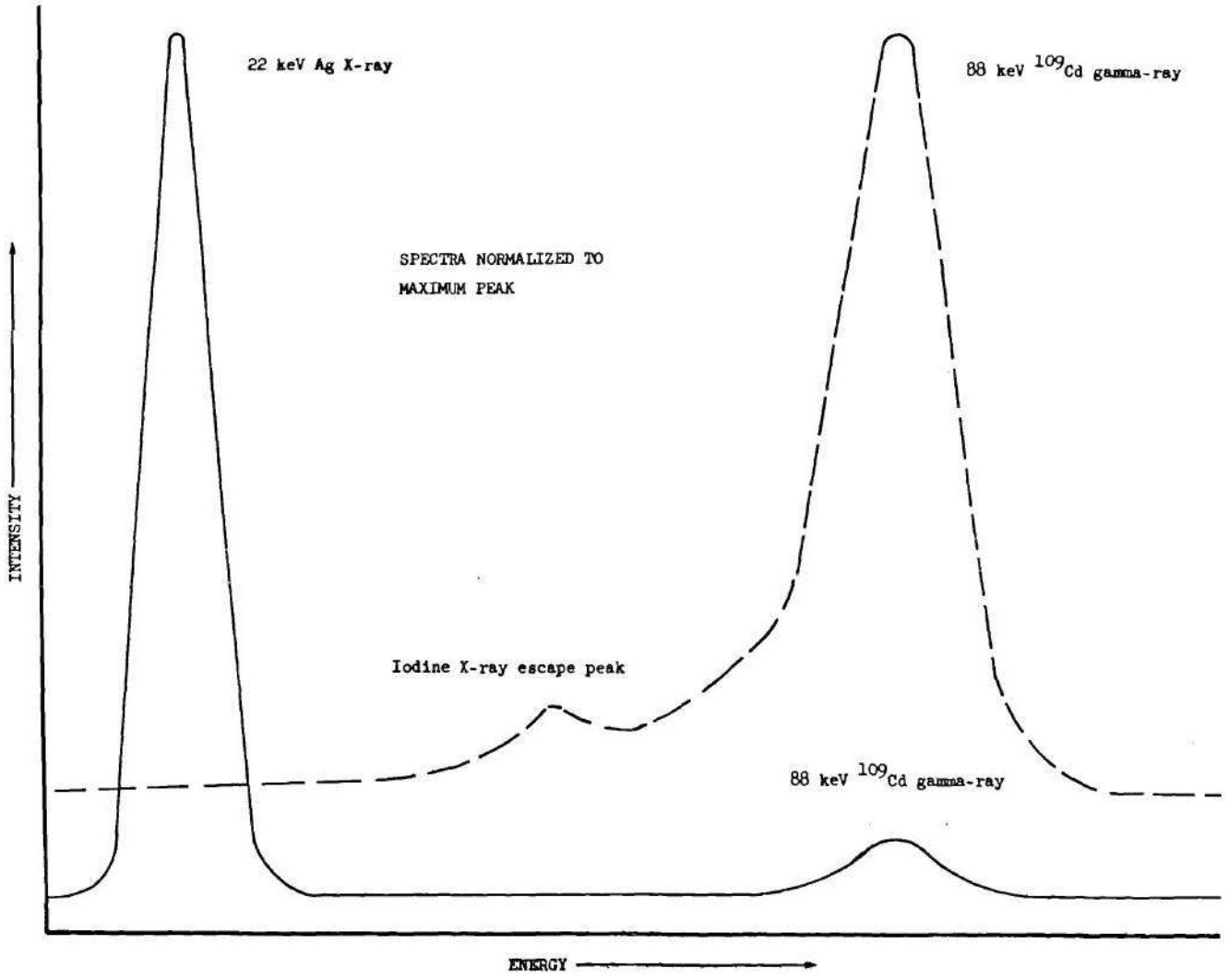

Figure 38. Gamma-Ray Spectra from ^{109}Cd
3 x 3 Inch NaI(Tl) Detector

of the Ge(Li) detector which will be described later, the decay scheme is too complex (multiple gamma-rays of similar energies) for resolution by the NaI(Tl) gamma-ray spectrometry system.

The reliable calculation of counting efficiencies for NaI(Tl) detectors has been well demonstrated (87). Since available data did not give the values for the exact energy and source-to-detector distance used in this study, it was necessary to interpolate. Figure 39 is a graph of counting efficiency versus the distance from a point source to the face of a three inch by three inch NaI(Tl) scintillation detector for gamma-rays of 150, 200, and 300 keV. The distance from the centerline of the xenon cold trap to the face of the NaI(Tl) detector was 3.5 cm when the one-eighth inch space between the aluminum can around the detector and the NaI(Tl) crystal is added to the 3.2 cm trap-to-detector distance already shown in Figure 36. Reading from this family of curves, one finds counting efficiency values of 14.6, 13.4, and 11.3 percent for the gamma-ray energies plotted, respectively. Next, these values were plotted versus energy as shown in Figure 40, and a counting efficiency for 249.6 keV read from the graph as 12.4 percent.

This value for counting efficiency does not consider the losses by absorption in the tube wall of the trap which was shown earlier to be substantial. Such absorption is described by the expression:

$$\frac{I}{I_o} = e^{-\mu x}$$

where

I_o = incident radiation intensity

I = transmitted radiation intensity

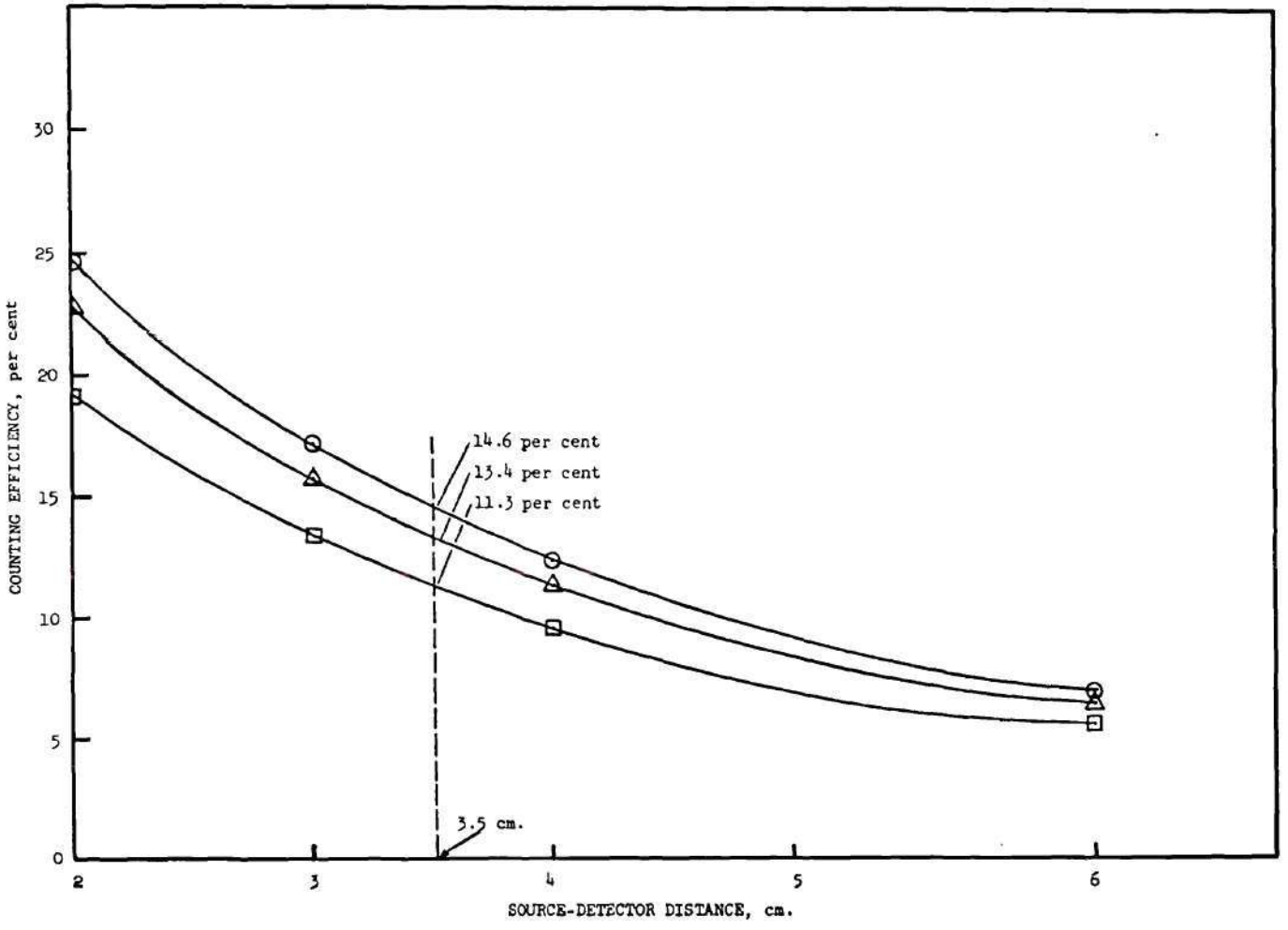

Figure 39. Counting Efficiency vs Point Source-Detector Distance for 3 x 3 Inch NaI(Tl) Scintillation Detector. ○ 150 keV; △ 200 keV; □ 300 keV

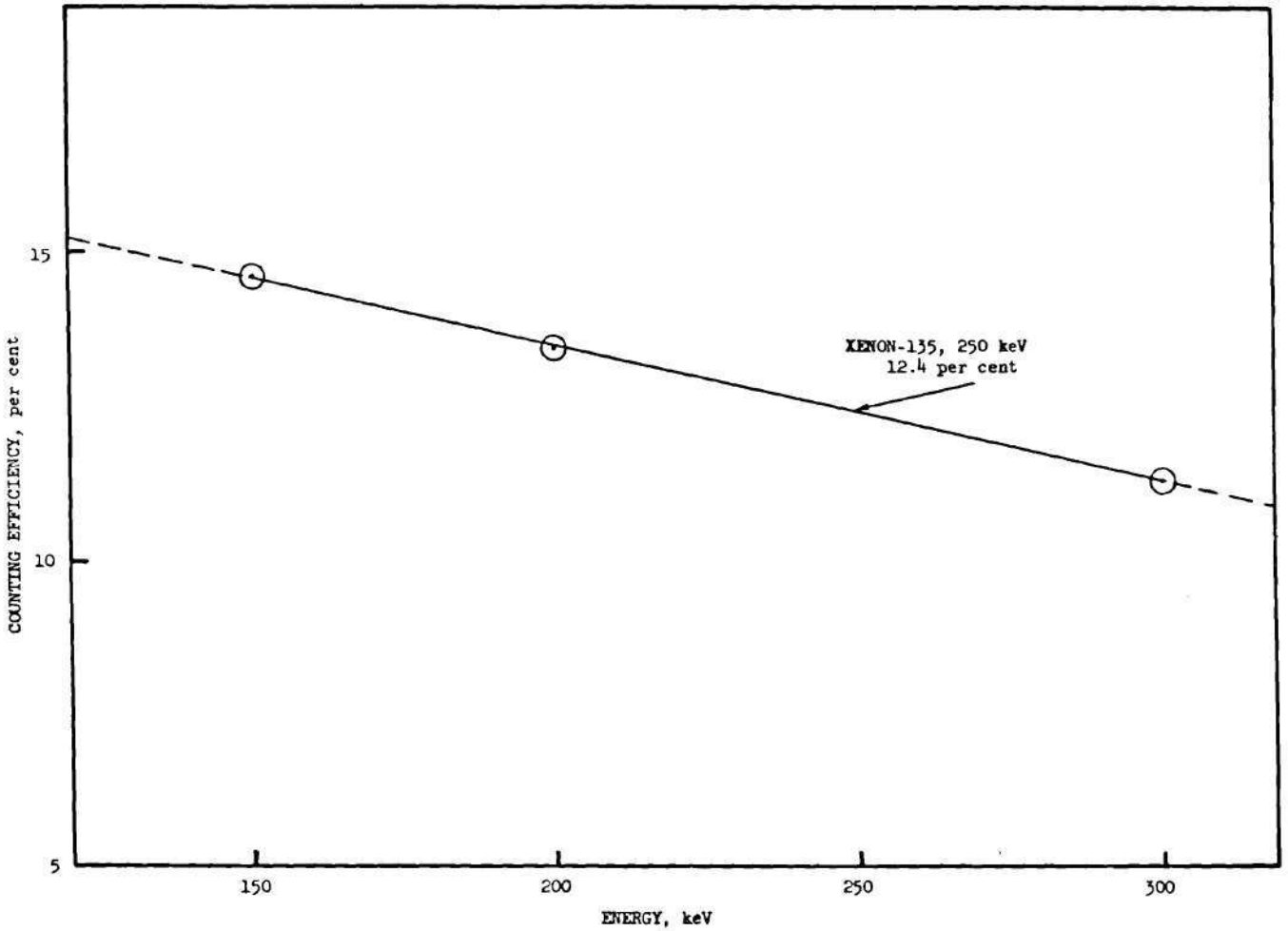

Figure 40. Counting Efficiency vs Gamma-Ray Energy for 3 x 3 Inch NaI(Tl) Scintillation Detector. Point Source-Detector Distance: 3.5 cm.

μ = linear absorption coefficient, cm^{-1}

x = absorbing material thickness, cm

Referring to a table of mass attenuation coefficients for various materials at different gamma-ray energies (88), the linear absorption coefficient for iron was obtained by multiplying the interpolated mass absorption coefficient by the density of iron (7.86 grams per cc). The value thus derived for iron at 250 keV was 1.01 cm^{-1}. The stainless steel tube used was approximately 75 percent iron and the use of this value for pure iron is a reasonable assumption. Also, the other components of the stainless steel, i.e., nickel and chromium, have mass absorption coefficients very close to that for iron.

Using the tube wall thickness of 0.89 mm (0.035 inch), the ratio I/I_o (or transmission) was calculated to be 0.91. This means that 91 percent of the 250 keV gamma-rays are expected to pass through the tube wall while nine percent are lost by absorption in the stainless steel. Correcting the calculated counting efficiency for the 250 keV xenon-135 gamma-rays for this loss by absorption gives an effective counting efficiency of 11.3 percent.

In order to verify the correctness of this calculational method for determination of counter efficiency values, the same type of calculation was made to predict the counting efficiency at the 81 keV energy of the xenon-133 gamma-ray. The unperturbed counting efficiency at 3.5 cm distance was found to be 15.8 percent. By applying the linear absorption coefficient of 3.80 for iron at 90 keV (88 keV cadmium-109 gamma-rays were being counted in the measurement of counter efficiency), the transmission was found to be only 71.4 percent. This calculated attenuation

coefficient of about 29 percent agrees well with the measured value of 33 percent determined experimentally as mentioned earlier.

This attenuation reduces the calculated counter efficiency to an effective value of 11.2 percent. This is in excellent agreement with the measured counting efficiency at 88 keV of 11.4 percent.

These calculations pointed out the importance of the fact that, although the basic detector response to the 81 keV xenon-133 gamma-rays and the 88 keV cadmium-109 standard gamma-rays was different by less than 0.5 percent (87), the strong dependence of the linear absorption coefficient for the stainless steel tube wall of the xenon cold trap on gamma-ray energy had a substantial effect on the overall effective counting efficiency. On this basis, the linear absorption coefficient for 80 keV gamma-rays in iron (4.68 cm^{-1}) was applied to the 15.8 percent counting efficiency calculated for 80 keV energy and an effective counting efficiency for the 81 keV xenon-133 gamma-rays was calculated to be 10.4 percent. This value is more accurate than the earlier measured value of 11.4 percent because it makes a correction for the difference in loss by absorption at the energy of the standard and the xenon-133 energy.

Determination of Xenon Configuration in the Cold Trap. All the preceding measurements and calculations pertaining to the efficiency of the NaI(Tl) detector for quantitative determination of trapped xenon have assumed a point-source geometry. In order to ascertain the location and dimensions of the trapped xenon the following experiments and tests were made.

The xenon cold trap containing the molecular sieve bed between two

supporting plugs of glass wool was loaded with approximately two μCi of xenon-133 obtained from a commercial supplier (New England Nuclear Corporation). The xenon activity was placed on the trap by injecting an aqueous solution of the isotope into a container sparged by helium sweep gas. The helium flow rate was 15 ml per minute. Within 10 minutes the xenon-133 was quantitatively transferred to the cold trap. By positioning a six mm diameter hole in a two mm thick lead sheet against the inlet side of the trap tube between the trap and the NaI(Tl) detector, a collimator was formed which permitted determination of the xenon-133 location to within ± 6 mm. By relocating the collimator and repeating the counting, the data represented in Figure 41 were obtained.

Definite information about the location of the glass wool plugs and the molecular sieves in the trap tube as shown in Figure 36 were not known. Radiographic examination of the trap was made unsuccessfully with 78 keV X-rays and 662 keV cesium-137 gamma-rays. Finally, a satisfactory radiograph was obtained by neutron radiography in the biomedical facility neutron beam from the GTRR. Measurements taken from the neutron radiograph were used to delineate the locations of the glass wool plugs and the molecular sieves as noted on Figure 41.

The results of these studies of trapped xenon were to verify the assumption that the xenon is concentrated in a small portion of the trap tube (estimated to be less than one cm in length). Since the flow rate of the helium sweep gas used in this determination was approximately twice that used in subsequent experiments, the distribution of xenon activity in the trap during the actual quantitative measurements would be expected to have been in an even more narrow band, validating the assumption of a

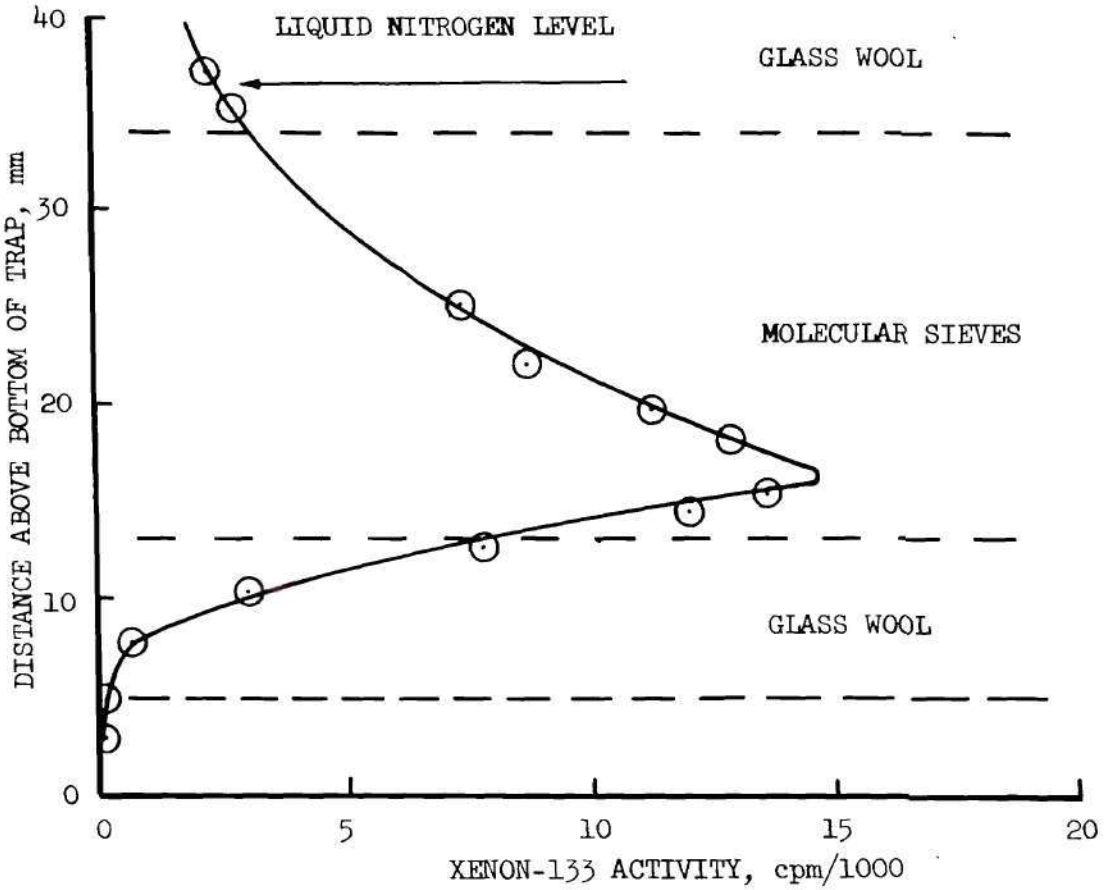

Figure 41. Distribution of ^{133}Xe on Cold Trap

small, point-source of xenon activity.

Ge(Li) Detector Calibration. The 54 cc Ge(Li) semiconductor detector was used to quantitatively determine three radionuclides during the course of this study: (1) xenon-135 for measurement of the absolute fission yield of this fission product, (2) cobalt-60 for neutron flux determination from irradiated flux wires, and (3) lanthanum-140 for calculation of fission rate in individual irradiated uranium-containing samples of targets.

It was determined by replotting existing counting efficiency versus gamma-ray energy data for the Ge(Li) detector that, for the energy range 100-500 keV, a plot of log(counting efficiency) versus log(gamma-ray energy) gave a straight line.

Counting standard sources of cobalt-57 (122 keV) and barium-133 (356 keV) from a set of standard sources for gamma-spectrometry (ICN-Tracerlab, Model No. R-34, Serial No. 514) on the fourth shelf of the sample support above the Ge(Li) detector (17 cm above the cap of the detector cryostat) gave a value of 0.132 percent counting efficiency at 122 keV and 0.0719 percent at 356 keV. When plotted as shown in Figure 42, the counting efficiency for 249.6 keV (xenon-135) was graphically interpolated to be 0.088 percent at this position relative to the detector.

A second determination of the counting efficiency of the 54 cc Ge(Li) detector was made with a standard of selenium-75 [National Bureau of Standards (NBS), Standard Reference Material (SRM) No. 4228]. Selenium-75 decays by beta decay accompanied by the emission of eleven gamma-rays. Table 19 is a tabulation of the gamma-ray energies and relative intensities of selenium-75 as provided by NBS. The absolute intensity of the

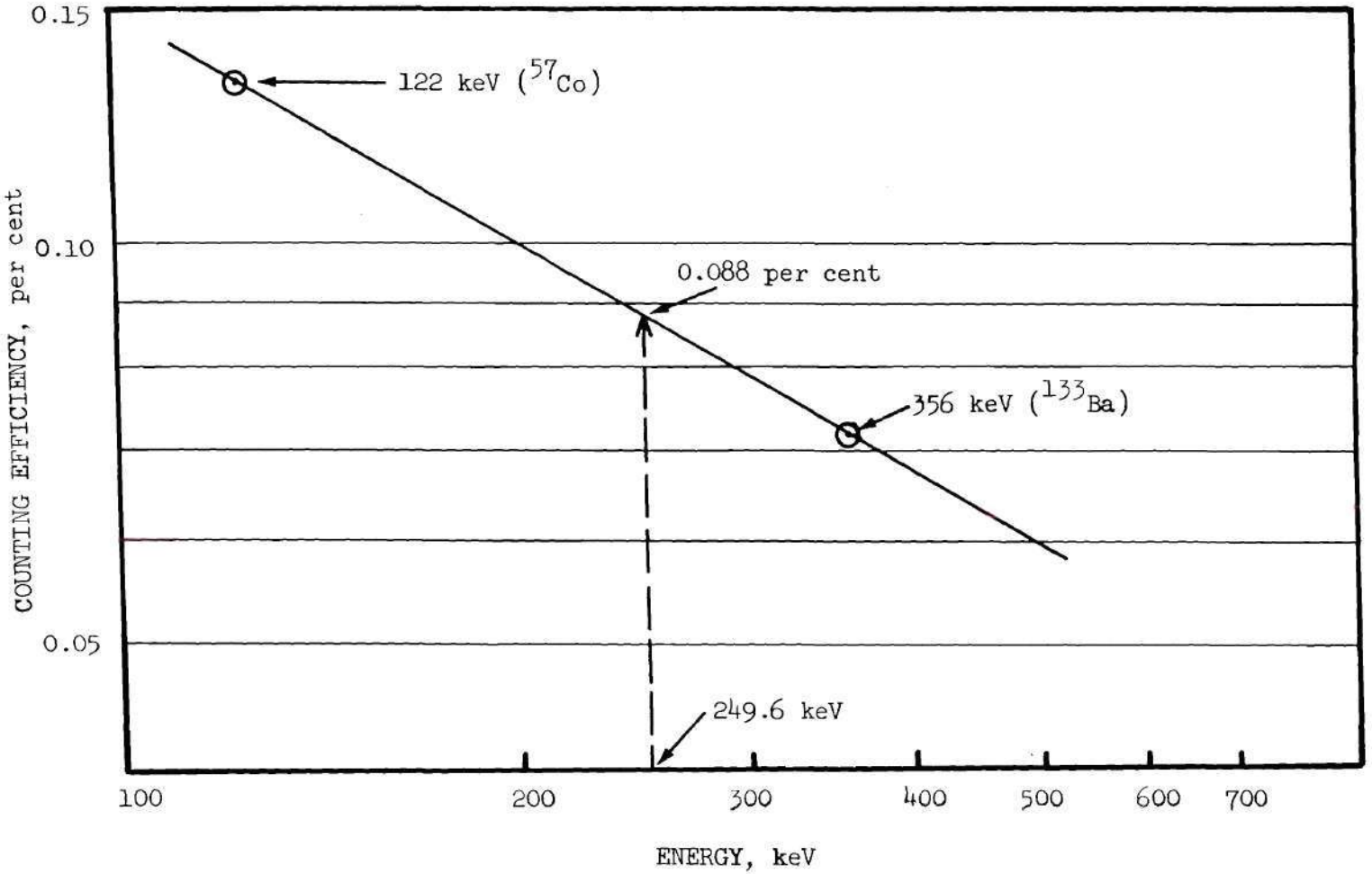

Figure 42. Counting Efficiency vs Gamma-Ray Energy on 54 cc Ge(Li) Detector, Shelf 4 (17 cm from Detector Cap)

400.64 keV gamma-ray was given by NBS as 0.125 per transition.

Table 19. ^{75}Se Gamma-Ray Emissions and Intensities

Energy (keV)	Relative Intensity
24.48	
66.048	1.77
80.91	0.03
96.732	5.60
121.113	28.19
135.998	98.25
198.600	2.43
264.651	100.00
279.525	43.22
303.895	2.31
400.640	19.56

These data permitted use of several of the gamma-rays emitted by this standard to determine the detector efficiency at 249.6 keV for xenon-135 with improved precision and a greater degree of confidence. The principal advantage to the use of selenium-75 was the availability of several gamma-ray energies in the energy region of interest and the dependence on only one standard value determined by the National Bureau of Standards. Figure 43 is a graph of measured counting efficiencies versus energy obtained using this selenium-75 standard. The interpolated value for the counting efficiency at 249.6 keV was 0.090 percent which (within the experimental error) is identical to the 0.088 percent value obtained using the cobalt-57, barium-133 standard pair. The value of 0.090 percent was used in all xenon-135 data calculations in this study when the sample was counted on the fourth shelf (17 cm) above the detector cryostat cap.

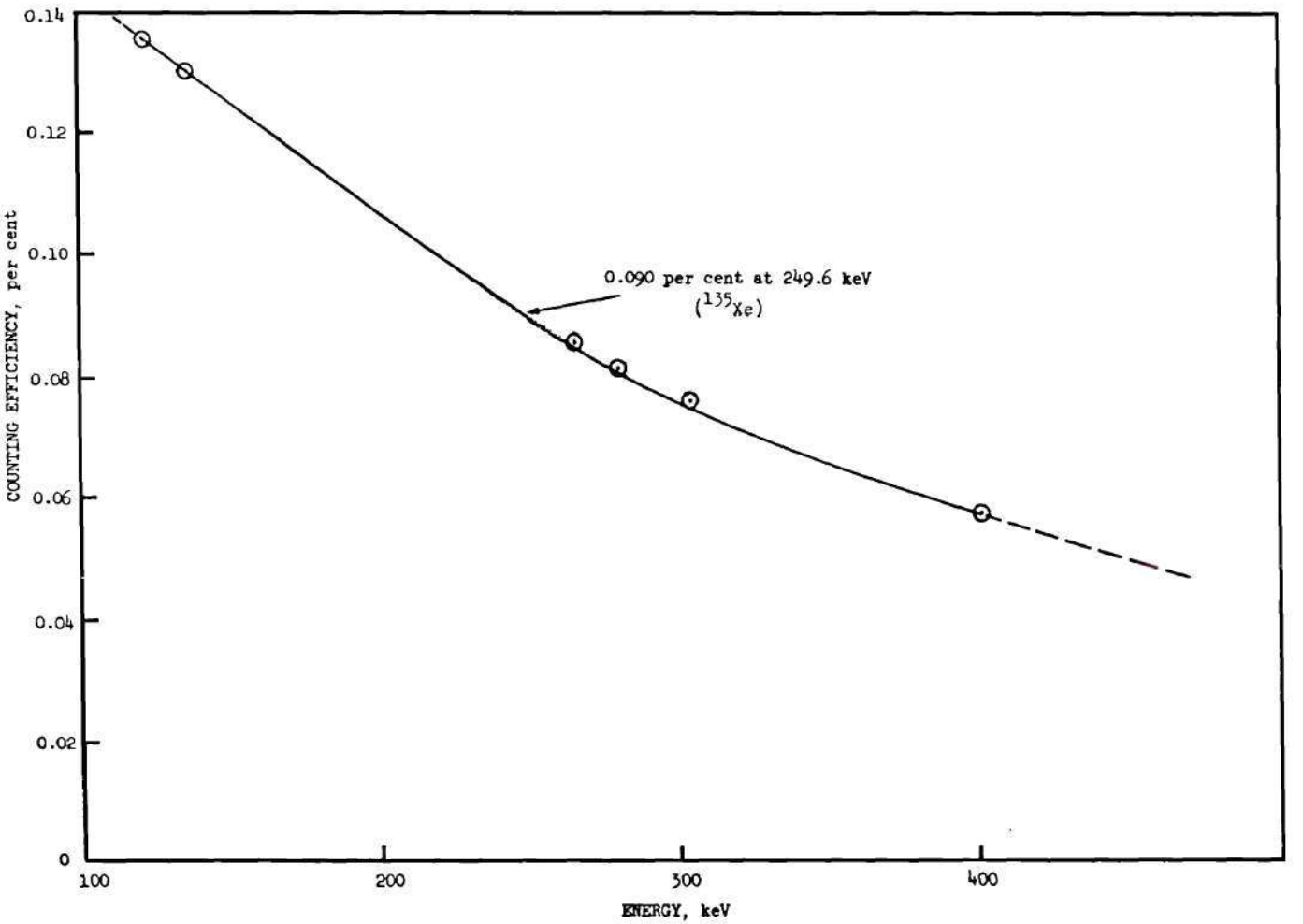

Figure 43. Counting Efficiency Curve from NBS ^{75}Se Standard on 54 cc. Ge(Li) Detector, Shelf 4 (17 cm. from Detector Cap)

Ge(Li) detector counting efficiency for the cobalt-60 activity induced in irradiated flux wires was required in order to permit calculation of the absolute disintegration rate of cobalt-60 in the wires. These data are needed to solve the flux equation:

$$\phi = \frac{A\, e^{\lambda t}}{\sigma N(1-e^{-\lambda T})}$$

where

ϕ = thermal neutron flux, n $cm^{-2} sec^{-1}$

A = activity, disintegrations per second

λ = decay constant for ^{60}Co

t = decay time

T = irradiation time

σ = thermal neutron activation cross section, cm^2

N = number of cobalt atoms in wire

The data obtained from the Ge(Li) gamma-ray spectrometer are in units of counts registered per unit time in the cobalt-60 gamma-ray spectrum peaks of 1173.2 and 1332.5 keV. The activity, A, is related to this count by:

$$A = \frac{\text{(counts per unit time)}}{\text{(counting efficiency)}}$$

The counting efficiency of the Ge(Li) detector for cobalt-60 was simplified (in comparison to the procedures just described for xenon-133 and xenon-135) by the availability of a NBS cobalt-60 standard source (SRM No. 4203).

The 1332.5 keV gamma-rays from cobalt-60 were used in counting

irradiated cobalt flux wires. The measured counting efficiencies of the 54 cc Ge(Li) detector at this energy were (Table 20):

Table 20. Counting Efficiencies of 54 cc Ge(Li) Detector at 1332.5 keV

Efficiency (%)	Location	Distance from Detector Cap (cm)
0.34	Shelf 1	1.8
0.15	Shelf 2	4.4
0.053	Shelf 3	9.4

The remaining application of the Ge(Li) detector was to determine the absolute disintegration rate of the fission-produced radionuclide lanthanum-140 in irradiated uranium containing samples. Knowing the total lanthanum-140 decay rate permitted calculation of the fission rate experienced by the sample while in the reactor neutron flux. This information on the fission rate allowed the total quantity of xenon to be calculated. This was discussed at length in Section 1 of this chapter.

There are 24 gamma-rays reported (86) to result from the decay of lanthanum-140. Of these, the most abundant occur at 1596.6 and 815.8 keV. In addition, the 1596.6 keV gamma-ray, because of its relatively high energy, is preferred as the indicator since interferences from gamma-rays of similar energy or from the Compton region from higher energy gamma-rays of other nuclides are less likely.

The detector calibration for the lanthanum-140 1596.6 keV gamma-ray was made on the third shelf above the detector which was equivalent

to 9.4 cm above the detector cap. Initially, no suitable standard was available which emitted such high energy gamma-rays. The method used was to count a pure lanthanum-140 sample prepared by irradiation of lanthanum oxide in the GTRR and determine the relative counting rates of the 815.8 and the 1596.6 keV gamma-rays. The counting efficiency for the 815.8 keV energy had been determined by using standards from the NBS of niobium-94 (SRM No. 4201), sodium-22 (SRM No. 4991), and cobalt-60 (SRM No. 4203). Figure 44 is a graph from which the counting efficiency of the Ge(Li) detector for the 815.8 keV lanthanum-140 gamma-ray was determined to be 0.086 percent. By applying reported relative intensities of the 815.8 and the 1596.6 keV gamma-rays (86), the ratio of counting efficiencies at the low and the high energy points was calculated to be 1.97 from the lanthanum-140 spectrum. Dividing the interpolated efficiency of 0.086 percent at the 815.8 keV energy by this ratio of 1.97 gives a counting efficiency at 1596.6 keV of 0.044 percent.

Later in the study it was possible to obtain a standard source of yttrium-88 from NBS (SRM No. 4209). This radionuclide emits gamma-rays at 898.2 and 1836.2 keV which permit a more reliable measurement of the counting efficiency at the 1596.6 keV lanthanum-140 energy. Data from this yttrium-88 standard as well as the cobalt-60 and sodium-22 standards used earlier are shown in Figure 45. Interpolation at 1596.6 keV gives a counting efficiency of 0.042 percent. This is in very close agreement with the extrapolated value of 0.044 percent obtained initially.

Correlation of Calculated and Measured Xenon Production. In order to perform the necessary experimental work in evaluating the performances of the high surface area targets as sources for production of the xenon

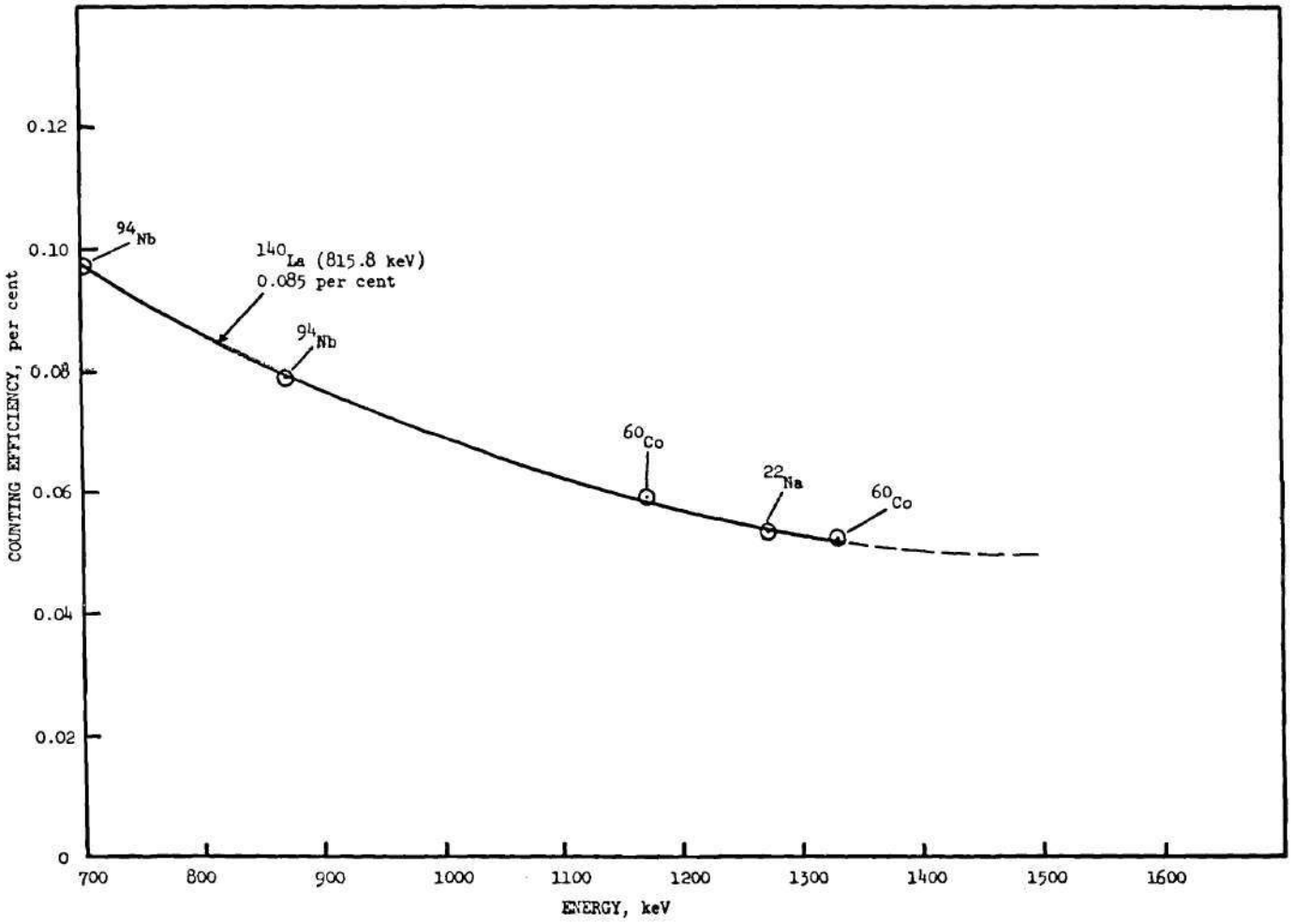

Figure 44. Determination of Counting Efficiency for 815.8 keV ^{140}La Gamma-Ray on Shelf 3 (9.4 cm.) above 54 cc. Ge(Li) Detector

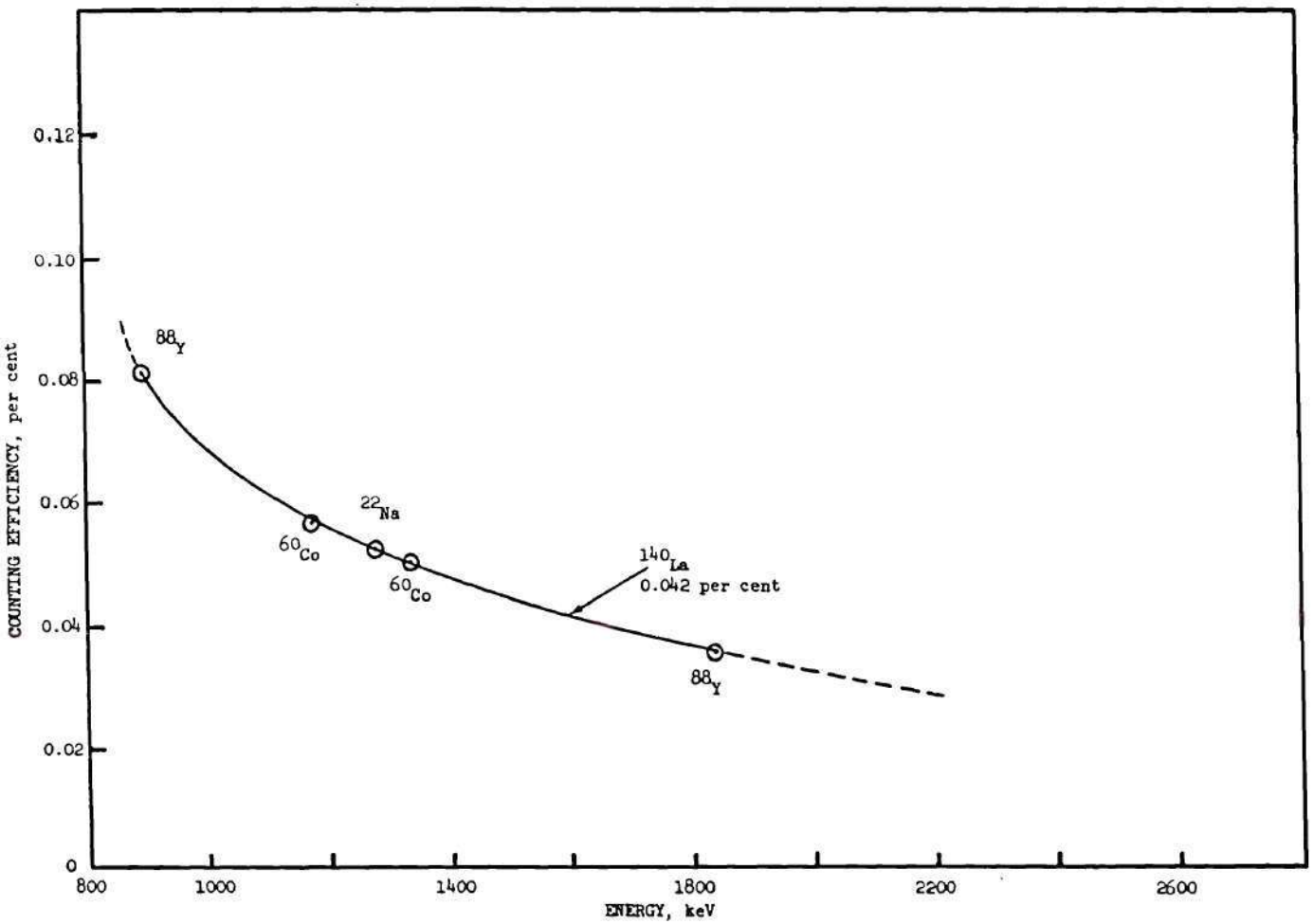

Figure 45. Determination of Counting Efficiency for 1596.6 keV ^{140}La Gamma-Ray on Shelf 3 (9.4 cm.) above 54 cc. Ge(Li) Detector

fission product gases, it was imperative that the calculated amounts of xenon-133 or xenon-135 present in an irradiated target be accurate. That is, the calculated and measured xenon quantities must agree.

Experiments were planned and carried out to determine the degree to which the calculated and measured quantities for xenon-133 and xenon-135 agreed.

The initial portions of this study were concerned with release of xenon-133 and all irradiations were carried out in the graphite reflector region of the reactor where the neutron population is well thermalized. This means that problems associated with the neutron energy spectrum and the variation of reaction cross section with neutron energy (excitation functions) are minimized. Using activation of flux wires to measure the absolute thermal neutron flux proved to be capable of providing calculated xenon-133 values which agreed closely with measured quantities in the standard samples of irradiated uranium. It was of interest, however, that the gold flux wires gave thermal neutron flux values which were ten percent higher than those obtained from cobalt flux wires when the measurements were made in the graphite reflector region of the reactor. This was due to a finite epithermal neutron flux which is capable of activating the gold wires, but had no effect on the cobalt wires. Cross section data for gold and cobalt (89) revealed a strong resonance absorption in gold at a neutron energy of 5 eV, while cobalt exhibited no such resonance at neutron energies below 100 eV. Further confirmation of this explanation for the discrepancy in neutron flux measured with gold and cobalt was found when these two flux wires were used to measure the flux in the pneumatic transfer systems of the GTRR which are located nearer to the reactor

core in a correspondingly higher fast neutron flux relative to the thermal flux. Thermal neutron flux measured at this location in the reactor with gold flux wires was approximately twice the value of the cobalt wire-measured flux.

This problem with gold wire activation determinations of thermal neutron flux is well known and can be minimized by appropriate corrections obtained from gold flux wires shielded by cadmium metal covers which absorb the neutrons having an energy below about one eV and prevent these neutrons from reaching the flux wire. The amount of activity induced in the cadmium-covered gold wire due to these "epicadmium" neutrons is then subtracted from the total activity in an irradiated bare gold wire to give a value which can be used to calculate a thermal neutron flux more closely representing the true number.

Since the activation of the cobalt flux wires did not suffer these complications just described for the gold wires and were otherwise satisfactory, the use of the cobalt flux wires was established as the standard method for thermal neutron flux measurement in this study.

A set of three samples of natural uranium metal foil (0.003 inch thick; Reactor Experiments, Incorporated) was prepared for irradiation and subsequent determination of xenon-133 content. These specimens were wrapped in aluminum foil of sufficient thickness to stop all the fission fragments (minimum thickness was 0.015 inch). To each sample packet was attached a piece of cobalt flux wire. Each sample packet was then sealed in a standard aluminum irradiation can and irradiated for six hours in position V-43 in the GTRR (in the graphite reflector region). After

cooling for approximately three weeks, the cans were punctured and the air space flushed out with helium into the trapping system to check for free xenon-133. None was found in any of the cans. The cans were then opened and the flux wires removed and counted.

Next the uranium foils (still wrapped in aluminum foil) were dissolved one at a time to effect the release of the xenon-133 trapped in the uranium foil and the aluminum foil wrapper. Helium sweep gas was used to sparge the dissolver to transport the xenon-133 into the cold trap where it could be counted.

The flux as calculated from the activated cobalt flux wires was used together with the known irradiation and decay times to calculate the quantity of xenon-133 anticipated as described earlier (in Section 1). Table 21 gives the values for the calculated xenon-133 in comparison with the measured xenon-133 released from the irradiated samples by dissolution. The agreement is excellent.

Table 21. Comparison of Calculated and Measured ^{133}Xe Production by ^{235}U Fission

Sample No.	^{133}Xe (μCi)	
	Measured	Calculated
1	0.36	0.34
2	0.32	0.30
3	0.39	0.38

The major portion of this investigation was concerned with the behavior of xenon-135, rather than xenon-133. The shorter half-life of the xenon-135 (9.16 hours) made its calculation a more dynamic problem than was the case with the 5.27 day half-life xenon-133. For this reason, it was necessary to be able to reliably calculate the quantity of xenon-135 at any time during or after the sample irradiation. Furthermore, the direct fission yield of xenon-135 is not zero or negligible as was the case with xenon-133 and this complicates the calculation (see Section 1 and Appendix B).

In order to minimize the calculational error in determination of the xenon-135 content of an irradiated sample, it is possible to utilize the relative fission yield of a second fission product to first calculate the fission rate experienced by the sample during irradiation and then, using this number, to calculate the quantity of xenon-135. This method was fully described in Section 1.

Applying this technique using the fission produced lanthanum-140 to determine the fission rate of a uranium-235 standard and comparing the calculated quantity of xenon-135 to that measured directly by gamma-ray spectrometry with the Ge(Li) detector system produced some interesting results.

The calculated quantity of xenon-135 during the initial part of the ingrowth of this fission product after irradiation is rather strongly influenced by the value of the direct fission yield for the xenon-135 which is used in the calculation. A value of 0.93 percent was given by the most recent reference available at the beginning of this study (90).

Figure 46 is a comparison of the calculated xenon-135 using this reported value for direct fission yield compared to the measured xenon-135 in an irradiated uranium-235 standard sample. Notable is the discrepancy between the two curves at points before the maximum xenon-135 content is reached. This could be due to an erroneous value for the direct fission yield of xenon-135 since the principal difference in the two curves is that the calculated quantity of xenon-135 is considerably greater than the measured amount in the initial portions of the data.

Figure 47 shows the effect of varying the value of the direct fission yield for xenon-135 on the calculated ingrowth and decay of this fission product. The experimentally determined curve is shown again with this family of curves calculated for different values of the direct fission yield. It can be seen that the experimental data most closely fits the curve calculated using a direct fission yield of 0.2 percent. This conclusion confirms several older references reporting similar direct fission yields for xenon-135 (91-93). It also corresponds very well to a more recent compilation (2) which quoted a value of 0.237 percent for this direct fission yield.

Summary and Conclusions. Neutron flux monitoring with cobalt flux wires permits the calculation of the xenon-133 content with good precision. The more sophisticated approach of calculation of the xenon-135 through the fission rate computed from another fission product content was demonstrated to provide good correlation between calculated and measured xenon-135. This method avoids the errors associated with uncertainties in absolute fission yields, neutron flux, neutron energy distribution, and uranium content of the target.

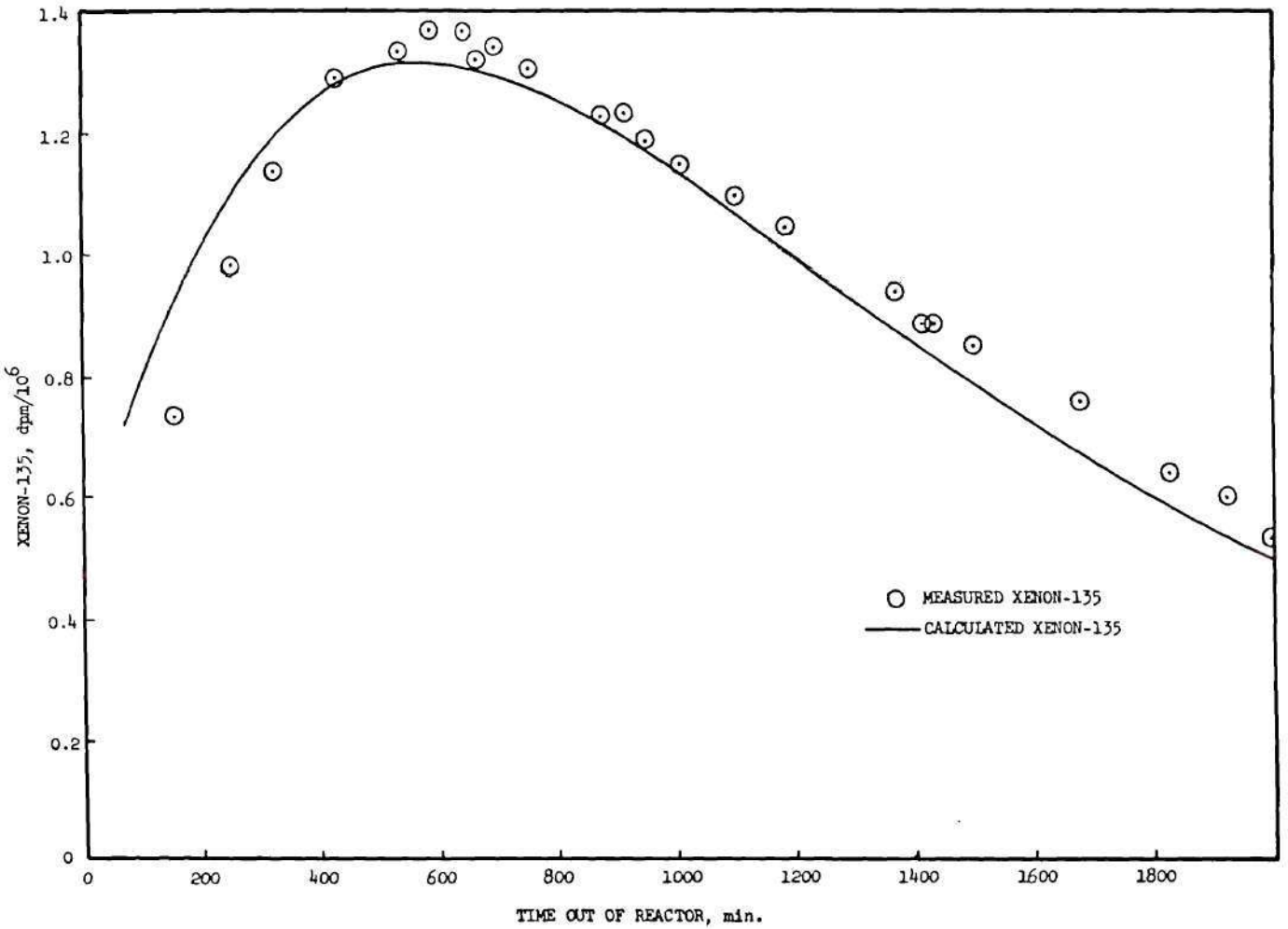

Figure 46. Measured ^{135}Xe Compared to Calculated ^{135}Xe Using a Direct Fission Yield Value of 0.93 Per Cent

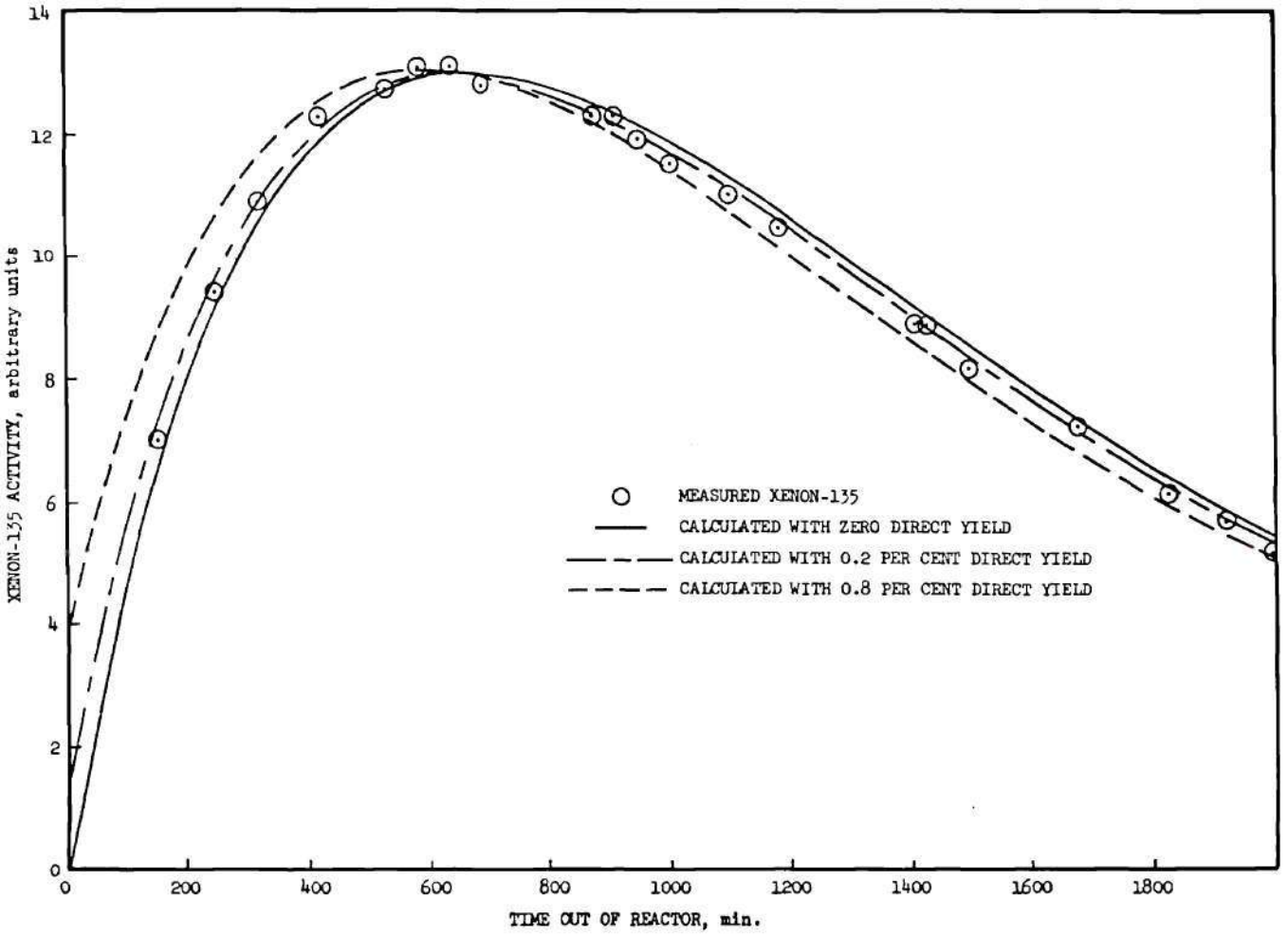

Figure 47. Effect of Direct Fission Yield Value on Calculated ^{135}Xe Ingrowth and Decay in Comparison to Measured ^{135}Xe

2.4 Xenon Release from Electrodeposited Uranium Oxide

From the standpoint of reactor safety as well as necessary experimental information, the temperature of a typical uranium oxide coated nickel tube target during irradiation was measured.

This was accomplished by attaching an iron-constantan thermocouple to the outer, uranium-coated surface of a two inch long nickel tube target prepared by the electrolysis of uranyl nitrate solution of natural isotopic composition as described in Chapter II. The total deposited uranium was 12.2 mg with a thickness of 0.8 mg cm^{-2} of tube surface. The appearance of the deposit was semi-gloss black and uniform. The thermocouple was attached with mylar-base pressure sensitive tape.

The instrumented target tube was placed in a standard aluminum irradiation can. The thermocouple wires passed through a hole drilled in the crimped top of the can. Epoxy cement was used to seal around the wires as they passed through the can top.

This assembly was then inserted into irradiation position V-37 of the GTRR (see Figure 31). The leads from the thermocouple were brought out through the penetration in a special shield plug and connected to the thermocouple reader. Temperature readings were recorded as the reactor was started up and operated at the one megawatt power level. According to previous measurements, the thermal neutron flux in this GTRR irradiation position is 6×10^{11} nv. Figure 48 is a presentation of the data gathered in this temperature measurement.

These data indicated that an overall rise in target temperature of about 20 °C occurred during the irradiation, but that only 5 °C of this

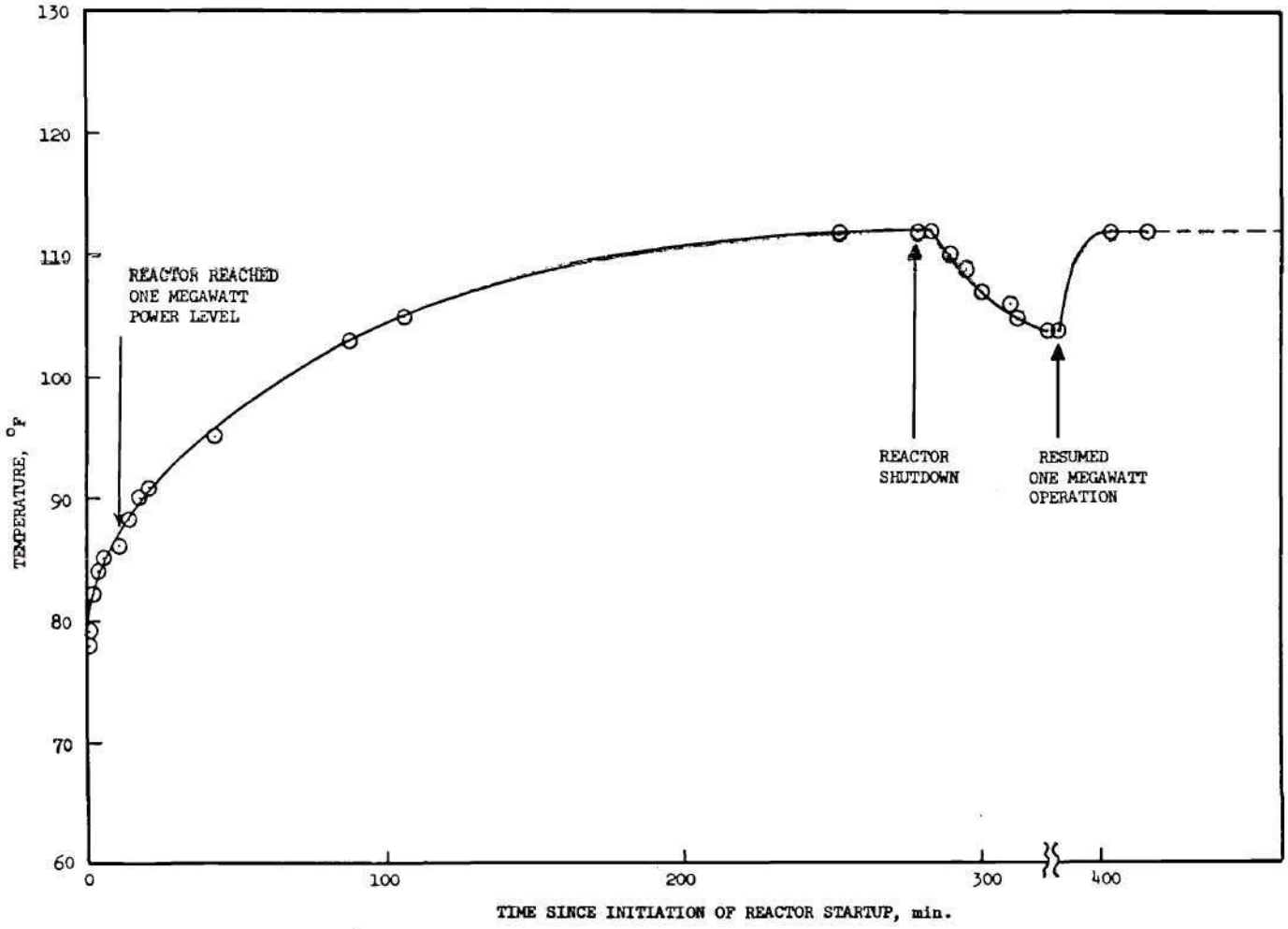

Figure 48. Heating of Natural Uranium Oxide-Coated Nickel Tube Irradiated in Position V-37 of the GTRR

temperature increase was directly attributable to the fission heat from the uranium coating on the target tube. This was deduced from the effect of the reactor shutdown at the 279 minute point in the experiment and subsequent startup. The remaining 15°C temperature increase is due to general heating of the reactor graphite reflector region in which position V-37 is located.

A uranium oxide coated nickel tube identical to the one used in the temperature rise measurement was sealed in an aluminum irradiation can and irradiated in position V-43 of the GTRR for a period of 10 hours at a thermal neutron flux of 5.6×10^{11} nv (as measured by activation of cobalt flux wires). After cooling for five days, the can was punctured and helium gas used to purge gaseous fission products from the can void space into the trapping system. The total xenon-133 in the air space of the can was measured to be 0.13 μCi. This is only three percent of the 3.6 μCi total xenon-133 present in the system at this time, as determined by calculation.

A trace of fission produced iodine-132 (half-life: 2.3 hours) was detected on the iodine trap. The presence of this short-lived nuclide so long after removal of the target from the neutron flux is explained by the fact that it is in equilibrium with its 3.2 day half-life parent, tellurium-132.

Gamma-ray spectra taken from the aluminum irradiation can revealed the presence of fission products which were deposited in the can wall as a result of recoil following the primary fission events. Likewise, counting of the nickel tube after removal of the irradiated uranium oxide by acid dissolution showed that fission fragments were imbedded in the

nickel tube surface as well. Chemical etching of the inside wall of the aluminum irradiation can and the nickel tube surface removed these deposited fission product activities.

An identical irradiated uranium coated nickel tube within a sealed aluminum irradiation can was swept with helium gas and the fraction of xenon-133 released (residing in the air space of the irradiation can) was found to be the same (three percent) as in the first measurement. After completion of the helium sweep, the target was transferred to a dissolver apparatus in which the uranium oxide deposit could be dissolved to release bound or trapped xenon while sparging the solution with helium into the trapping system. Contacting the target tube with 8 M nitric acid resulted in immediate dissolution of the uranium deposit (within five seconds). With a helium flow rate of 20 ml per minute the xenon-133 activity in the cold trap was monitored as the dissolution of the uranium coating occurred and the nitric acid began to etch the nickel tube surface. Figure 49 is a plot of the total xenon-133 released in the dissolution experiment as a function of contacting time with the dilute nitric acid. Most significant is that approximately 0.1 μCi resided in the uranium oxide coating and the remainder was apparently distributed between the surface of the nickel tube and the inner wall of the irradiation can as a result of the stopping of the recoiling fission fragments.

After no more xenon-133 was being collected by the cold trap in this experiment, the liquid nitrogen was removed from the trap and the trap was permitted to warm to room temperature. Noted in Figure 49 is the rapid evolution of the trapped xenon-133 as the trap returned to room temperature. The data indicated that 90 percent of the trapped xenon was

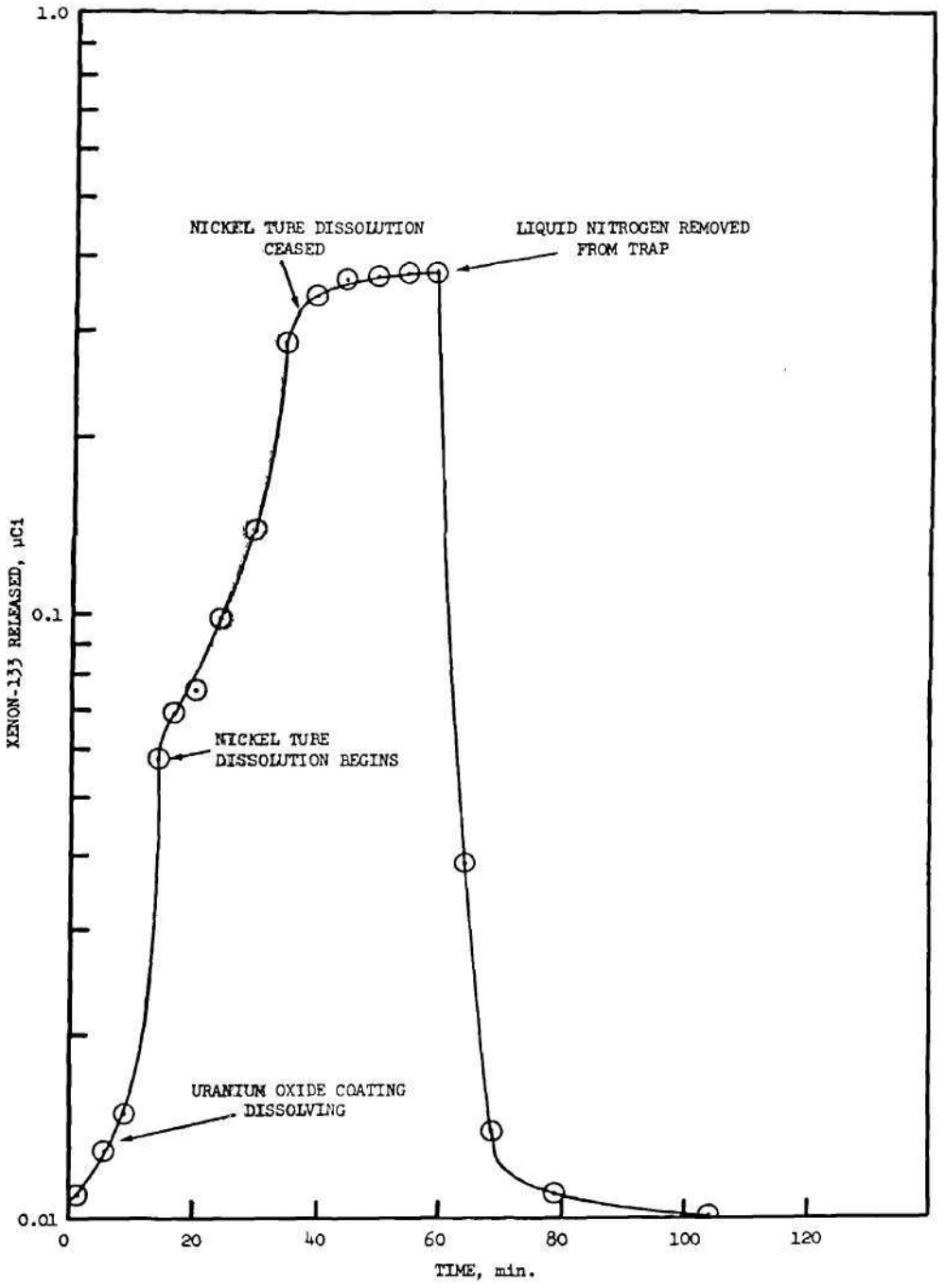

Figure 49. Release of ^{133}Xe from Uranium Oxide-Coated Nickel Tube while Dissolving in 8 M HNO_3

released in the first five minutes after the coolant was removed from the trap. This demonstrated the ease of regeneration of the cooled molecular sieve trap for xenon collection.

An experiment was conducted in which the void space in the aluminum irradiation can around the uranium oxide coated nickel tube was filled with water prior to sealing for irradiation. After irradiation and a decay time of four days, the can was punctured and the xenon-133 and water transferred to a vessel through which the helium gas passed to remove the sparingly soluble xenon from the water. This experiment demonstrated that 50 ± 10 percent of the fission produced xenon-133 was present in the water which occupied the normally void space of the irradiation container. This value is the average of three independent determinations.

Summary and Conclusions. The data gathered in studying the release of fission produced xenon-133 from the thin uranium oxide coatings on nickel metal surfaces indicate the following distribution of the xenon-133:

a) Three percent remaining in the uranium oxide coating

b) Approximately 48 percent in each boundary phase, i.e., the nickel metal surface and the void space (including the irradiation can wall).

These measurements are supported by the reported range of 10 μ for the heavy fission fragment in U_3O_8 (77). The coated nickel tubes used had a uranium oxide thickness of only 0.7 - 0.8 μ. Therefore, a relatively small fraction of the fission fragment xenon precursors would be expected to come to rest in this thin oxide layer.

Furthermore, the reported mean range of the fission fragments in

air is 2 cm (71) and the average distance between the nickel tube (uranium oxide) and the aluminum irradiation can wall is only 0.5 cm. This supports the experimental observation that a large fraction of the energetic fission fragments reaches the can wall before coming to rest. Thus, this portion of the total xenon produced in the fission process cannot be readily recovered by the helium sweep gas passing through the irradiation can void space.

The usefulness of this type of target configuration in the production and separation of the xenon fission product gases was shown to be inferior and no further consideration of its application to a practical production process was made.

2.5 Xenon-133 Release from Irradiated Uranium-Loaded Molecular Sieves

The first experiments with uranium-loaded molecular sieve targets were concerned with measurements of xenon-133 release rates and yields. Much effort went into the development of the procedures and equipment used for the quantitative determination of the xenon-133 released from the irradiated target material. Most of this has been described in Sections 2.2 and 2.3.

One set of data which is typical of the experimental results obtained from these studies with xenon-133 was from the irradiation of 8-12 mesh Type 13X molecular sieves (Davison Chemical Division, W. R. Grace & Company) which contained 93 percent enriched uranium-235 at a concentration of 62 micrograms uranium-235 per gram of molecular sieves.

A group of five samples of this lot of uranium-235 loaded molecular sieve beads was sealed into individual aluminum irradiation cans. Cobalt

flux wires were included inside the cans with the target material so as to place the flux monitor as close as possible to the target. This minimized flux measuring error due to spacial flux variations.

The sealed cans were irradiated in position V-43 of the GTRR for 9.27 hours. After allowing approximately five days for decay, the cans were punctured, one at a time, and the quantity of free xenon-133 in the can measured with the NaI(Tl) scintillation detector counting the xenon-133 in the cold trap. Figure 50 is a plot of the released xenon-133 activity versus time from such a can puncture and helium purging at 25°C. There is an initial rapid recovery of xenon present in the air space of the irradiation can followed by a very slow, small additional evolution of xenon-133.

Table 22 is a summary of the data obtained in these experiments.

Increases in the sample temperature up to 600°C resulted in the release of another 20 percent of the total xenon-133 as depicted in Figure 51 (a composite of data from several experimental runs). Most significant is the stepwise increase in released xenon-133 as the temperature is increased. This did not fit the release behavior expected from a purely diffusion-controlled mechanism which should have produced an increase in the slope of the released xenon versus time curve as the temperature was increased.

When the fraction of the total xenon-133 released at one temperature was plotted against the square root of the time (as was discussed in Section 1 of this chapter and applied earlier to the ion exchange studies described in Chapter II), negligible deviation from a straight line should be found at release fractions less than about 0.5 for the case of a purely

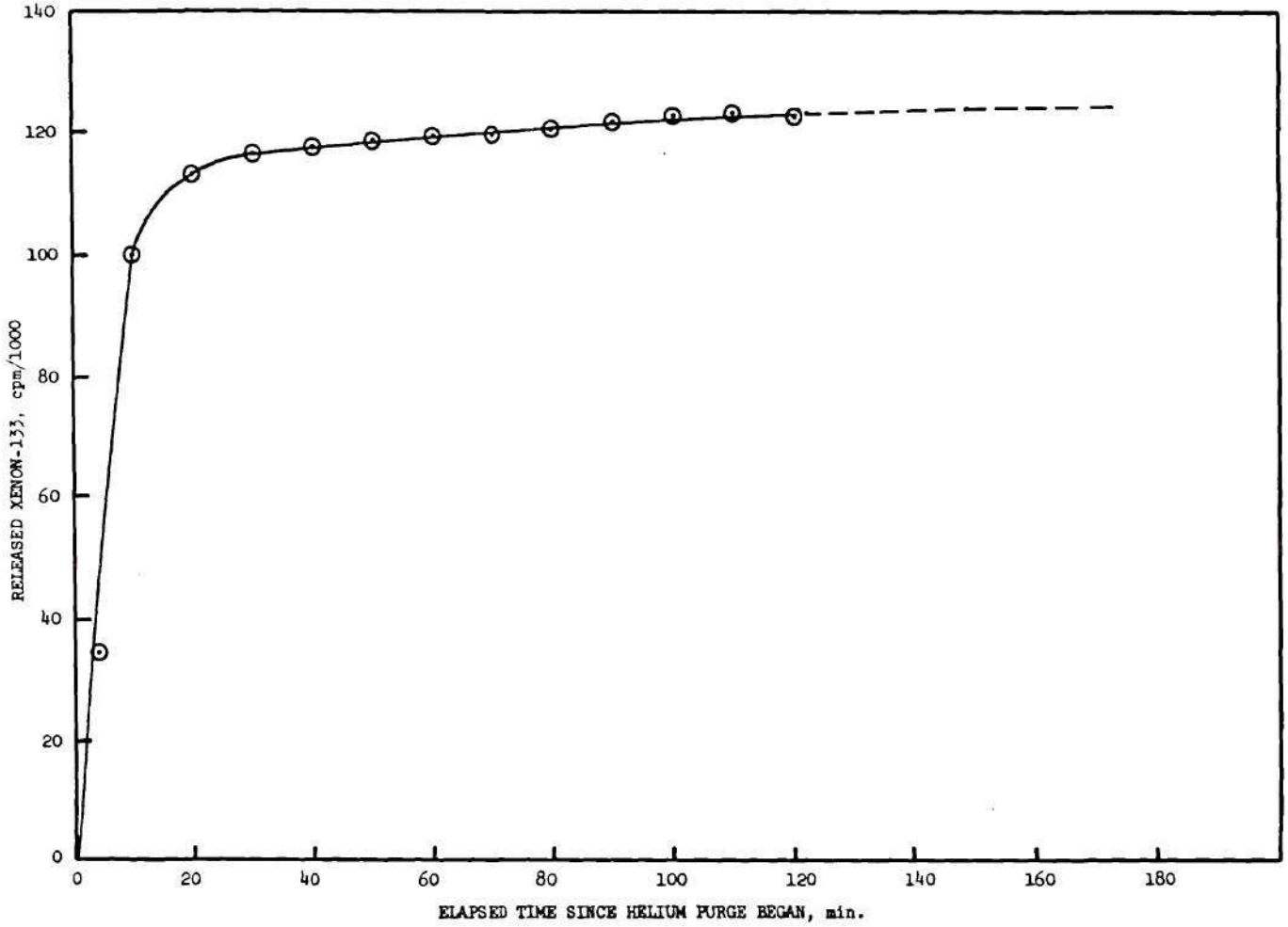

Figure 50. Rate of ^{133}Xe Recovery from ^{235}U-Loaded Type 13X Molecular Sieves by Helium Gas Purge of Irradiation Can

Table 22. ^{133}Xe Release from Irradiated ^{235}U-Loaded Type 13X Molecular Sieves at 25°C

Sample	^{235}U (μg)	Calculated Total ^{133}Xe (μCi)	^{133}Xe Released (μCi)	Percent Released
1	260	16.7	5.6	34
2	244	13.5	4.3	32
3	270	12.9	3.9	30
4	263	8.2	2.4	30
5	101	2.3	0.71	30
			Average:	31
			$\sigma = \pm 2$	

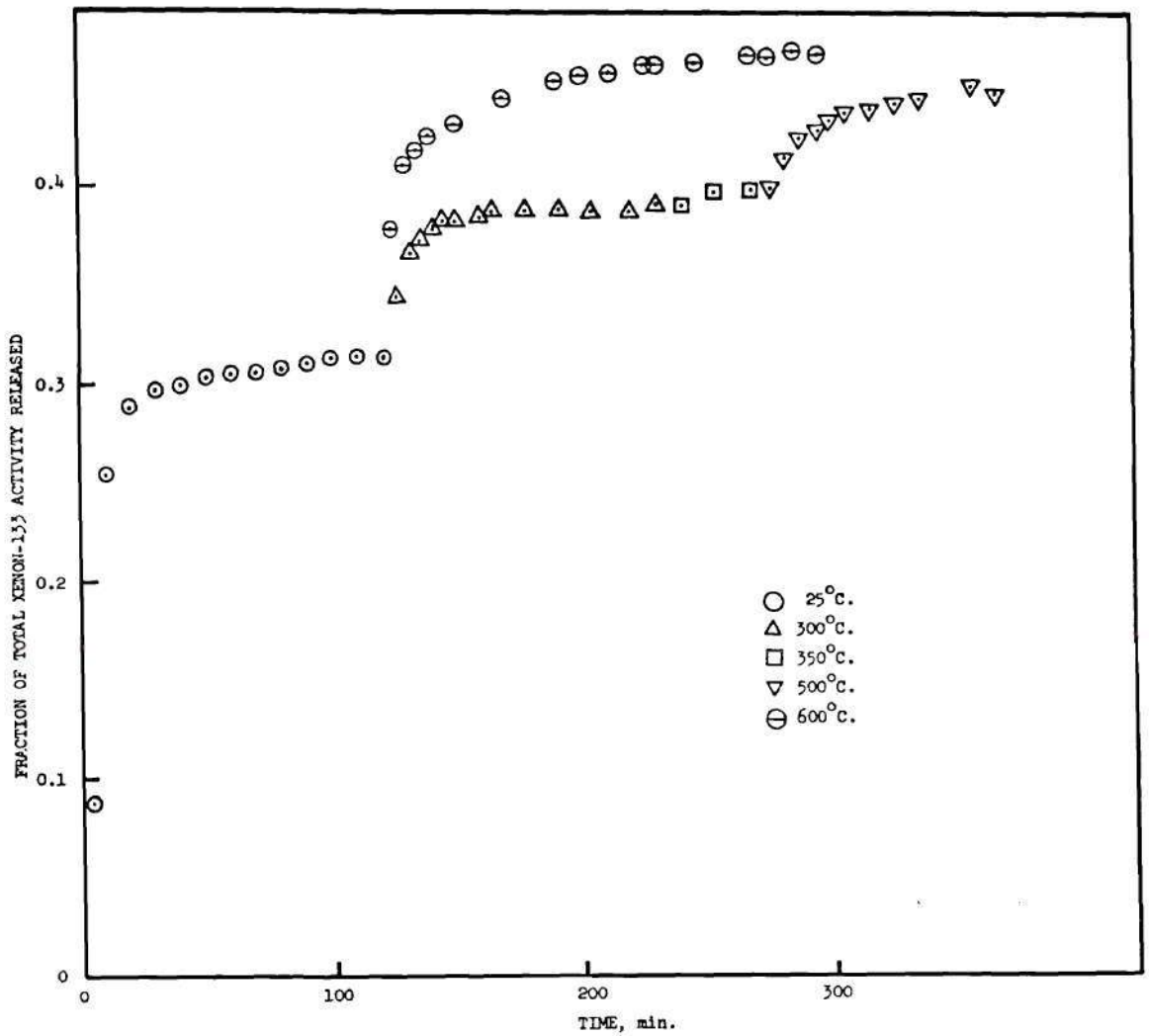

Figure 51. Release of ^{133}Xe from Type 13X Molecular Sieves at Successively Higher Temperatures (Composite Data from Several Experiments)

diffusion-controlled release. The slope of this line is a function of the particle radius and the effective or apparent diffusion coefficient as described earlier. When this was done with the data for xenon-133 release at 300°C and 600°C, the results shown in Figure 52 were obtained.

It is significant that the linear portions of these curves is so abbreviated (only linear up to less than 0.1 fractional release). This, also, is not characteristic of a solely diffusion-controlled release process.

If we calculate the slope of the initial portions of these release curves ($f \leqq 0.1$ and assuming linearity) and use the molecular sieve crystallite radius of one micron for the dimensions of the particle from which the xenon is diffusion, values of 5.6×10^{-15} and 2.3×10^{-14} cm^2 sec^{-1} are calculated for the apparent or effective diffusion coefficients at 300°C and 600°C, respectively, during the rapid release phase of these experiments.

Plotting these values for the apparent diffusion coefficient (as natural logarithms) versus reciprocal absolute temperature would give a line with a slope of (-E/R), where E is the activation energy for the rate controlling step in the xenon release and R is the gas constant. With only two points the value for the activation energy, E, was calculated algebraically to be 4.7 kilocalories per mole for this measured release of xenon-133 with a D_o value of 3.4×10^{-13} $cm^2 sec^{-1}$. The expression describing the xenon-133 release is, therefore:

$$D = 3.4 \times 10^{-13} \, e^{-4700/RT}$$

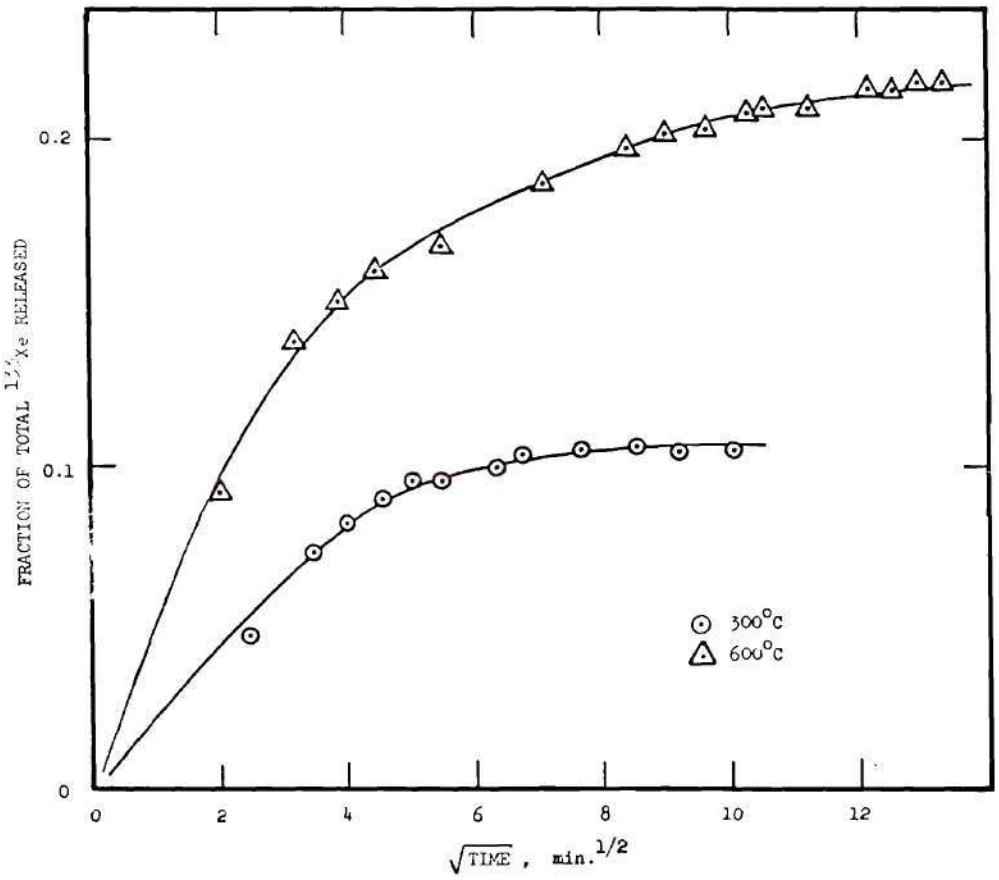

Figure 52. Fractional Release of ^{133}Xe vs Square Root of Time from Type 13X Molecular Sieves

where

D = the diffusion coefficient (apparent or effective)

R = the gas constant, 1.987 calories per degree per mole

T = the absolute temperature

Summary and Conclusions. These measurements of the release of xenon-133 from irradiated batches of uranium-loaded Type 13X molecular sieve beads demonstrated that:

1) Thirty percent of the xenon-133 present was found to be free from the molecular sieves when measured two to five days after removal from the reactor.

2) Heating up to 600°C could effect the rapid release of as much as an additional 20 percent of the xenon-133 present in two hours.

3) The shape of the xenon-133 release curves did not correspond to a classical diffusion controlled process.

4) The initial portions of the release curves can be related to apparent diffusion coefficients of 5.6×10^{-15} and 2.3×10^{-14} $cm^2 sec^{-1}$ at 300°C and 600°C, respectively. Calculations based on this influence of temperature on the apparent diffusion coefficient indicated an activation energy of 4.7 kilocalories per mole for the xenon-133 release. The calculations are based on the assumption that escape of the xenon from the 2 μ diameter aluminosilicate crystallites is the rate-determining step and that once the xenon has diffused into the intercrystallite space, it can escape readily from the molecular sieve bead. This was shown to be rapid by the data on release of xenon-133 from the molecular sieve filled cold trap as it warmed as shown in Figure 49.

These results are explained by a model which provides for trapping of the fission gas atoms in radiation-induced and pre-existing defect or structural traps in the molecular sieve structure. This trapped fate of the xenon atoms is in direct competition with the release by diffusion from the structure. The shape of the release curves is indicative of a high value for the trapping parameter as defined by MacEwan and Morel (78) or the rate constant for trapping as used by Ong and Elleman (79) relative to the rate constant for release or escape from the traps. Figure 30 shows the similarity in shape of calculated release curves (79) in comparison to the experimental data obtained in this investigation.

Quantitative evaluation of the trapping parameter or rate constant and associated trap release values is not possible due to the failure of the xenon to demonstrate a purely diffusion controlled release behavior even at the low fission densities (3×10^{12} fissions per gram of molecular sieve) encountered in these experiments. Calculations of these values requires that the true diffusion coefficient of the xenon in the system be known. Pure diffusion was not positively identified in these experiments.

The estimated activation energy calculated from the apparent diffusion coefficient variation with temperature (4.7 kcal per mole) is in general agreement with the activation energies reported for sorption of pentane onto the natural zeolites analcite and chabazite which fell in the range of 4-7 kcal per mole (94).

2.6 Xenon-135 Release from Uranium-Loaded Molecular Sieves

As explained in Chapter I, the decay characteristics of xenon-135 (250 keV gamma-ray with 97.1 percent absolute intensity) potentially make it the xenon isotope of choice in medical diagnostic scanning studies and

other applications.

In addition, the measurement of the release of xenon-135 from irradiated uranium targets as it grows in from its 6.68 hour half-life iodine-135 precursor may be made in a reasonable time period as compared to the 5.27 day xenon-133 ingrowth from 20 hour iodine-133. Such measurements may be useful in elucidating the behavior of the xenon release during the rapid phase of diffusion from the molecular sieve target. The xenon-133 measurements just described showed that this rapid release occurred in a time period that was short in comparison with the rate of xenon-133 ingrowth. This made it impossible to examine this phase of the release using xenon-133. For these reasons, the emphasis was shifted at this point to xenon-135.

The apparatus used was unchanged from that described in the preceding section. All xenon-135 release experiments were made, however, using targets of single molecular sieve beads or small quantities (typically 100 mg) of molecular sieve crystallite powder. This was practical due to the greater quantity of xenon-135 produced compared to xenon-133. Irradiation of the targets was made in the GTRR pneumatic transfer irradiation facilities at a thermal neutron flux of 8×10^{12} nv. Normal irradiation time was five minutes. This shorter irradiation at a higher flux in the pneumatic transfer irradiation facilities permitted rapid access to the irradiated targets so that xenon-135 release measurements could begin prior to significant ingrowth from the 6.68 hours half-life iodine-135 precursor.

Target materials were prepared as described in Chapter II by ion

exchange of uranyl ion from methanol solution onto 8-12 mesh Type 13X molecular sieve beads or Type 13X crystallite powder (Davison Chemical Division, W. R. Grace & Company). Uranium enriched in the mass-235 isotope was obtained from the National Bureau of Standards (SRM No. NBS-930) and contained 93 percent uranium-235.

Small quartz vials made from 4 mm outside diameter tubing were used to contain the uranium-loaded molecular sieves during irradiation. Experimental measurements demonstrated that only 1.0 and 1.6 percent of the heavy and light fission fragments (as indicated by tellurium-132 and molybdenum-99), respectively, were lost by recoil into the quartz tube inner wall. This is in agreement with the calculated recoil loss of approximately two percent made in Section 1.2.

It is essential that any loss of fission-produced iodine from the irradiated molecular sieve target be known. Measurements made with irradiated uranium-loaded molecular sieve targets in a helium sweep-gas atmosphere failed to detect any loss of iodine fission products from the molecular sieve in the temperature range used (up to 500 °C). This was determined by counting the irradiated uranium-loaded molecular sieve bead on the high-resolution Ge(Li) gamma-ray spectrometer before and after heating overnight and quantitatively comparing the iodine-133 content.

Procedure for Xenon-135 Release Measurements. The quartz irradiation vial was broken open and the target swept with helium gas to remove the xenon-135 which was then collected in the liquid nitrogen-cooled trap as previously described. For room temperature measurements, the quartz vial was placed in a short section of polyethylene tubing through which the helium was flowing. Pressure was then applied to the quartz vial by

compressing the polyethylene tube with pliers to break the quartz. This permitted the sweep gas to pass over the uranium-loaded target. The time required for the released xenon to reach the detector (cold trap) was calculated to be less than one minute at the 20 ml min^{-1} helium flow rate used.

For measurements at elevated temperatures, the irradiated molecular sieve bead was removed from the quartz vial and placed in the stainless steel heating chamber (Figure 35) through which the helium sweep gas passed. In the case of the molecular sieve crystallite powder, the ends of the quartz irradiation vial were broken off and the vial inserted between two glass wool plugs into a glass tube having an inside diameter very close to the outside diameter of the quartz irradiation vial so that the major portion of the helium sweep gas flow would pass through the opened quartz vial.

Lengthy runs were made with the help of the timer-controller which automatically accumulated a gamma-ray spectrum from the NaI(Tl) detector positioned near the xenon-collecting cold trap and then activated the paper tape punch unit to record the spectrum prior to the next spectrum accumulation. The normal procedure was to take data hourly. The liquid nitrogen level controller was also used to maintain the coolant level in the cold trap dewar during extended experimental runs.

After allowing the irradiated samples to decay for a minimum of one week, the lanthanum-140 content was determined by Ge(Li) gamma-ray spectrometry and applied to the calculation of the fission rate experienced by the target during irradiation. This minimum decay time was necessary to avoid high results due to the presence of lanthanum-140 from

the neutron activation of lanthanum impurities in the molecular sieves. This fission rate was then used to calculate the total xenon-135 present at any time after irradiation. Initially, as a check, another fission product, zirconium-95, was also used for calculation of the fission rate. The fission rates calculated by the two fission product indicators agreed within experimental error. Since the counting of the lower energy (724 keV) gamma-ray from zirconium-95 was more susceptible to interferences than the 1596 keV gamma-ray from lanthanum-140, the latter fission product was used as the fission rate indicator.

Two series of experiments were conducted, using 8-12 mesh Type 13X beads and powder-form Type 13X molecular sieves. Both targets contained 93 percent enriched uranium-235. The beads contained 18 mg uranium-235 per gram of molecular sieve, while the powder contained only 1.9 mg uranium-235 per gram. The principal difference was that, in the powder target, there was a homogeneous distribution of the uranium at a low concentration, while in the beads (as shown in Chapter II), the uranium resides in a narrow band at high concentration near the bead surface.

Electron microprobe examination of the uranium-loaded molecular sieve beads used in these release measurements (and in the reactor loop described in Chapter IV) revealed that in a 2.72 mm diameter bead the uranium was located in a 0.48 mm thick outer shell. Calculating the total volume of the bead and the volume of the uranium-loaded portion showed that the uranium-containing portion of the bead represented 73 percent of the total volume of the molecular sieve bead. This means that the actual uranium concentration in these beads is approximately 25 mg per gram when this volume correction is made.

Table 23 gives the conditions of the experimental runs and the resulting fractional releases of xenon-135 based on the maximum xenon-135 present in the system during the run. In some cases the bead fractured prior to the release measurements. Notable is the fact that this did not affect the measured fraction of the xenon-135 released when compared to a run made under the same conditions with an intact bead. This is evidence that the xenon diffuses readily from the bead macrostructure and reinforces the hypothesis that escape of the xenon from the aluminosilicate crystallites is the rate-controlling factor in the release of fission-produced xenon from molecular sieves.

Plotting the calculated ingrowth and decay of xenon-135 alongside the data from these experiments results in the graph shown in Figure 53. This was made from the data from Run B at 25°C. The curves representing the measured released xenon-135 and the calculated total are definitely similar in shape and appear to be symmetrical. If this were true, the percent released at any specific time during the run would be constant. Figure 54 depicts the percent xenon-135 released as a function of time out of the reactor. A definite lag in the escape of xenon-135 is seen.

The mean percent xenon-135 released at 25°C as shown in Figure 54 is 22.1 ± 0.4 percent which was determined by averaging the last 20 data points.

Applying the same treatment to the data from Run I which measured the xenon-135 release at 404°C resulted in the maximum release of 43.1 ± 0.6 percent of the xenon-135 present (Figure 54).

Run M (powder molecular sieve target) at 455°C released the xenon-135 as also shown in Figure 54. The mean maximum percent xenon-135

Table 23. Release of ^{135}Xe from Type 13X Molecular Sieves

Run No.	Temperature (°C)	Fission Rate (fps)	^{135}Xe (microcuries)		
			Calc. Max.	Max. Released	Percent Released
Beads:					
A	25	1.26×10^9	5.99	1.28	21
B*	25	1.22×10^9	5.81	1.23	21
C	101	1.49×10^9	7.07	2.46	35
D*	110	1.13×10^9	5.36	2.01	38
E	121	1.08×10^9	5.14	1.72	33
F	207	7.04×10^8	3.35	1.14	34
G	209	1.26×10^9	5.99	2.18	36
H	309	1.18×10^9	5.63	2.07	37
I	404	1.53×10^9	7.30	2.87	39
Powder:					
J	25	3.11×10^8	1.48	0.038	2.6
K	249	3.76×10^8	1.79	0.820	46
L	251	3.96×10^8	1.88	0.856	46
M	455	5.53×10^8	2.63	1.22	46

*Fractured beads

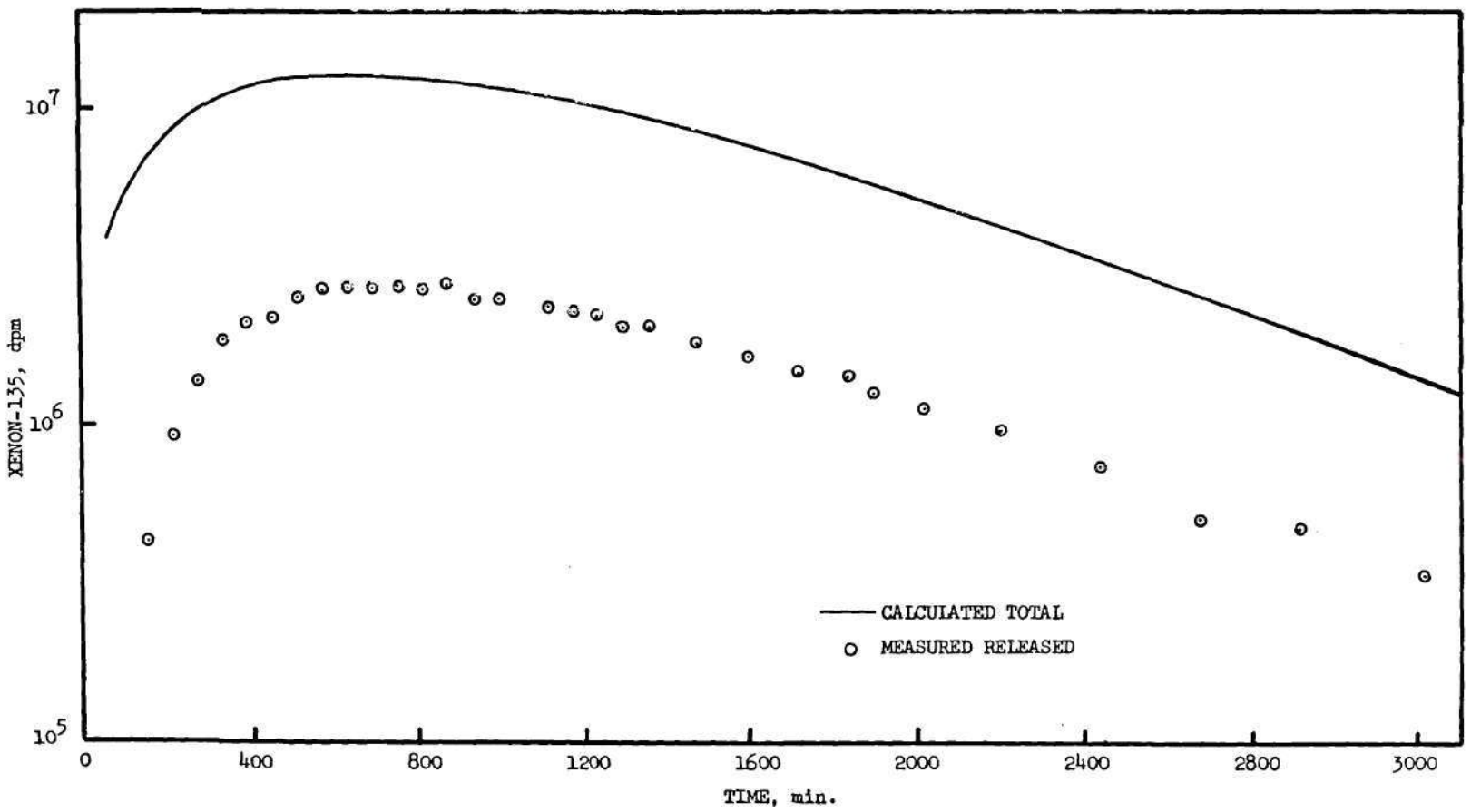

Figure 53. Comparison of Measured Released ^{135}Xe with Calculated Total ^{135}Xe (Run B, Table 23)

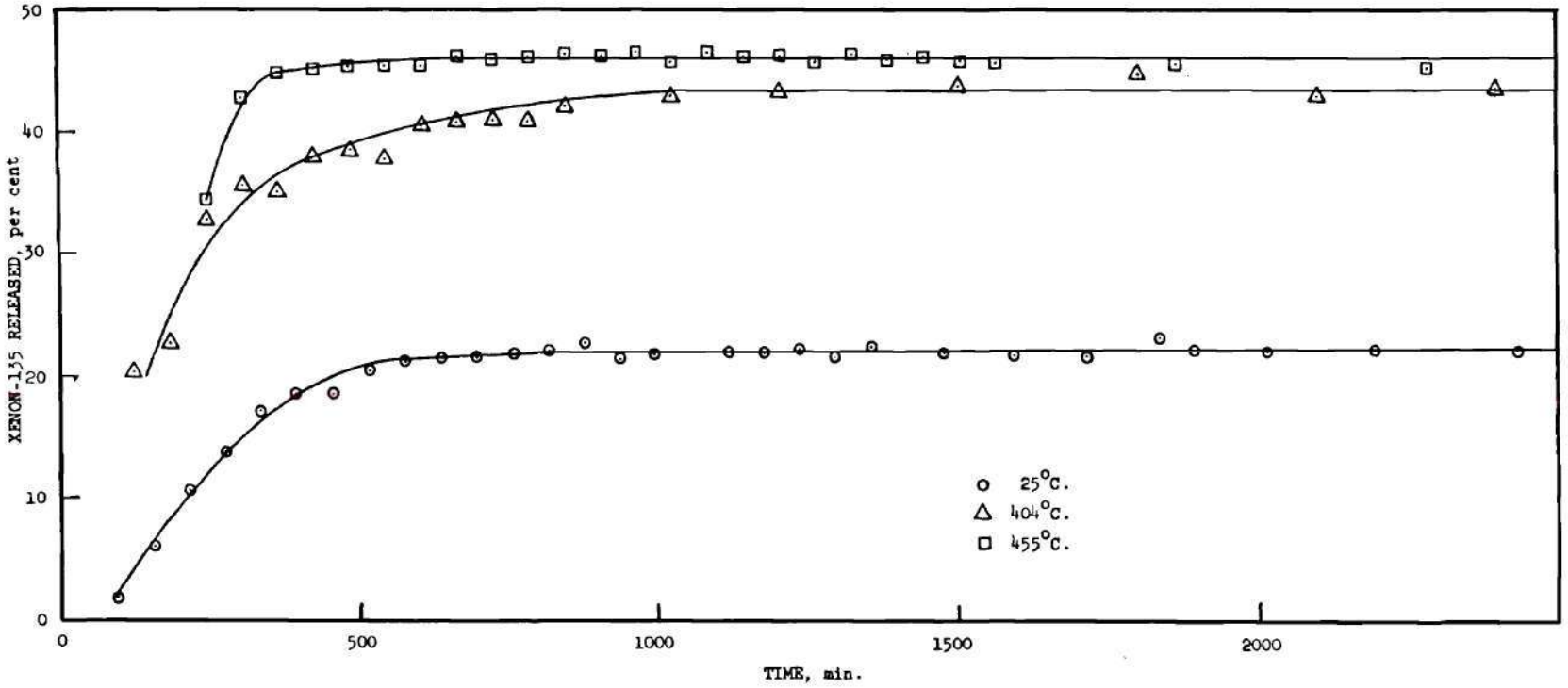

Figure 54. Per Cent ^{135}Xe Released vs Time

released from the molecular sieve powder was 46.0 ± 0.5 percent. If the higher temperature of this run is taken into consideration, the agreement with Run I at 404°C is very good.

An apparent increase in the fraction of xenon-135 released at higher temperatures by the molecular sieve powder target in comparison to the beads is noted in Table 23. This is explained by a slightly more rapid release of the xenon from the powdered material. Since the numerical values for the effective percent xenon-135 released given in Table 23 were obtained by comparison of the maximum calculated xenon-135 and the maximum released xenon-135, but not necessarily at the same elapsed time after removal from the reactor, these values are subject to the influence of the rate of release. As noted, if the equilibrium fraction released is calculated, the values are in good agreement for the two target materials.

3.0 Summary and Conclusions

The following conclusions may be drawn from the experimental data presented and the work described in this section:

1. The dynamic release of xenon-135 is consistent with the quantitative data for xenon-133 release presented in the previous section.

2. Since the fraction released remains constant after reaching a maximum, a constant fraction of xenon atoms must occupy locations with the molecular sieve structure from which they may escape under the conditions of the specific experiment. This must be due to the random location in the crystallites at which the energetic fission fragment comes to rest or the final position of the recoiling xenon atom after formation by iodine precursor decay.

3. The higher uranium concentration in the molecular sieve beads (Run A through Run I) appears to be the cause of the enhanced xenon release at lower temperature when compared to the molecular sieve powder target having a lower uranium concentration (Run J through Run M). This effect of increased permeability to gases as a result of divalent cation substitution in the zeolite has been noted for the natural zeolite, mordenite (95). Replacement of two monovalent sodium cations in the molecular sieve structure by a single divalent uranyl ion results in an overall increase in the effective aperture diameter into the zeolite cage structure.

4. The increased (but limited) release at higher temperatures is predicted by the diffusion-trapping competition discussed in Section 1 of this part. Comparison of the predicted release curves of Ong and Elleman (Figure 30) indicates the presence of traps for the diffusing xenon atoms. Furthermore, the rate of escape from these traps must be quite low. The estimated activation energy of 4.7 kcal $mole^{-1}$ calculated from the xenon-133 release data in Section 3.4 is in the range which might be predicted for deformation of the xenon atom or the zeolite structure. The traps are likely to be the pre-existing structure of small sodalite cages of the molecular sieve crystals rather than radiation damage-induced traps. This statement is based on the fact that the total fissions experienced by the samples in this study are so small (typically 10^{14} fissions per gram) and the observation that a factor of four difference in the fission density between the beads and the powder targets had no detectable influence on the release of the xenon-135. The nearness of the xenon atomic dimensions to the critical dimension of the smaller cage apertures makes it possible for a recoiling fission fragment or xenon atom from iodine

beta decay to pass through these openings and come to rest in a sterically trapped position within the molecular sieve structure. As discussed in Section 1, this has been demonstrated in the cases of argon and krypton by high temperature and pressure induced infiltration of the smaller cage structures of the Type A zeolite.

5. The application of uranium-loaded molecular sieves in the design of a high surface area target for the preparation of xenon fission product radionuclides has been demonstrated to be a practical and workable approach. The maximum of 46 percent xenon-135 released is far in excess of the highest value found in the literature for the release of xenon fission gases from powdered uranium dioxide at 1400°C which was only 23 percent (96).

CHAPTER IV

REACTOR XENON LOOP EXPERIMENT

1.0 Technical Background

Chapter II of this dissertation has described the successful incorporation of uranium into molecular sieves by ion exchange of uranyl ions for sodium cations present in the aluminosilicate structure. Chapter III described laboratory investigations which demonstrated the ability of the irradiated uranium-loaded molecular sieves to release a substantial fraction of the fission-produced xenon-133 and xenon-135 radionuclides. It remains for Chapter IV to relate the final phase of this study-the design, construction and operation of a reactor loop utilizing the uranium-loaded molecular sieve target for production of fission product gaseous isotopes. Operation of this prototype production unit will provide additional data on effects of radiation damage and limitations due to self-heating of the target which were not practical to explore in the laboratory study phase.

No references were found in the literature to such a reactor loop for gaseous radioisotope production. Related studies by Archer (11) were applied to rapid separation of microcurie quantities of xenon-138 (18 min. half-life) from irradiated targets of uranium adsorbed on zirconium dioxide. These targets were very susceptible to radiation damage and suffered a 50 percent loss of gas release after an irradiation equivalent to 1.3×10^{15} fissions per gram of zirconium dioxide.

The principal limitation in the operation of such a gaseous fission product radioisotope production unit was anticipated to be the fission heating and the resultant high target temperature. Up to approximately 600°C the elevation of temperature was expected to aid in the release of xenon-135 as indicated by the results of the laboratory studies reported in Chapter III. Above this temperature, there was concern that the porosity of the molecular sieve structure could be destroyed. This effect has been reported in the case of barium-loaded molecular sieves (97). Calculations for one gram of uranium-235 in a thermal neutron flux of 10^{13} nv give a fission rate of 1.49×10^{13} fissions per second. Since 3.3×10^{10} fissions per second is equivalent to the release of one watt, the postulated one gram of uranium-235 in the neutron flux specified would be subjected to 452 watts of self-heating. Consideration of this thermal heating in light of the poor heat transfer properties of the molecular sieve material led to the conclusion that operation of such a target at this flux with no cooling other than the slow flow of helium sweep gas was unlikely to remain within the desired temperature limit. As a result of this anticipated limitation, the reactor loop experiment was designed to permit adjustment of the target fission rate by selection of the neutron flux to which the target was exposed.

The methods for trapping and counting the xenon-135 product have been described in Chapter III and remain basically the same for use with the reactor loop experiment.

The method of calculation of xenon-135 production from known fission rate information as described in Chapter III is directly applicable

to the loop experiment provided accurate neutron flux data are available.

2.0 Experimental

2.1 Apparatus and Equipment

The Georgia Tech Research Reactor. The source of thermal neutrons for operation of the loop experiment was the Georgia Tech Research Reactor. Operation of this reactor at one megawatt provides thermal neutron fluxes up to 2×10^{13} nv. One of the two horizontal tangent tube irradiation facilities (designated as H-11, see Figure 31) was selected as the location for installation of the xenon loop experiment. This facility permits a range of neutron flux from about 10^{11} to 10^{13} nv for use in this study.

In order to gain access to the target while installed in the H-11 position in the GTRR for passage of helium sweep gas flow lines, and thermocouple and neutron flux monitor leads, a special shield plug assembly was designed and constructed. This assembly is shown in Figure 55.

Target Canister. The target was composed of 73 grams of 8-12 mesh Type 13X molecular sieve beads (Davison Chemical Division, W. R. Grace & Company) containing 1.35 grams of uranium-235. This was the same batch of uranium-loaded molecular sieve beads described in Chapter III.

The uranium-loaded molecular sieve beads were contained in a welded canister constructed of Type 304 stainless steel. Details of the canister design are shown in Figures 56 and 57. The bed of target material was held between two disks of porous, sintered stainless steel having an average pore diameter of 40 microns. This permitted ready passage of the helium sweep gas through the bed of molecular sieves. The bed volume was 100 cm^3.

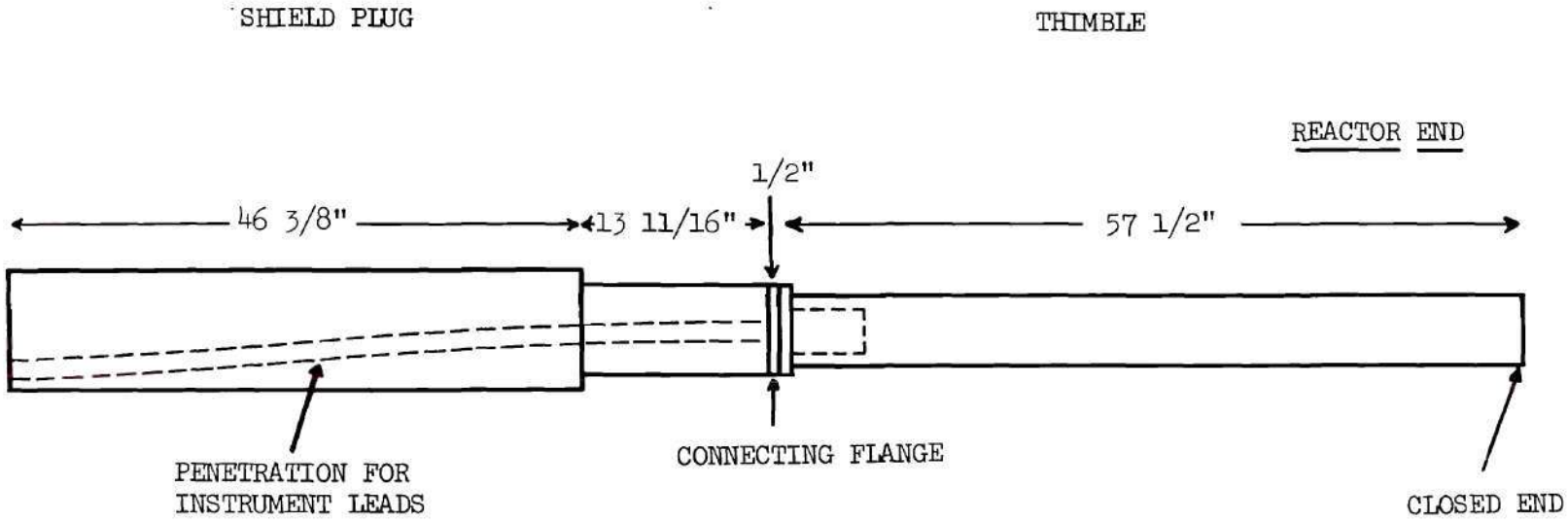

Figure 55. Special Shield Plug Assembly for GTRR Position H-11

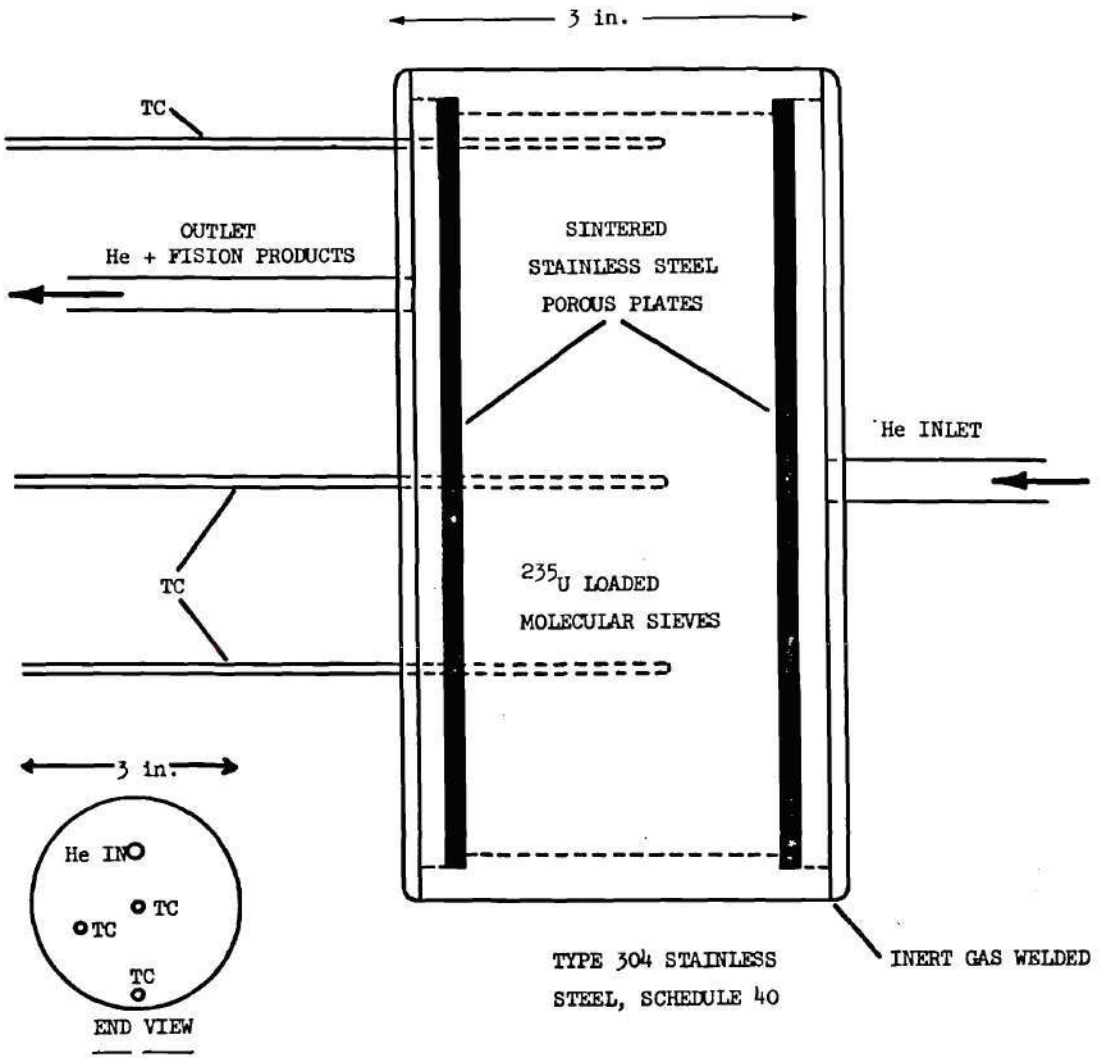

Figure 56. Target Canister Design

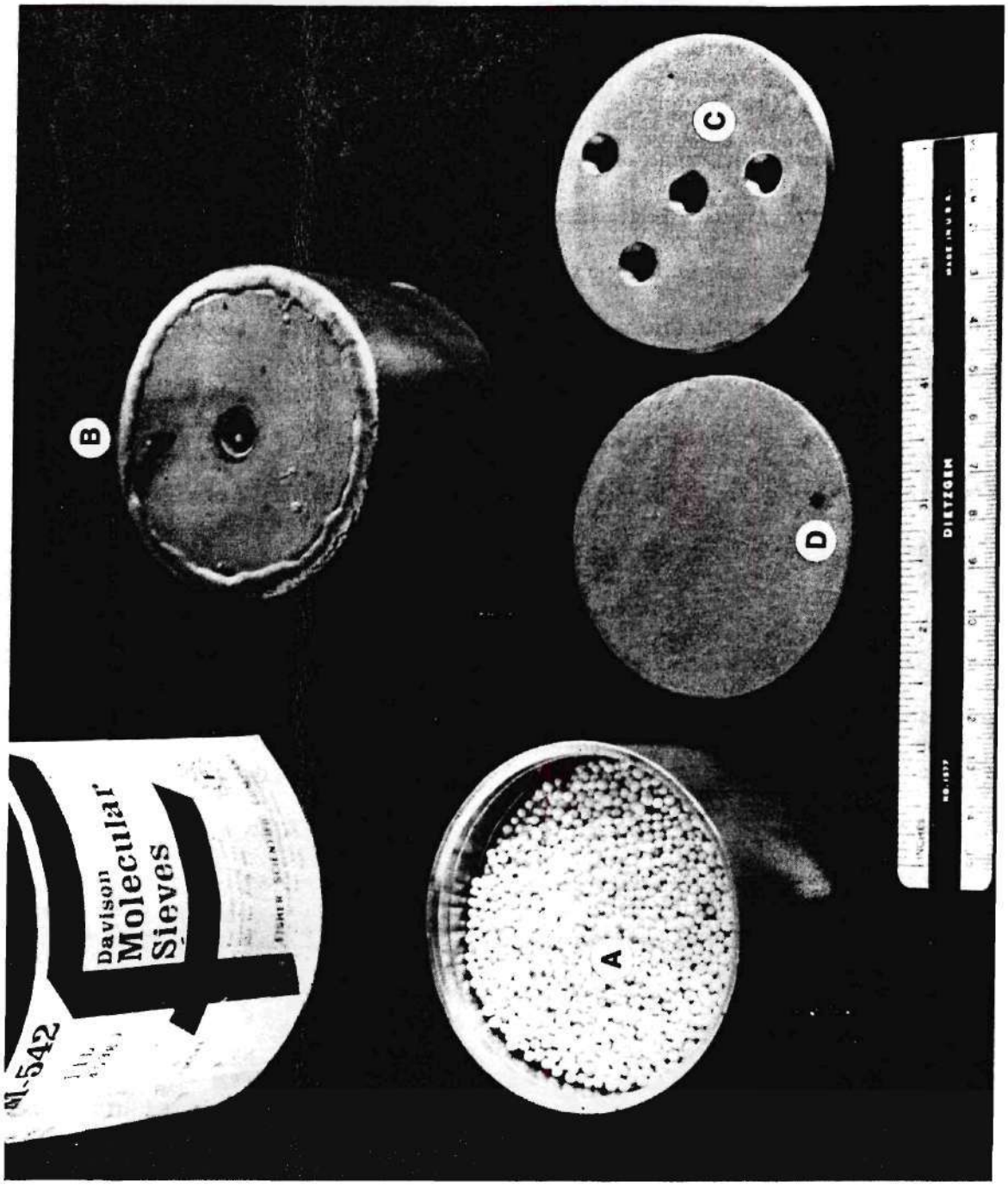

Figure 57. Partly Assembled Target Canister and Molecular Sieves.
A: Molecular sieves B: Helium inlet side
C: Helium outlet and thermocouple side
D: Porous stainless steel disk

As shown in Figure 56, the target canister was instrumented with three stainless-steel sheathed, iron-constantan thermocouples (Claude S. Gordon Company, No. 402-3103, magnesium oxide insulated) positioned so as to allow the temperature at the canister centerline, outer edge of the bed, and an intermediate location to be measured during irradiation. Temperatures were read by connecting the thermocouples to a millivoltmeter thermocouple reader (Thermo Electric Corporation, Model 10322). This particular model permits connection of up to six thermocouples. It was not, however, calibrated for the iron-constantan thermocouple and was further modified by installation of an optional shunt resistor and selector switch to provide two temperature measuring ranges: low range from ambient to 330°C, and high range from ambient to 700°C.

Also fitted at the outer surface of the target canister was a one-inch long, self-powered rhodium thermal neutron detector (Reuter-Stokes, Model RSN-202). This detector provides a current output proportional to the rate of decay of 40 second half-life rhodium-104 produced by thermal neutron activation of the detector rhodium element. The manufacturer's calibration value was 3.0×10^{-21} ampere per nv. The current measurements were made with a Keithley Model 610A electrometer.

Gas Trapping System. The xenon trapping system was constructed of one-fourth inch outside diameter hard brass tubing. Connections were made by soldering or with compression fittings. All valves used were of the bellows type to minimize possibilities of leaks. Figure 58 is a schematic representation of the trapping system and Figure 59 is a photograph of the actual apparatus as assembled on the reactor building floor.

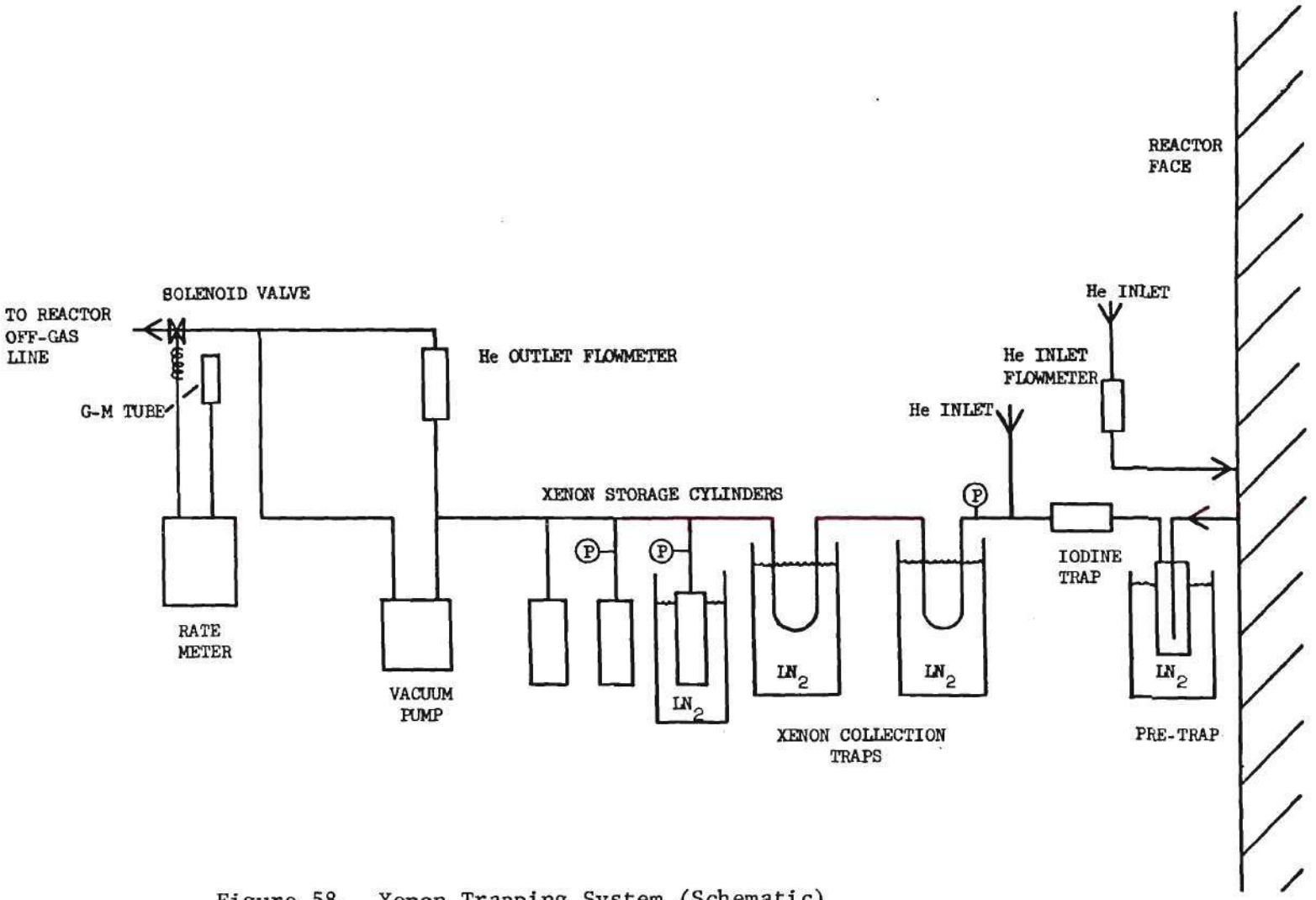

Figure 58. Xenon Trapping System (Schematic) for Reactor Loop (Valve Details Omitted)

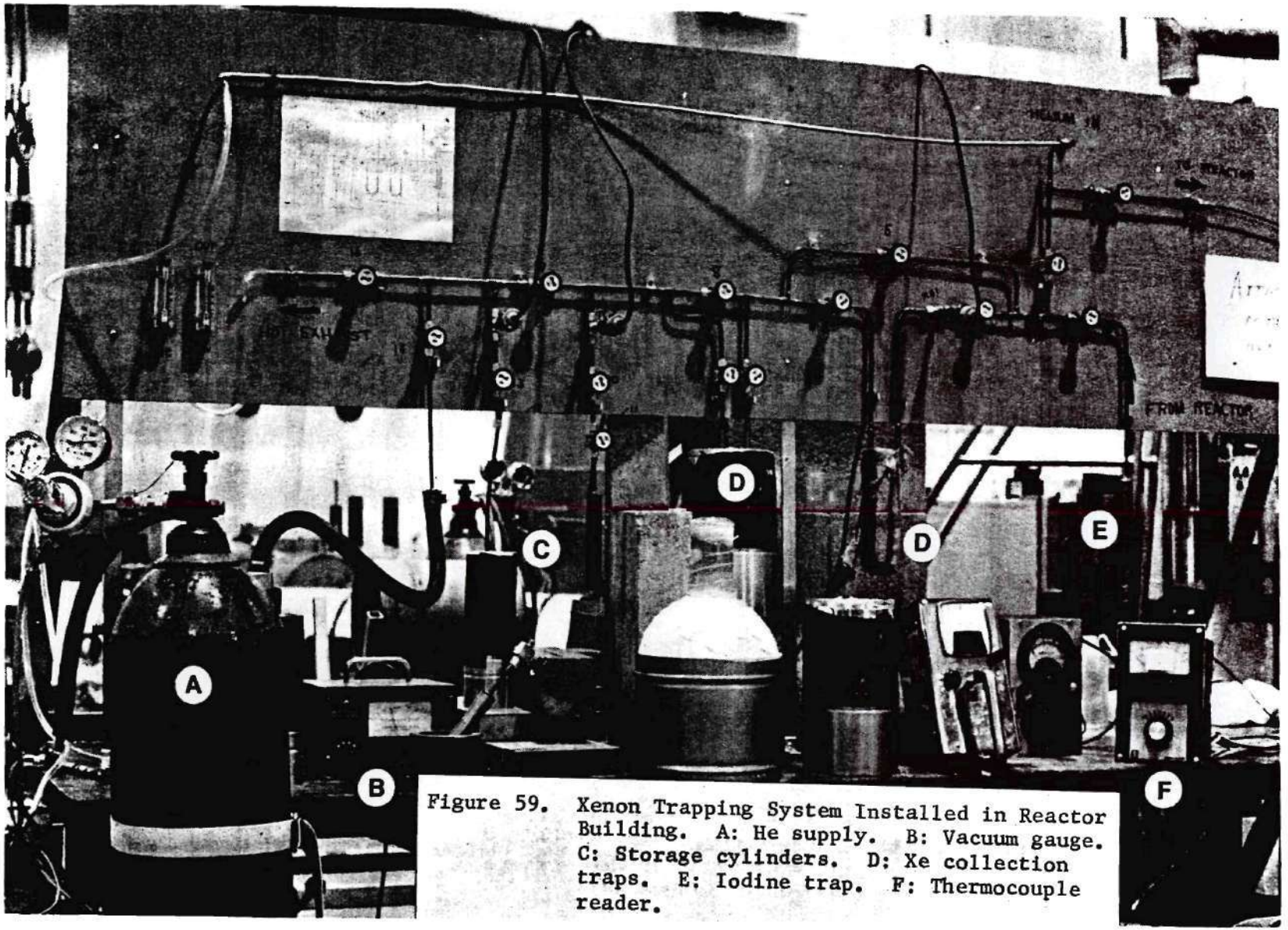

Figure 59. Xenon Trapping System Installed in Reactor Building. A: He supply. B: Vacuum gauge. C: Storage cylinders. D: Xe collection traps. E: Iodine trap. F: Thermocouple reader.

The pre-trap was a 2.5 cm diameter by 15 cm long copper tube filled with 8-12 mesh Type 13X molecular sieve beads. The gross gaseous fission products swept from the target canister during irradiation were caught on this liquid nitrogen cooled trap during the one-day operating cycle. This trap was shielded by six inches of lead. This pre-trap was required to collect the gross fission product effluent from the target which would otherwise result in excessively high radiation levels in the vicinity of the trapping system as a result of collection of the many short-lived krypton and xenon nuclides produced in the fission process. These short-lived species are permitted to decay in the pre-trap and the longer-lived xenon-135 is then transferred into the xenon collection traps.

The iodine trap was a 2.5 cm by 8 cm long bed of 45-60 mesh granules of silver-loaded Type 13X molecular sieves. As stated in Chapter III, this packing material is an efficient absorber of iodine in the event of release of fission product iodine from the irradiated target.

The xenon collection traps were constructed of one-half inch outside diameter copper tubing bent into a "U" shape. These traps were 25 cm high and were packed with 45-60 mesh Type 13X molecular sieve granules. The molecular sieve bed was 20 cm in length. These traps were cooled with liquid nitrogen to collect the fission product xenon when released from the warmed pre-trap. Both xenon collection traps were always used in series, but no activity was detected on the second trap.

The xenon storage cylinders were 2.5 cm in diameter by 15 cm in length and contained 20 cm^3 of 8-12 mesh Type 13X molecular sieve beads.

They were attached to the system by double valves, making it possible to disconnect the storage cylinders for removal to the laboratory for quantitative determination of the xenon-135 production.

The thermocouple vacuum gauges, labeled "P" in Figure 58, were connected to a Kinney Vacuum Corporation, Model III, KTG-3 indicator unit and were used to measure residual helium gas pressure in the system during pump-down prior to transfer of xenon-135 from the collection traps to the storage cylinders. This transfer was accomplished by cooling the storage cylinder with liquid nitrogen while warming the collection traps. The liquid nitrogen-cooled molecular sieve bed in the storage cylinder (-198°C) provided a cold, high surface area on which the xenon collects rapidly (xenon melting point: -112°C).

Flow meters monitored both inlet and outlet helium sweep gas flow rates so as to provide early indication of gross leaks or impending obstruction in the trapping system.

The off-gas line was vented into the reactor building vent system after passing through a liquid nitrogen-cooled trap and past a G-M tube detector coupled to a ratemeter which controlled a solenoid-powered shut-off valve in the off-gas line. Entry of the experiment off-gas into the reactor building vent system would be shut-off in the event radioactivity were detected by this detector.

Gamma-Ray Spectrometer. For quantitative determination of xenon-135 produced in the operation of the xenon reactor loop experiment, a high-resolution gamma-ray spectrometer was used. This apparatus consisted of a 16 cm^3 Ge(Li) detector (ORTEC, Model 8001-15) coupled to a 400 channel

pulse height analyzer (Technical Measurements Corporation, Model 404) through a preamplifier (Tennelec, Model TC-130) and a pulse-inverter (ORTEC, Model 433). The data output from the pulse height analyzer was through an integrator-resolver unit (Technical Measurements Corporation, Model 522), a typewriter control unit (Technical Measurements Corporation, Model 520P), and an IBM solenoid-operated electric typewriter.

2.2 Calibration of Apparatus

The counting efficiency of the Ge(Li) gamma-ray spectrometer for xenon-135 gamma-rays of 250 keV was determined using a selenium-75 source of 0.45 mCi which was calibrated against the National Bureau of Standards (SRM No. 4288) selenium-75 radioactivity standard. Since the quantity of xenon-135 to be measured was anticipated to be in the millicurie range, the 0.45 mCi standard was necessary in order to determine the counting efficiency at distances of 1, 2, and 3 meters from the detector center-line. Calculated corrections were made for the fact that the selenium-75 calibration standard was counted in a polyethylene container (negligible attenuation), while the xenon-135 would be counted in the copper storage cylinder where the 0.045 inch wall thickness would allow only 88 percent of the 250 keV xenon-135 gamma-rays to pass (calculated from the mass attenuation coefficient at this energy for copper).

After all the calibrations and necessary corrections were made, the fractional counting efficiencies for the 16 cm^3 Ge(Li) detector were:

8.66×10^{-6} at one meter

1.79×10^{-6} at two meters

9.15×10^{-7} at three meters.

All the iron-constantan thermocouples for use in the loop experiment were calibrated by comparison of the Thermo Electric thermocouple reader meter indications against a precision mercurial thermometer. This was accomplished by placing the thermocouples together with the thermometer in a laboratory tube furnace or oven. By permitting the oven or furnace temperature to come to equilibrium at each temperature setting, calibration curves for both high and low ranges of the reader were constructed. Least squares fits to these data gave equations for the calibration curves which were linear. This calculational approach to conversion of the thermocouple reader indications to temperature was found to be more precise than the graphical method and less time-consuming when a large number of indications were to be converted to temperature.

2.3 Flux Measurements

In order to provide input for a safety analysis of the proposed loop experiment and to predict the flux limitations to be found in the horizontal tangent tube irradiation facility of the GTRR (position H-11), a thorough flux mapping of the facility was conducted. This study also was needed to provide correlation between the rhodium flux monitor and the activation of cobalt flux wires as means of determining thermal neutron flux.

A fixture was constructed to permit placement of cobalt flux wires along the centerline of the thimble which was attached to the inner end of the special shield plug (see Figure 55). This fixture consisted of a one-fourth inch outside diameter aluminum tube the length of the thimble which was held at the centerline or axis of the thimble by several

aluminum spacer disks which fit snugly inside the thimble. In addition to providing a support for the flux wires, this fixture served as a housing for the self-powered rhodium neutron detector, permitting it to be positioned at any location along the thimble axis by insertion inside the aluminum tube.

The flux measurements were made using both cobalt flux wires (already shown in Chapter III to exhibit good correlation with measured xenon production) and the rhodium detector. Cobalt flux wires (0.66 percent cobalt in aluminum) were taped to the centerline tube of the support fixture at 10 cm intervals and to the outer surface of the thimble at 20 cm intervals. At each point on the thimble outer surface, four flux wires were attached, 90° apart around the outer surface. The direction to the reactor core center was normal to the line between one pair of these flux wires and parallel to the other pair.

The instrumented thimble and shield plug were inserted prior to reactor startup. With the reactor operating at a power level of one megawatt, the rhodium detector was used to map the flux variations along the centerline of H-11. Using the calibration given by the manufacturer, the data shown in Figure 60 were obtained as the detector was moved in 5 cm increments away from the reactor core centerline (plane X-Y, Figure 31).

After the one-day irradiation, the shield plug and thimble were removed from H-11 and the cobalt flux wires detached and counted on the gamma-ray spectrometer. Table 24 gives the thermal neutron flux values obtained from these flux wires. The rhodium detector values are given

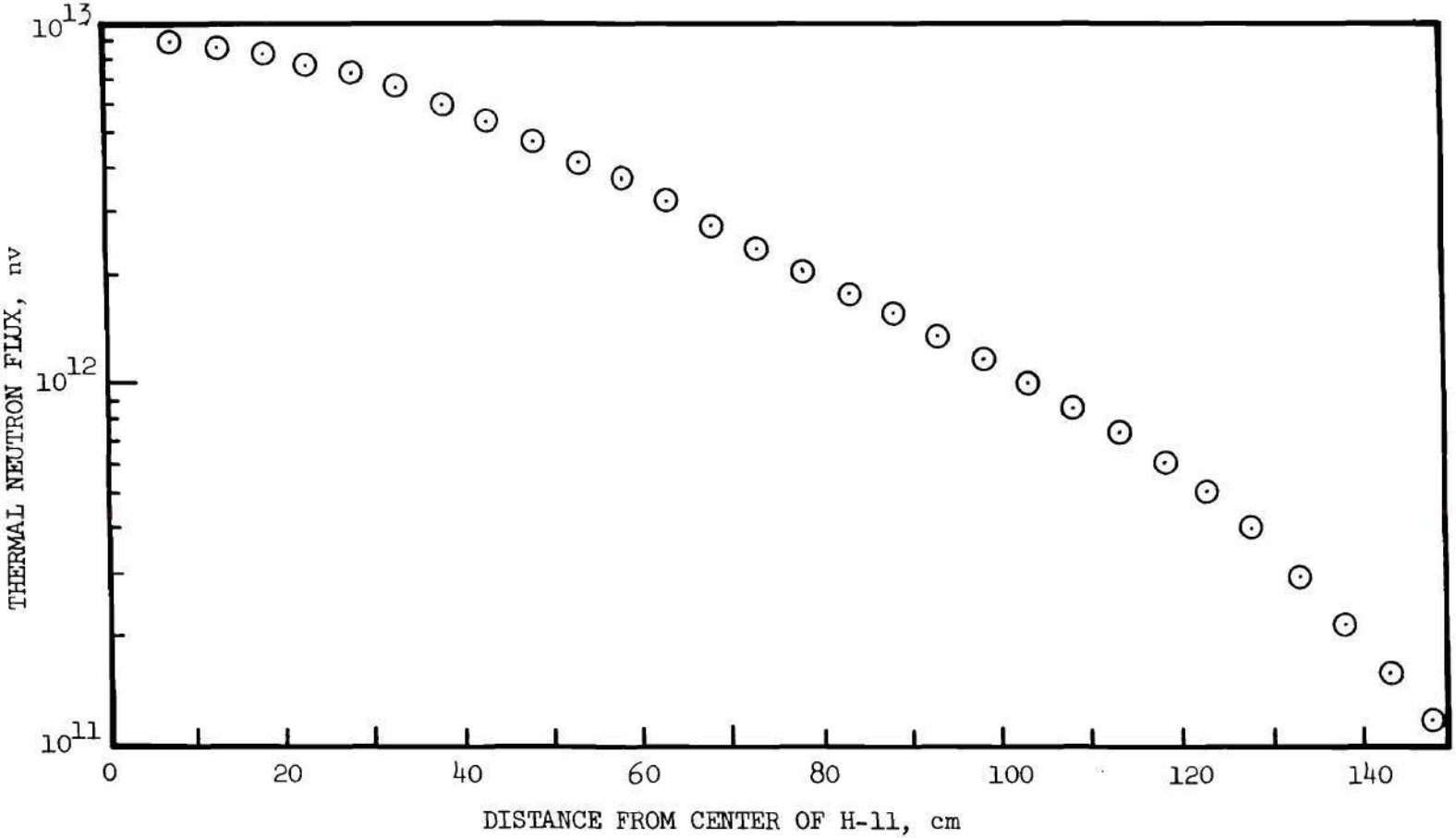

Figure 60. Rh Detector Flux Map Along Thimble Axis; Position H-11 of GTRR

Table 24. Thermal Neutron Flux Along Axis of Position H-11 of GTRR

Position (cm from centerline)	Neutron flux, nv		Ratio (Rh/Co)
	Co Wires	Rh Detector	
17	7.21×10^{12}	8.33×10^{12}	1.16
27	6.43	7.33	1.14
37	5.57	6.00	1.08
47	4.44	4.73	1.07
57	3.44	3.70	1.08
67	2.66	2.73	1.03
77	1.99	2.03	1.02
87	1.46	1.56	1.07
97	1.13	1.17	1.04
107	8.40×10^{11}	8.67×10^{11}	1.03
117	5.88	6.03	1.03
127	3.76	4.00	1.06
137	2.76	2.17	0.79
147	1.34	1.13	0.84
157	4.10×10^{10}	2.77×10^{10}	0.67

for comparison as well as the ratio of the neutron flux measured by the two methods. Noteworthy is the excellent agreement (within an average of 4 percent) between the two flux values in the region of 67 cm and 127 cm from the reactor centerline. Examination of the excitation functions for rhodium and for cobalt (89) revealed a strong resonance absorption at one eV neutron energy for rhodium whereas cobalt did not have an absorption resonance below 100 eV. Enrichment of the neutron flux with epithermal neutrons would explain the higher indicated flux of the rhodium detector near the core in comparison to the cobalt activation measured flux at that location. Correction for the influence of the neutron spectrum on the indicated flux by the rhodium detector was made in the calculation of the target fission rate during loop operation.

Analysis of the flux data from the flux wires placed at the four quadrants of the thimble outer surface indicated an average flux variation across the thimble diameter of 4 percent normal to the line-of-sight to the core center and 13 percent parallel to this direction. This means that a single value for the flux obtained with the rhodium detector attached to the target canister is not expected to be in error by more than 6 percent in comparison to the average neutron flux seen by the target volume. This is sufficiently precise for purposes of xenon production calculations.

The 1.35 grams of uranium-235 in the target represents 3.45×10^{21} atoms. The fission rate, R, is given by the following expression:

$$R = \phi\sigma N$$

where:

ϕ = neutron flux, n $cm^{-2}sec^{-1}$, or nv

σ = fission cross section, 5.82×10^{-22} cm^2

N = number of uranium-235 atoms

Therefore, for the loop target:

$$R = \phi(5.82 \times 10^{-22})(3.45 \times 10^{21})$$

$$= 2.01\phi \text{ fissions per second}$$

2.4 Insertion and Operation of the Xenon Loop

Pre-insertion Procedures. Prior to actual installation of the loop experiment into the reactor, the entire system was assembled and operated under the conditions anticipated to be representative of actual operation. The target canister was electrically heated externally to permit a check of the thermocouple function. The helium flow system, trapping system, and vacuum system were all checked for proper operation and freedom from leaks.

Insertion. The target canister was connected to the helium flow lines, thermocouples and rhodium neutron detector which had all been passed through the penetration in the special shield plug. The rhodium detector was attached to the helium inlet line where it passed by the target canister wall so as to have the detector in line with the center of the target volume.

The instrumented canister was then placed inside the aluminum thimble which was bolted to the inner face of the special shield plug. It was determined that when fully inserted inside the thimble that the centerline of the target canister was 8.5 cm from the end of the thimble.

This is equivalent to 15.5 cm from the reactor centerline (plane X-Y, Figure 31). When fully withdrawn against the shield plug (minimum flux position), the target canister centerline was 134 cm from the thimble end and 141 cm from the reactor centerline. A mechanical clamp had been designed and installed at the external end of the special shield plug to grasp the bundle of lines and leads from the target and prevent accidental movement of the target during operation. This was necessary to meet the requirements of the reactor operating license for experiments of substantial reactivity worth.

With the target canister installed in the thimble and the thimble bolted to the shield plug, the experimental assembly was inserted into the southern end of the horizontal tangent tube, H-11, of the GTRR on a non-operating day. The special shield plug replaced the standard shield plug normally inserted into H-11.

Connections were made with the trapping system (helium flow lines), the temperature indicator (thermocouple leads), and the electrometer (rhodium detector leads). The assembled and installed xenon loop apparatus is shown in Figure 61.

Operation. The reactor schedule during loop operation was a two-shift operation which gave a nominal operating day of 14 hours followed by approximately 10 hours of down time. It would have been much easier to evaluate the loop if the reactor had been operating continuously.

The calculated typical xenon-135 inventory in the loop under this reactor operating schedule is shown in Figure 62. Note that with the reactor shut down after 700 minutes of operation, the maximum xenon-135

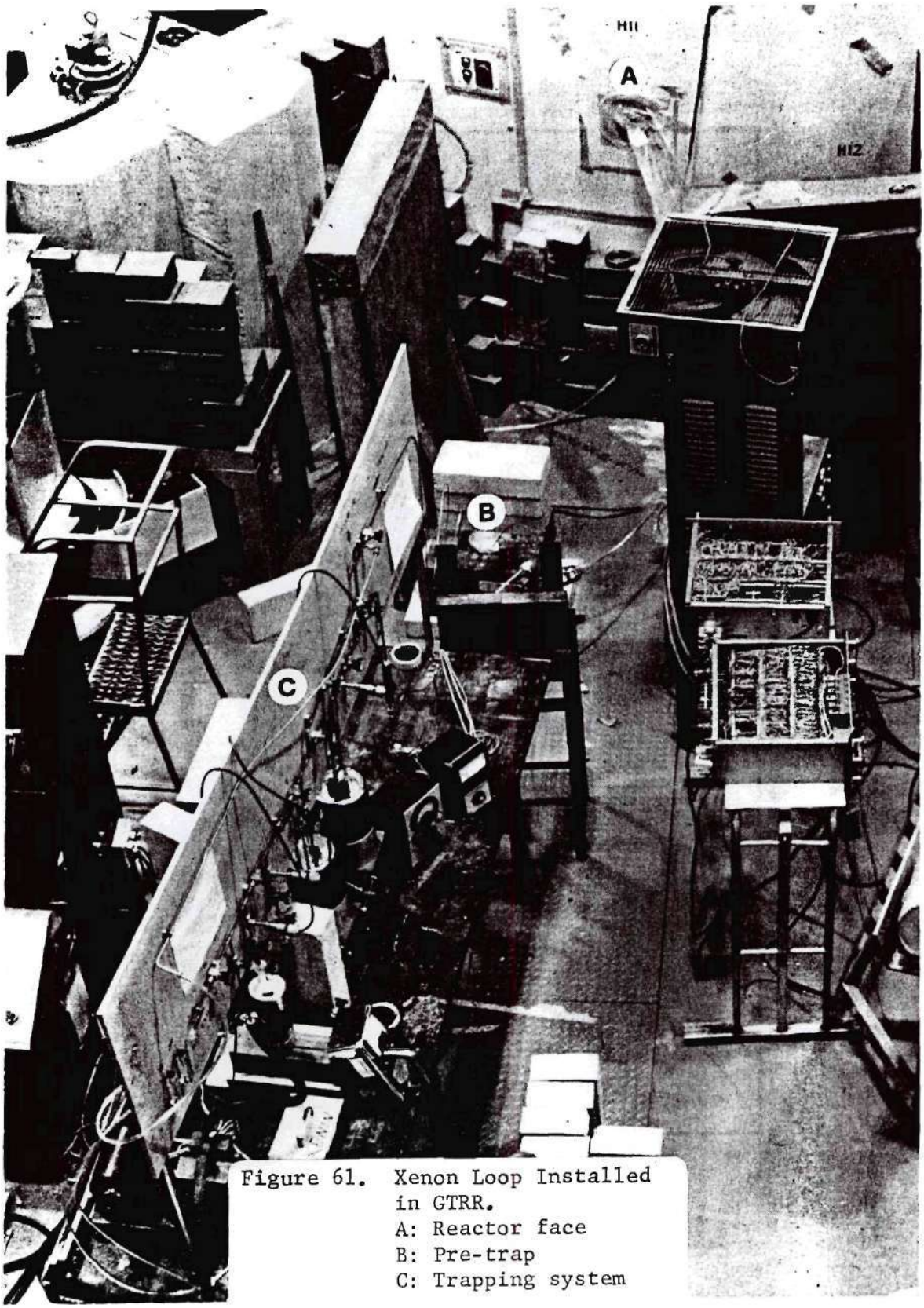

Figure 61. Xenon Loop Installed in GTRR.
A: Reactor face
B: Pre-trap
C: Trapping system

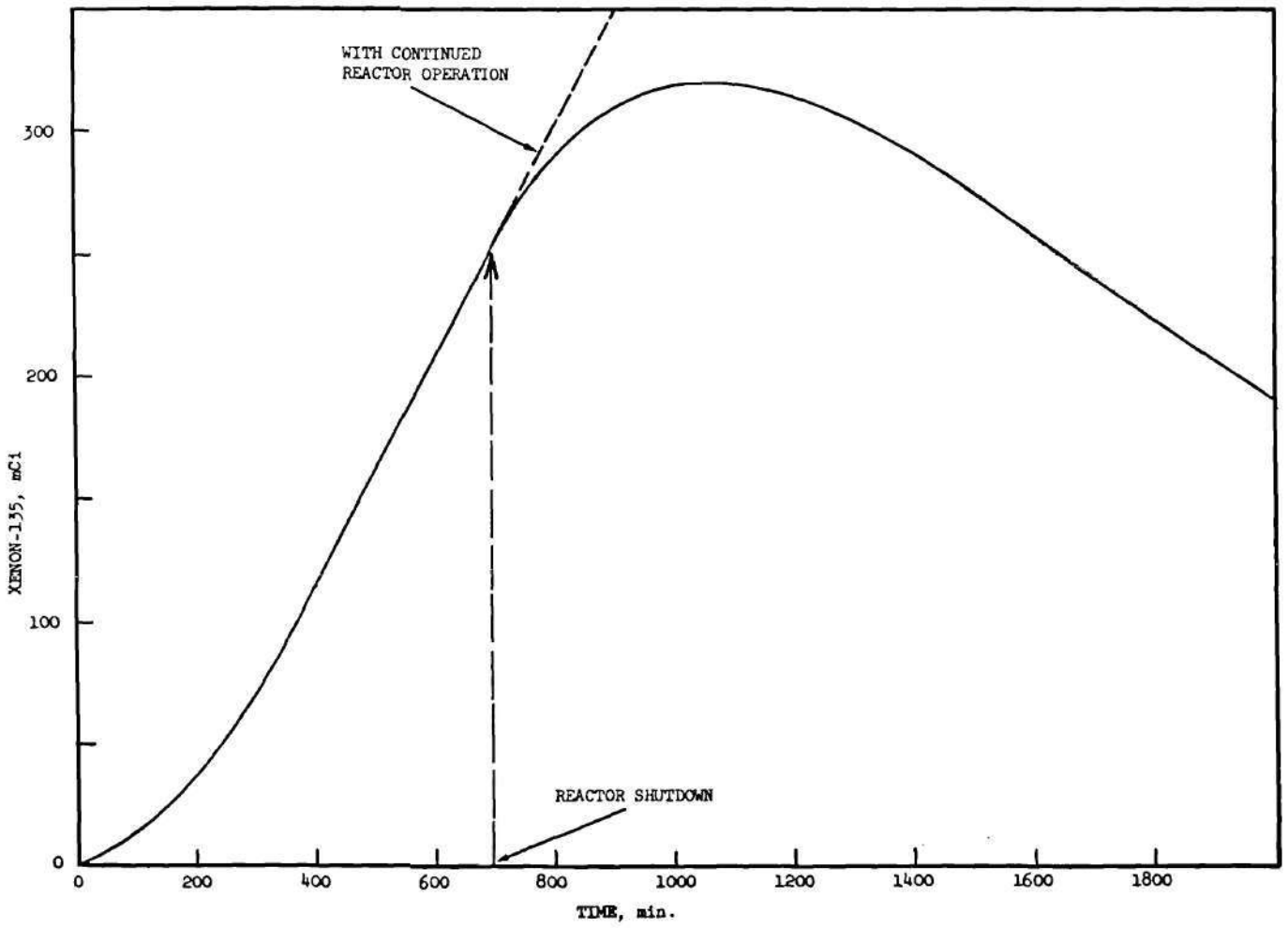

Figure 62. ^{135}Xe Loop Inventory Fluctuation During Two-Shift Reactor Operation

has not yet been reached. The calculations for this curve did not take into account burnup of xenon-135 by thermal neutron capture as a loss mechanism. If the probability of neutron capture, $\phi\sigma$, is examined, the effect of this removal mechanism at the low neutron flux used for this calculation (2.5×10^{11} nv) is negligible, i.e. only 2.4×10^{-3} $hour^{-1}$. This represents, where large numbers of atoms are involved, the fraction of xenon-135 atoms lost by neutron capture in this time period.

The following procedure was used in the operation and evaluation of the xenon reactor loop experiment:

1. Position the target canister in location for desired neutron flux prior to reactor startup.

2. Monitor target temperature during reactor startup to insure that the temperature does not exceed 550°C.

3. Maintain liquid nitrogen coolant levels in pre-trap and in both xenon collection traps during reactor operation and for 30 minutes after reactor shutdown. Maintain helium sweep gas flow rate at 40 cm^3 per minute.

4. Evacuate helium from target, pre-trap and xenon collection traps and close off valves to these components.

5. For 30 minutes prior to reactor startup the next day, flush target and warmed pre-trap into cooled xenon collection traps to recover previous day's production of xenon-135.

6. Isolate collection traps and storage cylinders and evacuate while maintaining liquid nitrogen cooling.

7. Cool storage cylinder with liquid nitrogen and warm collection

trap to cause transfer of xenon product to storage cylinder.

8. Isolate and disconnect storage cylinder. Remove to laboratory and count with calibrated 16 cm^3 Ge(Li) gamma-ray spectrometer system for determination of xenon-135 production.

The upper temperature limit of 550°C was based on the 660°C melting point of aluminum metal as well as the approximately 750°C melting point of the molecular sieves which make up the target material.

Each day of operation was termed a "run" and a daily revision of the system xenon-135 inventory was made, taking into account residual xenon-135 from preceding runs and the current production and release. The performance of the loop was, then, defined by the percent of the total xenon-135 inventory released from the target.

Gamma-ray spectra of the xenon product taken approximately 12 hours after reactor shutdown show the presence of small quantities of krypton-85m (4.4 hour half-life) and krypton-88 (2.8 hour half-life). No attempt was made to separate these krypton products from the xenon-135 since they did not interfere in the quantitative determination of the xenon isotope.

Table 25 summarizes the loop performance during the first six runs. After the initial four runs at minimum neutron flux, the target canister was repositioned at higher fluxes in order to evaluate the self-heating and radiation damage problems. The neutron flux was calculated from the rhodium detector readings and corrected for the neutron spectral effects noted in Table 24. The fission rate calculated from the corrected neutron flux value was then utilized in computing the xenon-135 production as described in Appendix B and in Chapter III.

Table 25. Xenon Reactor Loop Performance Summary

Run No.	Distance from Reactor Centerline (cm)	Temp. °C[a]	Thermal Neutron flux (nv)	Target Power (watts)[b]	Xenon-135 Inventory (mCi)	Xenon-135 Released (mCi)	Percent Xenon-135 Released	Target Cumulative Total Fissions
1	141	138	2.78×10^{11}	17	300	65	22	2.1×10^{16}
2	141	140	2.78×10^{11}	17	270	52	19	3.9×10^{16}
3	141	147	2.75×10^{11}	17	340	75	22	6.3×10^{16}
4	141	145	2.81×10^{11}	17	470	100	21	8.9×10^{16}
5	120	275	5.45×10^{11}	33	800	150	19	1.4×10^{17}
6	95	477[c]	1.16×10^{12}	74	1470	190	13	2.1×10^{17}

[a] Equilibrium temperature at target centerline

[b] Calculated from the equivalence: 3.3×10^{10} fissions per second per watt

[c] Temperature excursions during trial positioning of target. Target temperature exceeded 500 °C (indicated) with fast rise rate.

Run 6 was initially begun with the target canister at a location 68 cm from the reactor centerline. It was discovered that the fission heating at this location was too great for the target temperature to remain within the 550°C limit. The position of the target was adjusted until the location 95 cm from the reactor centerline was empirically shown to be satisfactory from the standpoint of equilibrium temperature. In the process of finding the flux which would provide an acceptable, but high operating temperature, the temperatures as indicated by the target centerline thermocouple went as high as 506°C. It is not known what the actual temperature of the uranium-containing individual molecular sieve beads may have been, but the rate of rise of the indicated temperature was greater than two degrees per minute when the reactor was shutdown to prevent further temperature rise.

Concurrently with the initial excessive temperature encounter, a release of water vapor from the molecular sieve target occurred. This temporarily caused a problem by plugging the pre-trap with ice which stopped the flow of helium sweep gas. The water vapor problem did not recur.

After these problems just described were alleviated, Run 6 was conducted. There was a significant reduction in the percent of the xenon-135 released in this run. To determine if this reduction were a result of damage to the target material, the target canister was pulled back to the minimum flux position against the inner end of the shield plug. This was the same location as previously used for Runs 1 through 4. Six more runs were made in this position with an average release of

only 5 percent of the total xenon-135 produced. This is only one-fourth of the original yield of xenon-135 at this location and target temperature. No further change in the fraction of xenon-135 released was detected in the conduct of the additional six runs.

Other observations of interest which were made during the operation of the loop were:

1. Flow of helium sweep gas at the normal rate of 40 cm^3 per minute provided a minimum of heat removal from the target canister. One measurement of the equilibrium temperature of the target centerline region with and without the helium flow demonstrated a 32°C lower equilibrium temperature with the helium flow on. These data were taken at a centerline temperature of 140°C (helium flow on).

2. The helium sweep gas emerging from the reactor carrying gaseous fission product was intensely radioactive. At a distance of 20 cm, using an ionization chamber survey instrument, the gamma-ray radiation levels were typically 150 mr hr^{-1}. It was noted that the rate of helium flow had a drastic effect on the radiation level from this one-eighth inch helium return line. The higher flow rates caused higher radiation levels. This is due to the presence of several short-lived (half-lives of seconds) fission gases in the helium flow from the irradiated target. Varying the flow rate changes the decay time between the source (the target canister) and the point at which the radiation level was monitored. The effect is displayed quantitatively in Figure 63. Decay of these short-lived fission products was measured with an ion chamber survey meter positioned near the pre-trap. The helium flow was interrupted and readings of the trap

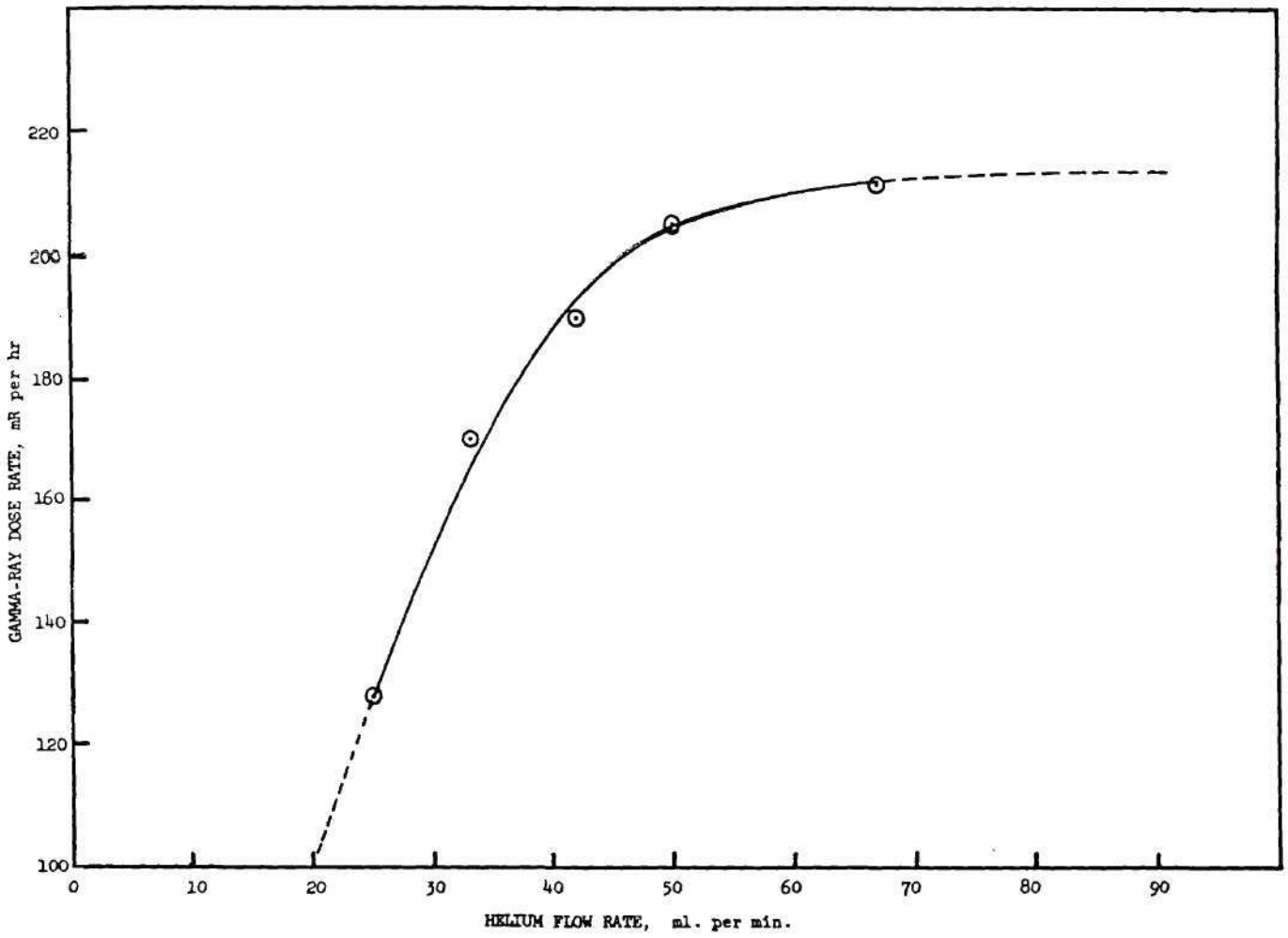

Figure 63. Gamma Dose Rate from Reactor Loop Helium Exit Line vs Flow Rate

radiation levels were taken periodically. The activity decayed with an apparent half-life of 34 minutes indicating that cesium-138 may have been the principal activity present in the trap. This was later verified by gamma-ray spectrometry.

3. The rate of rise of target temperature at the centerline location after the reactor reached one megawatt (maximum power) and the rate of decrease in target temperature after reactor shutdown were determined for Run 4 and Run 3, respectively, Figure 64 is a representation of these data.

4. The temperature difference from the highest reading at the target centerline to the outer thermocouple location was 11° at 140°C centerline temperature, 34° at 275°C centerline temperature, and 62° at 477°C centerline temperature.

5. Non-gaseous daughters of the gaseous fission products were deposited on the inner surfaces of the return helium line between the target and the pre-trap. A gamma-ray spectrum showed the presence of barium-140, lanthanum-140, strontium-91, yttrium-91m, cesium-138 and rubidium-88. All of these have gaseous xenon or krypton precursors. No iodine fission product activity was detected external to the reactor.

In order to learn more about the thermal stability of the uranium-loaded molecular sieves used in the target for this loop experiment, and thereby obtain data pertinent to the decrease in xenon release efficiency just described, the batch of depleted uranium-loaded Type 13X molecular sieve beads which were used for the neutron diffraction studies described in Chapter II were again studied. The earlier studies of these beads had

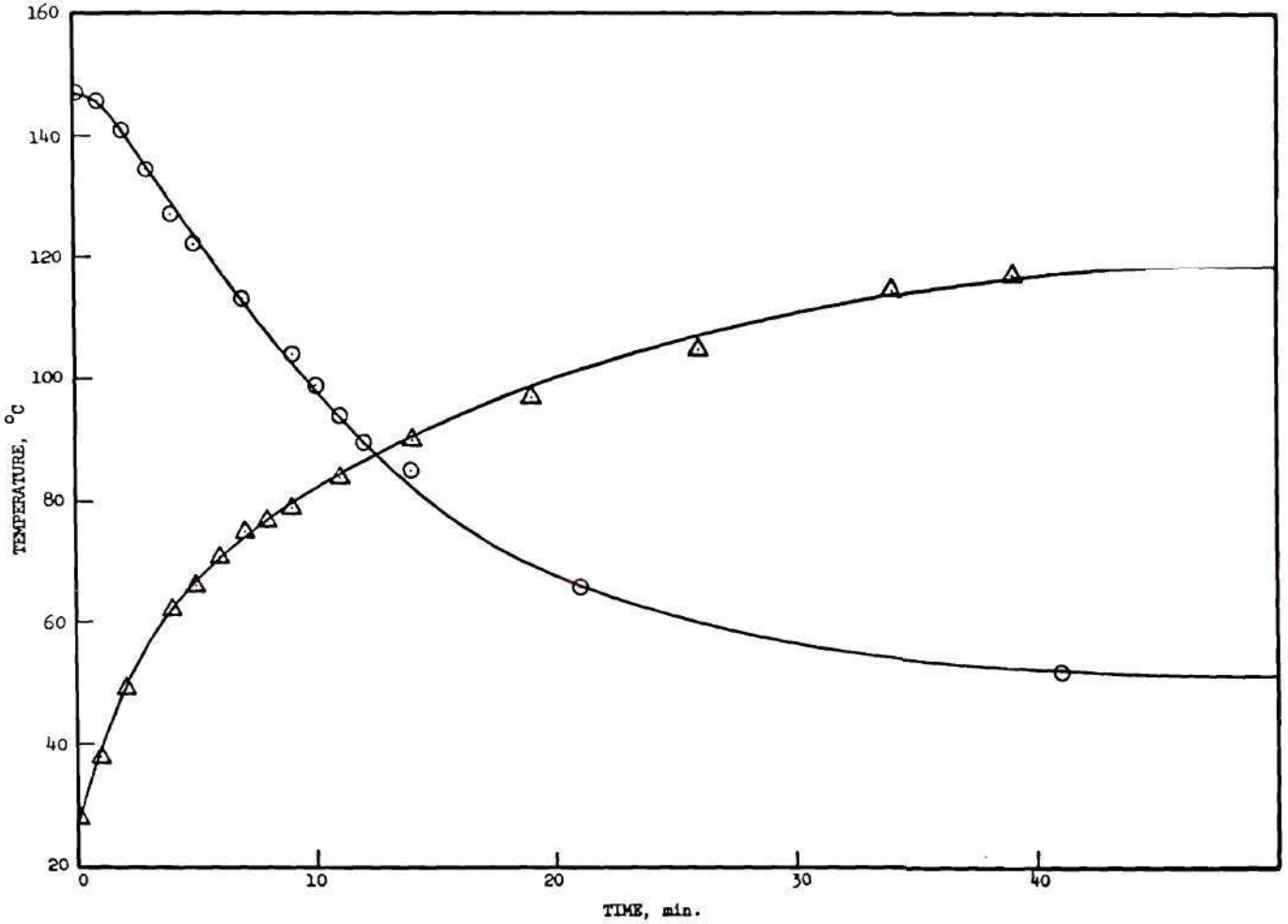

Figure 64. Loop Target Temperature Behavior
⊙ With Startup
△ After Shutdown

indicated no significant structural changes as a result of the uranium ion exchange or due to heating at 500°C. The same lot from which the the original neutron diffraction patterns were made was heated to 650°C for a period of one hour. Another neutron diffraction study was made and the results are shown in Figure 65 compared to the original pattern before heating to 650°C. It is significant that most of the features of the diffraction pattern have disappeared as a result of the heating to the higher temperature. This is indicative of a gross decrease of ordered structure within the molecular sieves.

Four months after removal of the loop target from the reactor, the radiation levels had decreased sufficiently due to fission product decay to permit safe disassembly of the canister for examination of the irradiated molecular sieves for evidence of damage. Almost all of the molecular sieve beads had either fractured or had developed fissures. No fine dust, however, was present. Examination of the fractured surface by the scanning electron microscope produced the photograph shown in Figure 66. The presence of the fused layer of former crystallites near the surface of the bead is additional evidence of the occurrence of excessive temperatures during the loop operation.

2.5 Conclusions

Measured releases of xenon-135 from the xenon reactor loop are consistent with the prior laboratory study results as described in Chapter III. Fission produced xenon-135 recovered from the irradiated uranium-loaded molecular sieve target installed within the reactor has been shown to be 20 percent of the total xenon-135 inventory. Continuous

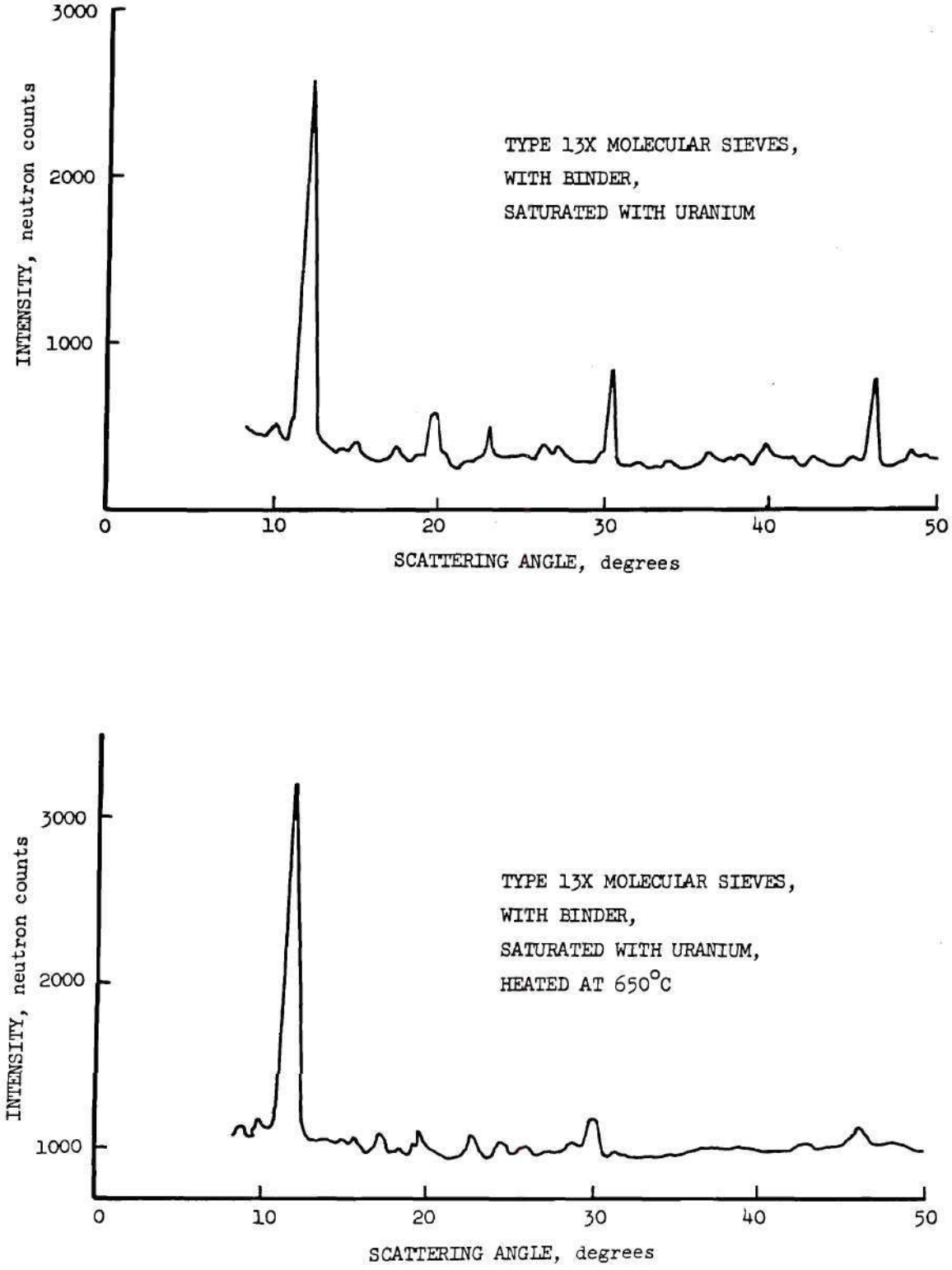

Figure 65. Effect of High Temperature on Neutron Diffraction Pattern of Uranium-Loaded Type 13X Molecular Sieves

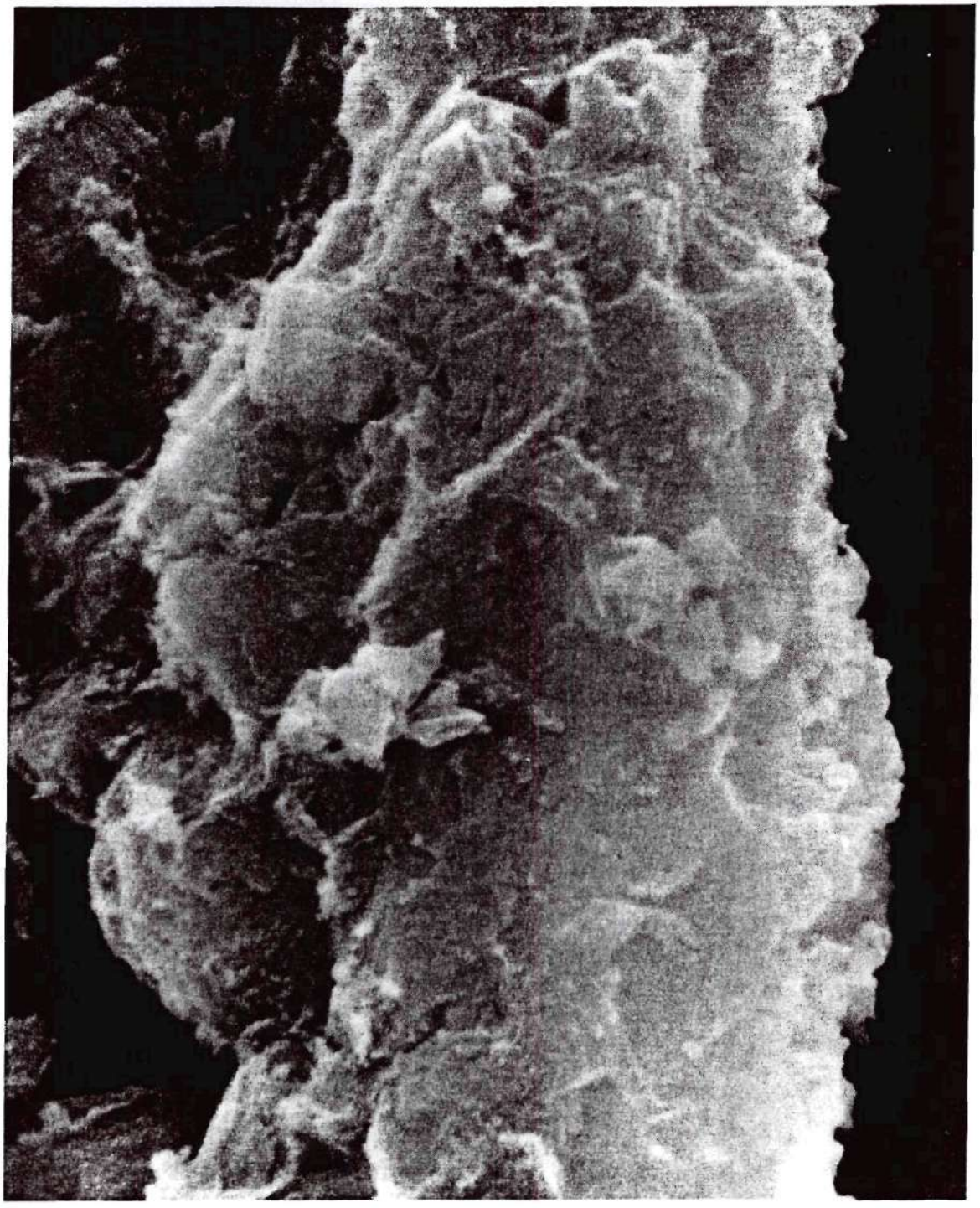

Figure 66. SEM Photograph Showing Damage to Irradiated Uranium-Loaded Molecular Sieve. Magnification: X18000

operation of the loop at high temperature would be expected to increase the fractional yield, but these conditions were not possible under the existing reactor operating schedule.

The primary limitation of the loop concept is the self-heating of the target by the fission process. The fission rate and, therefore, the xenon-135 production rate was restricted by the temperature tolerance of the system. The evidence gathered in this study indicates that at temperatures below 500°C there is no degradation of the xenon release fraction, but that at 650°C a drastic loss of crystallinity within the uranium-loaded molecular sieves occurs and may be responsible for a drastic reduction in the release of xenon fission gases.

No identifiable loss in loop performance directly attributable to radiation damage was seen. A total of 3.8×10^{17} fissions occurred in the target during the conduct of this evaluation.

CHAPTER V

EVALUATIONS AND RECOMMENDATIONS

The ability of the synthetic zeolites to incorporate uranium by ion exchange for sodium counterions in the three-dimensional Type X zeolite structure has been shown to be a practical method for the preparation of high surface area uranium targets. Targets of uranium-loaded molecular sieves can be prepared with a uranium content of greater than one milliequivalent of uranyl ion per gram of molecular sieve (greater than 10 percent uranium by weight).

After irradiation in the reactor thermal neutron flux, such targets were shown to be capable of releasing greater than 40 percent of the fission-produced xenon radionuclides.

The primary limitation of the uranium-loaded molecular sieve target material is temperature. Self-heating by the fission process increases the target temperature. Moderate temperatures will aid in the release of the xenon by diffusion processes, but temperatures in excess of $500^{\circ}C$ were shown to be capable of target damage by causing loss of crystallinity and a corresponding drastic reduction in the rate of xenon release.

The concept of the reactor loop incorporating the high surface area uranium target for the production of fission gas radionuclides has been proven practical. From the data gathered in the operation of this prototype apparatus, it can be recommended that the limitations imposed by self-heating may be minimized if a larger target volume containing

molecular sieves of a lower uranium-235 concentration were used. Future plans are to use the "isotope tunnels" which are 12 inch square ports passing beneath the GTRR core tank for such large volume, low flux irradiations. The estimated thermal neutron flux in these "isotope tunnels" is 5×10^{11} nv.

The development of another type high surface area target material of comparable xenon release efficiency, but having an improved high temperature tolerance, would be advantageous.

In addition to the previously stated uses for xenon-135 in medical diagnosis and other tracer applications, the ready availability of a supply of xenon-135 would permit the direct measurement of the exceptional thermal neutron cross section of this nuclide. If the most frequently quoted value of 2.7×10^{6} barns is used to calculate the burnout of xenon-135 at a thermal neutron flux of 10^{13} nv, it is found that the rate of xenon-135 loss by neutron absorption is approximately 10 percent per hour. This is comparable to the rate of loss by radioactive decay for this radioactive isotope. Such a burnout rate should be adequate for direct measurement of the absorption cross section by counting a sealed vial of xenon-135 before and after irradiation. The rate of xenon-135 disappearance in excess of the normal decay would be attributable to burnout. This promises to be an experimental technique capable of resolving the rather wide range of reported cross section values for this nuclide.

Although this study has concentrated exclusively on the xenon fission product gases, the concepts and methods described are applicable

to production of the krypton fission product nuclides, as well. Separation of the xenon and krypton gases has been described (98-100) and is rapid and relatively simple.

APPENDICES

APPENDIX A

ANALYTICAL PROCEDURES

Uranyl-peroxide Colorimetric Analysis (101)

1. Pipette a sample aliquot into a 50 ml volumetric flask.

2. Add 10 ml of 10 percent Na_2CO_3, 2 ml of 10 percent NaOH, and 1 ml of 10 percent H_2O_2 (all concentrations are wt/vol).

3. Dilute to approximately 40 ml and check pH. Adjust to pH 12, if necessary, with dilute NaOH.

4. Dilute to volume and mix well by shaking.

5. Read optical density at 400 millimicrons on the Coleman Junior Spectrophotometer.

6. Complete analysis by comparison of measured optical density of sample to standard curve prepared in same manner with known amounts of uranyl ion. Figure 67 is the standard curve used in these analyses. It represents the relationship:

$$\text{mg U per 50 ml} = 13.16(\text{Optical Density}) - 0.048$$

The regression coefficient for this set of data is 0.999.

Uranyl Determination with DPPD (102)

Reagents: DPPD solution--dissolve 1 gram DPPD (Eastman No. 2197) in 120 ml methanol.

Procedure: 1. Pipette aliquot of UO_2^{+2} solution to be analyzed

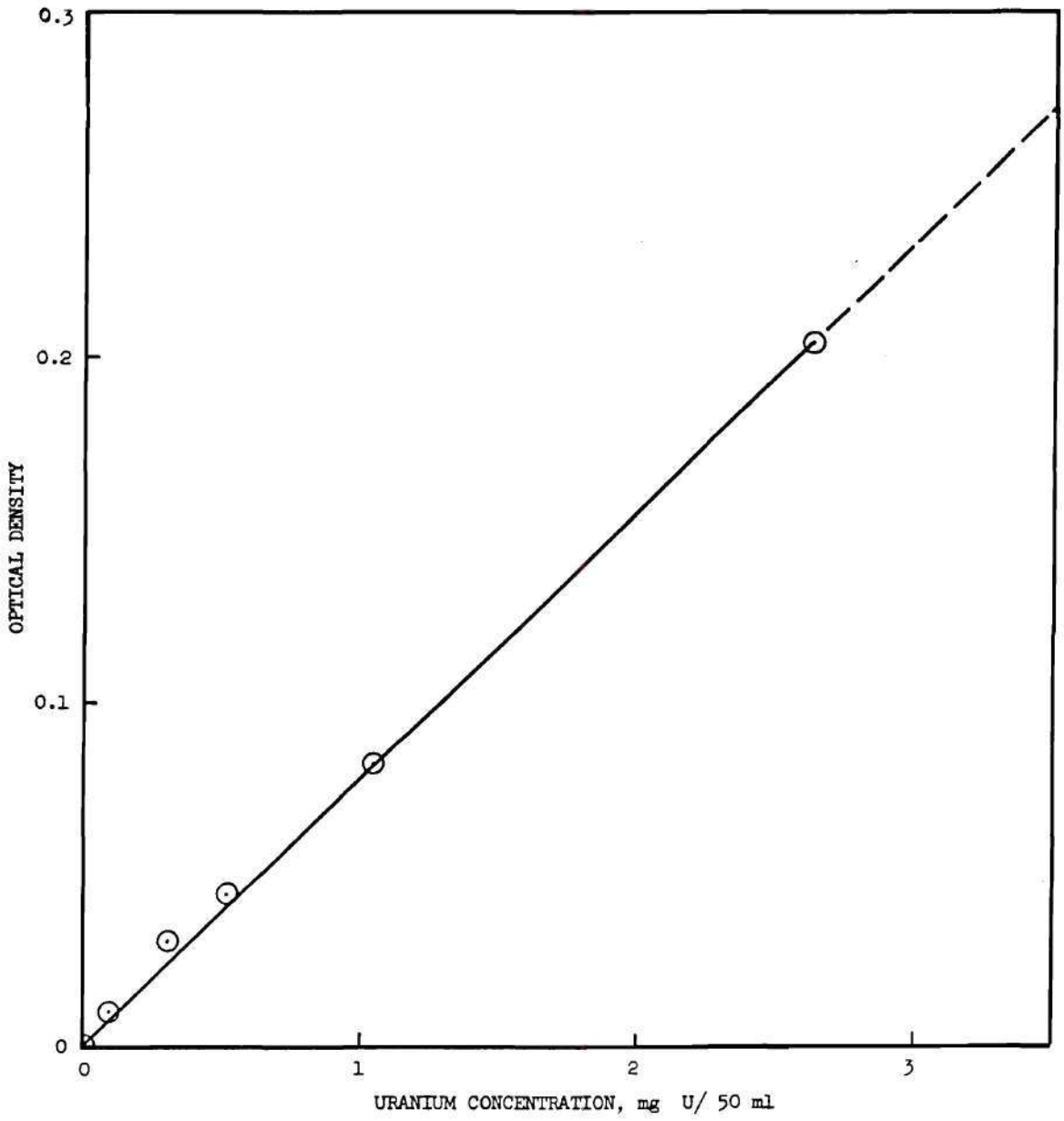

Figure 67. Standard Curve for Colorimetric Determination of UO_2^{+2} in Basic Peroxide Solution (2 cm Cell)

into 50 ml volumetric flask.

2. Add 30 ml methanol and 1 ml DPPD reagent solution.

3. Mix well and dilute to volume with methanol.

4. Read absorbance at 400 millimicrons in 1 cm pathlength Pyrex cells on a Beckman Model DU spectrophotometer versus a blank prepared by the same procedure without UNH.

The useful range for the method is 0.01 - 0.2 mg uranium. The standard curve is linear in this range of uranium (Figure 68) and is represented by the expression:

$$\text{mg U per 50 ml} = \frac{\text{absorbance}}{1.602} + 0.000$$

The regression coefficient for the least-squares fit to this standard curve is 0.998.

Neutron Activation Analysis Procedure

Samples were weighed or pipetted into two-fifths dram polyethylene vials and the vials heat-sealed to prevent leakage. Portions of suitable standards for sodium and/or uranium, previously prepared, were packaged in the same manner. Using the pneumatic transfer systems of the Georgia Tech Research Reactor (GTRR), the samples and standards were irradiated for 10 minutes at thermal neutron flux of 8×10^{12} neutrons per square cm per second (n $cm^{-2}sec^{-1}$). After approximately 15 hours decay, the irradiated samples and standards were counted on a 16 cc lithium-drifted germanium Ge(Li) gamma-ray detector coupled to a 1024-channel Nuclear Data pulse height analyzer. The neutron irradiation induced radioactive

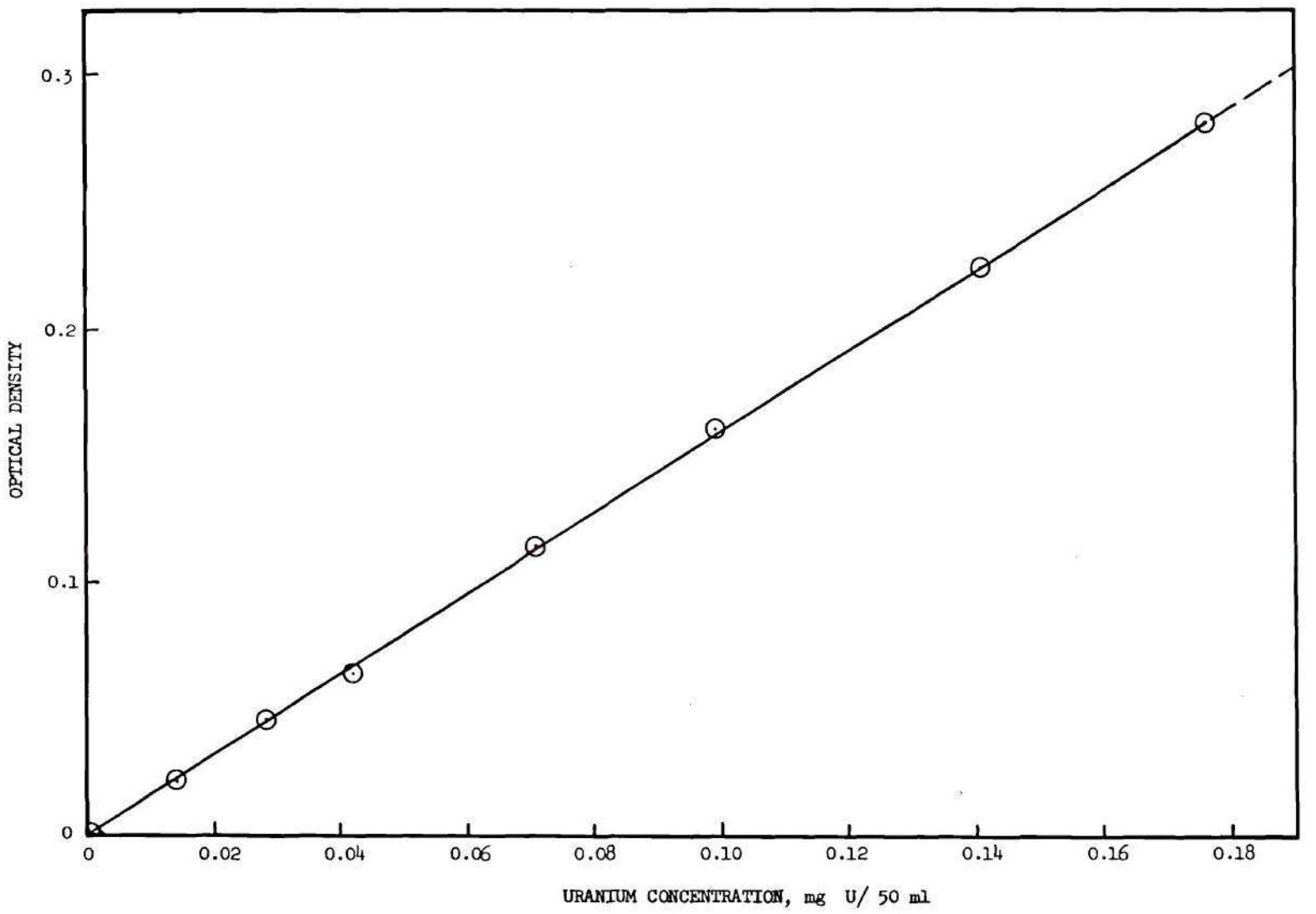

Figure 68. Standard Curve for Colorimetric Determination of UO_2^{+2} in Methanol Solution with Diphenylpropanedione (1 cm Cell)

sodium-24 and neptunium-239 from the sodium and uranium content, respectively. The nuclear reactions responsible for the generation of these radionuclides are:

$$^{23}\text{Na}\ (n,\gamma)\ ^{24}\text{Na}\left[\text{Half-life} = 15\ \text{h}\right]$$

$$^{238}\text{U}\ (n,\gamma)\ ^{239}\text{U} \xrightarrow[\text{half-life} = 23\ \text{m}]{\beta^-} {}^{239}\text{Np}\left[\text{Half-life} = 2.3\ \text{d}\right]$$

Sodium-24 gamma-rays of 1.368 MeV and 0.278 MeV gamma-rays from neptunium-239 were selected for quantitation from the gamma-ray spectra of the irradiated samples and standards. After appropriate decay corrections, the gamma-ray emission rates for these two energies in the samples when compared to the standards gave the quantitative data required for determination of the sodium and uranium contents of the samples.

APPENDIX B

DERIVATION OF FISSION PRODUCT DECAY CHAIN EQUATIONS

The process of nuclear fission of the uranium-235 atom by thermal neutron absorption normally results in two neutron-rich fission fragment nuclei. That is a way of expressing the fact that these primary fragment nuclei from the fission process have a high ratio of neutrons to protons which makes them unstable to decay by negatron emission. Such beta decay reduces the neutron:proton ratio and several successive beta decays may occur before a stable configuration is attained.

An example of a typical fission product decay chain may be represented by*:

$$\underset{Z}{\overset{N}{\overset{A}{\mathbf{A}}}} \xrightarrow{\lambda_1} \underset{Z+1}{\overset{N-1}{\overset{A}{\mathbf{B}}}} \xrightarrow{\lambda_2} \underset{Z+2}{\overset{N-2}{\overset{A}{\mathbf{C}}}} \xrightarrow{\lambda_3} \underset{Z+3}{\overset{N-3}{\overset{A}{\mathbf{D}}}}$$

(primary fission product) (stable)

where

N = number of neutrons in nucleus

Z = number of protons in nucleus (atomic number)

A = nuclear mass (mass number)

λ_i = decay constant, $\ell n\ 2$/half-life

During the exposure of a sample of uranium-235 to a constant neutron flux (a steady fission rate), the initial member of such a chain will

*The derivations given in this appendix are based on similar treatments by Benedict and Pigford (103).

be formed at a rate, P, and the net rate of change of the number of A atoms in the irradiated sample will be the rate of production less the rate of decay:

$$\frac{dN_1}{dt} = P - \lambda_1 N_1 \qquad (1)$$

where

N_1 = number of atoms of A, or first member of the decay chain.

The rate of production of the second member of the decay chain, B, is simply the rate of decay of A, and the net rate of change in the number of B atoms is:

$$\frac{dN_2}{dt} = \lambda_1 N_1 - \lambda_2 N_2 \qquad (2)$$

where

N_2 = number of atoms of B, or second member of decay chain.

In a like manner, the rate of production of the third member of the chain, C, is:

$$\frac{dN_3}{dt} = \lambda_2 N_2 - \lambda_3 N_3 \qquad (3)$$

where

N_3 = number of atoms of C, or third member of decay chain.

The increase in the number of atoms of the final member of the decay chain, D, being stable, can be given by:

$$\frac{dN_4}{dt} = \lambda_3 N_3 \qquad (4)$$

where

N_4 = number of atoms of D, or final (stable) product of decay chain.

If the irradiation is long in comparison to the half-lives of the members of the decay chain, a steady-state condition will be reached in which case the rates of formation will be equal to the rates of decay for each member of the chain, or $\frac{dN}{dt} = 0$, and

$$N_1^* = \frac{P}{\lambda_1} \tag{5}$$

$$N_2^* = \frac{\lambda_1 N_1^*}{\lambda_2} \quad \text{or} \quad N_2^* = \frac{P}{\lambda_2} \tag{6}$$

$$N_3^* = \frac{\lambda_2 N_2^*}{\lambda_3} \quad \text{or} \quad N_3^* = \frac{P}{\lambda_3} \tag{7}$$

Under the normal experimental conditions, where the uranium-235 sample contains no fission products at the beginning of the irradiation, and the initial member of the decay chain, A, is formed at a steady rate of P atoms per unit time, the expression for the quantities of each member of the decay chain present in the uranium sample after irradiation time T may be found by integration of equations (1) through (4) within the boundary conditions that N=0 at t=0 for each chain member. The results are:

$$N_1(T) = \frac{P}{\lambda_1}\left(1 - e^{-\lambda_1 T}\right) \tag{8}$$

$$N_2(T) = \lambda_1 P\left[\frac{1-e^{-\lambda_1 T}}{\lambda_1(\lambda_2-\lambda_1)} + \frac{1-e^{-\lambda_2 T}}{\lambda_2(\lambda_1-\lambda_2)}\right] \tag{9}$$

$$N_3(T) = \lambda_1\lambda_2 P \left[\frac{1-e^{-\lambda_1 T}}{\lambda_1(\lambda_2-\lambda_1)(\lambda_3-\lambda_1)} + \frac{1-e^{-\lambda_2 T}}{\lambda_2(\lambda_1-\lambda_2)(\lambda_3-\lambda_2)}\right. \tag{10}$$

$$\left. + \frac{1-e^{-\lambda_1 T}}{\lambda_3(\lambda_1-\lambda_3)(\lambda_2-\lambda_3)}\right]$$

Knowing the total production, PT, and the numbers of atoms of each intermediate member of the chain, the number of atoms of the final, stable chain member can be expressed by:

$$N_4 = PT - (N_1 + N_2 + N_3) \tag{11}$$

If the general case is considered for a radioactive decay chain where the first member is produced at a steady rate P and the other members are formed by precursor decay only, i.e.

$$N_1 \longrightarrow N_2 \longrightarrow N_3 \longrightarrow N_4 \longrightarrow \cdots \longrightarrow N_j \longrightarrow \cdots \longrightarrow N_i \longrightarrow \cdots$$

where no atoms of the decay chain are present at time zero, the number of atoms of the i^{th} chain member at time T can be arrived at by the general expression:

$$N_i = \lambda_1\lambda_2 \cdots \lambda_{i-1} P \sum_{j=1}^{i} \frac{1-e^{-\lambda_i T}}{\lambda_j \prod_{k\neq j} (\lambda_k-\lambda_j)} \tag{12}$$

All the foregoing derivations have ignored the decay of the decay chain members once the production has been terminated by removal of the uranium-235 fission source from the neutron flux. At decay time t after removal, the number of A atoms, $N_1(T,t)$, is obtained by applying the normal

radioactive decay relationship:

$$N_1(T,t) = N_1(T)e^{-\lambda_1 t} \tag{13}$$

If this expression is combined with equation (8), the following expression for the number of B atoms, after irradiation time T and decay time t, emerges:

$$N_1(T,t) = \frac{P}{\lambda_1}\,(1 - e^{-\lambda_1 T})e^{-\lambda_1 t} \tag{14}$$

Upon removal from the reactor or other source of neutron flux (t=0) the number of B atoms, $N_2(T)$ begins to decrease according to:

$$N_{2,2}(T,t) = N_2(T)e^{-\lambda_2 t} \tag{15}$$

Substitution of equation (9) for $N_2(T)$ gives:

$$N_{2,2}(T,t) = \lambda_1 P \left[\frac{1-e^{-\lambda_1 T}}{\lambda_1(\lambda_2-\lambda_1)} + \frac{1-e^{-\lambda_2 T}}{\lambda_2(\lambda_1-\lambda_2)}\right] e^{-\lambda_2 t} \tag{16}$$

While the B atoms present at t=0 have been decaying as described in equation (16) since removal from the neutron flux, more B atoms were formed from decay of A atoms. This contribution to the total number of B atoms is given by:

$$\frac{dN_2}{dt} = \lambda_1 N_1 - \lambda_2 N_2 \tag{17}$$

Integration of equation (17) for the boundary conditions $N_2=0$ at $t=0$ gives the following equation describing the contribution to B atoms at time t by A atoms decaying after removal of the sample from the neutron flux:

$$N_{2,1}(T,t) = \frac{\lambda_1 N_1(T)}{\lambda_2-\lambda_1} (e^{-\lambda_1 t} - e^{-\lambda_2 t}) \tag{18}$$

Substituting the value of N_1 as given by equation (8):

$$N_{2,1}(T,t) = \frac{P}{\lambda_2-\lambda_1} (1-e^{-\lambda_1 T})(e^{-\lambda_1 t} - e^{-\lambda_e t}) \tag{19}$$

The total number of B atoms, $N_2(T,t)$, is the sum of the number remaining from those present at the time of removal from the neutron flux ($t=0$) and those formed by precursor A decay:

$$N_2(T,t) = N_{2,2}(T,t) + N_{2,1}(T,t) \tag{20}$$

Substitution of equations (16) and (19) for the appropriate terms on the right side of equation (20), and simplifying, gives:

$$N_2(T,t) = \lambda_1 P \left[\frac{(1-e^{-\lambda_1 T})e^{-\lambda_1 t}}{\lambda_1(\lambda_2-\lambda_1)} + \frac{(1-e^{-\lambda_2 T})e^{-\lambda_2 t}}{\lambda_2(\lambda_1-\lambda_2)}\right] \tag{21}$$

A similar combination of the expressions for the number of C atoms at time t, $N_3(T,t)$, and subsequent simplification gives:

$$N_3(T,t) = \lambda_1\lambda_2 P \left[\frac{(1-e^{-\lambda_1 T})e^{-\lambda_1 t}}{\lambda_1(\lambda_2-\lambda_1)(\lambda_3-\lambda_1)} + \frac{(1-e^{-\lambda_2 T})e^{-\lambda_2 t}}{\lambda_2(\lambda_1-\lambda_2)(\lambda_3-\lambda_2)}\right. \tag{22}$$

(continued)

$$+ \frac{(1-e^{-\lambda_3 T})e^{-\lambda_3 t}}{\lambda_3(\lambda_1-\lambda_3)(\lambda_2-\lambda_3)}\Bigg]$$

Examination of the results of continuations of these derivations for longer decay chains reveals the general equation:

$$N_i(T,t) = \lambda_1\lambda_2 \cdots \lambda_{i-1} P \sum_{j=1}^{i} \frac{(1-e^{-\lambda_i T})e^{-\lambda_i t}}{\lambda_j \prod_{k\neq j} (\lambda_k-\lambda_j)} \qquad (23)$$

APPENDIX C

DEVELOPMENT OF DIFFUSION EQUATION FOR SPHERE

Barrer (104) has elaborated on the various solutions to Fick's Law of Diffusion. Equation (24) is the appropriate expression of the diffusion equation for the case of isotropic spherically symmetrical diffusion.

$$\frac{\partial C}{\partial t} = D\left(\frac{\partial^2 C}{\partial r^2} + \frac{2}{r}\frac{\partial C}{\partial r}\right) \tag{24}$$

where

D = diffusion coefficient

C = concentration of adsorbed material

t = time

r = radius of spherical particle

For the case where concentration of adsorbed material is constant throughout the sphere at t=0, the quantity adsorbed or desorbed per unit surface area, q, may be found by appropriate differentiation and integration to give:

$$q = \frac{(C_2 - C_0)r}{3}\left(1 - \frac{6}{\pi^2}\sum_{n=1}^{\infty}\frac{1}{n^2}\exp\left[-\frac{Dn^2\pi^2 t}{r^2}\right]\right) \tag{25}$$

where

C_0 = initial concentration in the sphere

C_2 = concentration at the sphere surface

The total amount Q adsorbed at any time is then:

$$Q = \frac{4\pi r^3 (C_2 - C_0)}{3} \exp\left[-\frac{Dn^2\pi^2 t}{r^2}\right] \tag{26}$$

Accordingly, the expression for fractional attainment of equilibrium adsorption or desorption, f, as given by Boyd, et al. (105) is:

$$f = \frac{Q}{Q_\infty} \tag{27}$$

where

Q_∞ = amount adsorbed or desorbed at equilibrium, i.e., $t = \infty$

Appropriate substitution of equation (26) into equation (27) gives:

$$f = 1 - \frac{6}{\pi^2} \sum_{n=1}^{\infty} \frac{1}{n^2} \exp(-n^2\pi^2 Dt/r^2) \tag{28}$$

In the systems of concern in this study, the spherical diffusion model is appropriate for both the molecular sieve beads and the individual zeolite crystallites (a close approximation in the case of the octahedral crystallites).

Booth and Rymer (106) have proposed solutions to equation (28) appropriate to the diffusion processes involved in xenon release or uranyl ion exchange.

When Dt/r^2 is equal to or greater than unity (equivalent to $f \geq 0.77$), the first term in the series expansion of equation (24) is a good approximation of the value of f, i.e.

$$f = 1 - \frac{6}{\pi^2} \exp(-\pi^2 Dt/r^2) \tag{29}$$

When $\pi^2 Dt/r^2$ is less than one (f less than 0.77), this approximation no longer is valid and an appropriate approximation can be obtained by the fact that, for small values of x, the sum (106):

$$1 + 2 \sum_{n=1}^{\infty} e^{-n^2 x} \equiv \sum_{n=-\infty}^{+\infty} e^{-n^2 x} \tag{30}$$

and is essentially equivalent to the integral,

$$\int_{-\infty}^{+\infty} e^{-xu^2} \, du = \sqrt{\frac{\pi}{x}} \tag{31}$$

Substituting the value of this integral into equation (30) gives:

$$\sum_{n=1}^{\infty} e^{-n^2 x} \approx \frac{1}{2} \left(\sqrt{\frac{\pi}{x}} - 1 \right) \tag{32}$$

Integration of both sides of equation (32) with respect to x from zero to K gives:

$$\sum_{n=1}^{\infty} \left(\frac{1 - e^{-n^2 K}}{n^2} \right) \approx \sqrt{\pi K} - \frac{K}{2} \tag{33}$$

from which

$$1 - \frac{6}{\pi^2} \sum_{n=1}^{\infty} \frac{1}{n^2} \cdot \exp(-n^2 K) \approx \frac{6}{\pi^2} \left(\sqrt{\pi K} - \frac{K}{2} \right) \tag{34}$$

Replacement of K by $\pi^2 Dt/r^2$ gives:

$$f = \frac{6}{r}\sqrt{\frac{Dt}{\pi}} - \frac{3\,Dt}{r^2} \qquad \text{when} \qquad \left[\frac{\pi^2 Dt}{r^2} \leq 1\right] \tag{35}$$

The second term on the right side of equation (35) becomes negligible for values of $\pi^2 Dt/r^2$ less than about 0.01 ($f = 0.105$). This equation is of the form which gives a straight line plot for small values of f when a graph of the fraction released or adsorbed by diffusion-controlled processes from spherical particles is plotted against $t^{\frac{1}{2}}$. The slope of this line is $\frac{6}{r}\,(D/\pi)^{\frac{1}{2}}$.

Using the measured slope of the plot of fractional gas release or ion exchange equilibrium attained versus $t^{\frac{1}{2}}$, the value of D may be determined. This apparent or effective diffusion coefficient is an expression of the rate of diffusion, but does not imply any mechanism for the diffusion process. For example, in ion exchange processes, the diffusional transport of ions into and from the exchange sites may be influenced by the generation of an electric potential gradient if the ions concerned exhibit differing mobilities (107). The effect of such an electric field on the diffusion of ions is quantitatively expressed by the Nernst-Planck equations which must be used if absolute values of the diffusion coefficient are sought. This was not an objective of this study.

BIBLIOGRAPHY*

1. P. Johnson, Radioisotope Tracers in Industry and Geophysics, Symposium Proceedings, Prague, 1966, p. 615, IAEA, Vienna (1967).

2. P. M. Grant, G. E. Miller, and F. S. Rowland, Report No. 1971-1, University of California (Irvine), (1971).

3. C. M. Lederer, J. M. Hollander, and I. Perlman, Table of Isotopes, 6th Edition, John Wiley and Sons, New York (1967).

4. Chart of the Nuclides, USAEC, Division of Isotope Development (1968).

5. E. Kondiah, N. RanaKumar, and R. W. Fink, USAEC Contractor Report ORO-3346-20 (1968); Nucl. Phys., A120, No. 2, p. 329 (1968).

6. K. Fritze and R. Robertson, Radiochim. Acta, 9, No. 4, p. 221 (1968).

7. S. J. Lyle and J. Sellars, Radiochim. Acta, 10, No. 3/4, p. 160 (1968).

8. M. T. Newhouse, et al., Respiration Physiology, 4, p. 141 (1968).

9. F. N. Case and E. H. Acree, USAEC Contractor Report ORNL-3840 (1966).

10. A. C. Wahl and N. A. Bonner, Radioactivity Applied to Chemistry, John Wiley and Sons, New York, p. 284 (1951).

11. N. P. Archer, Decay Characteristics of ^{138}Xe, Ph.D. Thesis, McMaster University, Canada (1965).

12. N. P. Archer and G. L. Keech, Can. J. Phys., 44, p. 1823 (1966).

13. D. Chleck, et al., Nucleonics, 21, No. 7, p. 53 (1963).

14. S. Ahrland, I. Grenthe, and B. Noren, Acta Chem. Scand., 14, p. 1059 (1960).

*The abbreviations used herein follow the form used in Nuclear Science Abstracts as listed in Appendix II, V. 26, No. 1 (1972) of that publication.

BIBLIOGRAPHY (Continued)

15. J. A. Knight, Jr., personal communication.

16. B. G. Harvey, Introduction to Nuclear Physics and Chemistry, Prentice Hall, Englewood Cliffs, N. J., p. 202 (1962).

17. F. I. Stubbs, P. J. Russell, and G. N. Walton, AERE (England) Report AERE-R2983 (1959).

18. H. J. Jenny, USAEC Report M-2294 (1945).

19. C. J. Rodden, Editor, Analytical Chemistry of the Manhattan Project, National Nuclear Energy Series, VIII-1, McGraw-Hill, New York, p. 523 (1950).

20. A. C. Graves and D. K. Froman, Miscellaneous Physical and Chemical Techniques of the Los Alamos Project, National Nuclear Energy Series, V-3, McGraw-Hill, New York, p. 22 (1952).

21. G. T. Seaborg; et al., The Transuranium Elements, Vol. 2, IV-14B, National Nuclear Energy Series, McGraw-Hill, New York, pp. 148, 1167 (1949).

22. G. T. Seaborg and J. J. Katz, The Actinide Elements, IV-14A, National Nuclear Energy Series, McGraw-Hill, New York, p. 705 (1954).

23. E. H. Fleming, Jr., et al., Phys. Rev., 83, p. 642 (1952).

24. H. D. Smyth, Atomic Energy for Military Purposes, Princeton University Press, Princeton, N. J. (1945).

25. G. R. Choppin, Experimental Nuclear Chemistry, Prentice-Hall, Englewood Cliffs, N. J., p. 136 (1961).

26. P. H. Emmett, Editor, Catalysis, Vol. I, Reinhold, New York, p. 341 (1954).

27. Technical Bulletin No. 303, Davison Granular Silica Gels, Davison Chemical Division, W. R. Grace and Company, Baltimore, Md. (1968).

28. C. J. Plank, U. S. Patent 2,499,680 (1950).

29. O. Samuelson, L. Lunden, and K. Schramm, Z. Anal. Chem., 140, p. 330 (1953).

30. C. D. Amphlett, Inorganic Ion Exchangers, Elsevier, New York, p. 89 (1964).

BIBLIOGRAPHY (Continued)

31. S. E. Ermatox, Izv. Akad. Nauk Kaz. SSR, Ser. Fiz.-Mat. Nauk, No. 4, p. 48 (1964).

32. B. C. Larson, G. W. Gibbs, and H. D. Bale, Bull. Amer. Phys. Soc., Series 2, 2, No. 4, p. 460 (1966).

33. G. Dalmai, et al., Silicate Industry, 29, No. 2, p. 43 (1964).

34. V. V. Gromov and V. I. Spitsyn, At. Energ. (USSR), 14, No. 5, p. 491 (1963).

35. G. Dalmai, B. Imelik, and M. Seguin, J. Chim. Phys., 58, p. 292 (1961).

36. C. K. Hersh, Molecular Sieves, Reinhold, New York, p. 2 (1961).

37. Ibid., p. 21.

38. F. C. Nachod and J. Schubert, Editors, Ion Exchange Technology, Academic Press, New York, p. 3 (1956).

39. O. Samuelson, Ion Exchange in Analytical Chemistry, John Wiley and Sons, New York, p. 18 (1963).

40. R. Gans, U. S. Patents 914,405 (1909); 943,535 (1909); and 1,131,503 (1915).

41. C. K. Hersh, op. cit., p. 34.

42. Ibid., p. 8.

43. F. Daniels, Outlines of Physical Chemistry, John Wiley and Sons, New York, p. 550 (1954).

44. J. W. McBain, Colloid Symposium Monograph, 4, p. 7 (1926).

45. Technical Booklet, Linde Molecular Sieves, Linde Division, Union Carbide Corporation, New York.

46. H. S. Sherry, "The Ion Exchange Properties of Zeolites" in Ion Exchange (J. A. Marinsky, Editor), Vol. 2, Chapter 3, Dekker, New York (1966).

47. R. A. LaBine, Chem. Eng., 66, No. 16, p. 104 (1959).

48. H. S. Sherry, J. Phys. Chem., 72, p. 4086 (1968).

BIBLIOGRAPHY (Continued)

49. L. Pauling, The Nature of the Chemical Bond, 3rd Edition, Cornell University Press, Ithaca, N. Y., p. 518 (1960).

50. R. C. Weast, Editor, Handbook of Chemistry and Physics, 46th Edition, Chemical Rubber, Cleveland, Ohio, p. F-117 (1965).

51. H. S. Sherry, J. Colloid Interface Sci., 28, No. 2, p. 288 (1968).

52. T. Moeller, Inorganic Chemistry, John Wiley and Sons, New York, p. 375 (1952).

53. S. V. Starodubtsev, et al., Radiats. Effekty v. Tverd. Telakh, Akad. Nauk USSR, Inst. Yadern. Fiz., p. 19 (1963).

54. H. T. J. Britten, Hydrogen Ions, 3rd Edition, Vol. II, Chapter XXIII, Chapman and Hall, London (1942).

55. Data Sheet, Linde Molecular Sieves as Cation Exchangers, No. ADL-87-101, Linde Division, Union Carbide Corporation, New York.

56. Linde Division, Union Carbide Corporation, New York, personal communication.

57. J. J. Katz and G. T. Seaborg, The Chemistry of the Actinide Elements, Methuen, London, p. 194 (1957).

58. R. K. Warner, Australian J. Appl. Sci., 4, p. 581 (1953).

59. P. C. Huang, A. Mizany, and J. L. Pauley, J. Phys. Chem., 68, No. 9, p. 2575 (1964).

60. V. M. Radak, J. Inorg. Nucl. Chem., 34, p. 1059 (1972).

61. W. F. Linke, Editor, Solubilities, Vol. II, American Chemical Society, p. 1081 (1965).

62. R. M. Barrer and L. Hinds, J. Chem. Soc., p. 1879 (1953).

63. R. M. Barrer and J. Falconer, Proc. Roy. Soc., A236, p.227 (1956).

64. E. Hoinkis and H. W. Levi, Proc. Conf. Ion Exchange in Chemical Process Industry, Soc. Chem. Ind., London, p. 339 (1970).

65. L. L. Ames, Amer. Mineral., 50, p. 465 (1965).

66. C. B. Amphlett, op. cit., p. 17.

BIBLIOGRAPHY (Continued)

67. Davison Chemical Division, W. R. Grace and Company, Baltimore, Md., personal communication.

68. H. Bateman, Proc. Cambridge Phil. Soc., 15, p. 423 (1910).

69. H. Farrar and R. H. Tomlinson, Nucl. Phys., 34, p. 367 (1962).

70. S. Glasstone and A. Sesonske, Nuclear Reactor Engineering, d. Van Nostrand, Princeton, N. J. (1963).

71. R. D. Evans, The Atomic Nucleus, McGraw-Hill, New York, p. 668 (1965).

72. Ibid., p. 669.

73. S. Katcoff, J. A. Miskel, and C. W. Stanley, Phys. Rev., 74, p. 631 (1948).

74. S. Glasstone and A. Sesonske, op. cit., p. 96.

75. W. B. Cottrell, et al., USAEC Contractor Report ORNL-2653, p. 111 (1959).

76. D. G. Hurst, AECL Report AECL-1550 (1962).

77. R. M. Carroll and O. Sisman, Nucl. Appl., 2, No. 2, p. 142 (1966).

78. J. R. McEwan and P. A. Morel, Nucl. Appl., 2, No. 2, p. 158 (1966).

79. A. Ong and T. S. Elleman, Nucl. Instrum. Methods, 86, p. 117 (1970).

80. D. W. Breck, J. Chem. Ed., 41, No. 12, p. 678 (1964).

81. W. J. Sesny and L. H. Shaffer, U. S. Patent 3,316,691 (1967).

82. S. Glasstone, Textbook of Physical Chemistry, 2nd Edition, d. Van Nostrand, New York, p. 268 (1946).

83. R. D. Evans, op. cit., p. 133.

84. L. Pauling, op. cit., p. 85.

85. C. M. Slansky, LOFT Chemical Development Assistance, Monthly Report November-December 1968, Idaho Nuclear Corporation, Idaho Falls, Idaho.

BIBLIOGRAPHY (Continued)

86. R. H. Filby, et al., Report No. WSUNRC-97(2), Washington State University, Pullman, Washington (1970).

87. E. A. Wolicki, R. Jastrow, and F. Brooks, Naval Research Laboratory Report NRL 4833 (1956).

88. National Bureau of Standards Report NSRDS-NBS 29 (1969).

89. D. J. Hughs and R. B. Schwartz, USAEC Contractor Report BNL-425 (1958).

90. M. R. Trammell and W. A. Henninger, USAEC Contractor Report WANL-TME-574, Revision 1 (1966).

91. M. Benedict and T. H. Pigford, Nuclear Chemical Engineering, McGraw-Hill, New York, p. 53 (1957).

92. S. Katcoff, Nucleonics, 18, No. 11, p. 201 (1960).

93. S. Katcoff, Nucleonics Data Sheet No. 24.

94. C. K. Hersh, op. cit., p. 38.

95. Ibid., pp. 45, 46.

96. D. Davies, G. Long, and W. P. Stanaway, AERE (England) Report AERE-R 4342 (1963).

97. H. S. Sherry, J. Phys. Chem., 70, p. 1332 (1966).

98. P. Amadesi and A. Cervellati, Nucl. Instrum. Meth., 33, p. 45 (1965).

99. R. C. Koch and G. L. Grandy, Anal. Chem., 33, p. 43 (1961); Nucleonics, 18, p. 76 (1960); USAEC Contractor Reports NSEC-7 (1957) and NSEC-12 (1958).

100. W. E. Browning and C. C. Bolta, USAEC Contractor Report ORNL-2116 (1956).

101. E. B. Sandell, Colorimetric Metal Analysis, 3rd Edition, Interscience, New York, p. 915 (1959).

102. Ibid., p. 918.

103. M. Benedict and T. H. Pigford, op. cit., p. 34.

BIBLIOGRAPHY (Concluded)

104. R. M. Barrer, Diffusion in and Through Solids, Cambridge Press, Cambridge, England, Chapter I (1951).

105. G. E. Boyd, A. W. Adamson, and L. S. Myers, Jr., J. Amer. Chem. Soc., 69, p. 2836 (1947).

106. A. H. Booth and G. T. Rymer, AECL Report AECL-692 (1958).

107. F. Helfferich, "Ion Exchange Kinetics" in Ion Exchange (J. A. Marinsky, Editor), Vol. 1, Dekker, New York, p. 68 (1966).

VITA

Milton Eccles McLain, Jr. was born in Marietta, Georgia on February 20, 1934. At the age of six years he moved to Buford, Georgia where he attended school, graduating from Buford High School in 1951. He graduated from Emory University in Atlanta, Georgia in 1955 with a Bachelor of Arts degree with a major in chemistry. While working for the Atomic Energy Division of Phillips Petroleum Company at the National Reactor Testing Station in Idaho Falls, Idaho in the field of reactor fuel reprocessing, he attended the University of Idaho. In 1960 he completed the requirements for a Master of Science degree in chemistry from this institution.

After several years of work in the general areas of radioisotope applications and radiochemistry, he returned to Atlanta in 1964 to work in the capacity of Laboratory Supervisor at the Nuclear Research Center of the Engineering Experiment Station at Georgia Tech. While continuing his employment at Georgia Tech he has pursued his graduate studies in the School of Nuclear Engineering in the areas of radiation and radioisotope technology. His principal research and development interests have been in new isotopes for medical applications and neutron activation analysis.

He married the former Miss Lila Jean Shirey of Chicago, Illinois in January 1956. They have three daughters, Loren, Kathryn, and Deborah. They live in Smyrna, Georgia.